

**Quantum dissipative dynamics with a  
Surrogate Hamiltonian.  
The method and applications**

D i s s e r t a t i o n

zur Erlangung des akademischen Grades  
d o c t o r   r e r u m   n a t u r a l i u m  
(dr. rer. nat.)  
im Fach Physik

eingereicht an der  
Mathematisch-Naturwissenschaftlichen Fakultät I  
Humboldt-Universität zu Berlin

von

**Dipl.-Phys. Christiane Koch**  
geboren am 8.1.1973 in Halle/Saale

Präsident der Humboldt-Universität zu Berlin:

Prof. Dr. J. Mlynek

Dekan der Mathematisch-Naturwissenschaftlichen Fakultät I:

Prof. Dr. M. Linscheid

Gutachter: 1. Priv.-Doz. Dr. Volkhard May  
2. Prof. Dr. Hans-Joachim Freund  
3. Prof. Ronnie Kosloff, Ph.D.

eingereicht am: 3. Juli 2002

Tag der mündlichen Prüfung: 18. Oktober 2002



When we invent worlds in physics we would have them to be mathematically consistent continuations of the visible world into the invisible...even when it is beyond human capability to decide which, if any, of those worlds is the true one.

*John S. Bell, Six possible worlds of quantum mechanics*



# Contents

<b>1</b>	<b>Introduction</b>	<b>5</b>
<b>2</b>	<b>The problem of quantum dissipation</b>	<b>9</b>
2.1	Statement of the problem . . . . .	9
2.2	Methods to treat quantum dissipation . . . . .	11
2.3	Non-Markovian approaches . . . . .	15
<b>3</b>	<b>The method of the Surrogate Hamiltonian</b>	<b>19</b>
3.1	The idea of the Surrogate Hamiltonian . . . . .	19
3.2	The interaction between system and bath . . . . .	25
3.3	Energy relaxation . . . . .	28
3.4	Dephasing . . . . .	36
<b>4</b>	<b>A first application: Charge transfer in a mixed valence system in solution</b>	<b>45</b>
4.1	Modeling a pump-probe charge transfer event . . . . .	46
4.2	Spectra . . . . .	51
4.2.1	Correlation functions and CW absorption . . . . .	51
4.2.2	Excitation by the pump pulse . . . . .	54
4.2.3	Transient absorption and emission . . . . .	56
4.3	The interplay of diabatic coupling and coupling to the bath – the turnover . . . . .	61
4.4	Discussion . . . . .	62
<b>5</b>	<b>Laser induced desorption</b>	<b>65</b>
5.1	Theoretical models for laser induced desorption from surfaces .	66
5.2	Laser induced desorption for NO/NiO(100) . . . . .	69
<b>6</b>	<b>NO/NiO(100): Prelude</b>	<b>73</b>
6.1	The primary system: NO on a NiO-cluster . . . . .	73
6.2	A model with diabatic coupling . . . . .	77
6.2.1	The idea of quasi-diabatization . . . . .	77
6.2.2	A three-state model with diabatic coupling . . . . .	78

6.3	A stochastic wave packet approach . . . . .	85
6.3.1	The Monte Carlo wave function method . . . . .	85
6.3.2	Results for NO/NiO(100) . . . . .	89
<b>7</b>	<b>NO/NiO(100): A Surrogate Hamiltonian treatment</b>	<b>97</b>
7.1	A microscopic model for bath and interaction . . . . .	97
7.2	How to obtain convergence . . . . .	102
7.2.1	Switching off the bath . . . . .	102
7.2.2	Increasing the number of modes and restricting simul- taneously allowed excitations . . . . .	104
7.2.3	Role of bath parameters . . . . .	105
7.2.4	Convergence of asymptotic observables . . . . .	113
7.3	Dependence on the experimentally adjustable parameters of the model . . . . .	121
7.3.1	Dipole strength . . . . .	121
7.3.2	Laser pulse . . . . .	124
7.4	Comparison with other approaches and with experiment . . .	128
<b>8</b>	<b>Summary</b>	<b>133</b>
<b>A</b>	<b>The representation and propagation of a wave function</b>	<b>137</b>
A.1	The grid representation . . . . .	137
A.2	The Chebychev propagator . . . . .	139
A.3	The split propagator . . . . .	140
A.4	Eigenfunctions through imaginary time propagation . . . . .	141
A.5	Spectral range . . . . .	142
A.6	Grid change . . . . .	143
<b>B</b>	<b>Perturbational treatment of weak fields: The window oper- ator</b>	<b>147</b>
<b>C</b>	<b>Tools for data analysis</b>	<b>151</b>
C.1	The Wigner function . . . . .	151
C.2	Filter Diagonalization . . . . .	155
<b>D</b>	<b>The Rotating wave approximation for a system coupled to a bath</b>	<b>157</b>
<b>E</b>	<b>The bit representation of the two level system bath</b>	<b>161</b>
E.1	The wave function . . . . .	161
E.2	The operators . . . . .	163
<b>F</b>	<b>Mapping a 2D bath onto 1D</b>	<b>167</b>

---

<b>G Numerics</b>	<b>171</b>
G.1 The structure of the program . . . . .	171
G.2 Parameters of the calculations . . . . .	172
<b>References</b>	<b>179</b>





# Chapter 1

## Introduction

Modern physics and chemistry cannot be thought of without quantum mechanics [1]. Recent experimental developments such as femtosecond spectroscopy allow for the direct observation of quantum dynamical phenomena, i.e. quantum coherences. The experiments are often performed in condensed phase, for example on atoms or small molecules which are solvated or adsorbed on a surface. The solvent or surface constitutes an environment for the system to be studied. The interaction of system and environment causes energy and phase exchange which leads to a perturbation or even destruction of the quantum coherences. This limits the applicability of quantum phenomena in prospective technologies. It has therefore been a major concern in research toward quantum computing.

The interaction with light is not only a source of information about the quantum dynamics of the atoms or molecules studied, it can also initiate charge and energy transfer processes, i.e. chemical reactions. A very simple example of a chemical reaction is the breaking of a bond between a molecule and a surface leading to the detachment and hence desorption of the molecule. Desorption furthermore constitutes an elementary step of catalysis. Compared to other condensed phase problems, a molecule adsorbed on a surface represents a very well characterized system due to the exceptionally developed techniques of surface science. The comprehensive information from experiment about the properties of the system as well as the environment is an invaluable prerequisite in the development of a theoretical model.

The interaction of a quantum system with its environment is the focus of

this thesis. It is treated with the recently developed Surrogate Hamiltonian method [2]. In a field as complex as quantum dissipation, approximations are unavoidable. It is the advantage of the Surrogate Hamiltonian over other available theoretical approaches that the approximation made is controllable and that correlations between system and environment can – at least in principle – be fully accounted for. To apply the Surrogate Hamiltonian to ultrafast charge transfer reactions, a generalization of the method was necessary.

This thesis is organized as follows: A brief overview over the field of quantum dissipation is given in the next chapter. The main problems are explained, and possible theoretical approaches are outlined. The Surrogate Hamiltonian as one potential method to treat quantum dissipative systems is introduced in Chapter 3 and the possible dissipative processes are discussed. A few basic examples are chosen to demonstrate, how the method works and, specifically, how reliable calculations of observables can be obtained. The different dissipative processes are combined in Chapter 4 and applied to a standard model of a charge transfer reaction in condensed phase, two nonadiabatically coupled harmonic oscillators interacting with a bath. While this model is adequate to capture all qualitative features of the reaction, it is sufficiently simple to verify the consistency of the description.

The theoretical description of laser induced desorption serves as next step in exploring the potential of the Surrogate Hamiltonian method. It is the subject of the second part of this thesis. The Surrogate Hamiltonian is employed to treat the electronic relaxation of the excited intermediate. This is a crucial step in the sequence of events leading to the cleavage of the molecule-surface bond which has so far been treated only semi-phenomenologically.

An introduction to the phenomenon of laser induced desorption is given in Chapter 5. The experimental and previous theoretical findings for the system NO/NiO(100) are briefly reviewed. The requirements which need to be met by a theoretical description, in particular with regard to recent experimental developments, are discussed. The separation into the primary system and the environment which causes the relaxation is given in Chapter 6, and possible excitation mechanisms induced by the laser pulse are discussed. Furthermore, results of two semi-phenomenological approaches

are presented. A Surrogate Hamiltonian treatment of the photodesorption dynamics is given in Chapter 7. In particular, a microscopic model for the interaction between system and environment is developed. The convergence of observables is discussed in detail, and the dependence on experimentally adjustable parameters is studied. Chapter 8 concludes.

A computer program for the numerical solution of the time-dependent Schrödinger equation has been developed on the basis of existing wave packet programs [3,4]. The necessary theoretical and numerical prerequisites as well as developments, and the parameters of the calculations are summarized in the Appendix. Throughout this thesis, atomic units with  $\hbar = 1$  have been employed. The simulations presented in this thesis were performed on the SGI workstation clusters of the Fritz-Haber-Institut der Max-Planck-Gesellschaft Berlin and of the Fritz Haber Research Center at the Hebrew University Jerusalem.



# Chapter 2

## The problem of quantum dissipation

### 2.1 Statement of the problem

When a quantum system interacts with its environment losing energy and phase, the term quantum dissipation is used. The latter process termed dephasing is a phenomenon specific for quantum mechanics while energy relaxation can also be observed for a classical system. Both processes lead to the creation of quantum correlations or entanglement between system and environment [5, 6]. It is entanglement which causes quantum dissipation to be an extremely difficult problem for which so far no standard method exists. However, entanglement is also the reason which makes quantum dissipation such an interesting field promising the exploitation of quantum coherences in applications such as quantum information processing [7, 8]. Since dissipative processes may destroy quantum coherences, they are furthermore at the core of the question of the border between the quantum and the classical world [9].

The statement of the problem of quantum dissipation assumes that the total system of interest can be separated into one or a few active degrees of freedom which shall be called the (primary) system and which are described by the Hamiltonian  $\hat{\mathbf{H}}_S$ , and many degrees of freedom called environment or bath modeled by  $\hat{\mathbf{H}}_B$ . The total problem is then described by a Hamiltonian,

$$\hat{\mathbf{H}}_{tot} = \hat{\mathbf{H}}_S + \hat{\mathbf{H}}_B + \hat{\mathbf{H}}_{SB} , \quad (2.1)$$

where  $\hat{\mathbf{H}}_{SB}$  describes the interaction between system and bath degrees of freedom. Examples can be found in nuclear magnetic resonance [10] and quantum optics [11, 12] where a spin or atom, respectively, is coupled to the electromagnetic field. Condensed matter phenomena constitute another class of applications of quantum dissipation. They range from surface photochemistry [13] to atoms or molecules caged in a cluster [14, 15] or photosynthesis [16, 17]. In these condensed matter phenomena, an electronic or vibrational excitation of the system couples to electronic or vibrational degrees of freedom of the environment. The excitation is often initiated by an external field, with for example ultraviolet laser pulses causing electronic excitation, i.e. charge transfer and infrared laser pulses causing vibrational excitation.

The separation into primary system and secondary environment is motivated by the fact that the environment itself is not interesting, and only its influence onto the system is important. The environment or bath is therefore treated implicitly and described by abstract modes. There are two general classes of commonly used bath descriptions: The bath modes can be modeled by harmonic oscillators [18] or by two level systems (TLS) [19]. The idea of a harmonic bath originates from a normal mode analysis combined with a weak system-bath coupling which guarantees that the harmonic approximation is valid [18]. A spin bath can be thought of as originating from a prediagonalization of the bath to its energy levels. It then represents the energy spectrum by a set of two level systems.

The harmonic bath has been the starting point of many system-bath studies which are based on either path integrals or semiclassical approximations [20, 21, 22]. The influence of the harmonic bath on the system is completely specified by the spectral density function  $J(\omega)$  [23]. The spectral density is the Fourier transform of the bath correlation function, and it is determined by the density of bath states weighted by the system-bath coupling. The harmonic oscillator is not a generic quantum system [24] (cf. Appendix C.1), and the harmonic bath is hence not a generic quantum bath. This is of particular importance for the modeling of pure dephasing [25]. However, the similarity between classical and quantum harmonic baths allows one to obtain the spectral density from classical molecular dynamics

(MD) simulations of the bath [26]. The treatment of rather complex, e.g. biological systems [27], thus becomes feasible, which is one reason for the popularity of the harmonic bath. Furthermore, the harmonic bath potentials in a path integral approach lead to Gaussian integrals which can be integrated out. This results in an analytical influence functional which describes the bath's influence on the system [18, 28, 29].

The spin bath is harder to construct, but for weak coupling and sufficiently low temperature it coincides with the harmonic bath [19]. For higher temperature the parameters of the spin bath can be obtained by a scaling term which is applied to the spectral density of the harmonic bath [19, 30, 31, 32, 33]:

$$J_{osc}(\omega) = \tanh\left(\frac{1}{2}\hbar\omega\beta\right) J_{spin}(\omega) \quad (2.2)$$

with inverse temperature  $\beta = 1/k_B T$ . The scaling relies on the equivalence of harmonic and spin baths in a second order cumulant expansion in the system-bath coupling [19, 30, 32]. This procedure is employed whenever one compares the spin to a harmonic bath (cf. Chapters 3 and 4). From the point of view of prediagonalization of the bath, the spin bath can also be considered in its own right. The coupling constants should then be derived from a microscopic model of the environment (cf. Chapter 7).

The decomposition into system and bath is non-trivial [34, 25], i.e. it needs to be chosen such that the bath is stable, that the interaction is non-singular, and that the Hamiltonian  $\hat{\mathbf{H}}_{tot}$  of the total system is well-defined and possesses a ground state. From such an analysis, it follows particularly that the commonly used model of a linearly coupled harmonic bath is singular in the infrared or low energy region. While the singularity might not affect energy relaxation, it becomes important in treating pure dephasing [25]. The treatment of pure dephasing does not pose a problem for the spin bath [19].

## 2.2 Methods to treat quantum dissipation

Historically, there have been two different approaches to the problem of open quantum systems, perturbation theory and the dynamical semigroup formalism. Perturbation theory [22, 23] starts from Eq. (2.1) and assumes the

coupling between system and bath,  $\hat{\mathbf{H}}_{SB}$ , to be weak. Equations of motion for the reduced density operator, i.e. the density operator of the system,

$$\hat{\rho}_S = \text{tr}_B\{|\Psi_{tot}\rangle\langle\Psi_{tot}|\}, \quad (2.3)$$

can then be derived which depend upon system operators only.  $|\Psi_{tot}\rangle$  is the wave function of the total system, and  $\text{tr}_B$  denotes the trace over the bath degrees of freedom. The derivation in a most general sense is done by the projection operator technique [35, 23].

In the interaction picture, the equation of motion of the reduced density operator is given in terms of the total density operator  $\hat{\rho}^I$ ,

$$\frac{\partial}{\partial t}\hat{\rho}_S^I(t) = -\frac{i}{\hbar}[\hat{\mathbf{H}}_{SB}^I(t), \hat{\rho}^I(t)]_- . \quad (2.4)$$

An operator  $\mathbb{P}$  projecting onto the Hilbert space of the primary system and its orthogonal complement are defined,  $\mathbb{P}\hat{\mathbf{O}} = \hat{\mathbf{O}}_B \text{tr}_B\{\hat{\mathbf{O}}\}$  and  $\mathbb{Q} = \mathbb{1} - \mathbb{P}$ .  $\hat{\mathbf{O}}$  denotes an arbitrary operator acting on the total space,  $\text{tr}_B\{\hat{\mathbf{O}}\}$  denotes the part of  $\hat{\mathbf{O}}$  acting on the Hilbert space of the primary system and  $\hat{\mathbf{O}}_B$  is a bath operator. By applying these operators, the equation of motion of the total density operator can be split into system and bath parts,

$$\begin{aligned} \frac{\partial}{\partial t}\hat{\rho}_S^I(t) &= \text{tr}_B\left\{\mathbb{P}\frac{\partial}{\partial t}\hat{\rho}^I(t)\right\} \\ &= -\frac{i}{\hbar}\text{tr}_B\left\{[\hat{\mathbf{H}}_{SB}^I(t), \hat{\rho}_B^{eq}\hat{\rho}_S^I(t) + \mathbb{Q}\hat{\rho}^I(t)]_-\right\}, \end{aligned} \quad (2.5)$$

and

$$\mathbb{Q}\frac{\partial}{\partial t}\hat{\rho}^I(t) = -\frac{i}{\hbar}\mathbb{Q}[\hat{\mathbf{H}}_{SB}^I, \hat{\rho}_B^{eq}\hat{\rho}_S^I + \mathbb{Q}\hat{\rho}^I]_-, \quad (2.6)$$

where for simplicity the bath has been assumed to stay in equilibrium. Eq. (2.6) can be solved formally and inserted into Eq. (2.5). When approximated to first order in the system-bath coupling, this formal solution is given by

$$\mathbb{Q}\hat{\rho}^I(t) \approx \mathbb{Q}\hat{\rho}^I(0) - \frac{i}{\hbar}\mathbb{Q}\int_0^t d\tau \mathbb{Q}[\hat{\mathbf{H}}_{SB}^I, \hat{\rho}_B^{eq}\hat{\rho}_S^I]_- . \quad (2.7)$$

A second order approximation for the density operator of the system is then arrived at,

$$\begin{aligned} \frac{\partial}{\partial t}\hat{\rho}_S^I(t) &= -\frac{i}{\hbar}\text{tr}_B\left\{\hat{\rho}_B^{eq}[\hat{\mathbf{H}}_{SB}^I(t), \hat{\rho}_S^I(t)]_-\right\} \\ &\quad - \frac{1}{\hbar^2}\int_0^t d\tau \text{tr}_B\left\{[\hat{\mathbf{H}}_{SB}^I(t), \mathbb{Q}[\hat{\mathbf{H}}_{SB}^I(\tau), \hat{\rho}_B^{eq}\hat{\rho}_S^I]_-]_-\right\}, \end{aligned} \quad (2.8)$$



where possible initial correlations,  $\mathbb{Q}\hat{\rho}^I(0)$ , have been neglected. The first term on the right-hand side of Eq. (2.8) is of first order in the system-bath coupling. It corresponds to a mean field approximation of the bath and leads to a shift in energy only. To model relaxation, the second order term in Eq. (2.8) is necessary. If the interaction Hamiltonian can be written as a sum of products of system operators  $\hat{\mathbf{A}}_j$  and bath operators  $\hat{\mathbf{B}}_j$ ,

$$\hat{\mathbf{H}}_{SB} = \sum_j \hat{\mathbf{A}}_j \hat{\mathbf{B}}_j, \quad (2.9)$$

and bath correlation functions are introduced,

$$C_{jk}(t) = \langle \Delta \hat{\mathbf{B}}_j(t) \Delta \hat{\mathbf{B}}_k(0) \rangle_B, \quad \Delta \hat{\mathbf{B}}_j(t) = \hat{\mathbf{B}}_j(t) - \langle \hat{\mathbf{B}}_j \rangle_B, \quad (2.10)$$

Eq. (2.8) can be rewritten,

$$\begin{aligned} \frac{\partial}{\partial t} \hat{\rho}_S^I(t) = & -\frac{i}{\hbar} \sum_j \langle \hat{\mathbf{B}}_j \rangle_B [\hat{\mathbf{A}}_j^I, \hat{\rho}_S^I(t)]_- \\ & - \frac{1}{\hbar^2} \sum_{jk} \int_0^t d\tau \{ C_{jk}(t-\tau) [\hat{\mathbf{A}}_j^I(t), \hat{\mathbf{A}}_k^I(\tau) \hat{\rho}_S^I(\tau)]_- \\ & + C_{jk}^*(t-\tau) [\hat{\mathbf{A}}_j^I(t), \hat{\rho}_S^I(\tau) \hat{\mathbf{A}}_k^I(\tau)]_- \}. \end{aligned} \quad (2.11)$$

Eq. (2.11) is called the Quantum Master Equation. From the definition of the bath correlation functions, it is obvious that dissipation is caused by quantum fluctuations,  $\Delta \hat{\mathbf{B}}_j(t)$ , of the bath. For a bath of harmonic oscillators, analytical expressions for the correlation functions can be derived.

If the Quantum Master Equation is transformed from the interaction into the Schrödinger picture, the system density operator appears with a retarded time argument in the right-hand side,  $\hat{\rho}_S(t-\tau)$ , i.e. Eq. (2.11) is *non-Markovian*. These memory effects are the price to pay for the reduction of the equation of motion of the total system to a reduced equation of motion of the primary system only. They describe the correlations between system and bath. In the derivation of Eq. (2.11) weak coupling between system and bath has been assumed. The projection operator technique offers a rigorous way to obtain higher-order equations, and in principle an exact expansion is possible.

An alternative to the projection operator technique is given by a cumulant expansion in the system-bath coupling [36]. However, the two approaches are

equivalent only when considered up to infinite order [37]. Equations obtained from higher-order perturbation theory become even more involved, and already solution of Eq. (2.11) in the Markov approximation, i.e. neglecting memory effects, poses a computational challenge [38].

If the Markov approximation is made, and the eigenstates of the system are chosen as the basis, the second term in the right-hand side of Eq. (2.11) can be written in terms of a tetradic matrix  $R_{ab,cd}$  called the Redfield tensor [22, 23]. It allows for a classification of dissipative processes: The matrix elements  $R_{aa,cc}$  describe energy relaxation, while  $R_{ab,ab}$  describe dephasing. All other elements describe mixing of coherences (off-diagonal density matrix elements) and transformation of coherences into populations (diagonal density matrix elements) and vice versa. It turns out, however, that the reduced density operator does not obey complete positivity, e.g. [39]. This obscures the interpretation of diagonal matrix elements of  $\hat{\rho}_S$  as probabilities.

The condition of complete positivity together with the Markov assumption is the starting point of the second approach [40, 41]. The time dependence of the reduced density operator in this approach is given by

$$\hat{\rho}_S(t) = \Lambda(t)\hat{\rho}_S(0) = e^{(\mathcal{L}_0 + \mathcal{L}_D)t}\hat{\rho}_S(0), \quad (2.12)$$

where  $\Lambda(t) = e^{\mathcal{L}t}$  is the propagation (super)operator and  $\mathcal{L}(\circ) = -\frac{i}{\hbar}[\hat{\mathbf{H}}, \circ]_-$  the Liouville (super)operator which can be separated into a system, i.e. Hamiltonian part  $\mathcal{L}_0$  and a dissipative part  $\mathcal{L}_D$ . The term superoperator has been introduced to differentiate operators acting on operators from operators acting on wave functions [36]. The propagation superoperator must preserve the positivity of  $\hat{\rho}_S$  for all times  $t > 0$ , and the Markov property can be written as  $\Lambda(t)\Lambda(s) = \Lambda(t+s)$  for all times  $t, s > 0$ . Mathematically, the latter is the definition of the semigroup property after which the method was named. It was shown in [40, 41] that these conditions are fulfilled if the Liouville (super)operator is of the form,

$$\mathcal{L}\hat{\rho}_S = -\frac{i}{\hbar}[\hat{\mathbf{H}}_S, \hat{\rho}_S]_- + \frac{1}{2} \sum_{jk} A_{jk} \left( [\hat{\mathbf{F}}_j \hat{\rho}_S, \hat{\mathbf{F}}_k^+]_- + [\hat{\mathbf{F}}_k, \hat{\rho}_S \hat{\mathbf{F}}_j^+]_- \right), \quad (2.13)$$

which can be diagonalized to the so called Lindblad form,

$$\mathcal{L}\hat{\rho}_S = -\frac{i}{\hbar}[\hat{\mathbf{H}}_S, \hat{\rho}_S]_- + \sum_j \Gamma_j \left( \hat{\mathbf{V}}_j \hat{\rho}_S \hat{\mathbf{V}}_j^\dagger - \frac{1}{2} [\hat{\mathbf{V}}_j^\dagger \hat{\mathbf{V}}_j, \hat{\rho}_S]_+ \right), \quad (2.14)$$

where the  $\hat{\mathbf{V}}_k$  are system operators modeling dissipation and  $\Gamma_j$  are coupling constants. The operators  $\hat{\mathbf{V}}_k$  have to be chosen semi-phenomenologically. Three specific cases exist [42]: Unitary operators describe Poissonian processes, while Hermitian operators describe Gaussian random processes. Resonant energy transfer is described if the  $\hat{\mathbf{V}}_k$  are creation or annihilation operators of the system.

Both perturbation theory and the semigroup formalism lead to an equation of motion for the density operator of the system which needs to be solved. A description based on the system wave function with a more favorable scaling in the numerical solution is also possible. The influence of the bath on the system is then treated as a stochastic force and the method is hence termed stochastic wave packet or Monte Carlo wave function (MCWF) method [43, 44, 45, 46]. The MCWF method was shown to be equivalent to the semigroup formalism [43, 44, 45]. This equivalence will be utilized in Chapter 6.

While the Markov approximation is intrinsic for the semigroup approach, the Quantum Master Equation in general is non-Markovian. Since, however, the solution of integro-differential equations is far from being straightforward, the Quantum Master Equation is most often used in its Markovian form. The Markov approximation assumes that bath correlations decay on a timescale much shorter than all other timescales involved. This is not necessarily true in, for example, the case of moderate or strong coupling between system and bath. The next section therefore briefly reviews available non-Markovian approaches and relates them to the Surrogate Hamiltonian method which will be described in detail in Chapter 3.

## 2.3 Non-Markovian approaches

An obvious way to go beyond the Quantum Master Equation in the Markovian limit is opened up by higher-order perturbation theory. It is, however, of practical use only, if an explicit averaging over the bath can be performed such that a closed set of equations for the reduced density operator is obtained. This has recently been accomplished to fourth-order [37, 47]. Two simple model systems in the high temperature Markovian bath limit have

been analyzed [37]. Fourth-order corrections in the low temperature regime and for more realistic systems still have to be investigated.

Within second order perturbation theory different approaches exist to treat the memory kernel in the Quantum Master Equation. One possibility consists in transforming the integro-differential equation of motion of the reduced density operator into an algebraic equation which can be solved with considerably less numerical effort. This transformation can be achieved by expanding the reduced density operator in a suitable polynomial basis, e.g. Laguerre polynomials [48]. The method is limited, however, to weak field excitation. In this case, the excitation can be modeled by a source term in the equation of motion replacing off-diagonal density matrix elements [48]. If the interaction with strong external fields shall be considered, the non-Markovian equation of motion for the system density matrix can be transformed into a set of coupled Markovian equations for the reduced density matrix and auxiliary density matrices which incorporate the memory effects [49]. This transformation rests on a special parameterization of the spectral density. The number of needed auxiliary density matrices depends on coupling strength and temperature. Low temperature requires a large number of auxiliary density matrices. The method is thus best suited for high temperature calculations. No further assumptions other than the weak coupling approximation need to be made [49]. However, solving the equation of motion for the density matrix alone requires considerable numerical effort, and the effort is further increased by solving the equations of motion for the auxiliary density matrices.

In the derivation of the Quantum Master Equation, there is some arbitrariness in the choice of the projection operator  $\mathbb{P}$  [50]. The choice of  $\mathbb{P}$  in particular may determine the choice of initial conditions [50, 51]. Recently, a non-Hermitian projection operator has been proposed to include the treatment of memory in the bath [52]. The non-Hermiticity leads to bath modes with a finite lifetime. The trace over the bath is approximated by a statistical average. The proposal lacks, however, a procedure to get the parameters of this statistical average from first principles.

A perspective onto quantum dissipative dynamics completely different from the approach of perturbation theory is given by the path integral for-

mulation of quantum mechanics [18, 28, 29]. The wave function or density matrix at time  $t$  is then given by the quantum mechanical propagator which is the sum over paths starting at a specified initial point at time  $t = 0$ . For a linearly coupled bath of harmonic oscillators, the integration over bath variables can be done analytically leading to an influence functional [18]. The reduction from the total system to the reduced description, which in perturbation theory led to the memory kernel in the Quantum Master Equation, for path integrals leads to an influence functional containing correlations in time between different paths [27]. Non-Markovian effects can therefore in principle be accounted for. This might, however, be limited by numerical feasibility. The bath correlation time enters as convergence parameter which allows for *controlling* the validity of the Markov approximation. Time-local integration for non-Markovian dynamics can be achieved by introducing a stochastic potential and integrating along a complex instead of a real contour [53]. However, this method has so far only been applied to model systems. The application of (real time) path integrals has long been limited by a numerical problem called the "sign problem", which is caused by the rapid phase oscillations of the integrand. For the harmonic bath, improved propagators can be constructed using physically motivated reference systems [27]. The numerical evaluation of a multi-dimensional integral nevertheless is computationally challenging, limiting the applications of path integrals to relatively simple model systems. Furthermore, the treatment of time-dependent Hamiltonians is not possible. Path integrals are therefore best suited for the high temperature limit when the main contribution to the propagator comes from the classical path and the quantum corrections around the classical path are small [54]. The fact that path integral results are numerically exact and that all approximations are made when specifying the Hamiltonian makes path integral calculations a popular benchmark for newly developed methods [49, 31, 47].

The Surrogate Hamiltonian method [2] is complementary to these approaches which start from a reduced description of the system and improve on it by the various means. This is particularly interesting in light of the rigorous proof that a reduced dynamics in general does not exist for quantum systems [55]. For the Surrogate Hamiltonian the starting point is a

description of the total system and bath. This description is transformed and approximated in a controlled way yielding a model whose treatment is numerically feasible but whose validity is limited in time (cf. Chapter 3). No weak coupling assumption needs to be made, and the treatment of time-dependent fields can be included naturally into the description. Different from the above listed methods the strength of the Surrogate Hamiltonian lies in the low temperature regime. The Surrogate Hamiltonian method is outlined in Chapter 3, and its advantages and disadvantages are discussed.

The mentioned approaches are a few examples of existing methods for going beyond the Markov approximation and possibly the weak coupling limit. Each method is well-suited for particular limiting cases. It is therefore crucial to consider the physical processes to be studied to decide which of the currently available methods is best-suited for the problem at hand.

# Chapter 3

## The method of the Surrogate Hamiltonian

### 3.1 The idea of the Surrogate Hamiltonian

When the total system is separated into primary system and bath parts, its Hamiltonian can be written as

$$\hat{\mathbf{H}} = \hat{\mathbf{H}}_S + \hat{\mathbf{H}}_{SF}(t) + \hat{\mathbf{H}}_{SB} + \hat{\mathbf{H}}_{BF}(t) + \hat{\mathbf{H}}_B , \quad (3.1)$$

where  $\hat{\mathbf{H}}_S$  is the Hamiltonian of the system and  $\hat{\mathbf{H}}_B$  the Hamiltonian of the bath. The coupling between system and bath degrees of freedom is described by the interaction term  $\hat{\mathbf{H}}_{SB}$ . A time-dependent external field can be applied to the total system, its interaction is described by the terms  $\hat{\mathbf{H}}_{SF}(t)$  and  $\hat{\mathbf{H}}_{BF}(t)$ .  $\hat{\mathbf{H}}_{BF}(t)$  is often neglected, here it is mentioned to allow for a complete discussion of excitation mechanisms.

In quantum mechanics the effort to solve a problem scales exponentially with the number of degrees of freedom. Except for a few special, analytically solvable cases, Eq. (3.1) therefore states an extremely complicated problem for which approximations are unavoidable. The suggestive separation of the total problem into (primary) system and (secondary) bath itself is still exact. It points, however, to the fact that the bath degrees of freedom themselves are not interesting, and only their influence on the system is important. The first step of approximation, therefore, consists in an implicit description of the bath by abstract, representative modes.

The core idea of the Surrogate Hamiltonian [2] is the truncation of the infinite number of bath modes in a well-defined way. This is possible if the transformation from true to representative modes,

$$\hat{\mathbf{H}}_B \sim \sum_{k=1}^{\infty} \hat{\mathbf{n}}_k^{\text{true}} \longrightarrow \sum_{k=1}^N \hat{\mathbf{n}}_k^{\text{rep}}, \quad (3.2)$$

is chosen such that the modes which interact strongest with the system are always included in the description. This leads to a new, "Surrogate" Hamiltonian for the total system which generates the time evolution of a "surrogate" wave function. Observables are associated with operators of the primary system. They can be determined from the (reduced) system density operator:

$$\hat{\rho}_S(Q, Q') = \text{tr}_B\{|\Psi(Q)\rangle\langle\Psi(Q')|\} \quad (3.3)$$

where  $\text{tr}_B\{ \}$  denotes a partial trace over the bath degrees of freedom. The system density operator is thus constructed from the total system-bath wave function while only this wave function is propagated. The explicit construction of the reduced density operator is only necessary if the operator corresponding to the desired observable is not diagonal in coordinate space. This *a posteriori* construction of the density operator is different from most other approaches to dissipative quantum dynamics [10, 21, 23] where the trace over the bath is performed before time propagation. Correlations between system and bath may then be neglected [55] and special effort is required to include them using, for example, auxiliary density matrices [49]. As a consequence of describing a total, if surrogate system, all correlations between system and bath for which the Hamiltonian allows are included in the Surrogate Hamiltonian method. Furthermore, since the Schrödinger equation for a wave function is solved, the treatment of a time-dependent external field poses no additional problems.

In the limit of an infinite number of bath modes, the Surrogate Hamiltonian is completely equivalent to the original, "true" Hamiltonian. Since, at least in principle, the number of modes  $N$  can be increased, it is possible to check convergence. The number of bath modes used in the calculations is comparatively small. Weiss claims that about twenty modes are usually a satisfactory approximation of infinity [21]. This statement should certainly



be qualified by the timescale of the system, the bath and the external field involved and by the interaction strength between system and bath. The truncation leading to the Surrogate Hamiltonian, Eq. (3.2), relies on a time-energy uncertainty argument (cf. Fig. 3.1): In a finite time,  $t \ll \infty$ , the system can only resolve a finite number,  $N \ll \infty$ , of bath states and not the full density of states of the bath. The sampling density in energy of the finite set of bath states is determined by the inverse of the time interval. This argument leads to two observations – the Surrogate Hamiltonian is well-suited for the description of ultrashort events, and the number of needed modes increases with the interaction strength between system and bath. Strong and intermediate coupling strengths might therefore pose a computational challenge. From the above derivation, it is clear, however, that no weak coupling assumption was needed. In addition, and this is the major difference to standard approaches, and therefore the major advantage, the Surrogate Hamiltonian method yields a controllable approximation.

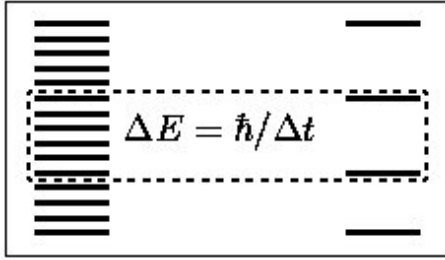


Figure 3.1: In a finite time the system can only resolve a finite number of energy levels of the bath.

The two level system (TLS) bath is described by the Hamiltonian

$$\hat{\mathbf{H}}_B = \mathbb{1}_S \otimes \sum_i \varepsilon_i \hat{\sigma}_i^+ \hat{\sigma}_i \quad (3.4)$$

with  $\hat{\mathbf{n}}_i = \hat{\sigma}_i^+ \hat{\sigma}_i$  the occupation number operator and  $\varepsilon_i$  the energy of the  $i$ th bath mode.  $\mathbb{1}_S$  denotes the identity in the Hilbert space  $\mathcal{H}_S$  of the system, i.e.  $\hat{\mathbf{H}}_B$  acts on the total Hilbert space  $\mathcal{H}_S \otimes \mathcal{H}_B$ .

For  $N$  bath modes the Hilbert space  $\mathcal{H}_B$  of the bath has dimension  $2^N$ . This results from a single TLS or spin- $\frac{1}{2}$  being defined on a two-dimensional Hilbert space and the possibility to combine each of the two basis states for all  $N$  modes. The dimension of the total Hilbert space  $\mathcal{H}_S \otimes \mathcal{H}_B$  is then given by the product of the dimensions of  $\mathcal{H}_S$  and  $2^N$ . If, for example, the state of the system is described by a wave function represented on a grid (cf. Appendix A.1) and the dimension of the grid is  $N_g$ , the state of the total system is described by  $2^N N_g$ -dimensional wave functions. Obviously, this dimension quickly gets very large when the number of bath modes  $N$  is increased. However, considering all  $2^N$  possibilities of combining the bath

modes corresponds to considering *all* possible system-bath correlations which might not be necessary. The number of simultaneously allowed excitations can then be restricted. In an extreme case, only single excitations are considered. This reduces the dimension of the total Hilbert space from  $2^N$  to  $N+1$ . The approximation made can again be checked by increasing the number of simultaneously allowed excitations, i.e. it is controllable.

The basis of the TLS Hilbert space was chosen to be the spin-down and spin-up states. Spin-up corresponds to the TLS being excited while for spin-down the TLS is deexcited. This representation proved to be particularly useful, since the index labeling the  $2^N$  components of the wave function contains the information of the TLS being excited or deexcited, respectively. The details of this representation and the restriction of simultaneously allowed excitations are given in Appendix E.

As explained in Section 2.1, there are two possibilities to look at the TLS bath. So far it has been introduced in its own right, assuming the eigenvalues  $\varepsilon_i$  and eigenstates  $n_i$  have been obtained in a prediagonalization of the bath. This perspective will be used in Chapter 7. However, a TLS can also be thought of as a low temperature approximation to a harmonic oscillator. At low temperature, only the ground and first excited state of a harmonic oscillator should be significantly populated. The TLS bath can therefore be viewed as a low temperature approximation to a harmonic oscillator bath, and the parameters of the two can be connected. In particular, the role of the spectral density for the TLS bath should become clear. This approach has been pursued when the Surrogate Hamiltonian was first introduced [2] and it shall briefly be reviewed here.

The starting point is the Heisenberg equations of motion for the primary system. For simplicity, the primary system is taken to be one-dimensional with Hamiltonian

$$\hat{\mathbf{H}}_S = \hat{\mathbf{T}} + V(\hat{\mathbf{R}}) = \frac{\hat{\mathbf{P}}^2}{2m} + V(\hat{\mathbf{R}}) . \quad (3.5)$$

A generalization to more nuclear degrees of freedom is straightforward, and the treatment of more than electronic ground state dynamics will be discussed in the following section. The interaction between system and bath can generally be written as a sum of products of system and bath operators [23, 56],

$$\hat{\mathbf{H}}_{SB} = f(\hat{\mathbf{R}}) \sum_i \hat{\mathbf{K}}_i \quad (3.6)$$

with Hermitian operators  $\hat{\mathbf{K}}_i$  acting on the bath Hilbert space. The  $\hat{\mathbf{K}}_i$  can be written in terms of creation and annihilation operators, for simplicity real coupling matrix elements and a linear combination of creation and annihilation operators are assumed. Higher order terms will be discussed in Section 3.2. The interaction Hamiltonian is then given by

$$\hat{\mathbf{H}}_{SB} = f(\hat{\mathbf{R}}) \sum_i V_i \left( \hat{\mathbf{A}}_i^+ + \hat{\mathbf{A}}_i \right), \quad (3.7)$$

where  $\hat{\mathbf{A}}_i^+$  and  $\hat{\mathbf{A}}_i$  are creation and annihilation operators, respectively, of an abstract bath mode  $i$ . The interaction is characterized by the coupling function  $f(\hat{\mathbf{R}})$  and coupling constants  $V_i$ . The Heisenberg equations of motion for the system are then given by

$$\begin{aligned} \frac{d}{dt} \hat{\mathbf{R}} &= \frac{\hat{\mathbf{P}}}{m}, \\ \frac{d}{dt} \hat{\mathbf{P}} &= -\frac{d}{d\hat{\mathbf{R}}} V(\hat{\mathbf{R}}) - \frac{d}{d\hat{\mathbf{R}}} f(\hat{\mathbf{R}}) \sum_i V_i \left( \hat{\mathbf{A}}_i^+ + \hat{\mathbf{A}}_i \right). \end{aligned} \quad (3.8)$$

For infinitely many modes, the sum in Eq. (3.8) can be replaced by an integral,  $\sum_i \longrightarrow \int d\varepsilon \rho(\varepsilon)$ ,

$$\sum_i V_i \left( \hat{\mathbf{A}}_i^+ + \hat{\mathbf{A}}_i \right) = \int d\varepsilon \rho(\varepsilon) \sqrt{J(\varepsilon)} \left( \hat{\mathbf{a}}^+(\varepsilon) + \hat{\mathbf{a}}(\varepsilon) \right), \quad (3.9)$$

where the density of states  $\rho(\varepsilon)$  and the spectral density  $J(\varepsilon)$  of the bath have been introduced. The creation operators are related by

$$\hat{\mathbf{a}}^+(\varepsilon) = \frac{1}{\sqrt{J(\varepsilon)}} \sum_i V_i \hat{\mathbf{A}}_i^+ \delta(\varepsilon - \varepsilon_i), \quad (3.10)$$

and an analogous equation holds for the annihilators. The new operators  $\hat{\mathbf{a}}^+(\varepsilon)$ ,  $\hat{\mathbf{a}}(\varepsilon)$  can be viewed as creator and annihilator, respectively, of an interaction mode. They enter the new, *Surrogate* Hamiltonian describing the total system+bath,

$$\begin{aligned} \hat{\mathbf{H}}_{Surr} &= \hat{\mathbf{T}} + V(\hat{\mathbf{R}}) + \int d\varepsilon \rho(\varepsilon) \varepsilon \hat{\mathbf{a}}^+(\varepsilon) \hat{\mathbf{a}}(\varepsilon) \\ &\quad + f(\hat{\mathbf{R}}) \int d\varepsilon \rho(\varepsilon) \sqrt{J(\varepsilon)} \left( \hat{\mathbf{a}}^+(\varepsilon) + \hat{\mathbf{a}}(\varepsilon) \right). \end{aligned} \quad (3.11)$$

If the spectral density is of finite support  $[\varepsilon_0, \varepsilon_c]$ , the integrals in Eq. (3.11) can be sampled by a finite number of energies,  $N \ll \infty$ . In the limit  $N \rightarrow \infty$  the full system-bath dynamics is then recovered. The finite sampling  $\varepsilon_i$ ,  $i = 0, \dots, N-1$  specifies the energies at which creation and annihilation operators are defined,

$$\hat{\mathbf{a}}_i^+ = \hat{\mathbf{a}}^+(\varepsilon_i), \quad \hat{\mathbf{a}}_i = \hat{\mathbf{a}}(\varepsilon_i) \quad (3.12)$$

and

$$v_i \hat{\mathbf{a}}_i^+ \rho(\varepsilon_i) = \sqrt{J(\varepsilon_i)} \hat{\mathbf{a}}^+(\varepsilon_i), \quad \text{and} \quad \text{c.c.} \quad (3.13)$$

The interaction of mode  $i$  with the system is then given by

$$v_i = \sqrt{J(\varepsilon_i)/\rho(\varepsilon_i)}. \quad (3.14)$$

A similar procedure to obtain the coupling constants is followed in [57]. The discretized Surrogate Hamiltonian then reads [2]

$$\hat{\mathbf{H}}_{Surr} = \hat{\mathbf{T}} + V(\hat{\mathbf{R}}) + \sum_{i=0}^{N-1} \varepsilon_i \hat{\mathbf{a}}_i^+ \hat{\mathbf{a}}_i + f(\hat{\mathbf{R}}) \sum_{i=0}^{N-1} v_i (\hat{\mathbf{a}}_i^+ + \hat{\mathbf{a}}_i). \quad (3.15)$$

The spectral density  $J(\varepsilon)$  enters the above expressions, Eq. (3.9) and Eq. (3.10) as a normalization factor. Unfortunately, as no unique definition of the spectral density exists, some care must be devoted to ensure the same definition is used when comparing different methods. For the harmonic oscillator bath, the spectral density is introduced as Fourier transform of the bath correlation function [58, 23]. Depending on the definition of the integrals, it may or may not contain a factor  $\pi/2$  and the density of states. The definition of spectral density is chosen to include the density of states [58, 57],

$$J(\varepsilon) = \sum_i |V_i|^2 \rho(\varepsilon) \delta(\varepsilon - \varepsilon_i). \quad (3.16)$$

The meaning of spectral density then becomes obvious: It is the system-bath coupling weighted by the density of states, i.e. it specifies the effective interaction. The influence of the bath on the system is thus fully characterized by  $J(\varepsilon)$ . However, the transformation of the sum into an integral, Eq.(3.9), is subtle since depending on the system-bath interaction it might involve singularities [25]. The popularity of the spectral density is probably explained

by its straightforward application in the harmonic oscillator bath model (cf. Section 2.2). From the point of view of the Surrogate Hamiltonian with finite sampling, it seems rather like a detour. It is then more straightforward to approach the problem by directly specifying the system-bath interaction.

Eq. (3.15) and Eq. (3.14) or Eq. (3.15) together with a microscopic model for the interaction are the starting point of the simulations. Since TLS are used as bath modes, the abstract operators  $\hat{\mathbf{a}}_i^+$ ,  $\hat{\mathbf{a}}_i$  are replaced by TLS or spin operators  $\hat{\boldsymbol{\sigma}}_i^+$ ,  $\hat{\boldsymbol{\sigma}}_i$ . The time-dependent Schrödinger equation with  $\hat{\mathbf{H}}_{Surr}$  is solved for a wave function, or rather a spinor of  $2^N$  wave functions on a grid (cf. Appendix A.1). So far, temperature has been neglected. If a finite temperature shall be considered, a Boltzmann average,

$$\hat{\rho}(0) = \sum_j \frac{e^{-\beta E_j}}{Z} |\Psi_j\rangle \langle \Psi_j| \quad (3.17)$$

with  $\beta = 1/k_b T$  and  $Z = \sum_j e^{-\beta E_j}$ , needs to be performed when constructing the density operator, Eq. (3.3), of the system,

$$\hat{\rho}_s(t) = \text{tr}_B \left\{ \hat{\mathbf{U}}(t) \hat{\rho}(0) \hat{\mathbf{U}}^\dagger(t) \right\} . \quad (3.18)$$

$E_j$  is the energy of the  $j$ th eigenfunction  $|\Psi_j\rangle$ , and  $\hat{\mathbf{U}}(t) = \exp(-i\hat{\mathbf{H}}t)$  denotes the time evolution operator. The initial condition for the density operator  $\hat{\rho}(0)$  is obtained by calculating the lowest energy eigenfunctions of the combined system-bath Hamiltonian.

So far the general idea of the Surrogate Hamiltonian has been discussed. The next section will show how different dissipative processes are modeled within the Surrogate Hamiltonian framework.

## 3.2 The interaction between system and bath

In condensed phase problems nuclear and electronic degrees of freedom are usually separated. In addition to energy relaxation known from classical mechanics, a quantum system can also display phase relaxation. Energy relaxation is traditionally characterized by a time  $T_1$  while dephasing is characterized by  $T_2$  [10]. There are then four different dissipative processes which have to be modeled: nuclear relaxation (nr), electronic relaxation or quench-

ing (er), nuclear dephasing (nd), and electronic dephasing (ed),

$$\hat{\mathbf{H}}_{SB} = \hat{\mathbf{H}}_{SB}^{nr} + \hat{\mathbf{H}}_{SB}^{er} + \hat{\mathbf{H}}_{SB}^{nd} + \hat{\mathbf{H}}_{SB}^{ed} . \quad (3.19)$$

The system Hamiltonian  $\hat{\mathbf{H}}_S$  shall be described by two electronic states and one nuclear degree of freedom. The generalization to more electronic levels and more nuclear degrees of freedom is straightforward.

Energy relaxation is an exchange of energy between the system and bath which will eventually lead to thermal equilibrium. The process can be imagined as taking energy out of the primary system and simultaneously creating an excitation in a bath mode ( $\hat{\sigma}_i^+$ ). The inverse process of destroying an excitation in a bath mode ( $\hat{\sigma}_i$ ) and transferring this energy to the system is also possible. The operator describing the exchange of energy of the bath modes with the nuclear degree of freedom is a generalization to two electronic surfaces of the interaction term of Eq. (3.7),

$$\hat{\mathbf{H}}_{SB}^{nr} = \begin{pmatrix} f_g(\hat{\mathbf{Q}}) & 0 \\ 0 & f_e(\hat{\mathbf{Q}}) \end{pmatrix} \otimes \sum_i d_i^{nr} (\hat{\sigma}_i^+ + \hat{\sigma}_i) , \quad (3.20)$$

where  $f_{e/g}(\hat{\mathbf{Q}})$  are functions of the system displacement operator. This means that the system-bath coupling can be different for the ground or excited state potential. As described in the previous section, the constants  $d_i^{nr}$  can be related to the bath spectral density,

$$d_i^{nr} = \sqrt{J(\varepsilon_i)/\rho(\varepsilon_i)} . \quad (3.21)$$

For electronic quenching, the electronic degree of freedom couples to the bath creation and annihilation operators: Electronic excitation of the system is created or destroyed by creating or annihilating excitation in a bath mode,

$$\hat{\mathbf{H}}_{SB}^{er} = \frac{1}{2} \begin{pmatrix} 0 & 1 \\ 1 & 0 \end{pmatrix} \otimes \sum_i d_i^{er} (\hat{\sigma}_i^+ + \hat{\sigma}_i) . \quad (3.22)$$

A similar relation as Eq. (3.21) holds for the  $d_i^{er}$ , but the spectral density will be different. Alternatively, also the  $d_i^{er}$  can be derived from a microscopic model of the interaction without reference to the spectral density (cf. Chapter 7).

Dephasing is a process caused by an almost elastic interaction between the system and the bath which alters the accumulated phase of the system but

does not change the energy of the bath. A qualitative picture is therefore based on an almost elastic exchange of energy between two bath modes. This is described by creating an excitation in one mode at the expense of an excitation in another mode, and vice versa. The modes must be almost degenerate. This process modulates the excitation of the primary system. For nuclear dephasing, the bath modulates the vibrational Hamiltonian:

$$\hat{\mathbf{H}}_{SB}^{nd} = \begin{pmatrix} \hat{\mathbf{H}}_g & 0 \\ 0 & \hat{\mathbf{H}}_e \end{pmatrix} \otimes \sum_{ij} c_{ij}^{nd} (\hat{\boldsymbol{\sigma}}_i^+ \hat{\boldsymbol{\sigma}}_j + \hat{\boldsymbol{\sigma}}_j^+ \hat{\boldsymbol{\sigma}}_i) . \quad (3.23)$$

The coefficients  $c_{ij}$  are biased to represent almost elastic encounters,

$$c_{ij} = \frac{1}{N(N-1)} \bar{c} e^{-\frac{(\varepsilon_i - \varepsilon_j)^2}{2\sigma_\varepsilon^2}} , \quad (3.24)$$

where  $\bar{c}$  is a global dephasing parameter, and  $\sigma_\varepsilon$  determines the inelastic bias.  $\hat{\boldsymbol{\sigma}}_i^+ \hat{\boldsymbol{\sigma}}_j + \hat{\boldsymbol{\sigma}}_j^+ \hat{\boldsymbol{\sigma}}_i$  describes a two (quasi-)particle interaction, it must therefore be scaled by  $N(N-1)$  with  $N$  the number of modes to ensure a convergent procedure if  $N$  is increased. For electronic dephasing, the bath modulates the electronic excitation:

$$\hat{\mathbf{H}}_{SB}^{ed} = \Delta_V(\hat{\mathbf{Q}}) \frac{1}{2} \begin{pmatrix} -1 & 0 \\ 0 & 1 \end{pmatrix} \otimes \sum_{ij} c_{ij}^{ed} (\hat{\boldsymbol{\sigma}}_i^+ \hat{\boldsymbol{\sigma}}_j + \hat{\boldsymbol{\sigma}}_j^+ \hat{\boldsymbol{\sigma}}_i) . \quad (3.25)$$

$\Delta_V(\hat{\mathbf{Q}})$  is the difference potential describing the dependence of the modulation on the nuclear displacement. The constants  $c_{ij}^{ed}$  are chosen analogously to Eq. (3.24).

Since the number of bath excitations is not changed by  $\hat{\boldsymbol{\sigma}}_i^+ \hat{\boldsymbol{\sigma}}_j + \hat{\boldsymbol{\sigma}}_j^+ \hat{\boldsymbol{\sigma}}_i$  it is clear that the bath has to be initially excited for dephasing to take place. Therefore, when the temperature is decreased, dephasing processes are frozen.

So far the dephasing model has been introduced guided by a phenomenological description of the elastic interaction causing dephasing. However, for the case of a TLS coupled to a TLS bath, a microscopic model for dephasing has been derived [19] which is connected to the qualitative picture presented above. This derivation which was done in the context of magnetism and superconductivity led to a general effective Hamiltonian called the central spin model. The central spin model is the equivalent to the spin boson

model [20, 21] for which the bath consists of harmonic oscillators. It shows dephasing also at  $T = 0$ . The interaction term between the central spin and the bath spins describing dephasing is given by

$$\hat{\mathbf{H}}^{ed} \sim \hat{\boldsymbol{\sigma}}_x \cos[\Phi + \sum_i \vec{V}_i \hat{\boldsymbol{\sigma}}_i], \quad (3.26)$$

where  $\Phi$  is the renormalized phase of the system given by  $\hat{\boldsymbol{\sigma}}_z$  and the sum over bath phases,  $\vec{V}_i$  is the coupling constant and  $\hat{\boldsymbol{\sigma}}_i$  are the Pauli operators of the  $i$ th bath mode. If the cosine is expanded to second order in the system-bath coupling, a Hamiltonian of the form of Eq. (3.25) is obtained. The dephasing model of Eq. (3.25) can therefore be viewed as a second order approximation of the more general description of dephasing in the central spin model. The zero temperature decoherence must hence be a higher order effect.

### 3.3 Energy relaxation

The standard benchmark model for dissipative dynamics is the harmonic oscillator linearly coupled to a bath. For weak coupling, an analytical solution exists [58]. The vibrational relaxation of this system,

$$\hat{\mathbf{H}}_{\text{harm}} = \frac{\hat{\mathbf{P}}^2}{2m} + \frac{1}{2}m\omega^2\hat{\mathbf{Q}}^2 + \sum_i \varepsilon_i \hat{\boldsymbol{\sigma}}_i^+ \hat{\boldsymbol{\sigma}}_i + \hat{\mathbf{Q}} \sum_i d_i^{nr} (\hat{\boldsymbol{\sigma}}_i^+ + \hat{\boldsymbol{\sigma}}_i), \quad (3.27)$$

has previously been tested for the Surrogate Hamiltonian method [2]. To this end, an Ohmic form with exponential cutoff has been assumed for the spectral density,

$$J(\varepsilon) = \eta \varepsilon e^{-\varepsilon/\varepsilon_c}, \quad (3.28)$$

from which the coefficients  $d_i^{nr}$  are determined using Eq. (3.21).  $\varepsilon_c$  is the cutoff frequency, and  $\eta$  the coupling strength. The initial state was taken to be  $|\Psi(t=0)\rangle = \hat{\mathbf{Q}}|\Psi_g\rangle$  corresponding to an infrared excitation of the ground state. The results of this standard problem will be discussed in some detail to show how the Surrogate Hamiltonian works.

Fig. 3.2 shows the energy relaxation for a harmonic oscillator with unit mass and frequency ( $m = 1$ ,  $\omega = 1$ ). The dotted lines in Fig. 3.2 correspond to the initial state being correlated, i.e.  $|\Psi_g\rangle$  for the system coupled



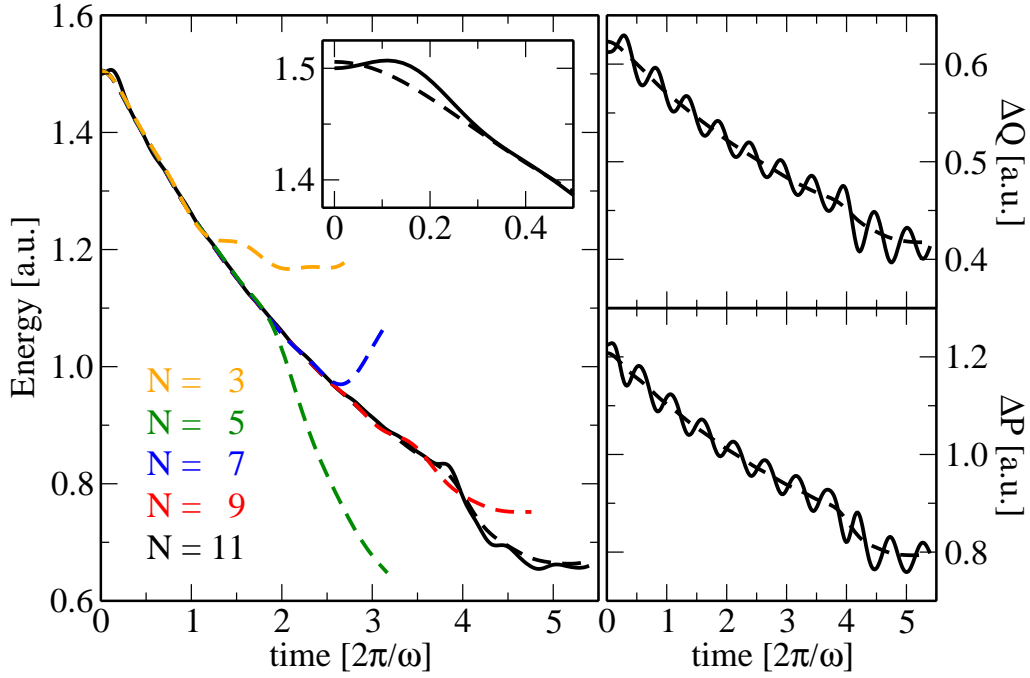


Figure 3.2: Energy relaxation of the harmonic oscillator: The decay is exponential with rate  $2\pi\eta\omega$  as predicted by the analytical solution for weak coupling ( $\eta = 0.01$ ). A correlated initial state (dashed lines) must be used to capture the short time dynamics. If an uncorrelated initial state (solid lines) is used, an initial slippage [50] in energy can be observed (inset in the left panel) and the standard deviations in coordinate and momentum show fast oscillations (right top and bottom panel). The time unit is equal to one period of the oscillator,  $N$  is the number of bath modes.

to the bath has been obtained using imaginary time propagation (cf. Appendix A.4). The dynamics of the initially correlated state are compared to that of an initially uncorrelated state, which is the ground state of the system and the system-bath coupling is switched on at time  $t = 0$  (solid lines in Fig. 3.2). The uncorrelated state has the "wrong" width, the standard deviations of coordinate and momentum show therefore fast oscillations which are absent in the correlated case (cf. Fig. 3.2, right top and bottom panel). The short time dynamics deviate for the correlated and uncorrelated initial states (inset in Fig. 3.2), since the correlations need to be built up in the uncorrelated case [50]. The overall decay is exponential, and the decay rate agrees with the analytical result for weak coupling [58]. As the number of

modes is increased, the time interval for which converged results are obtained is prolonged.

The convergence with respect to the number of bath modes does not have to be linear (cf. Fig. 3.2). It rather depends on the sampling of bath energies. As explained in Section 3.1, the finite size of the system will eventually lead to recurrences. A measure of recurrences is the population  $P_0$  of the state with no bath mode excited. In the bit representation of the TLS bath, it is given by the probability density of the zero spinor component (cf. Appendix E). An increase of this population corresponds to an overall flow of population and energy from the bath into the system. The time at which an increase of  $P_0$  is observed is an upper limit for the convergence time. The left-hand side of Fig. 3.3 shows the population  $P_0$  vs. time, while the population of all other bath modes  $P_i$ ,  $i = 1, \dots, N$ , is shown on the right for a simulation with  $N = 5$  and  $N = 7$  modes (top and bottom, respectively). For  $N = 5$ , recurrences occur after four periods of the oscillator, while for  $N = 7$ , an increase of  $P_0$  can already be observed at time  $t \approx 2.5$ . This can be understood by examining the sampling energies and population of the bath modes, and it points to a peculiarity of the harmonic oscillator. For the results presented in Figs. 3.2-3.4, the energy interval in which the bath energies  $\varepsilon_i$  were sampled, was kept fixed, and the  $\varepsilon_i$  were chosen equidistantly. In the case of  $N = 5$ , one bath energy happened to be equal to the system frequency  $\omega$ . It is the mode with this energy which receives almost all the population of the bath (dotted line in the top right panel of Fig. 3.3). For  $N = 7$  none of the bath energies coincide with  $\omega$ , the two modes with energies closest to  $\omega$  receive the most population. This observation leads to two conclusions: For the harmonic oscillator a resonance phenomenon is observed. This might intrinsically limit the convergence time interval unless more than one mode is chosen to be on resonance with the system. The resonance is disturbed for anharmonic systems (see below). Second, the optimal choice of bath modes, at least for simulations with a small number of modes, is system-dependent. While choosing several bath modes with  $\varepsilon_i = \omega$  contradicts the interpretation of the bath modes as normal modes of the environment, physically more meaningful discretizations are possible. An alternative sampling scheme is, for example, given by assuming a density of states as in the Debye theory of

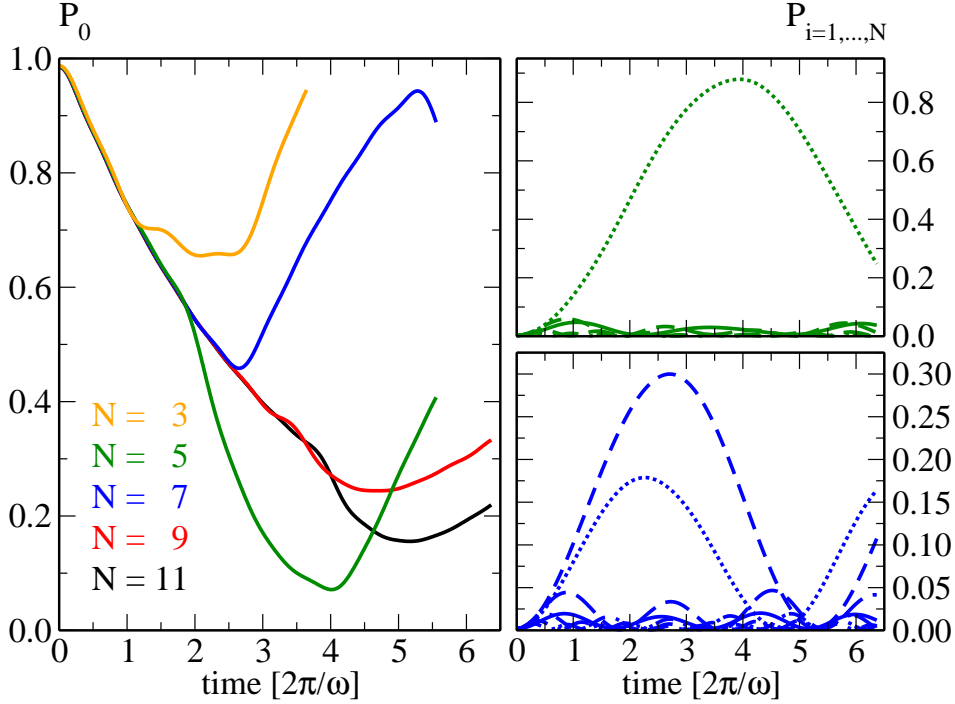


Figure 3.3: Population  $P_0$  corresponding to none of the bath modes excited (left) and population of single bath modes with the number of modes  $N = 5$  (top right) and  $N = 7$  (bottom right panel). For  $N = 5$ , almost all the population which is transferred to the bath ends up in a single bath mode, the energy of which is on resonance with the system frequency. For  $N = 7$ , no mode is resonant, and the two modes with energies closest to the system frequency are populated most strongly. ( $\eta = 0.01$ ).

solids [57]. This leads to an exponentially decreasing distance between bath energies.

As explained in Section 3.1, the computational effort scales with  $2^N$ , where  $N$  is the number of bath modes, in both cpu time and storage. This scaling can be made more favorable if the number of simultaneously allowed excitations can be restricted (cf. Appendix E). This is possible particularly in the case of weak coupling. Fig. 3.4 shows how many bath modes are simultaneously populated for weak and strong coupling and compares simulations in which all simultaneous excitations have been considered (solid lines) to simulations with a restricted number of simultaneous excitations (dotted and dashed lines). For weak coupling three simultaneously allowed excitations are completely sufficient to reproduce the results with all simultaneous

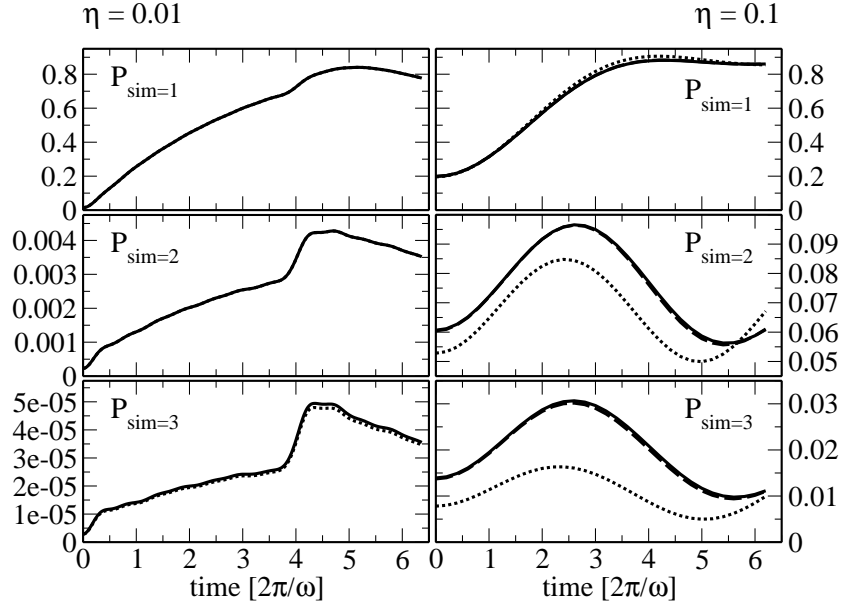


Figure 3.4: Population  $P_{sim}$  of 1, 2, and 3 simultaneous bath excitations for weak and strong coupling ( $\eta = 0.01$  and  $\eta = 0.1$ , respectively) and  $N = 11$  modes. The solid lines correspond to considering all simultaneous excitations, while simultaneously allowed excitations have been restricted to 3 for dotted and 5 for dashed lines.

excitations allowed, the curves are hardly distinguishable even for  $P_{sim=3}$ . More simultaneously allowed excitations need to be considered, however, in the case of strong coupling since more correlations are being built up in the bath. The population of simultaneous excitations gives an estimate of the timescale of the bath. If most of the bath population is in  $P_{sim=1}$  and the  $P_{sim>1}$  are negligibly small, the time-energy uncertainty relation gives an upper limit for the bath timescale of  $\approx 1/\varepsilon_i$ . However, if the population of more than one simultaneously allowed excitation becomes significant, differences of bath energies which can be much smaller than the energies itself enter the time-energy uncertainty relation thus prolonging the timescale of the bath. This argument is not valid in the case of a resonance phenomenon. But since one bath mode is singled out in that case, resonance leads to a breakdown of the system-bath description suggesting the inclusion of the resonant degree of freedom into the system or a sampling of many bath energies close to the resonance.

The importance of including initial correlations was shown in Fig. 3.2. For this purpose the ground state of the total system and bath needs to be calculated. This itself might require considerable numerical effort. However, since the obtained ground state energy converges with the number of bath modes  $N$  (cf. Fig. 3.5, left), it also gives an estimate of the number of

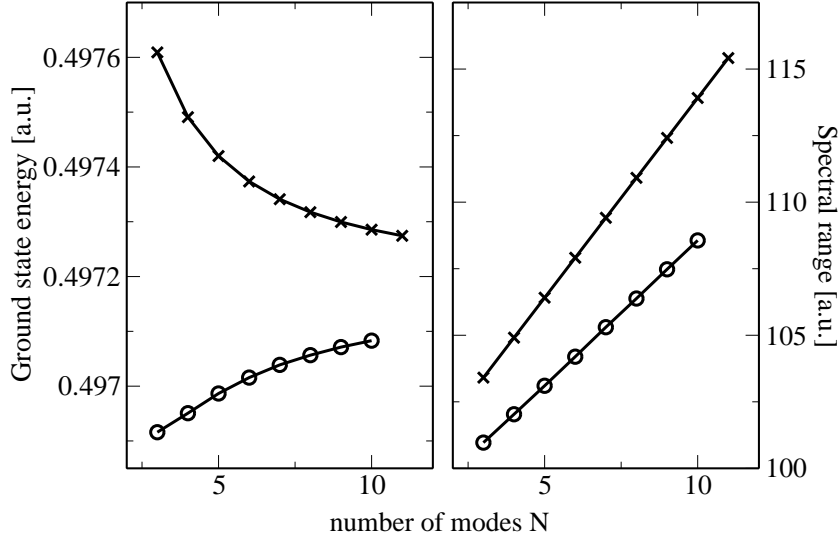


Figure 3.5: Ground state energy and spectral range of the total system and bath. Different sampling strategies are employed (equidistant sampling x, exponential sampling o).

modes which are necessary to recover equilibrium. In the example of Fig. 3.2 this means, how many modes are needed to reach the ground state energy of about 0.5 a.u. It furthermore shows the convergence behavior of different sampling strategies. Equidistant sampling is compared with the above mentioned exponential sampling [57] in Fig. 3.5. Both sampling strategies converge rather slowly to a common ground state energy. This illustrates the fact that the Surrogate Hamiltonian while it nicely captures the dynamics at short times is *not* well-suited to study equilibrium properties which require long propagation times. The right-hand side of Fig. 3.5 shows the increase of the spectral range with the number of modes. The determination of the spectral range is necessary when using the Chebychev propagator (cf. Appendices A.2 and A.5). Since the increase of the spectral range turned out to be linear,  $\Delta E$  can be estimated by a linear fit avoiding the numerical

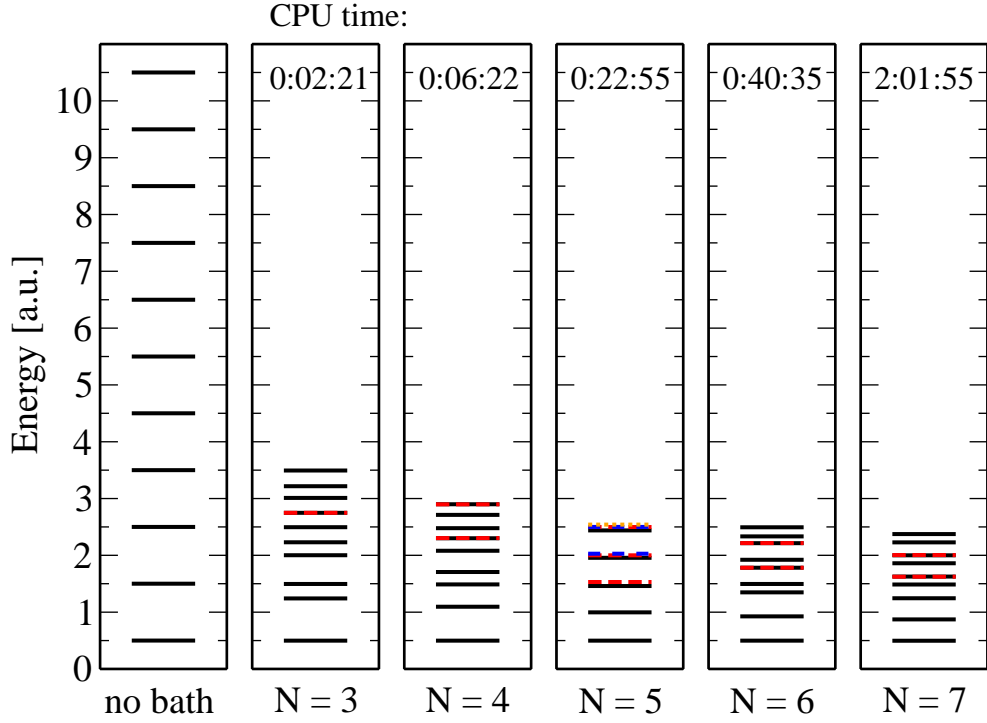


Figure 3.6: The 11 first eigenenergies of the total system and bath (equally spaced sampling, weak coupling).

computation when increasing  $N$ .

So far, the properties of the relaxing harmonic oscillator have been studied for zero temperature. For higher temperatures, a Boltzmann average according to Eq. (3.17) is necessary. However, since the Hilbert space of the total system and bath,  $\mathcal{H}_S \otimes \mathcal{H}_B$ , contains many more states than the Hilbert space of the system alone,  $\mathcal{H}_S$ , computing the eigenstates required in Eq. (3.17) might become computationally demanding. This is illustrated in Fig. 3.6. In addition to the increase in the number of eigenstates with increasing number of bath modes  $N$ , the bath may lead to degeneracies (colored lines in Fig. 3.6). Resolving degenerate eigenvalues requires long propagation times in imaginary time propagation which is used to obtain the eigenstates (cf. Appendix A.4). While the problem of degeneracies may be partially resolved by incorporating an energy filter into imaginary time propagation (cf. Appendix C.2), the exponentially increasing number of eigenstates cannot be avoided. The Surrogate Hamiltonian is therefore well-suited only for

low temperature problems with the meaning of low being determined by the relevant system energies.

The grid representation of the primary system allows for the treatment of a general anharmonic potential. The vibrational relaxation study is therefore extended to the case of an anharmonic oscillator in a bath,

$$\hat{\mathbf{H}}_{anh} = \hat{\mathbf{H}}_{harm} + V_{anh}(\hat{\mathbf{Q}}) . \quad (3.29)$$

The anharmonic part of the potential is given by third and fourth order terms in  $\hat{\mathbf{Q}}$ :

$$V_{anh}(\hat{\mathbf{Q}}) = \gamma_3 \hat{\mathbf{Q}}^3 + \gamma_4 \hat{\mathbf{Q}}^4 , \quad (3.30)$$

where  $\gamma_3$  was used as free parameter and  $\gamma_4$  was chosen to balance the third order term,  $\gamma_4 = -\gamma_3/Q_b$  with  $Q_b = 1.8$  a.u. (cf. Fig. 3.7). To obtain the initial state, the correlated ground state of system and bath was displaced by  $Q_0 = 0.3$  a.u., this is indicated by the arrows in Fig. 3.7. The qualitative shapes of the energy relaxation curves for different anharmonicities shown in Fig. 3.7 are quite similar. Examining the potentials in the left part of Fig. 3.7, it becomes clear that with increasing anharmonicity the average initial energy decreases. With 11 bath modes, the method converges to a timescale of  $\sim 1000$  fs. The artificial recurrence of energy for the harmonic case after  $\sim 1000$  fs should be noticed (Fig. 3.7). For anharmonic cases, the recurrence is less significant due to a spread of the system energy to more bath modes. The above mentioned resonance phenomenon is thus avoided for an anharmonic system.

The system energy is not an observable accessible in an experiment. An experimentally accessible observable is, however, given by the absorption of a pulse. This can be calculated using the window operator (cf. Appendix B). The absorption of a probe pulse (bottom right of Fig. 3.7, cf. Appendix B) shows larger differences due to the anharmonicity of the potential. The choice of positioning the window function (as indicated in Fig. 3.7) enhances the second harmonic component. This results from the double passage of the wave packet for each vibrational period. The decay of spectral modulations is faster when the anharmonicity increases, in particular the double peak reflecting the second harmonic component is lost much faster. These observations are similar to those seen in a vibrational relaxation model based

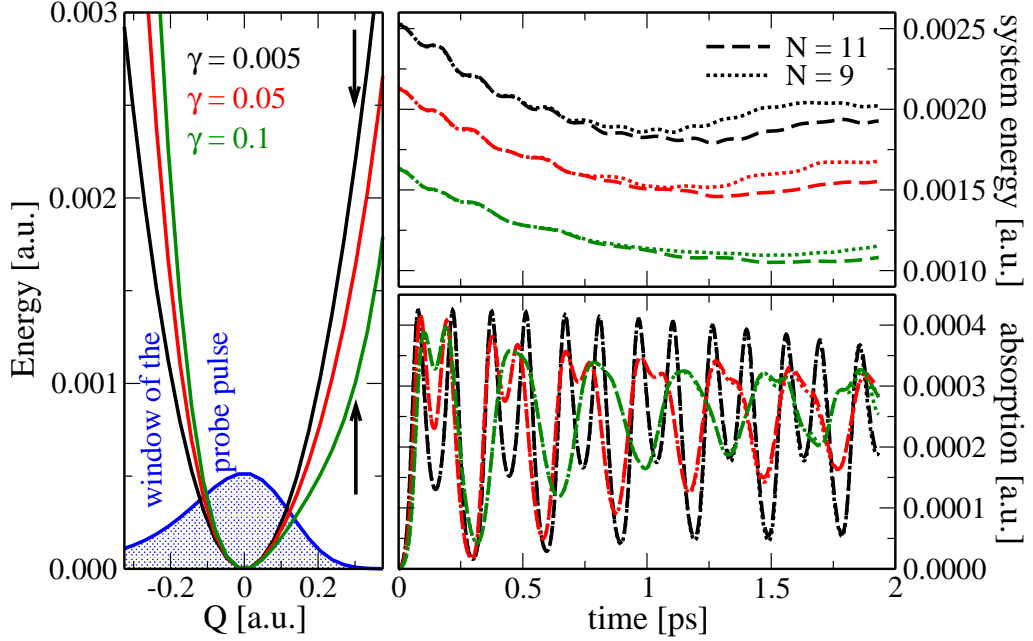


Figure 3.7: Potentials for the anharmonic oscillator with increasing third order term  $\gamma_3$  given in the legend. The arrows indicate the position of the initial state. The window operator which was used to calculate the absorption is also plotted. The average energy as a function of time for increasing anharmonicity (top) and the ground state absorption for increasing anharmonicity (bottom) are shown on the right.  $N$  is the number of bath modes, the system-bath coupling is  $\eta = 2$  and the cutoff frequency of the spectral density is equal to the system frequency,  $\varepsilon = \omega$ .

on solving the semi-group Liouville von Neumann equation [59]. The phenomenon is the result of the initially compact wave function falling out of phase when the energy level spacing is not constant. For an isolated quantum system with discrete eigenstates, coherent revivals of the wave packet can be observed. Dissipative forces originating from the bath, however, exclude such wave packet revivals [60].

### 3.4 Dephasing

When modeling dissipative processes, often both relaxation and dephasing are important and need to be considered. From the remarks of the previous section it is clear that two different types of baths are then required in a Surrogate Hamiltonian description with a limited number of bath modes.



For relaxation the bath should have a broad spectrum of modes which can absorb energy from the system, particularly if the system is anharmonic, while for dephasing the bath energy levels have to be quasi-degenerate. Since furthermore the mechanisms of relaxation and dephasing are quite different, *pure* dephasing will be considered in the following. As explained above, pure dephasing requires an initial population of bath modes. The initial state was therefore assumed to have all modes equally populated. While this is a somewhat artificial choice and a Boltzmann weighted population of bath modes bears more physical significance, it ensured fast convergence and the observation of phenomena related to the dephasing model only.

The harmonic oscillator was also used to test nuclear dephasing,

$$\begin{aligned} \hat{\mathbf{H}}_{\text{harm}} = & \frac{\hat{\mathbf{P}}^2}{2m} + \frac{1}{2}m\omega^2\hat{\mathbf{Q}}^2 + \sum_i \varepsilon_i \hat{\sigma}_i^+ \hat{\sigma}_i + \\ & \left( \frac{\hat{\mathbf{P}}^2}{2m} + \frac{1}{2}m\omega^2\hat{\mathbf{Q}}^2 \right) \otimes \sum_{ij} c_{ij}^{nd} (\hat{\sigma}_i^+ \hat{\sigma}_j + \hat{\sigma}_j^+ \hat{\sigma}_i) . \end{aligned} \quad (3.31)$$

Its ground state was displaced by 0.4 a.u. and evolved in time. Pure vibrational dephasing leads to a spreading of the wave packet in phase space, shown in Fig. 3.8. The sign of each individual term  $c_{ij}^{nd}$  in Eq. (3.23) or Eq. (3.31), respectively, determines if its contribution advances or delays the phase (cf. Fig. 3.9). Negative  $c_{ij}^{nd}$  advances the phase, while positive  $c_{ij}^{nd}$  delays it. A random choice of the sign of  $c_{ij}^{nd}$  will cause a phase diffusion in both directions without affecting the average phase propagation determined by  $\hat{\mathbf{H}}_S$ .

Higher harmonic motion was generated by placing two, three and four Gaussian wave packets symmetrically on a specified ellipse in phase space, the ellipse was determined by the displacement of 0.4 a.u. of the first harmonic. The Wigner function of two Gaussian wave packets is shown in Appendix C.1. It displays non-classical correlations. The transient absorption at the turning point of this initial state was recorded and fitted with the use of the Filter Diagonalization method (cf. Appendix C.2). The frequencies with the highest amplitudes were the second, third and fourth harmonics. Analysis of the decay rates corresponding to these frequencies shows a 1:2 ratio between the first and second, 1:3 between the first and third and 1:4 between the first and fourth harmonic (cf. Table 3.4). These ratios deviate

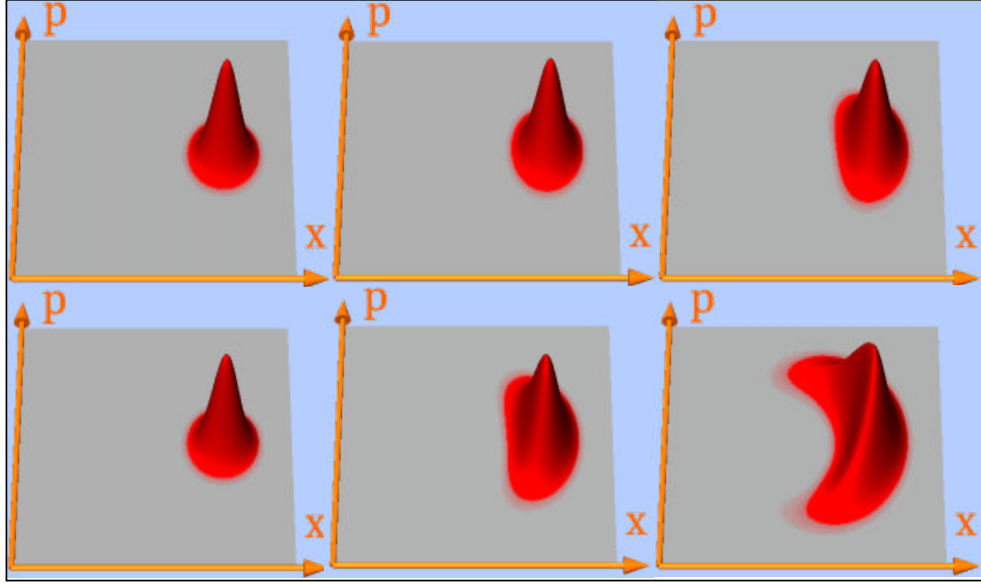


Figure 3.8: The Wigner function of an initially displaced Gaussian state in a harmonic potential. The state is plotted after 0, 2 and 4 periods for the nuclear dephasing parameter  $\bar{c} = 0.2$  (top) and for  $\bar{c} = 0.5$  (bottom). Nuclear dephasing leads to a spreading of the wave packet which occurs faster for stronger dephasing.

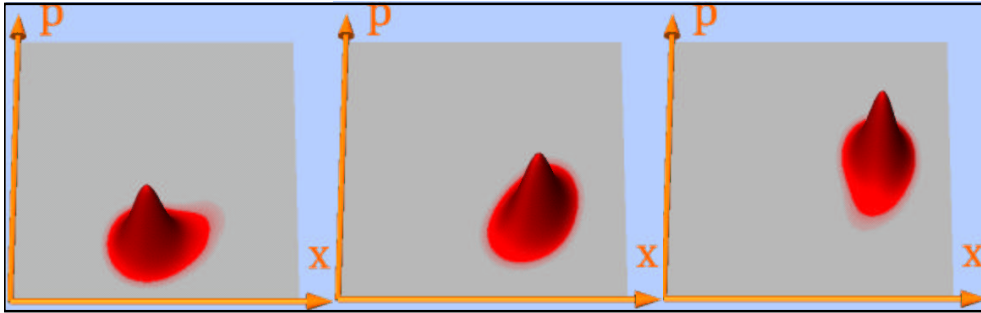


Figure 3.9: The sign of dephasing constants determines the direction of the spread (left: positive  $c_{ij}^{nd}$ , middle: random choice of the sign, right: negative  $c_{ij}^{nd}$ ).

harmonic	frequency	decay rate	error
1	0.5614E-03	0.110E-05	0.57E-08
2	0.1123E-02	0.199E-05	0.66E-07
3	0.1701E-02	0.288E-05	0.84E-07
4	0.2246E-02	0.434E-05	0.86E-08
harmonic	frequency	decay rate	error
1	0.5002E-03	0.180E-05	0.75E-08
2	0.1000E-02	0.364E-05	0.30E-07
3	0.1500E-02	0.565E-05	0.12E-05
4	0.2243E-02	0.625E-05	0.66E-06

Table 3.1: Frequencies and decay rates of dephasing for higher harmonics obtained by filter diagonalization of transient absorption ( $N = 11$  top,  $N = 10$  bottom).

from the 1:4, 1:9 and 1:16 ratios expected in a Gaussian dephasing model, and indicate that the dephasing mechanism is Poisson-like [61,62]. Dephasing can be imagined as elastic scattering of for example solvent molecules with a solute with binary collisions causing the phase changes. If the collisions are frequent but induce only small phase changes, the probability distribution of the single phase changes is given by a Gaussian, if the collisions are rare events but lead to larger phase changes, the distribution is Poissonian. The Poisson model of dephasing reduces to a Gaussian one in the limit of frequent and small phase changes, it can therefore considered to be more general [61].

A simple model to study pure electronic dephasing is a TLS which is resonantly excited by a pulse with field  $E(t)$  and which is coupled to a bath,

$$\hat{\mathbf{H}} = \begin{pmatrix} -\frac{1}{2}\omega_0 & E(t) \\ E(t) & \frac{1}{2}\omega_0 \end{pmatrix} \otimes \mathbb{1}_B + \frac{1}{2} \begin{pmatrix} -1 & 0 \\ 0 & 1 \end{pmatrix} \otimes \sum_{ij} c_{ij}^{ed} (\hat{\sigma}_i^+ \hat{\sigma}_j + \hat{\sigma}_j^+ \hat{\sigma}_i) . \quad (3.32)$$

The initial state was chosen such that the system is in its ground state and the bath states are equally populated. If the pulse is a  $\pi$ -pulse [63], it will lead to complete population transfer as long as there is no coupling to the bath. The effect of pure electronic dephasing is shown in Figs. 3.10 to 3.12. For zero dephasing, the  $\pi$ -pulse indeed leads to a complete population inversion (black

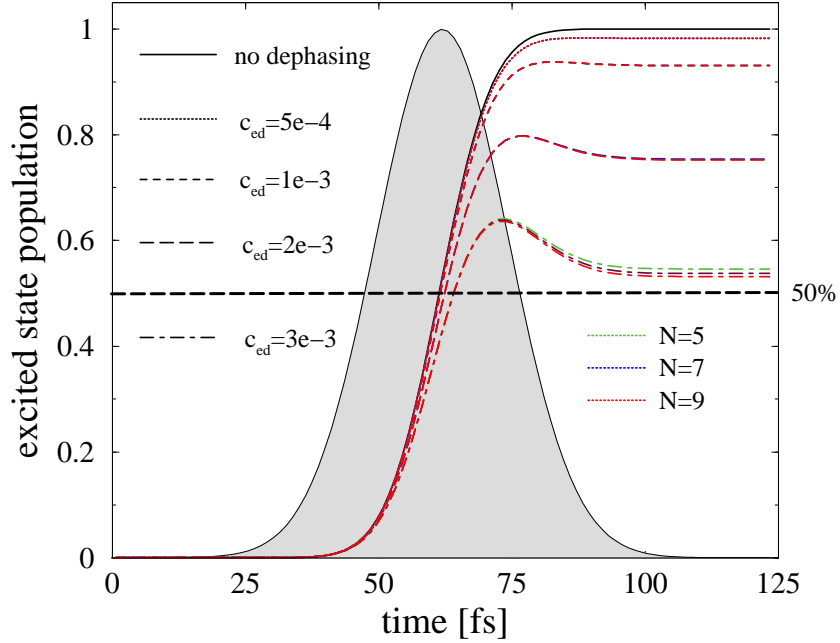


Figure 3.10: Electronic dephasing: Decrease of population excited by a  $\pi$ -pulse for increasing dephasing strength  $c_{ed}$ ,  $N$  is the number of bath modes. The pulse envelope (not to scale) is shown in the background.

curve in Fig. 3.10). Once dephasing is included, the amount of population transfer decreases, eventually reaching 50% conversion which corresponds to a random electronic phase. For stronger dephasing, more modes are required to obtain converged results.

For the radiation, a time-dependent semiclassical approximation is used. The power absorbed or emitted from the radiation field is then given by the expectation value [64]:

$$\mathcal{P} = \left\langle \frac{\partial \hat{\mathbf{H}}_{SF}}{\partial t} \right\rangle = \text{tr}_S \left\{ \hat{\boldsymbol{\rho}}_S \frac{\partial}{\partial t} \hat{\mathbf{H}}_{SF} \right\}. \quad (3.33)$$

To obtain the total energy absorbed by the pulse, Eq. (3.33) is integrated for the total pulse duration. When the radiation field is represented by a rotating field,  $E(t) = \bar{e}e^{i\omega_L t}$ , one obtains [64]

$$\Delta E = \int \mathcal{P} dt = -\hbar\omega_L \Delta N_g. \quad (3.34)$$

Eq. (3.34) allows for associating the change in population from the ground to the excited electronic state,  $\Delta N_g$ , to the energy  $\Delta E$  absorbed from the

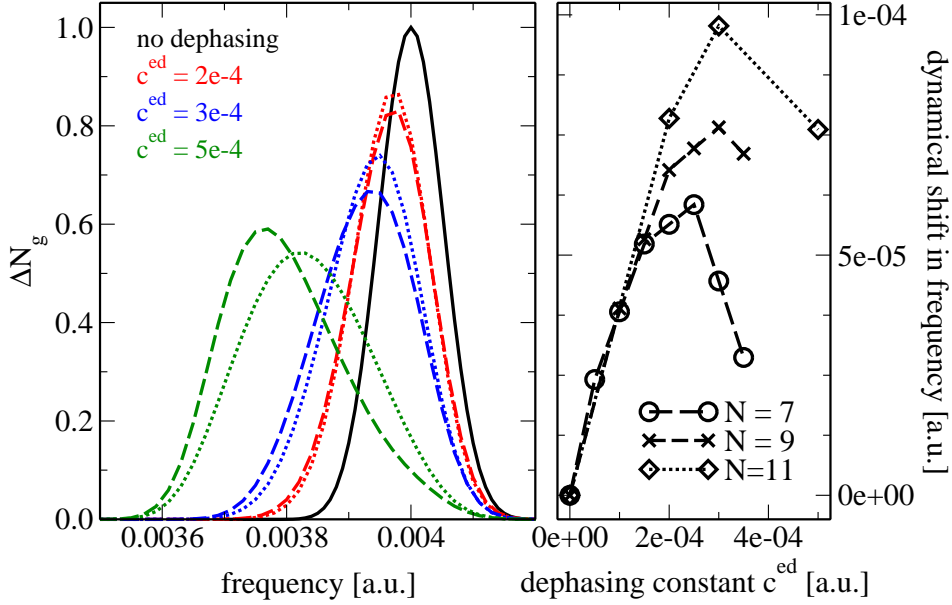


Figure 3.11: Absorption spectrum: Dephasing leads to a shift and a broadening of the absorption peak. The shift contains two contributions: a static one corresponding to the value  $\langle \hat{\mathbf{H}}_{SB}^{ed} \rangle(t=0)$  and a dynamic one which is plotted on the right.

field. By varying the carrier frequency  $\omega_L$  of the pulse and calculating  $\Delta E$ , a spectrum of absorbed energy vs. frequency can be obtained. The minimum width of the spectrum is determined by the Fourier transform of the pulse (black curve in the left panel of Fig. 3.11). Once dephasing is introduced, the frequency of the absorption peak is shifted corresponding to the initial value of the system-bath interaction energy  $\langle \hat{\mathbf{H}}_{SB}^{ed} \rangle$ . An additional dynamical shift is also observed which is linear in  $c^{ed}$  for small values (cf. Fig. 3.11, right). The dephasing furthermore leads to a broadening of the absorption peak (cf. Fig. 3.11, left). The width of the peak (FWHM) can be determined and plotted vs. the dephasing parameter  $c^{ed}$  (Fig. 3.12). A quadratic scaling of the width with  $c^{ed}$  is observed.

The dephasing rate is furthermore found to be proportional to the square of the band width of bath energies which is related to the band width of the  $c_{ij}$  (cf. Fig. 3.13). To this end, the ground and excited states of the TLS have been equally populated and the expectation values of  $\hat{\sigma}_x$  and  $\hat{\sigma}_y$  which measure the electronic coherence have been recorded. For an isolated

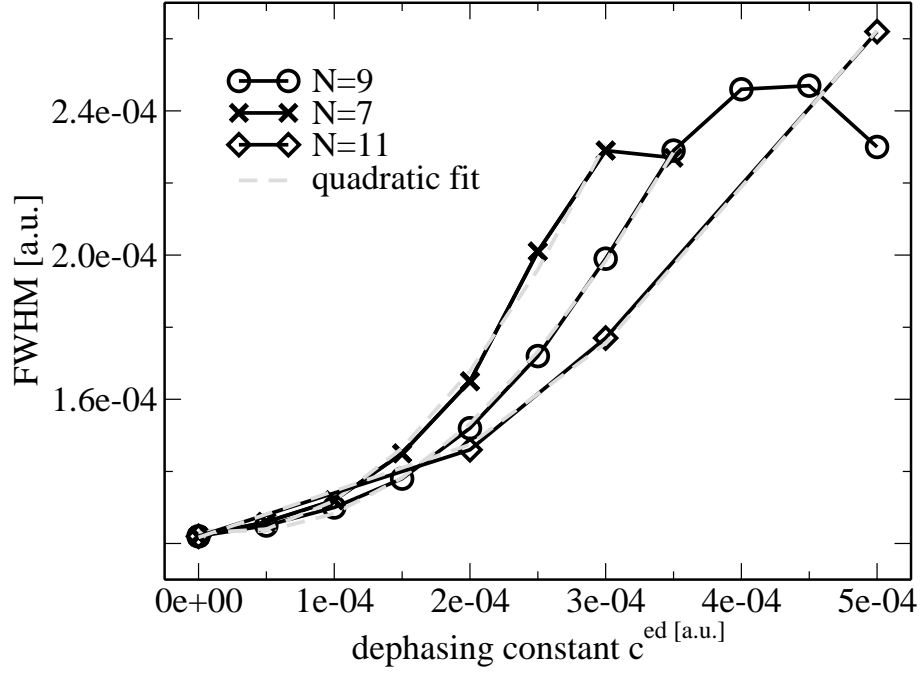


Figure 3.12: The FWHM of the pulse spectrum as a function of dephasing constant  $c^{ed}$  for increasing number of bath modes. The deviation from a quadratic fit indicates the breakdown of convergence.

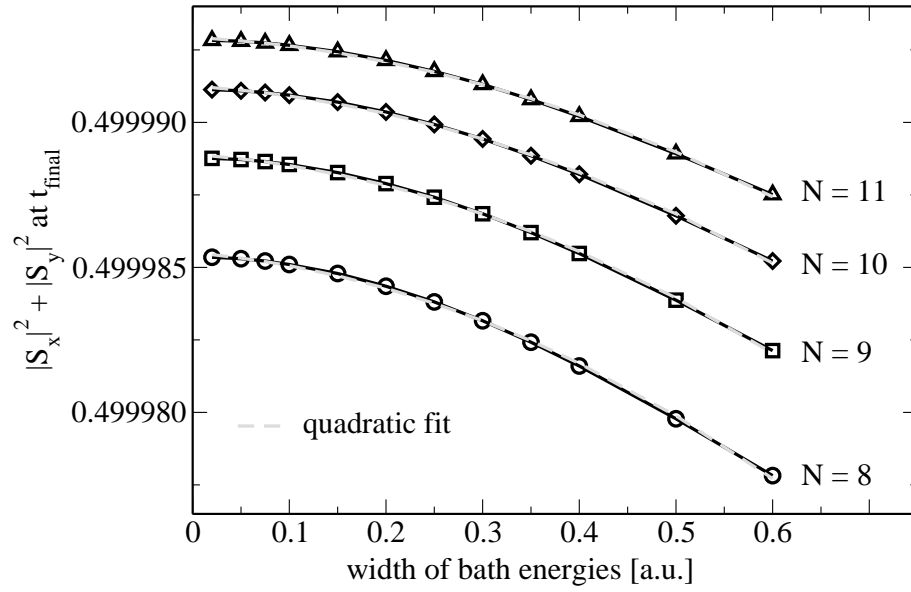


Figure 3.13: Quadratic scaling of dephasing with bath energy bandwidth.

system, these expectation values oscillate but the sum of their squares is constantly equal to 0.5. If dephasing is included, a decrease of  $|S_x|^2 + |S_y|^2$  is observed. The amount of this monotonic decrease at some final time has been chosen as a measure for the dephasing rate. It is plotted for different dephasing constants in Fig. 3.13. The quadratic scaling of dephasing with the band width, as well as with the dephasing constant  $c^{ed}$ , indicates that the Surrogate Hamiltonian dephasing process is second order in the system-bath coupling. This is consistent with the dephasing terms being a second order expansion of the more general cosine-term mentioned in Section 3.2.

The above examples demonstrate the ability of the Surrogate Hamiltonian method to model the four isolated dissipative phenomenon and to establish the requirements for convergence.





## Chapter 4

# A first application: Charge transfer in a mixed valence system in solution

In the previous chapter the Surrogate Hamiltonian method has been introduced and generalized to treat problems including two (or more) electronic states. The single dissipation processes have been discussed. In this chapter, these dissipation processes will be combined to comprehensively describe a charge transfer event in condensed phase.

The simplest model for the primary system in that case consists of two harmonic potentials which are coupled nonadiabatically. The parameters of the model are chosen to mimic the mixed valence system  $(\text{NH}_3)_5\text{RuNCRu}(\text{CN})_5^-$  [65] which has recently been investigated in a femtosecond pump-probe experiment [66,67]. The observed electron transfer time, vibrational relaxation rate and dephasing time of vibrational coherences showed a strong solvent dependence.

That the environment plays an important role in determining the fate of the charge transfer reaction has been realized early on [68,69]. The shift in charge distribution during the reaction forces a complete rearrangement of the solvation shell. Additionally, the decoherence caused by the solvent eventually forces the system to localize onto a particular charged state. This localization marks the qualitative change from a dynamical to a kinetic picture. For weak to moderate system-bath coupling, an increase in the dissi-

pative forces will cause an increase in the rate of charge transfer. A further increase in the system-bath coupling will cause a turnover and the rate will decrease [65]. This general quantum phenomenon has been termed the quantum anti-Zeno effect [70].

New insight into the charge transfer process has come from ultrafast pump-probe experiments [71, 66]. This technique constitutes a dynamical probe which allows for the unraveling of the sequence of events that lead eventually to the charge transfer product. A direct signature of the ultrafast dynamics are transient modulations of optical observables reflecting the promotion of ground and excited state vibrational modes. A comprehensive quantum dynamical model which can describe consistently the experimental observations has therefore to take into account the influence of the environment as well as the time-dependence of the laser pulse. The use of the Surrogate Hamiltonian method is justified by the ultrafast nature of the observations which restrict the timescale.

## 4.1 Modeling a pump-probe charge transfer event

Before specifying the model to describe the charge transfer event, the steps that make up a charge transfer cycle (cf. Fig. 4.1) and related theoretical considerations shall briefly be reviewed:

1. The initial state of the process is a strongly solvated chromophore which results in a system and bath which are highly correlated. The phenomenon is related to *nuclear relaxation*. This issue is addressed by constructing a correlated initial state as described in Section 3.3. The initial correlation has been a major concern for quantum treatments of system-bath dynamics, e.g. [50]. The common approach is to approximate the initial state as a tensor product between the system and the bath state. A correction to the problem within the context of perturbation theory using auxiliary density matrices (cf. Section 2.3) has recently been suggested [51]. The issue of initial correlations has been tested within the current context (cf. Section 4.2.1) showing only a small effect on the dynamics. This is in line

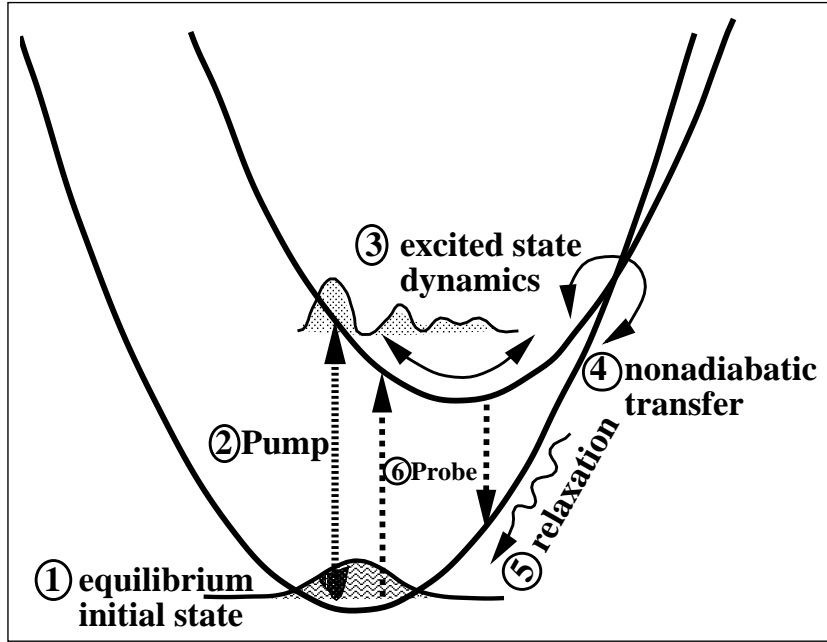


Figure 4.1: The charge transfer cycle: An initial correlated state (1) is partially promoted to the excited electronic state by the pump pulse (2), leaving a "hole" in the ground state density. The excited state population moves to the crossing point (3) where it can cross back to the ground state potential via a nonadiabatic transition (4). Once on the electronic ground state surface the hot vibration cools back to the bottom of the well (5). The dynamics is followed in time by a short and weak probe pulse (6).

with the argument that the influence of the laser field establishes new, non-equilibrium initial conditions [48].

2. The excitation by the pump pulse is the second step in the sequence of events. In most cases the pump intensity is sufficient to promote a significant fraction of population to the excited state (cf. Section 4.2.2). The void or "hole" left on the ground electronic state creates a nonstationary density which then oscillates periodically with the ground state vibrational frequencies [72, 59]. This phenomenon is known experimentally as **R**esonance **i**mpulsive **s**timulated **R**aman **s**cattering (RISRS). The creation of this "hole" can be explained by coordinate dependent Rabi cycling. A consistent description of the excitation process therefore has to include the *interaction with the radiation field* explicitly. Moreover, the strong interaction with the field has been shown to modify the system-

bath coupling [73, 74, 49]. Since the time scale of electronic dephasing for charge transfer events in solution is of the same order as the pulse duration, the description should also take into account *electronic dephasing*. Furthermore, an interference between the radiation induced excitation and back transfer caused by the diabatic coupling is observed. If the diabatic coupling potential is not localized on the crossing point this effect turns out to be significant (cf. Section 4.2.2). The explicit time dependence in the Surrogate Hamiltonian theory is designed to include all these effects within the model. The state of the system has to reflect the full *nonadiabatic* picture. Therefore the dynamics on the two potential energy surfaces has to be considered simultaneously. This is in contrast to the common perturbation theory picture which places the ground state wave packet on the excited electronic surface [65].

3. Once the excitation has promoted population to the electronically excited state, the wave function starts to evolve under the influence of the excited state potential, eventually reaching the crossing point. This evolution is also strongly influenced by the bath. Strong *vibrational relaxation* on the excited state can stop the motion before it reaches the crossing point (cf. Section 4.3). The nonstationary "hole" left on the electronic ground state will also start to evolve. This causes periodic modulations with frequencies characteristic of Raman transitions [59]. The decay of these modulations is influenced by *vibrational dephasing and relaxation*.
4. The density on the electronically excited state approaches the crossing point. By nonadiabatic charge transfer it can cross back to the electronic ground state. This step is crucially influenced by the environment. The dynamics has to reflect the turnover from an enhancement of the charge transfer rate caused by an increase in dissipation to a suppression of the rate. The difficulty in analyzing this step is that it is influenced by *all the dissipative processes*.
5. The charge transfer converts electronic excitation energy into nuclear potential energy (cf. Fig. 4.1). Following the charge transfer event, the vibrational modes of the electronic ground state are therefore highly excited. If the timescale of the charge transfer event is fast relative to a vibrational period, the new wave packet will have coherent properties.

The final stage in closing the cycle of events is the recovery of the initial equilibrium state. This is the result of *vibrational relaxation* of the excess energy to the bath (cf. Section 4.2.3).

6. The probe pulse can be applied at any stage in the cycle of events. Typically, the probe pulse is short and weak. In this case a perturbative picture is justified which allows for the use of the window operator (cf. Appendix B). For weak fields, this operator describes the total energy balance absorbed or emitted from the pulse. Its application as opposed to direct solution of the Schrödinger equation for all time delays between the pump and probe pulses can save significant computational effort. The probe pulse can promote both an excitation, i.e. absorption of energy, or deexcitation resulting in stimulated emission.

The total Hamiltonian is written as

$$\hat{\mathbf{H}} = \hat{\mathbf{H}}_S + \hat{\mathbf{H}}_{SF}(t) + \hat{\mathbf{H}}_{SB} + \hat{\mathbf{H}}_B, \quad (4.1)$$

where  $\hat{\mathbf{H}}_S$  is the Hamiltonian of the primary system and  $\hat{\mathbf{H}}_B$  is the Hamiltonian of the bath. The interaction of the system with the laser pulse is described by  $\hat{\mathbf{H}}_{SF}(t)$ , and the interaction of system and bath is captured by  $\hat{\mathbf{H}}_{SB}$ . The Hamiltonian of the primary system is constructed with two electronic states and with one nuclear degree of freedom in a diabatic representation,

$$\hat{\mathbf{H}}_S = \begin{pmatrix} \hat{\mathbf{H}}_g & V_d(\hat{\mathbf{Q}}) \\ V_d(\hat{\mathbf{Q}}) & \hat{\mathbf{H}}_e \end{pmatrix} \otimes \mathbb{1}_B \quad (4.2)$$

with  $\hat{\mathbf{H}}_{g/e} = \hat{\mathbf{T}} + V_{g/e}(\hat{\mathbf{Q}})$ .  $\hat{\mathbf{T}} = \hat{\mathbf{P}}^2/2M$  is the kinetic energy operator,  $V_g$  and  $V_e$  are the potential energy operators on the electronic ground and excited state, and  $V_d$  is the diabatic coupling (cf. also Section 6.2.1). The electronic potential energy levels are chosen to be displaced harmonic oscillators:

$$V_g(\hat{\mathbf{Q}}) = \frac{1}{2}M\omega_g^2\hat{\mathbf{Q}}^2, \quad (4.3)$$

$$V_e(\hat{\mathbf{Q}}) = \frac{1}{2}M\omega_e^2(\hat{\mathbf{Q}} - Q_0)^2 + \Delta, \quad (4.4)$$

where  $\omega_{g/e}$  are the vibrational frequencies of the ground and excited surfaces,  $Q_0$  is the shift in equilibrium position and  $\Delta$  is the energy shift between the minima. The system parameters were chosen as  $\omega_g = 5.0 \cdot 10^{-4}$ ,  $\omega_e = 0.7\omega_g$ ,

$Q_0 = 0.2$  and  $\Delta = 0.004$  (all in atomic units). The diabatic coupling function is described as

$$V_d(\hat{\mathbf{Q}}) = J_d e^{-\frac{(\hat{\mathbf{Q}} - Q_{cr})^2}{2\sigma_d^2}}, \quad (4.5)$$

where  $Q_{cr}$  is the position of the maximum coupling point,  $\sigma_d$  is the variance of the coupling function and  $J_d$  its amplitude. By varying the parameters of the diabatic coupling its influence can change from a localized effect at  $Q_{cr}$  to a constant function independent of  $Q_{cr}$ .

The interaction of the system with the electric field of the laser pulse in the electric dipole approximation is given by

$$\hat{\mathbf{H}}_{SF} = \begin{pmatrix} 0 & -E(t)\hat{\boldsymbol{\mu}}_{tr} \\ -E^*(t)\hat{\boldsymbol{\mu}}_{tr} & 0 \end{pmatrix} \otimes \mathbb{1}_B. \quad (4.6)$$

$\hat{\boldsymbol{\mu}}_{tr} = \hat{\boldsymbol{\mu}}_{tr}(\hat{\mathbf{Q}})$  is the transition dipole operator which can be a function of the nuclear configuration, and  $E(t)$  is the time-dependent electric field. Employing the long wavelength or optical approximation, the spatial dependence of  $E(t)$  is neglected. The pump pulse envelope was modeled as a Gaussian,

$$E(t) = E_0 e^{-\frac{(t-t_{max})^2}{2\sigma_L^2}} e^{-i\omega_L t}. \quad (4.7)$$

The intensity  $E_0$  was adjusted such that about 10% of the ground state population was transferred to the excited state which is typical in experiments [62]. The carrier frequency  $\omega_L$  was chosen to match the difference between the ground and excited state potentials at the minimum of the ground state. The width (FWHM) of the pulse which is connected to  $\sigma_L$  was chosen as 20 fs. This corresponds to approximately 1/10 of the ground state vibrational period and to 1/15 of the excited state vibrational period, and typical for charge transfer experiments [66].  $t_{max}$  was fixed by starting the propagation at  $t_0 = t_{max} - 3\sigma_L$ . The probe pulse profile was identical to the pump pulse profile but with 10% of the pump intensity.

The bath Hamiltonian is given by Eq. (3.4). The interaction Hamiltonian, Eq. (3.19), has been described in detail in Section 3.2. Eq. (3.20) together with Eq. (3.21) as well as Eqs. (3.23) and (3.25) together with Eq. (3.24) will be employed. In particular, an Ohmic spectral density  $J(\omega)$  with exponential cutoff is assumed. It is characterized by the coupling strength  $\eta$  and the cutoff frequency  $\omega_c$ .

Once the system-bath Hamiltonian is defined, the correlated ground state can be determined by propagation in imaginary time (cf. Appendix A.4). For temperatures which are low relative to the electronic energy difference,  $k_B T \ll \Delta$ , the initial state can be determined using only the Hamiltonian of the electronic ground state,  $\hat{\mathbf{H}}_g$ . The energy stored in the system-bath coupling,  $\langle \hat{\mathbf{H}}_{SB} \rangle$ , was computed. Its value depends on the coupling parameter, in our simulations we could get converged results for relatively large coupling with  $\langle \hat{\mathbf{H}}_{SB} \rangle$  reaching 30% of the total energy.

## 4.2 Spectra

### 4.2.1 Correlation functions and CW absorption

The continuous wave (CW) absorption spectrum reflects part of the photoreaction dynamics. It can be calculated by employing the theory of linear response. The weak field spectral response of matter is then associated to the Fourier transforms of time correlation functions. The correlation functions are calculated using the system and bath Hamiltonian without the external field. For example, the CW absorption spectrum is calculated using the following autocorrelation function [59],

$$C(t) = \langle \Psi_i | \hat{\mathbf{M}}(t) | \Psi_i \rangle , \quad (4.8)$$

where  $|\Psi_i\rangle$  is the initial state. The time-dependent propagator  $\hat{\mathbf{M}}$  is defined as

$$\hat{\mathbf{M}}(t) = \hat{\boldsymbol{\mu}}_{tr} \left\{ e^{-i(\hat{\mathbf{H}}_S + \hat{\mathbf{H}}_{SB} + \hat{\mathbf{H}}_B)t} \right\} \hat{\boldsymbol{\mu}}_{tr} . \quad (4.9)$$

For finite temperature, a Boltzmann weighted sum over all populated stationary states needs to be considered in Eq. (4.8). The absorption cross section  $\sigma_A(\omega_L)$  is related to the Fourier transform of the autocorrelation function of the initial state [36],

$$\sigma_A(\omega_L) \propto \omega_L \text{Im} \left( \int_0^\infty e^{i(\omega_L + \epsilon_i)t} C(t) dt \right) , \quad (4.10)$$

where  $\epsilon_i$  is the energy of the initial state  $|\Psi_i\rangle$ .

At time  $t = 0$  the vibrational ground state of the electronic ground state potential is promoted to the electronically excited state, and the diabatic

coupling as well as the coupling to the bath are switched on. The frequency of the ground state potential was chosen as  $\omega_g = 10^{-3}\text{au}$ , i.e. about  $220\text{cm}^{-1}$ , and the frequency of the excited state potential as  $\omega_e = 0.7\omega_g$ .

Fig. 4.2 shows the autocorrelation function calculated by Eq. (4.8), while the absorption cross section, obtained from Eq. (4.10), is plotted in Fig. 4.3. Constant diabatic coupling and localized diabatic coupling are compared (top and bottom, respectively). Since the Surrogate Hamiltonian is converged for a finite time only, the autocorrelation function cannot be Fourier transformed directly. Instead, the frequencies and decay rates contained in the signal were extracted by Filter Diagonalization (cf. Appendix C.2). The CW absorption spectrum was then reconstructed as a sum of Lorentzians. The data window in time is confined by the convergence time of the Surrogate Hamiltonian. This is indicated by comparing the results for  $N = 9$  to the results for  $N = 11$  modes. The actual data window had to be chosen carefully since it is used for extrapolation to longer times (cf. Appendix C.2). In Fig. 4.2, the data between 50 fs and 530 fs was used in Filter Diagonalization.

In addition to the spectrum, the eigenfrequencies of the system Hamiltonian  $\hat{\mathbf{H}}_S$ , including the diabatic coupling, are indicated as thin lines in Fig. 4.3. The nonstationary initial state can be expanded into eigenstates of the system as can be seen in Fig. 4.3. In the case of constant diabatic coupling all eigenstates within a certain energy range are excited while for localized diabatic coupling only a few eigenstates contribute. In the case of localized coupling (cf. Fig. 4.3 bottom), the eigenstates corresponding to the three peaks with highest intensity carry 80% of their weight on the excited state while the eigenstates in between carry less intensity on the electronically excited state. For constant diabatic coupling, more peaks are excited (cf. Fig. 4.3, top). In this case it is the eigenstates with peaks close to the classical turning point which contribute most. The influence of the bath is twofold: It leads to a finite width of the peaks which increases with increasing system-bath coupling  $\eta$ . Furthermore, the bath shifts the spectrum first towards lower frequencies but then, due to mixing, the frequencies can increase (cf. Sec. 4.2.3).



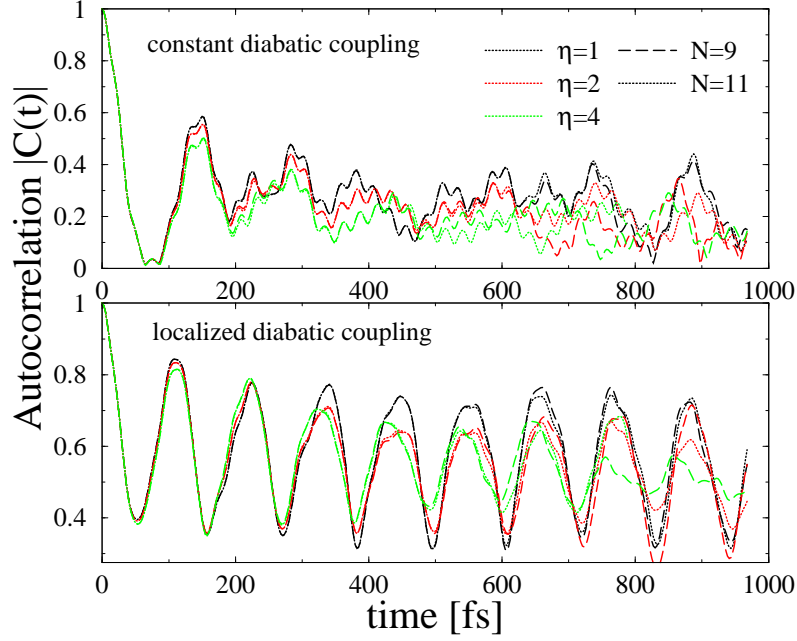


Figure 4.2: The absolute value of the autocorrelation function is plotted for constant diabatic coupling,  $J_d = \omega_g$ , (top) and localized diabatic coupling,  $J_d = 5\omega_g$ ,  $\sigma_d = 0.1$ , (bottom). The system-bath coupling  $\eta$  is increased.

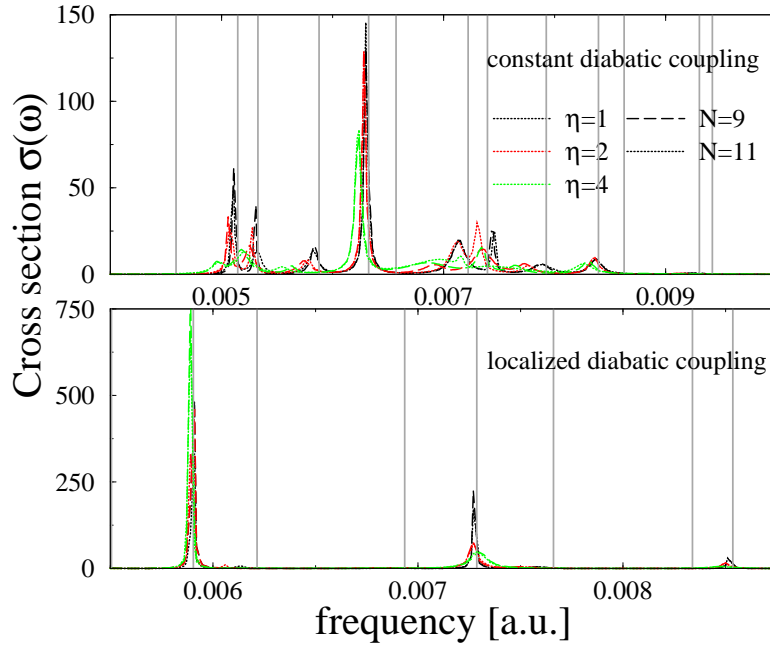


Figure 4.3: The absorption cross section, corresponding to the autocorrelation function of Fig. 4.2 vs. frequency. The eigenfrequencies of the system Hamiltonian are indicated by thin grey lines.

### 4.2.2 Excitation by the pump pulse

The correlated initial state of system and bath is the starting point for launching the pump-probe simulation. This state is propagated with the time-dependent Hamiltonian, Eq. (4.1), leading to population transfer to the excited state. The phase space density of the excited state wave function at different times during the pump pulse is shown Fig. 4.4. Due to the slope of the excited state potential the population transfer is not symmetric (cf. Fig. 4.4, left and middle). Toward the end of the duration of the pump pulse, the wave packet starts to move away from the Franck-Condon point and develops a coordinate-momentum correlation.

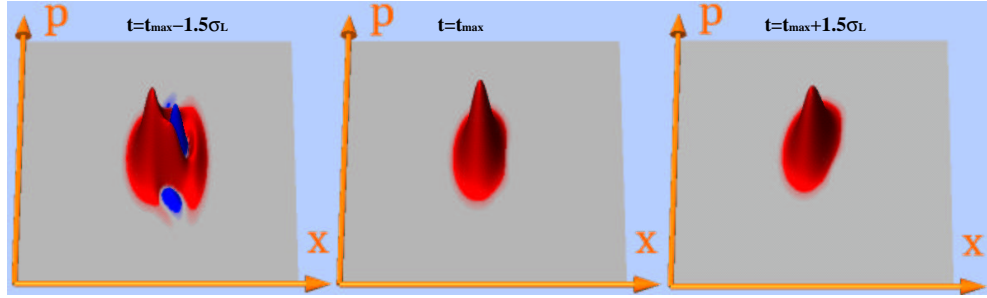


Figure 4.4: Normalized Wigner function for the excited state wave function during the pump pulse at  $t = t_{max} - 1.5\sigma_L$ ,  $t = t_{max}$  and  $t = t_{max} + 1.5\sigma_L$  (from left to right) with  $\omega_e = 0.7\omega_g$ ,  $\eta = 1.0$ ,  $J_d = 5\omega_g$ ,  $\sigma_d = 0.1$ ,  $N_{modes} = 11$

In almost all previous studies of the charge transfer problem, the initial state was chosen to be an uncorrelated Gaussian wave packet. It was positioned at the Franck-Condon point in the electronically excited state, and a coordinate-independent, i.e. global, diabatic coupling was switched on at time  $t = 0$ . When the excitation process induced by the pump pulse is considered explicitly, such a choice of diabatic coupling leads to unphysical spurious results. This is shown in the upper panel of Fig. 4.5. Due to the global diabatic coupling, the electronically excited state is already populated before the excitation. Therefore the pump pulse results in both stimulated absorption and emission. This choice of diabatic coupling furthermore induces immediately population transfer between the electronic states. This can be seen in the oscillations in Fig. 4.5 (upper panel). Such an unphysical phenomenon can be avoided by using a localized diabatic coupling operator

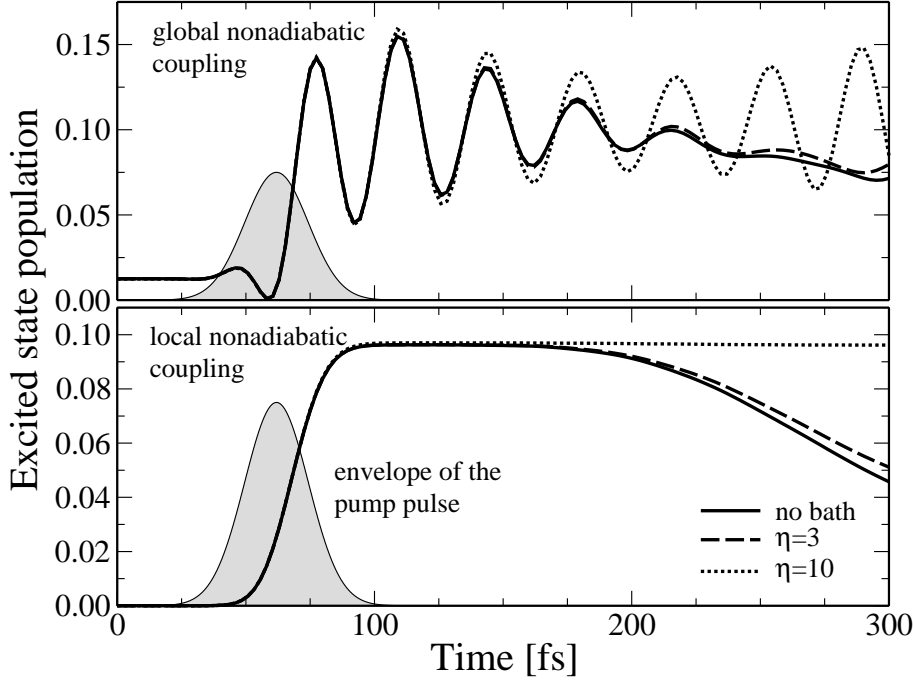


Figure 4.5: The population on the excited state for global and for local diabatic coupling ( $J_d = 1.0\omega_g$ ,  $\sigma_d = 0.1$ ), with and without vibrational relaxation ( $\eta$ ). The initial state, which is the ground state of the total system and bath, is partially excited to the electronically excited state due to the pump pulse (not to scale).

(cf. Fig. 4.5, lower panel). This is well justified since diabatic coupling functions obtained from *ab initio* calculations turn out to be localized [75, 76]. For this case, the electronically excited state is not populated initially. The transfer of population starts only after the pump pulse has been applied, and the wave packet has traveled to the crossing region of the potentials.

For localized diabatic coupling and strong vibrational relaxation, a new phenomenon can be observed: trapping on the excited state. This results from the wave packet relaxing so fast that it can not reach the crossing region of the potentials anymore (cf. the dotted curve in the lower panel of Fig. 4.5). This observation is part of the turnover phenomenon and will be discussed in Section 4.3.

### 4.2.3 Transient absorption and emission

Transient absorption and emission result from the application of the probe pulse. Since the probe pulse is assumed to be weak, the window operator (cf. Appendix B) has been employed.

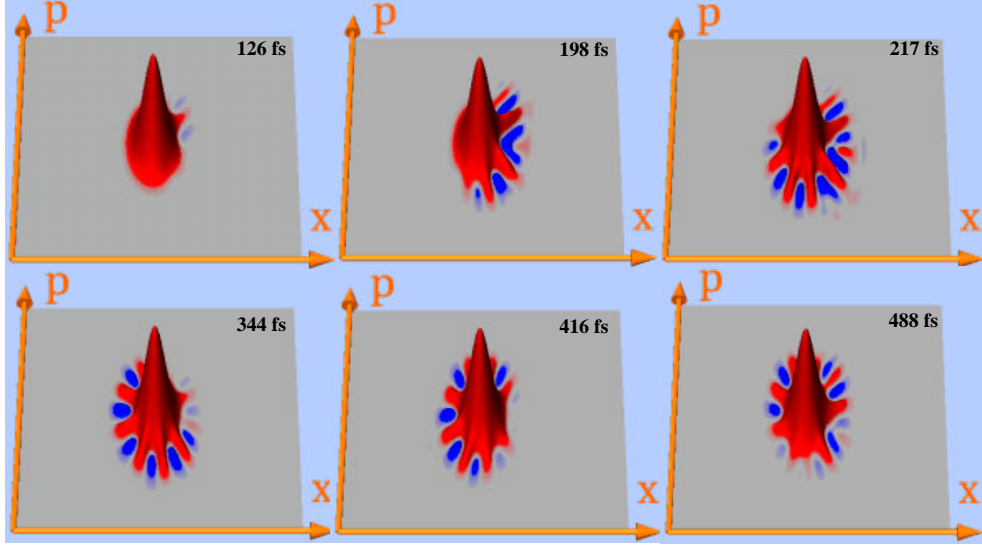


Figure 4.6: The Wigner function of the ground state wave function at subsequent times (126 fs, 198 fs, 271 fs, 344 fs, 416 fs, 488 fs from top left to bottom right). The system-bath coupling is  $\eta = 1\omega_g$  and the local diabatic coupling is  $J_d = 5\omega_g$ , with width  $\sigma_d = 0.1$ .

The absorption of the probe pulse reflects the ground state dynamics. Fig. 4.6 displays the Wigner function of the ground state wave packet after the excitation and Fig. 4.7 shows several dynamical expectation values. The time steps at which the Wigner function is plotted are indicated by arrows in the middle panel of Fig. 4.7. Since the pump pulse excites about 10% of the ground state population to the electronically excited state, the ground state wave packet is only weakly perturbed by the excitation process. However, after the excited state wave packet has reached the crossing point, population is nonadiabatically transferred back to the ground state. Due to the locality of the diabatic coupling, this population transfer occurs in spurts. The spurts are caused by a splitting of the Wigner function on the excited state surface when it hits the crossing point.

In Fig. 4.7, the loss of ground state population due to the pump pulse

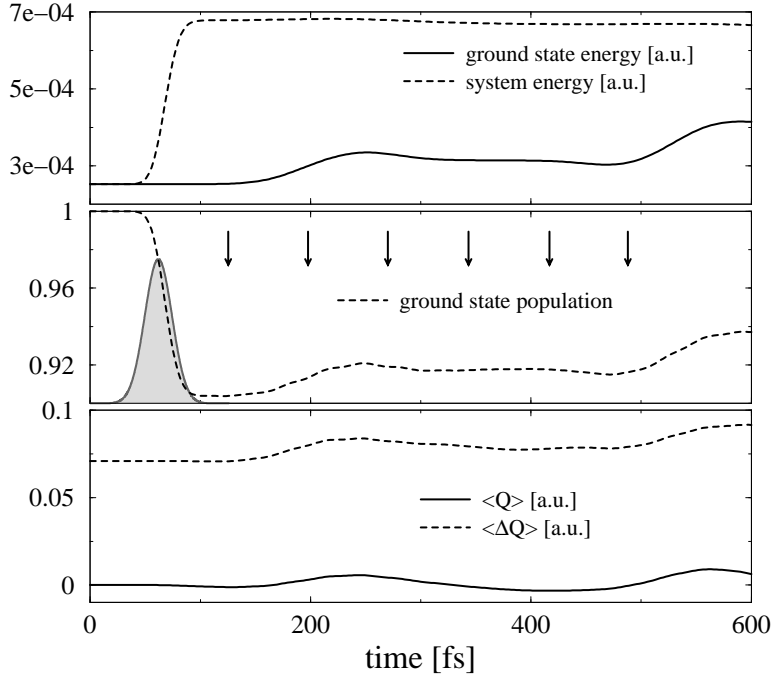


Figure 4.7: The expectation values of  $\hat{\mathbf{H}}_g$  and  $\hat{\mathbf{H}}_S$  (upper panel), the ground state population (middle panel), and the expectation value of  $\hat{\mathbf{Q}}$  and  $\Delta\hat{\mathbf{Q}} = \sqrt{\langle\hat{\mathbf{Q}}^2\rangle - \langle\hat{\mathbf{Q}}\rangle^2}$  on the ground state (lower panel) versus time. The envelope of the pump pulse and the times at which the Wigner function is plotted in Fig. 4.6 are indicated.

and then the recovery of the population due to nonadiabatic transfer (middle panel) are observed. The population newly created in the electronic ground state is vibrationally excited (top panel). The appearance of this population in the observation window of the probe is delayed by the timescale of vibrational relaxation (cf. Fig. 4.8 left, bottom panel). This phenomenon has been termed the "recovery of the bleach" or recovery of the ground state equilibrium. Finally, the transient absorption and emission signals and their spectra are plotted in Figs. 4.8 and 4.9. Higher harmonics corresponding to the non-Gaussian features in the Wigner function (Fig. 4.6) can be observed (see insets in Fig. 4.9). These features cannot be seen in the coordinate expectation value,  $\langle\hat{\mathbf{Q}}\rangle$ , or the coordinate standard deviation,  $\langle\Delta\hat{\mathbf{Q}}\rangle$  (Fig. 4.7, bottom panel). Fig. 4.8 shows furthermore the influence of electronic dephasing on the transient emission and absorption signals. Nuclear dephasing with reasonable parameters did not influence the dynamics.

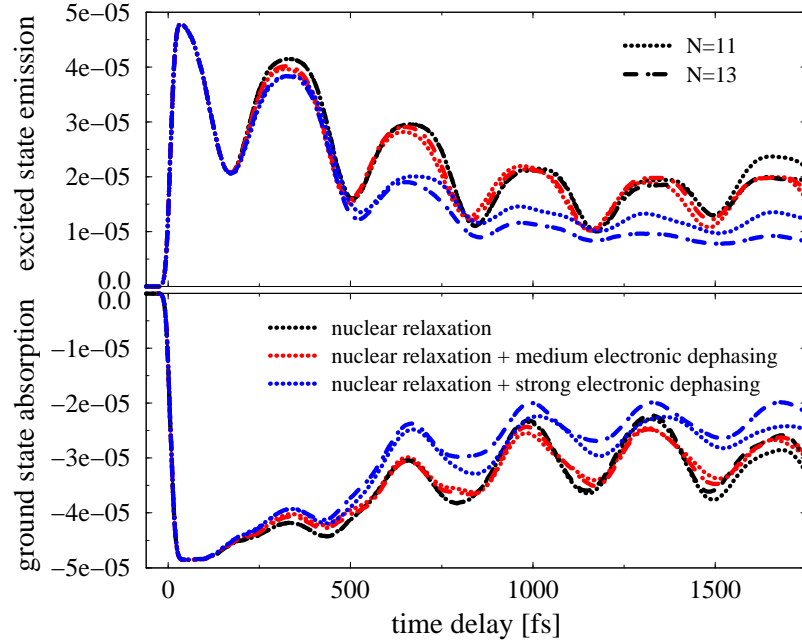


Figure 4.8: Stimulated transient emission (upper panel) and transient absorption (lower panel) for nuclear relaxation and for nuclear relaxation plus electronic dephasing. The relaxation parameter is  $\eta = 1$  with cutoff frequency  $\varepsilon_c = 2\varepsilon_g$ . The dephasing parameter is  $\bar{c} = 0.005$  for medium dephasing and  $\bar{c} = 0.01$  for strong dephasing. The pump and probe frequencies are chosen to correspond to the bottom of the ground state electronic potential.

The shape of the transient emission and absorption is caused by both electronic oscillations and nuclear vibrations. Therefore the observed frequencies do not correspond to the vibrational frequencies of the diabatic potentials or to the eigenvalues of the system Hamiltonian  $H_S$  (in contrast to the absorption cross section, cf. Sec. 4.2.1). The observed frequencies are rather a result of a subtle interplay between system and bath. To illustrate this, the system-bath coupling parameter was varied and the frequencies of the ground state absorption, obtained by Filter Diagonalization, are plotted vs. the system-bath coupling in Fig. 4.10. A pattern of avoided crossings as a function of the system-bath coupling parameter  $\eta$  is clearly visible.

The amplitude of the electronic oscillations is decreased by electronic dephasing. This leads to a decrease in amplitude of the oscillations in the transient emission/absorption (cf. Fig. 4.8). Filter Diagonalization was applied to obtain spectra, and a data window between 250 fs and 1410 fs was chosen.

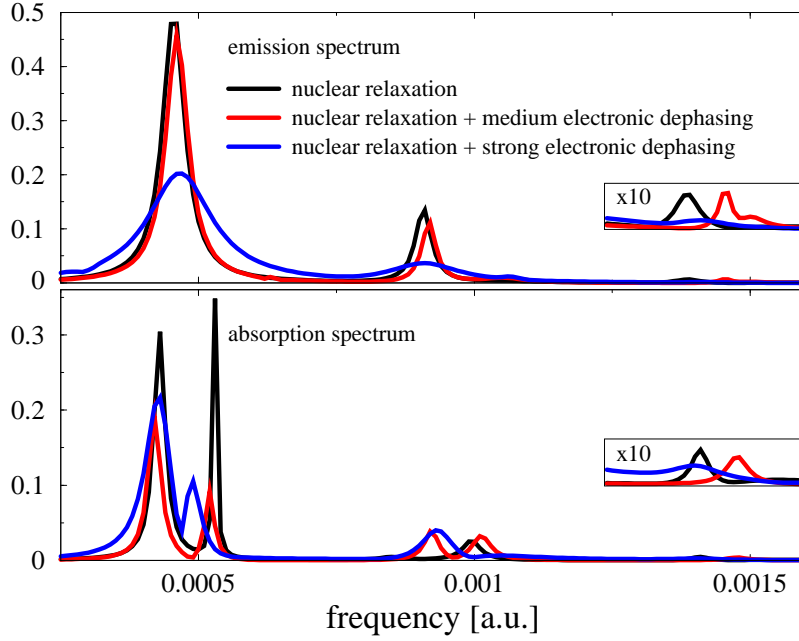


Figure 4.9: Stimulated transient emission (top) and absorption (bottom) spectra (right) corresponding to Fig. 4.8.

Dephasing causes a widening of the peaks in the spectra (cf. Fig. 4.9).

The "recovery of the bleach" or the recovery of the ground state absorption is observed in the bottom panel of Fig. 4.8. This recovery is due to the filling of the observation window which is caused by the nonadiabatic transfer from the excited state and by cooling of the vibrational excitation on the ground electronic potential (cf. Fig. 4.1).

The probe pulse can be positioned in resonance to the inner and outer turning points of the ground state potential. One would expect a half a period time delay between the peaks in the two signals [66]. We found that the electronic oscillations due to the nonadiabatic population transfer completely destroy this half a period time delay pattern.

The timescale for the recovery which corresponds to the decay rate of zero frequency is  $\sim 1.5$  ps. To estimate the influence of dephasing, the highest peak intensities were compared. For data windows between 770 fs and 1430 fs, a linear dependence of the intensity versus the dephasing parameter was obtained and the slope varied between  $-0.9 \cdot 10^{-4}$  and  $-1.5 \cdot 10^{-4}$ .

The effect of the initial correlations on the dynamics, for CW absorp-

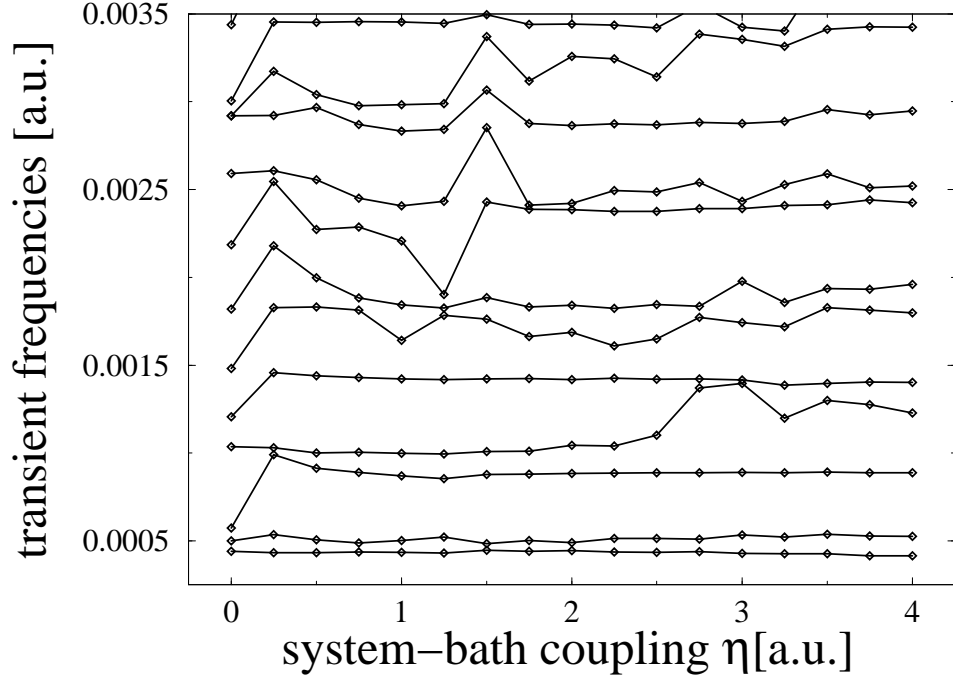


Figure 4.10: The frequencies in the transient ground state absorption obtained by Filter Diagonalization vs. the system-bath coupling parameter. No electronic dephasing is included. The remaining parameters are the same as in the previous figure.

tion as well as for the transient absorption and emission, was found to be small even for the strong coupling case. To this end, the autocorrelation function and the transient emission were compared for a correlated and an uncorrelated initial state. In the uncorrelated case, the initial state is the ground state of  $\hat{\mathbf{H}}_g$ , while in the correlated case it is the ground state of  $\hat{\mathbf{H}}_g + \hat{\mathbf{H}}_{SB}^{nr} + \hat{\mathbf{H}}_B$ . The comparison was made with a set of different coupling functions  $f_{g/e}(\hat{\mathbf{Q}})$  in Eq.(3.20). The observed effect was small for linear as well as nonlinear coupling although the system-bath coupling term caused a significant shift of the modulation frequency in both cases. This is in line with the argument that the influence of the laser field establishes new, non-equilibrium initial conditions [48]. In the cases studied here, the influence of the field on the initial conditions is obviously much stronger than the influence of the bath.



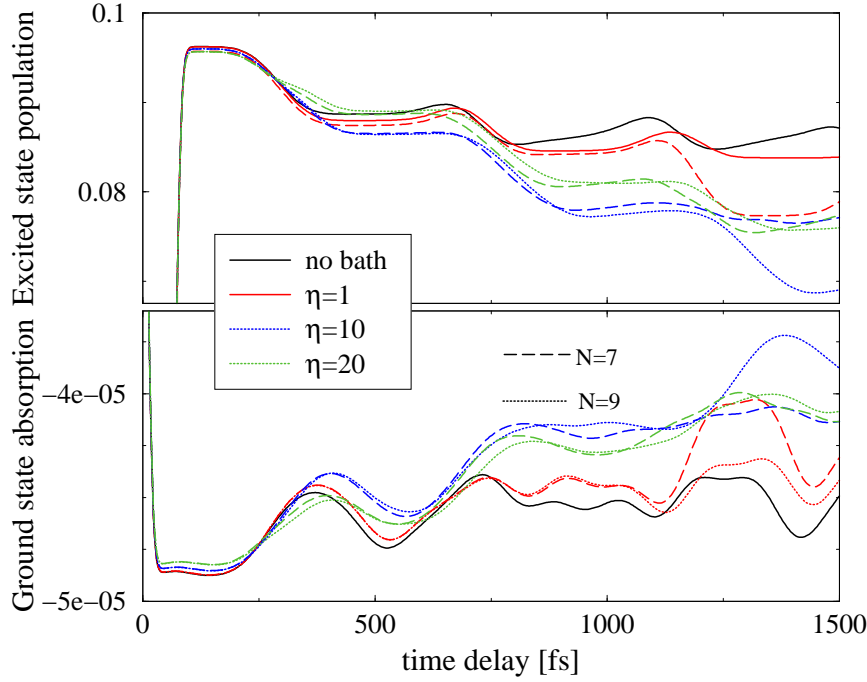


Figure 4.11: Turnover: The population of the excited state (upper panel) and the ground state transient absorption (lower panel) for different  $\eta$  with the parameters of the diabatic coupling  $J_d = 0.2\omega_g$  and  $\sigma_d = 0.1$ .

### 4.3 The interplay of diabatic coupling and coupling to the bath – the turnover

Nonadiabatic charge transfer is a complex event which is sensitive to all dynamical parameters. Previously, based on a semigroup model of dissipation, a turnover of the charge transfer rate as a function of almost any external variable has been observed [65]. Turnover describes the fact that the charge transfer rate first increased and then decreased as a function of the nuclear relaxation and the nuclear dephasing rate, the electronic dephasing rate, as well as the diabatic coupling parameter  $J$ .

Fig. 4.11 demonstrates the turnover phenomenon as a function of the nuclear relaxation rate. The excited state population is first created by the pump pulse and then lost through the diabatic coupling to the ground state. The rate of loss increases with  $\eta$  but eventually the turnover takes place and the population becomes trapped in the lowest part of the potential well of the excited state. From this position the nonadiabatic transfer can only occur

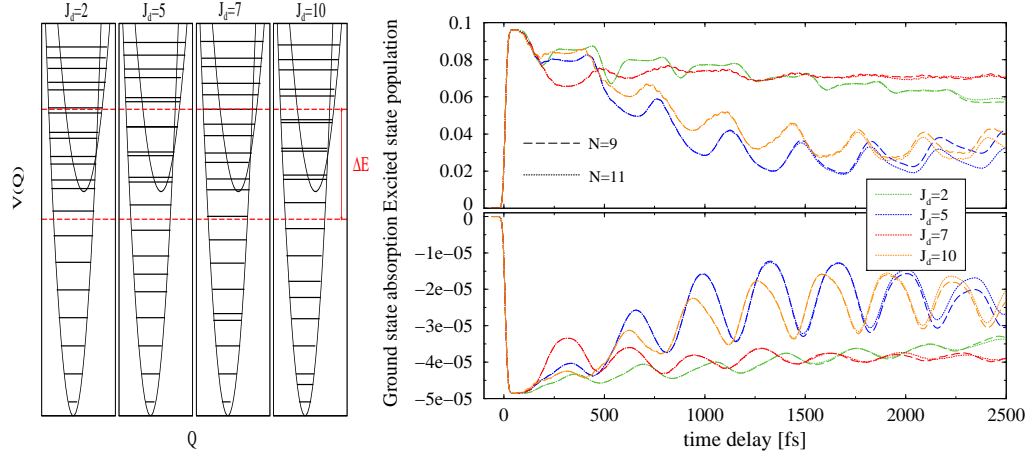


Figure 4.12: Turnover: Resonance phenomenon due to variation of  $J_d$ . The diabatic potentials with the energy levels of  $H_S$  are shown on the left, also plotted is the band width  $\Delta E$  due to the pulse. For  $J_d = 5$  and  $J_d = 10$ , there are quasi-degeneracies within the energy window given by  $\Delta E$ , this leads to an enhanced population transfer (right, upper panel) which can be detected in the ground state absorption (right, lower panel).

by tunneling, which is slow relative to the other processes.

The transient absorption of the probe pulse from the ground state reflects the increase in population which is known experimentally as the "recovery of the bleach" [66]. The slow recovery of the bleach for high  $\eta$  implies that the turnover phenomenon can be observed by ultrafast pump-probe spectroscopy.

A more complex turnover phenomenon is observed with respect to the diabatic coupling constant  $J_d$ . In addition to a general turnover trend, oscillations in the rate as a function of  $J_d$  are observed (cf. Fig. 4.12). These oscillations can be attributed to accidental degeneracies between the electronic ground and excited state (cf. Fig. 4.12 left). These degeneracies are not observed in the global diabatic coupling case.

## 4.4 Discussion

The present study is the first construction of a comprehensive model for the ultrafast pump-probe spectroscopy of the charge transfer cycle. The use of the Surrogate Hamiltonian has the advantage of a consistent treatment of initial correlations, non-Markovian dynamics and explicit description of the

interaction with the pulse.

This exploration has identified severe flaws in previous descriptions [65, 77, 78]. The main shortcoming consists in in the vertical Franck-Condon transition of the ground state as the initial state for the nonadiabatic process. This choice ignores the initial system-bath correlation and in particular the dynamical aspects of the interaction with the pump pulse.

It was found that the initial system-bath correlation has only a small influence on the short-time observables investigated here. However, an effect of initial correlations on non-exponential long-time dynamics has been reported within a path integral approach on a single electronic state [79]. The interaction between system and bath strongly influences the dynamics. In combination with the nonadiabatic character of the excited vibrational eigenstates, it induces mixing of the states which results in a complicated pattern of frequency shifts. The phase shift between different locations of the probe pulse transition does not correspond to simple ground state coherent motion. Moreover the population transfer to the excited surface due to the pump pulse is strongly influenced by the diabatic coupling term as well as by the electronic dephasing term. The analysis shows that only the localized version of the diabatic coupling term has physical meaning.

The present study does confirm the general turnover phenomenon in the charge transfer reaction [65] which was first identified in a qualitative semi-group study. The present modeling of the pump-probe experiment shows that the transient absorption can be used to indicate the turnover phenomenon. The turnover phenomenon also imposes restrictions on the maximum rate which can be observed in the recovery of the bleach. With the current set of parameters this timescale is approximately 1.5 ps which is a factor of two slower than the experimental findings.

The present model could reproduce all steps of the charge-transfer cycle. It is nevertheless still over-simplified. The main discrepancy is the result of the single nuclear degree of freedom. It is well documented that nonadiabatic transfer events are extremely sensitive to the nuclear topology [80]. An additional nuclear degree of freedom allows the existence of conical intersections which open a new fast route or funnel from the excited to the ground state [77]. This could be the reason for the discrepancy between the current

one-dimensional calculations and the experimental findings. In principle the description of the primary system could be extended to include additional degrees of freedom. This addition however, would increase considerably the required computational resources. Adding a single high frequency vibrational mode becomes, however, feasible by just including the two lowest levels as an additional spin. An additional electronic degree of freedom would be described in a similar fashion.

Another serious simplification is given by the assumption of harmonic potentials. In the second part of this thesis, the Surrogate Hamiltonian is therefore be applied in combination with *ab initio* potential energy surfaces to laser induced desorption of small molecules from surfaces. While this is also a condensed phase process, the system is very well characterized both experimentally and theoretically. This allows for the development of a *microscopic* picture of the interaction between system and environment. The main dissipation process in this case is given by electronic quenching. Electronic quenching has not been considered so far, since for a chromophore in a bath it is not efficient. The reason is that there are no dipoles in the solvent which are in resonance with the electronic transition dipole. This is, of course, solvent dependent. A polar solvent, for example, might require the treatment of electronic relaxation. It furthermore becomes important for a molecule on a surface. Due to accepting bath modes in the appropriate frequency range electronic quenching will turn out to be substantial. This will be the subject of the second part of this thesis.

# Chapter 5

## Laser induced desorption

Laser induced desorption describes the detachment of molecules adsorbed on a surface after laser irradiation. It is a special case of Desorption Induced by Electronic Transitions (DIET). If the molecules are chemisorbed, it involves the cleavage of a chemical bond. The systems which have most intensively been studied are those of small molecules, such as

O<sub>2</sub>, CO, or NO, adsorbed on single crystal metal or metal oxide surfaces, such as platinum, copper, nickel oxide, or chromium oxide surfaces [81, 82]. A desorption experiment requires the preparation and characterization of the surface under UHV conditions, the adsorption of molecules on the surface and the detection of desorbing molecules. Observables in a desorption experiment are hence the desorption cross section and the kinetic energy of the desorbate. If the detection proceeds state-resolved, also vibrational and rotational energies or the alignment of the desorbing molecules can be determined [83].

Desorption can be induced by two different processes – besides electronic transitions also heating of the system leads to desorption, consequently termed thermal. The observed kinetic energy distributions, for example, differ greatly pointing to the two distinct mechanisms which cause desorption. Thermal desorption results in the distribution of energy onto all degrees of

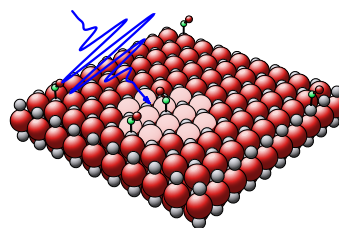


Figure 5.1: Laser irradiation of a surface with molecules adsorbed on it (here NO/NiO(100)) leads to desorption of the molecules.

freedom while for laser induced desorption the excitation of specific quantum states can be observed resulting in a non-thermal distribution of energy.

An attempted theoretical description of laser induced desorption must therefore be quantum mechanical. One-dimensional models will at best be able to describe experimentally observed desorption yields and kinetic energy distributions. Vibrational and rotational energies can only be captured in a higher-dimensional model including the internal degrees of freedom of the molecules.

## 5.1 Theoretical models for laser induced desorption from surfaces

Two popular schemes have been used to explain the mechanism underlying laser induced desorption, e.g. [13,82], both involve a short-lived electronically excited state. The Menzel-Gomer-Redhead (MGR) model [84,85] assumes the electronically excited state to be repulsive, while in a variation of the MGR model going back to Antoniewicz [86] the excited state is bound (cf. Fig. 5.1). In both models, the excitation by the laser pulse is modeled as

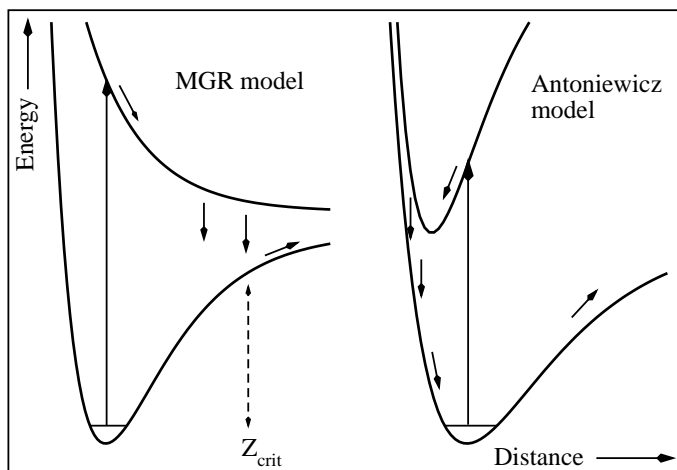


Figure 5.2: Menzel-Gomer-Redhead and Antoniewicz mechanisms to explain laser induced desorption.

a Franck-Condon transition from the electronic ground to an excited state. Electronic quenching brings the wave packet back to the ground or another lower lying state. It is thought of as a second vertical transition. Desorption occurs in the MGR model when the transition from the electronically excited state back to the ground state happens after the wave packet describing

the center of mass motion of the molecule has passed a critical distance  $Z_0$  and gained sufficient kinetic energy to escape the potential well. In the Antoniewicz model, which corresponds to an ionic excited state, the wave packet is accelerated toward the surface. The electronic deexcitation leaves the wave packet in the repulsive part of the ground state potential where it may also gain kinetic energy for desorption.

The MGR model was originally developed for classical trajectories describing the center of mass motion of the molecule. A widely used improvement was introduced by Gadzuk [87, 88]: The classical point particle is replaced by a quantum mechanical wave packet. An ensemble of such wave packets is considered with each wave packet "living" on the excited state for a certain residence time. Expectation values are computed as stochastic averages of the ensemble where the resonance time, i.e. the lifetime of the excited state, enters as a weight.

If the theoretical description shall be more than qualitative, a more rigorous approach is needed regarding the involved potential energy surfaces and the excitation and deexcitation mechanisms. The calculation of reliable potential energy surfaces in general, and for excited states in particular, is still an open problem. However, for the systems NO/NiO(100) [89, 3] and CO/Cr<sub>2</sub>O<sub>3</sub>(0001) [90, 91] excited state potentials were obtained. The topology of the representative excited state potential for NO/NiO(100) which was used in the calculations will be discussed in Section 6.1.

Irradiation by nanosecond pulses can well be described by a Franck-Condon transition. The theoretical description of femtosecond experiments, however, requires an improved model since excitation, excited state dynamics and relaxation all happen on the same timescale. For metals, the two-temperature model [13] has been introduced to describe femtosecond excitation of the surface. The excitation mechanism is assumed to be substrate-mediated, i.e. the pulse generates a cloud of hot electrons which can attach to or scatter from the adsorbate. The hot electrons are characterized by a temperature  $T_e$ , and they equilibrate due to interaction with phonons characterized by temperature  $T_p$ . The time-dependence of these two temperatures can be described by coupled diffusion equations. While the electronic peak temperature is reached on the timescale of the pulse, the equilibration pro-

ceeds on the timescale of picoseconds. The two-temperature model is a zeroth order description of the substrate response and neglects the non-thermal nature of excited electrons. On oxides, the substrate is also involved in the excitation process. This can be seen in the linear dependence of the desorption cross section on the laser energy once the laser energy is larger than the band gap, e.g. [92]. The excitation mechanism can, however, be thought of as semi-direct (cf. the discussion in Section 6.1), then the full time-dependence of the pulse enters the theoretical model.

The electronic excitation of the adsorbate is dissipated into the surface due to interaction with surface electrons and holes or phonons. The lifetime of the electronic excitation is extremely short [93]. For metals it is estimated to be  $\tau \lesssim 1$  fs while for oxides it is assumed to be somewhat larger,  $\tau \approx 20 \dots 30$  fs. If the interaction with charge carriers in the surface is seen as the primary cause of relaxation, this difference corresponds to the different density of states in metals and insulators. In both cases the short lifetime leads to the conclusion that the interaction with the surface must be strong [13]. If a fully quantum mechanical description of the problem is desired, an open quantum system approach should be used with the surface electron-hole pairs and phonons modeled as environment. Remembering the possible theoretical methods described in Chapter 2, this poses a theoretical dilemma: Strong interaction with the environment excludes perturbation theory. The impossible separation of excitation and relaxation timescales makes non-Markovian effects likely to be important. An anharmonic environment (the electron-hole pairs in the surface), comparatively low temperature and an explicit time-dependence of the Hamiltonian are not in favor of a path-integral approach.

The number of existing theoretical studies on femtosecond laser induced desorption is therefore rather small. The above mentioned two-temperature model was used in a semigroup treatment for NO/Pt(111) [94, 95]. The lifetime of the excited state was assumed to be 2 fs while the pulse had a full-width half-maximum (FWHM) of 50 fs. The excitation timescale, however, was prolonged due to the indirect treatment of the pulse in the two-temperature model. This justified, at least partially, the Markov assumption inherent in the semigroup approach. Another indirect treatment



of the excitation has been applied to CO/Cu(111) [96,97]. The pulse induces a dipole moment in the surface to which the adsorbate responds. The surface is treated as stochastic environment leading to an optical potential in the system Hamiltonian. Memory effects were argued to be negligible due to internal energy transfer in the surface, a consideration of timescales or interaction strengths was, however, not given. Direct optical excitation without further justification has been assumed for NH<sub>3</sub>/Cu(111) [98] although the excitation is known to be substrate-mediated [99]. The deexcitation was also modeled by an optical potential, i.e. assuming a  $\delta$ -correlated environment. However, the field is known to affect the dissipation. In a perturbational treatment of the system-bath coupling (cf. Chapter 2), for example, the field enters the memory kernel describing the influence of the bath [74]. Since excitation and deexcitation are both caused by electrons in the copper surface, and the timescales of excitation and relaxation are comparable (the pulse FWHM was varied between 5 fs and 90 fs and excited state lifetimes between 2.5 fs and 25 fs), correlation between excitation and dissipation is to be expected. The treatment of [98] does therefore not seem to be methodologically sound.

The next section briefly reviews previous experimental and theoretical findings for the laser induced desorption of NO from NiO(100) before summarizing the questions to and possible answers from a theoretical description.

## 5.2 Laser induced desorption for NO/NiO(100)

Using thermal desorption spectroscopy NO was found to be weakly chemisorbed on NiO(100) with an adsorption energy of about 0.5 eV [100, 101]. The adsorption geometry was determined by NEXAFS (Near Edge X-Ray Absorption Fine Structure) and HREELS (High Resolution Electron Energy Loss Spectroscopy) as NO on top of a regular nickel site with a tilt angle between NO axis and surface normal of 45° [100]. Photoelectron diffraction revealed a somewhat larger tilt angle of 60° [102].

Laser induced desorption experiments with nanosecond pulses [103, 92] yielded the following observations: The desorption cross section shows a linear dependence on laser energy above the band gap of nickel oxide [92]. This indicates a correlation of desorption with charge transfer excitations in nickel

oxide. The velocity distributions of desorbing molecules show a pronounced bimodality within a range from 0 m/s to 2000 m/s. An example is shown in Fig. 5.2. The two peaks have been related to two desorption channels

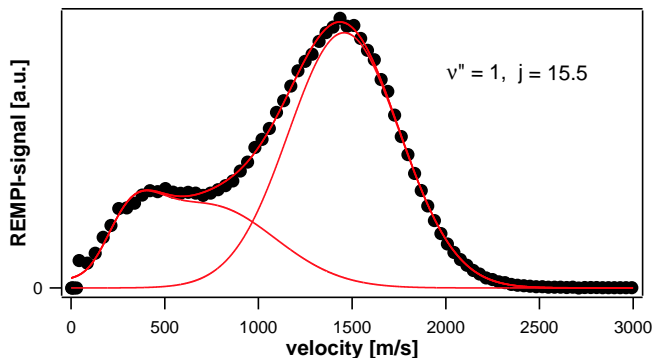


Figure 5.3: Experimentally obtained state-resolved velocity distribution.

which are both *non-thermal* owing to the high vibrational and rotational temperatures of the desorbate [103]. State-resolved detection of the molecules furthermore revealed a correlation between rotation and translation for the fast desorption channel, while no correlation between vibration and translation was found.

A theoretical description of the laser induced desorption experiments with nanosecond pulses has recently been given within a two-dimensional stochastic wave packet treatment [105, 89, 106]. The lifetime of the excited state as an empirical parameter was adjusted such that the desorption yield was compatible with experimental results. Velocity distributions in the correct range of velocities and the bimodality of the distributions could be reproduced by the model. The bimodality was explained in terms of the topology of the excited state potential which lead to a bifurcation as well as the vibrational excitation of the wave packet. The excited state dynamics could furthermore explain the coupling of translational and rotational degrees of freedom.

Subpicosecond experiments [107, 108] with the pulse duration estimated as 550 fs revealed no substantial differences as compared to the results of the experiments employing nanosecond pulses. In particular, the yield was found to exhibit a linear dependence on laser fluence. The linearity indicated a DIET as opposed to a DIMET (Desorption Induced by *Multiple* Electronic Transitions) mechanism. Since ultrashort pulses are usually intense, a crossover from a linear to a power-law dependence of the yield on fluence pointing to a crossover from DIET to DIMET mechanisms could

be expected. Such a crossover has been observed for another system, although with a metal substrate and shorter and more intense pulses [109]. The pulses applied to NO/NiO(100) were rather long and of only moderate intensity which renders the observed linearity reasonable. Furthermore no pronounced differences were observed in the state-resolved velocity distributions. However, a vibrational period in desorption coordinate in the excited state potential region which is probed by the pulse assuming resonant excitation is about 220 fs. The estimated excited state lifetime of about 25 fs is even a magnitude shorter. A pulse of 550 fs width can, therefore, not be expected to probe the nuclear dynamics of the excited state. Preliminary results have been reported using a pulse of 100 fs FWHM [110] which suggested a coupling of the internal NO vibration and translation. For specific rovibrational states, velocity distributions with an inversed population of the desorption channels were observed. This was, however, not investigated for all rovibrational states [110]. A laser desorption experiment applying two pulses is in progress [104]. The objective is to use the second pulse to probe the excited state dynamics. Such an experiment could directly yield the excited state lifetime, the implicit assumption being that the lifetime is long enough for the pulses and the pulse delay to compete with it. With the laser technology available today this can at best be expected for excited states on oxides, while the lifetime of excited states on metals is still beyond reach.

The demands on a theoretical description of laser induced desorption of NO from NiO(100) from first principles, i.e. with as few free parameters as possible, can be summarized as follows. The complicated electronic structure of an adsorbate on a transition metal oxide requires a reliable excited state potential energy surface. This has been accomplished on an *ab initio* level [89]. The non-thermal desorption mechanism demands a quantum dynamical treatment, and the coupling between different degrees of freedom can only be captured in a multidimensional approach. This has been realized with, however, a simplified treatment of the relaxation of the excited state [105, 90]. The introduction of femtosecond laser technology requires a theoretical treatment of excitation and deexcitation mechanisms on the same level of rigor. In particular, a microscopic description of the dissipation has not been attempted so far. The simultaneous fulfillment of all requirements

is one of today's great challenges of theory. The next two chapters are therefore dedicated to the theoretical modeling of the excitation by the laser pulse and the deexcitation due to interaction of the adsorbate with the substrate. Since the focus is on developing a microscopic understanding of the interaction between substrate, adsorbate and laser pulse, a one-dimensional model will be employed. Observables of interest are therefore desorption yield and desorption velocities. Once a fully quantum mechanical description of the desorption event including electronic states, excitation and relaxation mechanisms has been obtained, a generalization to more degrees of freedom is possible. This would allow for calculating furthermore rotational and vibrational distributions. Such a generalization is beyond the scope of this thesis which serves as one more step toward a complete quantum description of laser induced desorption.

# Chapter 6

## NO/NiO(100): Prelude

### 6.1 The primary system: NO on a NiO-cluster

The Hamiltonian describing a NO molecule adsorbed on a NiO(100) surface is given by

$$\hat{\mathbf{H}} = \hat{\mathbf{H}}_S + \hat{\mathbf{H}}_{SF}(t) + \hat{\mathbf{H}}_{SB} + \hat{\mathbf{H}}_{BF}(t) + \hat{\mathbf{H}}_B . \quad (6.1)$$

The system Hamiltonian  $\hat{\mathbf{H}}_S$  describes the adsorbate on a finite part of the NiO-surface, while the remaining part of the surface is modeled as environment or bath ( $\hat{\mathbf{H}}_B$ ). The effect of this environment on the (primary) system is captured in the interaction term  $\hat{\mathbf{H}}_{SB}$ . Both system and environment can interact with the time-dependent external field of a laser pulse,  $\hat{\mathbf{H}}_{SF}(t)$  and  $\hat{\mathbf{H}}_{BF}(t)$ , respectively.

The Hamiltonian of the primary system,  $\hat{\mathbf{H}}_S$ , describes two electronic states and one nuclear degree of freedom,  $\hat{\mathbf{Z}}$ , which is the distance of the molecule from the surface,

$$\hat{\mathbf{H}}_S = \begin{pmatrix} \hat{\mathbf{T}} + V_g(\hat{\mathbf{Z}}) & 0 \\ 0 & \hat{\mathbf{T}} + V_e(\hat{\mathbf{Z}}) \end{pmatrix} . \quad (6.2)$$

The reduction to one nuclear degree of freedom denotes a great simplification and can only serve as a first step in investigating the interaction between system and bath. Higher dimensional studies for the desorption from oxide surfaces have been performed [105,90,111] treating the finite excited state lifetime, however, semi-phenomenologically and neglecting the time-dependence of the pulse. Eq. (6.2) assumes the Born-Oppenheimer approximation [112]

separating electronic and nuclear motion. The Born-Oppenheimer approximation involves two steps. First, the kinetic energy of nuclei is neglected, and the nuclear coordinates are treated as parameters. The electronic Schrödinger equation is obtained. The eigenvalues of the electronic Schrödinger equation depend parametrically on the nuclear coordinates as parameters. In a second step the dynamics of nuclei generated by Eq. (6.1) with the electronic eigenvalues as potential energy surfaces is solved.

The electronic Schrödinger equation for NO/NiO(100) has been solved and potential energy surfaces constructed by Klüner and co-workers [89, 3]. In Eq. (6.2),  $\hat{\mathbf{T}}$  is the (nuclear) kinetic energy operator which is applied in momentum space (cf. Appendix A.1).  $V_g$  is the ground state empirical potential and  $V_e$  the excited state *ab initio* potential [89]. The potentials have been constructed in two degrees of freedom - distance  $Z$  and the angle  $\theta$  between the NO molecular axis and the surface normal. Since only one dimension will be considered, the angle is kept fixed at the equilibrium value  $\theta = 45^\circ$ . The ground state potential shows a Morse-like dependence on the distance  $Z$  with the minimum at about  $Z = 5.5$  a.u. and an adsorption energy of about 0.5 eV. The excited state potential has been calculated in a valence configuration interaction (CI) approach for a  $\text{NO}/\text{NiO}_5^{8-}$  cluster embedded in a point charge field (PCF) [89, 3]. The excited state is a charge-transfer state which is characterized by a deep potential well due to Coulomb interaction between  $\text{NO}^-$  and the positively charged cluster and by a potential minimum at a distance about 1.5 a.u. smaller than the electronic ground state minimum. The wave packet will therefore be accelerated toward the surface upon excitation and desorption will occur according to the Antoniewicz mechanism (cf. Section 5.1).

Configuration interaction has so far been the only method to obtain excited states for adsorbates on transition metal oxides [89, 90]. However, within such an approach of a finite cluster in a point charge field only relative energies and the topology of the potential energy surface can be expected to be reliable. Vertical excitation energies can only be estimated due to orbital relaxation within the cluster and due to extra cluster polarization [113]. Orbital relaxation is a result of employing orbitals in the CI calculations which were obtained by CASSCF calculations for  $\text{NO}^-/\text{NiO}(100)$  instead of

$\text{NO}^-/\text{NiO}(100)^+$ . Extra cluster polarization is caused by the non-polarizable point charge field modeling a polarizable surface. Since many excited states are located in the energy range probed by the laser pulse, the field is likely to cause a resonant transition. The topology of these states is very similar [3]. It is therefore possible to choose one representative state. The vertical energy of this representative excited state can be assumed to coincide with the laser energy in the following.

The Hamiltonian Eq. (6.1) includes both direct ( $\hat{\mathbf{H}}_{SF}(t)$ ) and substrate-mediated ( $\hat{\mathbf{H}}_{BF}(t)$ ) excitation of the primary system. However, in the following only direct optical excitation will be considered. For metal surfaces direct optical excitation can be excluded due to the strong quenching of electrons in the conduction band. This situation is different for oxide surfaces which have a considerable band gap. Measurements with different polarizations of the laser pulse found a dependence of the desorption yield on the polarization while the desorption velocities were not influenced [108]. If the excitation is mediated by the substrate [13], electron-hole pairs in the surface are created. These electron-hole pairs have a very short lifetime due to electron-electron scattering which creates secondary electrons. The secondary electrons dissipate their energy via electron-phonon scattering. These multiple scattering events rule out a symmetry-dependence of the excitation. In contrast, a direct excitation is determined by the transition dipole matrix elements and hence by the symmetry of the states involved. The polarization dependence of the desorption yield for NO/NiO(100) favoring s-polarized light [108] is compatible with calculated oscillator strengths [89, 3]. It therefore supports an electronic excitation mechanism which is determined by optical selection rules, i.e. a direct optical excitation within the adsorbate-substrate complex.

If a direct optical excitation of the adsorbate-substrate complex is assumed, the primary system interacts with the electric field  $E(t)$  of the laser pulse which causes an electronic transition,

$$\hat{\mathbf{H}}_{SF}(t) = \begin{pmatrix} 0 & E(t)\hat{\boldsymbol{\mu}}_{tr}(\hat{\mathbf{Z}}) \\ E^*(t)\hat{\boldsymbol{\mu}}_{tr}(\hat{\mathbf{Z}}) & 0 \end{pmatrix}. \quad (6.3)$$

$\hat{\boldsymbol{\mu}}_{tr}(\hat{\mathbf{Z}})$  is the transition dipole operator depending on the nuclear coordinate. The field  $E(t)$  is treated semi-classically, and its spatial dependence is neglected, i.e. the optical approximation is made. The shape of the field is

assumed to be Gaussian,

$$E(t) = E_0 \mathrm{e}^{-\frac{(t-t_{max})^2}{2\sigma_P^2}} \mathrm{e}^{i\omega_L t} . \quad (6.4)$$

As explained above, the excitation is taken to be resonant. The laser frequency  $\omega_L$  therefore coincides with the difference of  $\hat{\mathbf{V}}_g$  and  $\hat{\mathbf{V}}_e$  at the minimum of the ground state potential. The standard deviation  $\sigma_P$  is related to the full width half maximum (FWHM)  $\tau_P$  of the pulse by  $\tau_P = 2\sigma_P\sqrt{2\ln 2}$ . The parameters characterizing the pulse are its frequency  $\omega_L$ , the intensity  $E_0$  or the pulse fluence which is related to  $E_0$ , and the FWHM  $\tau_P$ . The transition dipole  $\hat{\mu}_{tr}(\hat{\mathbf{Z}})$  is related to the oscillator strength  $f$ ,

$$f = \frac{2}{3} E_{fi} |\mu_{fi}|^2 \quad (6.5)$$

(in atomic units), which is known from *ab initio* calculations [89, 3]. The oscillator strength  $f$  is approximately given by  $f = \exp(-\hat{\mathbf{Z}})$  and  $E_{fi} = 4\text{eV} = 0.15\text{au}$ , therefore

$$\mu_{tr}(\hat{\mathbf{Z}}) = \sqrt{\frac{3 \exp(-\hat{\mathbf{Z}})}{2 \cdot 0.15}} . \quad (6.6)$$

The lifetime of the excited state has been estimated as about 15 to 25 fs, i.e. the charge transfer state is extremely short-lived [89], but the lifetime is still considerably larger than those estimated for desorption from metal surfaces [13]. The relaxation mechanism must therefore be very efficient. Optical deexcitation and interaction with phonons require lifetimes at least on the picosecond to nanosecond timescale and can therefore be excluded as possible relaxation channels. The interaction with phonons is furthermore not likely to play a role since the temperature dependence of desorption observables could be explained purely by initial population of ground state vibrational states [114]. The remaining possible relaxation channel is electronic quenching caused by the interaction with electron-hole pairs, i.e. O2p→Ni3d charge transfer states in the surface. It is a nonadiabatic process which will be modeled in three different ways: First, off-diagonal matrix elements are guessed and one representative O2p→Ni3d charge transfer state is coupled to the system yielding a three-state model (cf. Section 6.2). Second, a phenomenological lifetime of the excited state is introduced in Section 6.3 which



adds a non-Hermitian term to the system Hamiltonian, Eq. (6.2). This corresponds to the system-bath approach for open quantum systems. However, the operators causing the quenching have to be guessed. Finally, in Chapter 7 the O2p→Ni3d charge transfer states are treated as bath in a Surrogate Hamiltonian framework and a microscopic model for the interaction between system and bath is developed.

## 6.2 A model with diabatic coupling

### 6.2.1 The idea of quasi-diabatization

The quenching of electronic excitation pumped into the system by a laser pulse marks the breakdown of the Born-Oppenheimer approximation: A continuum of electronic states in the surface is nonadiabatically coupled to the excited state. This coupling causes a finite lifetime of excitation. In a first attempt to model this breakdown of the Born-Oppenheimer approximation, one representative state of this continuum shall be diabatically coupled to the excited state.

The approach is based on the idea of quasidiabatization [76] which shall be outlined briefly. The total wave function can be written as product of electronic and nuclear wave functions,

$$\Psi(r, R) = \sum_{n,l} c_{n,l} \Psi_{n,l}(r, R) = \sum_n \varphi_n(r, R) \chi_n(R), \quad (6.7)$$

where  $r$  represents all electronic and  $R$  all nuclear coordinates, and  $l$  labels electronic, and  $n$  labels nuclear eigenstates. The nuclear wave functions are vectors containing the expansion coefficients,  $\chi_n(R) = \sum_l c_{n,l} \tilde{\chi}_{n,l}(R)$ . This ansatz can be inserted into the Schrödinger equation,

$$\left( \frac{1}{2M} \frac{d^2}{dR^2} + \frac{1}{2m} \frac{d^2}{dr^2} + U(r, R) - E \right) \Psi(r, R) = 0. \quad (6.8)$$

If the electronic coordinates are integrated over, a Schrödinger equation for the nuclei is obtained containing matrix elements which are non-diagonal in electronic coordinates. These non-diagonal or nonadiabatic coupling matrix elements result from the kinetic energy operator of the nuclei and can be written in terms of derivatives  $d/dR$ . They describe the dynamic interaction

between electrons and nuclei which is neglected in the Born-Oppenheimer approximation. If the matrix elements of nonadiabatic coupling are written as

$$A = \sum_{n,m} A_{nm} = \sum_{n,m} \left\langle \varphi_n(r, R) \left| \frac{d}{dR} \right| \varphi_m(r, R) \right\rangle, \quad (6.9)$$

one can look for a unitary transformation which minimizes  $A$ . This transformation yields a (quasi)diabatic basis. For diatomic molecules it is possible to find a basis in which  $A$  is zero, this (electronic) basis is hence called diabatic. For larger molecules,  $A$  can only be minimized, and the obtained basis is called quasi-diabatic [115]. As a result of the transformation, potential energy terms which are off-diagonal in the electronic basis replace the kinetic coupling terms  $A_{nm}$ . Quasi-diabatization therefore represents – at least in principle – a possibility to go beyond the Born-Oppenheimer approximation on an *ab initio* level and facilitates a fully quantum-mechanical description.

### 6.2.2 A three-state model with diabatic coupling

The calculation of the transformation and hence (quasi)diabatic basis is feasible, however, only for comparatively simple systems such as  $\text{HeH}^+$  [3,75]. The approach breaks down for systems requiring a multi-configurational treatment [116]. For the NO/NiO(100)-system, the diabatic coupling therefore has to be constructed empirically. The functional form of the coupling was assumed to be Lorentzian,

$$\lambda = \lambda(Z) = \frac{\lambda_0}{\gamma^2 + (Z - Z_0)^2} \quad (6.10)$$

with nuclear coordinate  $Z$  describing the distance of the NO center of mass from the surface. The coupling function is characterized by three parameters – coupling strength  $\lambda_0$ , location  $Z_0$  and width  $\gamma$ . The diabatic coupling  $\hat{\lambda}$  enters the Hamiltonian,

$$\hat{\mathbf{H}} = \begin{pmatrix} \hat{\mathbf{T}} + \hat{\mathbf{V}}_g & E(t)\hat{\boldsymbol{\mu}}_{tr} & 0 \\ E^*(t)\hat{\boldsymbol{\mu}}_{tr} & \hat{\mathbf{T}} + \hat{\mathbf{V}}_e & \hat{\lambda} \\ 0 & \hat{\lambda} & \hat{\mathbf{T}} + \hat{\mathbf{V}}_d \end{pmatrix}, \quad (6.11)$$

where  $\hat{\mathbf{T}}$  and  $\hat{\mathbf{V}}$  are kinetic and potential energy operators, respectively,  $\hat{\boldsymbol{\mu}}_{tr}$  is the transition dipole operator, and  $E(t)$  the electric field of the laser pulse.

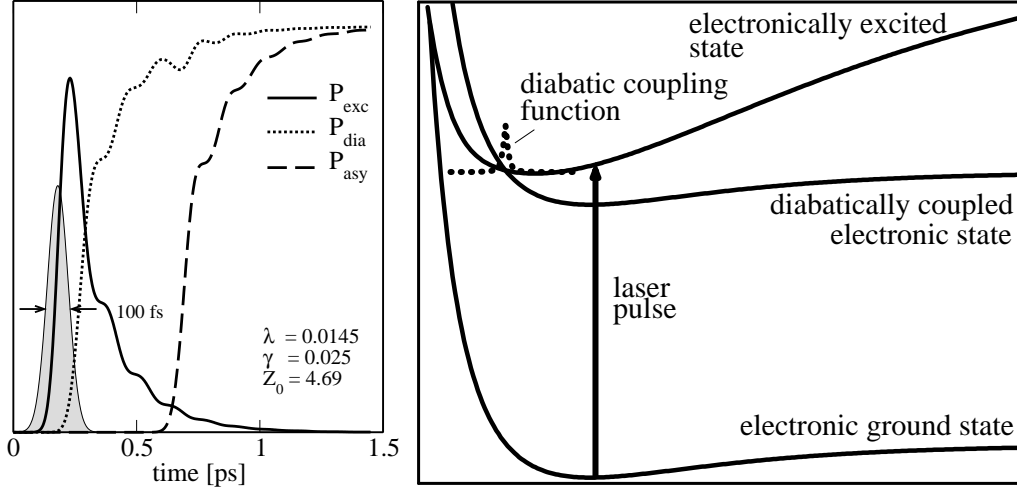


Figure 6.1: Diabatic coupling scheme (right) : A laser pulse promotes part of the ground state wave packet onto the electronically excited state where the wave packet is subject to acceleration toward the surface. When the wave packet reaches the region with non-zero diabatic coupling, population is transferred onto the ground state-like diabatically coupled state where desorption can take place. The left hand side shows the population of the excited state (solid curve), the population of the diabatically coupled state (dotted) and the population in the asymptotic region of the diabatically coupled state, i.e. the desorbed population (dashed). The plateaus correspond to oscillations in coordinate space, i.e. to the wave packet being close to the outer classical turning point far from the center  $Z_0$  of diabatic coupling. It is a non-realistic feature of the method that basically all population which has been transferred onto the diabatically coupled state reaches the asymptotic region. The shape of the laser pulse is indicated in grey.

The diabatically coupled state is assumed to be like the ground state. Its energy is determined by the location of the diabatic coupling. An illustration of the scheme is given in Fig. 6.1 (right). The left-hand side of Fig. 6.1 shows the population of the electronically excited state which decays due to population transfer to the diabatically coupled state once the wave packet has reached the region where the diabatic coupling is non-zero.

The observables in laser desorption experiments of NO/NiO(100) have been the desorption cross section which is related to the desorption probability and the state resolved velocity of the desorbing molecules [103, 110, 107]. If the population of the diabatically coupled state approaches a constant, the desorption probability can be defined in the present scheme. It is given

by the ratio of the population in the asymptotic region vs. the total population which has been excited from the ground state,  $1 - \langle \Psi_g | \Psi_g \rangle$ . In a one-dimensional model, only velocity distributions integrated over all rovibrational states can be observed. The integrated velocity distribution corresponds to the probability density of the wave packet in the asymptotic region in momentum representation (cf. Appendix A.6). The dependence of these observables on the strength, width and location of diabatic coupling has been investigated.

Fig. 6.2 shows the mean velocity as a function of the location  $Z_0$  of di-

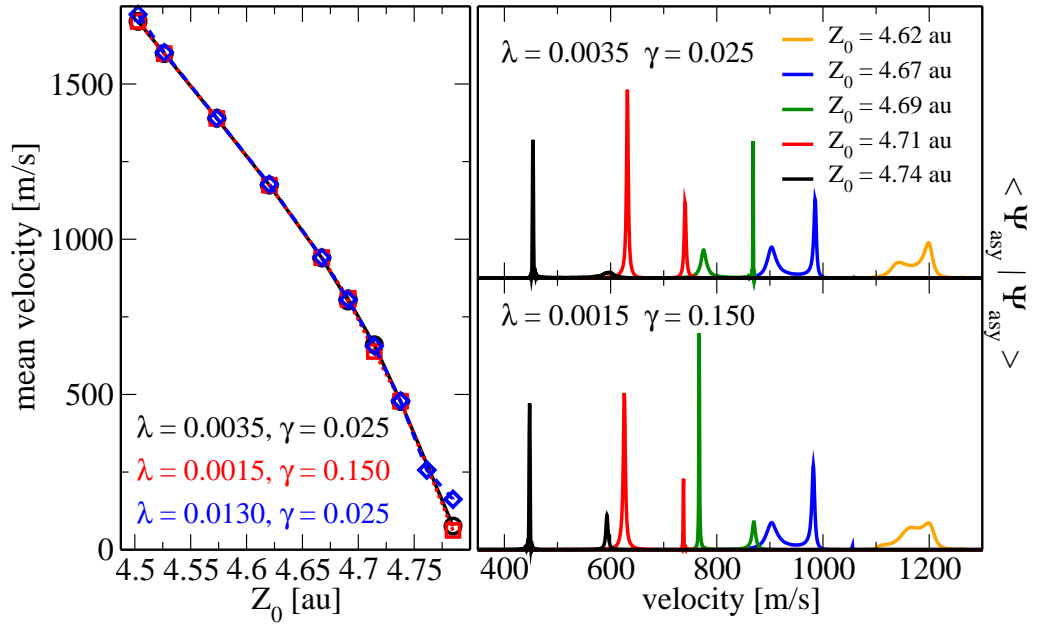


Figure 6.2: The velocity of desorbing molecules depends on the location  $Z_0$  of the diabatic coupling. It is roughly independent of the two other diabatic coupling parameters  $\lambda_0$  and  $\gamma$  (left). Experimentally observed velocities lie in the range between 0 m/s and 2000 m/s. To obtain velocities in this range, the location of diabatic coupling needs to be smaller than the left classical turning point at  $Z = 4.79$  au (right).

abatic coupling (left) and velocity distributions (right). Both the mean velocity and the qualitative shape of the velocity distributions are independent of width and strength of diabatic coupling, while the peak intensity depends on  $\gamma$  and  $\lambda_0$ . The velocity increases if the location is shifted toward smaller distances from the surface. A shift toward smaller distances  $Z_0$  moves the diabatic coupling up the repulsive part of the diabatically coupled potential

(cf. Fig. 6.1). The part of the wave packet which is transferred onto the diabatic state is then subject to stronger acceleration.

The location  $Z_0$  of diabatic coupling determines not only the desorption velocity, but also the desorption probability (cf. Table 6.1). The excitation

location $Z_0$	yield	mean velocity
4.79 a.u.	8 - 18 %	70 - 160 m/s
4.76 a.u.	84 %	260 m/s
4.74 a.u.	> 99 %	475 - 485 m/s

Table 6.1: Desorption yield and mean desorption velocity depend very sensitively on the location of diabatic coupling  $Z_0$ . It is not possible to find a  $Z_0$  s.t. both yield and velocity agree with experimentally found values [103,110]. A range indicates values found for different width  $\gamma$  and strength  $\lambda_0$  of the coupling.

by the laser pulse determines the classical turning points of wave packet motion on the electronically excited state (cf. Fig. 6.1). If the location of diabatic coupling is shifted to distances only slightly smaller than the left classical turning point ( $Z_t = 4.79$  a.u.), the desorption probability jumps quickly to almost 100 % (cf. Table 6.1). This high desorption probability is a result of the strong acceleration for small values of  $Z_0$ : All parts of the wave packet which are transferred onto the diabatically coupled state gain enough kinetic energy to reach the asymptotic region. If the obtained desorption probabilities are reasonable, i.e.  $P_{des} \ll 1$ , the obtained desorption velocities  $< 200$  m/s are much smaller than the experimentally observed velocities which show one peak between 300 m/s and 500 m/s and a second peak between 1200 m/s and 1500 m/s [103,110].

Finally, Fig. 6.3 shows the dependence of excited state population decay on width  $\gamma$  and strength  $\lambda_0$  of the diabatic coupling. Exponential decay and trapping on the excited state can be observed. Trapping occurs most pronounced for narrow and weak coupling (solid curve in the upper left panel). If the diabatic coupling is narrow the lower-energetic parts of the wave packet cannot reach the region with non-zero diabatic coupling and remain on the excited state. The decay of excited state population is never purely exponential as small oscillations can be observed. These oscillations correspond

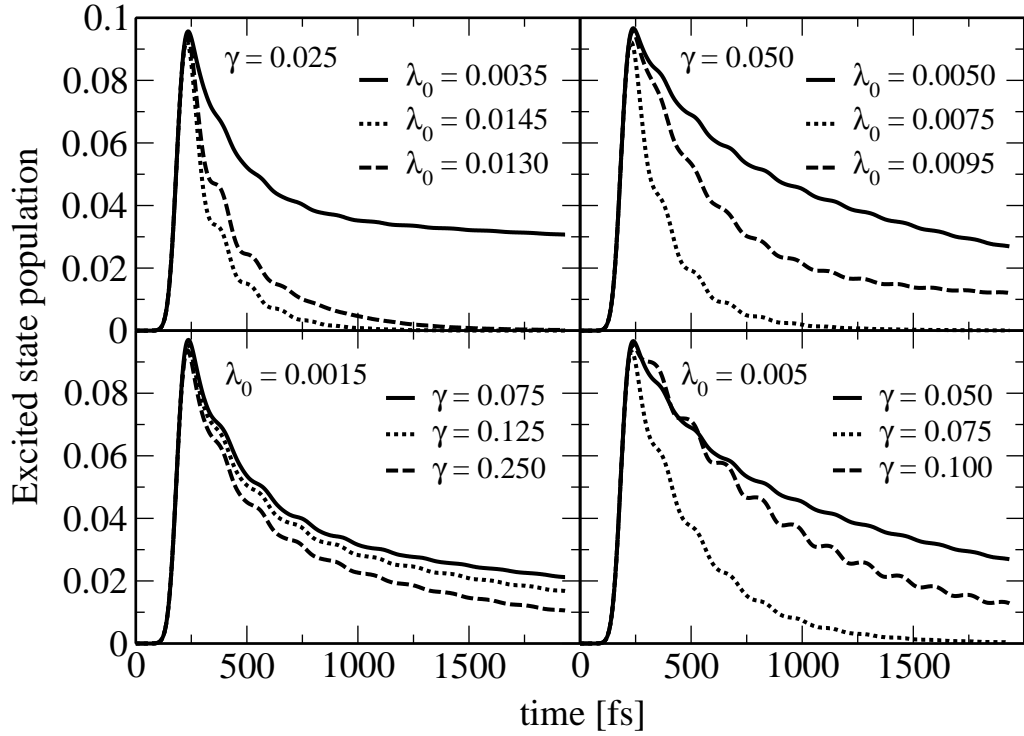


Figure 6.3: The decay of excited state population depends on the parameters of diabatic coupling (top left - narrow Lorentzian, top right - wide Lorentzian, bottom left - weak coupling, bottom right - strong coupling,  $Z_0 = 4.69$  au in all cases). Exponential decay and trapping of excited state population (top left, solid curve) can be observed. There is no simple dependence of the decay rate on the width and strength of diabatic coupling.

to oscillations of the wave packet in coordinate space, i.e. the plateaus occur when the wave packet is close to the right classical turning point far from the location of diabatic coupling. If the excited state population decay is fitted to an exponential, lifetimes of about 150 fs and longer have been obtained. These lifetimes are unrealistically long. No simple functional dependence of excited state lifetime on width and strength of diabatic coupling can be observed, since the lifetime oscillates in both  $\gamma$  and  $\lambda_0$ . To clarify this behavior on the shape of diabatic coupling, a free wave packet with initial non-zero momentum has been propagated on two grids which were coupled by  $\lambda(Z)$ . In this simple test, the wave packet passes the region with diabatic coupling only once. The amount of transferred population can be considered as the transition probability. This transition probability oscillates both in  $\gamma$  and

$\lambda_0$ . Such oscillatory behavior has also been reported for a Gaussian shape of the diabatic coupling function [117, 118].

In [117] velocity distributions have been analyzed in terms of wave packet motion on the excited state. The ground state wave packet was promoted onto the excited state neglecting the explicit time-dependence due to the laser pulse, i.e. assuming a  $\delta$ -like pulse. Velocity distributions showing a complicated interference pattern were obtained with interference resulting from different pathways of partial wave packets. It was argued that the obtained velocity distributions need to be convoluted with a Gaussian taking into account the finite velocity resolution in experiment. The width of the convolution function then determines how many peaks are observed in the velocity distribution. The introduction of such a convolution function in a simple one-dimensional model is reasonable to account for the complicated processes in experiment which have been left out. One might notice, however, that a finite resolution is more naturally included into the description by taking into account the finite width of the laser pulse. The finite width of the pulse causes a finite width in energy, i.e. a finite number of states with energy close to the resonance are excited (a similar argument is sketched for the window operator, cf. Appendix B). Fig. 6.4 shows velocity distributions for increasing pulse duration. A very short pulse of 20 fs FWHM results in nine visible peaks in the velocity distribution (black curve in Fig. 6.4), while a continuous wave (CW) excitation leads to a single peak (blue curve). A pulse of 100 fs FWHM, as recently used in experiment [110], brings about a bimodal velocity distribution (red curve). This is a fingerprint of the time-energy-uncertainty relation: the shorter the time in which the pulse interacts with the system, the more nuclear eigenstates of the electronically excited state are excited and build up the wave packet. The explanation in terms of excited state eigenstates is illustrated in Fig. 6.5 which compares the velocity distribution for a  $\delta$ -like excitation of the ground state wave packet (black solid curve) with velocity distributions of simulations with the eight lowest eigenstates of the electronically excited state as initial state and diabatic coupling switched on at time  $t = 0$  (red dotted curves). Fig. 6.5 shows that the peak positions of the velocity distribution can be explained by propagating excited state eigenstates, and the largest contributions arise from the

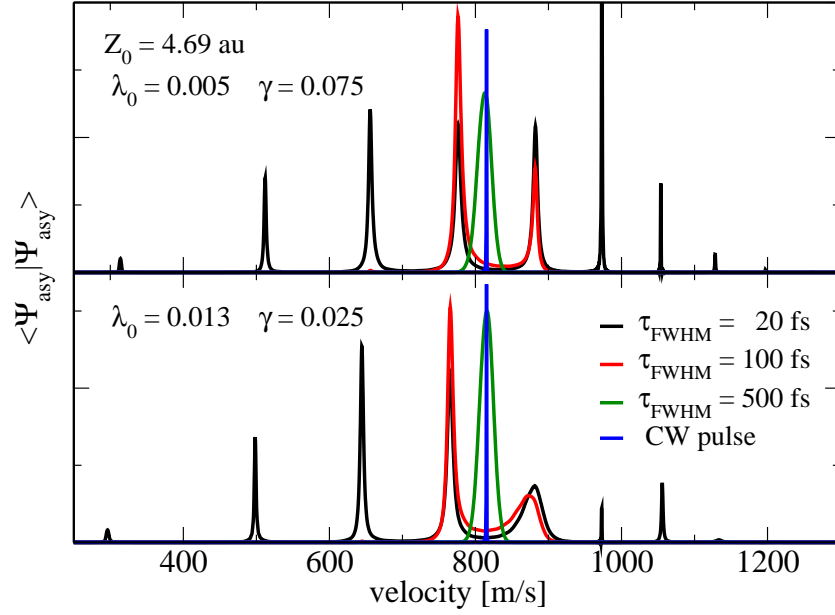


Figure 6.4: The number of peaks observed in the final velocity distribution of the desorbed part of the wave packet depends on pulse duration: The shorter the pulse, the more modes are observed. The distributions have been scaled for comparison.

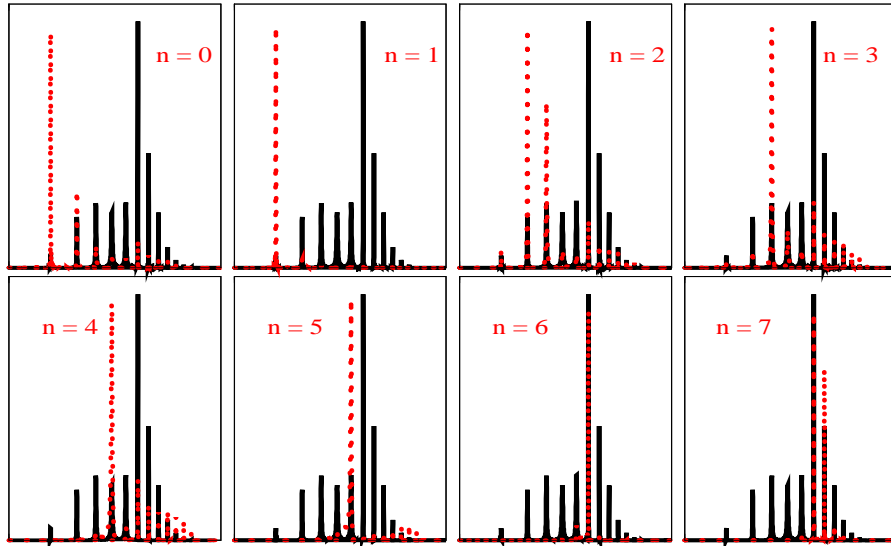


Figure 6.5: The peaks in the velocity distribution of the desorbed part of the wave packet (here for instantaneous, i.e.  $\delta$ -pulse excitation, black) correspond to the nuclear eigenstates of the electronically excited state propagated in the diabatic model (red). The parameters of the coupling were chosen as in the upper panel of the previous figure, and the peaks lie in the range between 280 m/s and 1400 m/s.



eigenstates with  $n = 6$  and  $n = 7$ .

To summarize the results of this section, it is not possible to find parameters of diabatic coupling leading to desorption probabilities and desorption velocities which both agree with experimentally found values. Since a Lorentzian (or Gaussian) shape of diabatic coupling is only an empirical guess and the systematic way to improve on this guess, i.e. an *ab initio* calculation of diabatic coupling elements, is numerically not feasible at the time, this problem has not been investigated further. In addition to the problem of parameterization of diabatic coupling, two more general problems are inherent in the approach. First, the (primary) system is modeled as isolated and hence described by a Hermitian Hamiltonian. This leads to population and energy transfer back and forth between the electronically excited and the diabatically coupled states. Second, the angular dependence of diabatic coupling elements has not been investigated, and there are no physical arguments to motivate an empirical guess of the angular dependence. It is thus not possible to go to a higher dimensional model and to check for artifacts of the one-dimensional description.

In conclusion, one additional electronic state diabatically coupled to the system does not yield a reasonable model to describe electronic quenching and desorption. It is therefore necessary to apply a system-bath approach. This shall be done in two different ways. The following section presents a reduced description of the total system with *implicit* treatment of the bath by introducing a non-Hermitian Hamiltonian while in Chapter 7 many states are *explicitly* coupled to the electronic ground and excited states of the NO/NiO<sub>5</sub><sup>8-</sup> cluster.

## 6.3 A stochastic wave packet approach

### 6.3.1 The Monte Carlo wave function method

The Monte Carlo wave function (MCWF) method can be viewed as a tool to solve the equation of motion for an open quantum system,

$$\frac{\partial}{\partial t} \hat{\rho}_S = i[\hat{\rho}_S, \hat{\mathbf{H}}_S]_- + \hat{\mathcal{L}}(\hat{\rho}_S), \quad (6.12)$$

in the Markov approximation [119]. The state of the system is given by its density operator,  $\hat{\rho}_S$ , its dynamics are governed by the Hamiltonian,  $\hat{\mathbf{H}}_S$ , and the interaction with the environment is described by the dissipative superoperator  $\hat{\mathcal{L}}(\hat{\rho}_S)$ . If the Markov approximation is made,  $\hat{\mathcal{L}}$  is of Lindblad form [23],

$$\hat{\mathcal{L}}(\bullet) = -\frac{1}{2} \sum_k \left[ \hat{\mathbf{C}}_k^+ \hat{\mathbf{C}}_k, \bullet \right]_+ + \sum_k \hat{\mathbf{C}}_k \bullet \hat{\mathbf{C}}_k^+. \quad (6.13)$$

The  $\hat{\mathbf{C}}_k$  are operators which act in the Hilbert space of the system and describe the different dissipative effects. They need to be chosen semi-phenomenologically [120]. The label  $k$  runs over all possible decay channels.

Instead of solving Eq. (6.12) for the density operator directly, an approximate solution can be obtained by calculating the non-Hermitian dynamics for a wave function and averaging over many such quantum trajectories. The Monte Carlo procedure consists of two steps [119]:

1. The non-Hermitian Hamiltonian ,

$$\hat{\mathbf{H}} = \hat{\mathbf{H}}_S - \frac{i}{2} \sum_k \hat{\mathbf{C}}_k^+ \hat{\mathbf{C}}_k, \quad (6.14)$$

generates the dynamics of the wave function

$$|\Psi^j(t + \Delta t)\rangle = e^{-i\hat{\mathbf{H}}\Delta t} |\Psi^j(t)\rangle \approx \left( \mathbb{1} - i\hat{\mathbf{H}}\Delta t \right) |\Psi^j(t)\rangle \quad (6.15)$$

with the time step assumed to be small,  $\Delta t \ll 1$ . The approximation in Eq. (6.15) can be applied to higher order in  $\Delta t$  by employing, for example, a Runge-Kutta scheme [119]. The loss of norm due to the non-Hermiticity of  $\hat{\mathbf{H}}$  is given to first order in  $\Delta t$  by

$$\begin{aligned} \delta p &= 1 - \langle \Psi^j(t + \Delta t) | \Psi^j(t + \Delta t) \rangle \\ &= 1 - \langle \Psi^j(t) | \left( 1 + i\hat{\mathbf{H}}\Delta t \right) \left( 1 - i\hat{\mathbf{H}}\Delta t \right) | \Psi^j(t) \rangle \\ &= i\Delta t \langle \Psi^j(t) | \hat{\mathbf{H}} - \hat{\mathbf{H}}^+ | \Psi^j(t) \rangle \\ &= \sum_k \Delta t \langle \Psi^j(t) | \hat{\mathbf{C}}_k^+ \hat{\mathbf{C}}_k | \Psi^j(t) \rangle = \sum_k \delta p_k. \end{aligned} \quad (6.16)$$

2. A random number,  $\varepsilon \in [0, 1]$ , is drawn and compared to the loss of norm,  $\delta p$ . If  $\delta p$  is smaller than  $\varepsilon$ , which is mostly the case since  $\delta p \ll 1$  and  $\varepsilon$  is uniformly distributed over  $[0, 1]$ , no quantum jump occurs and the wave

function is simply renormalized. If the random number is larger than  $\delta p$ , a quantum jump occurs and the wave function is taken to be

$$|\Psi^j(t + \Delta t)\rangle = \sum_k \frac{\delta p_k}{\delta p} \frac{1}{\sqrt{\langle \hat{\mathbf{C}}_k \Psi^j(t) | \hat{\mathbf{C}}_k \Psi^j(t) \rangle}} \hat{\mathbf{C}}_k |\Psi^j(t)\rangle . \quad (6.17)$$

These two steps need to be repeated for many realizations of the wave function,  $|\Psi^j(t)\rangle$ ,  $j = 1, \dots, N$ . The density operator of the system can then be constructed [46],

$$\hat{\rho}_S(t) = \lim_{N \rightarrow \infty} \frac{1}{N} \sum_{j=1}^N |\Psi^j(t)\rangle \langle \Psi^j(t)| , \quad (6.18)$$

and observables can be obtained,

$$\langle A \rangle(t) = \frac{1}{N} \sum_{j=1}^N \langle \Psi^j(t) | \hat{\mathbf{A}} | \Psi^j(t) \rangle . \quad (6.19)$$

An extensive discussion has been concerned with the physical interpretation of the quantum jump [9, 46], in particular with the question whether it can be related to the measurement of a quantum state [43, 119, 12, 121, 44, 122]. In this thesis, however, it has merely been used as a practical means to calculate the dissipative dynamics of Eq. (6.12).

As a tool to study photodesorption from surfaces, the Monte Carlo wave function method in this form has first been used by Saalfrank [123] and compared to the wave packet jumping method introduced by Gadzuk [87, 88]. The two methods were shown to be equivalent both numerically [123] and analytically [124]. The operator describing electronic quenching is  $\hat{\mathbf{C}}_k = \sqrt{\Gamma_{ge}} |g\rangle \langle e|$  which leads to the effective Hamiltonian

$$\hat{\mathbf{H}} = \hat{\mathbf{H}}_S - \frac{i}{2} \Gamma_{ge} |e\rangle \langle e| \quad (6.20)$$

with  $|g/e\rangle$  labeling the electronic ground and excited state, respectively. If the decay rate  $\Gamma_{ge}$  does not depend on the nuclear coordinate, the loss of norm is known analytically,

$$\delta p = \Gamma_{ge} \Delta t + \mathcal{O}(\Delta t^2) \quad \text{or} \quad \delta p = 1 - e^{-\Gamma_{ge} \Delta t} . \quad (6.21)$$

Since only one deexcitation channel and no excitation channels are modeled (DIET regime), the population of the electronically excited state should decay with rate  $\Gamma_{ge}$ . This is true, however, only if the complete wave packet is

assumed to be initially in the electronically excited state, i.e. the laser excitation results in a complete population inversion. If the wave packet is only partially excited, the lifetime of the excited state and hence observables such as the desorption yield depend on both decay rate  $\Gamma_{ge}$  and the initial population of the excited state. This unphysical feature can be removed by renormalizing the range, from which the random number  $\varepsilon$  is drawn, by the excited state population. Equivalently, the loss of norm  $\delta p$  which now depends on the excited state population (from Eq. (6.16)  $\delta p = \Delta t \Gamma_{ge} ||\langle e | \Psi^j(t) \rangle||^2$  and  $||\langle e | \Psi^j(t) \rangle||^2 \neq 1$ ) can be renormalized while keeping the range  $[0, 1]$  of  $\varepsilon$  and hence Eq. (6.21). Note that this problem does not arise when using Gadzuk's wave packet jumping algorithm due to different stochastic sampling [125]. The jump criterion is then given by the time spent on the excited state (residence time) *independent* of population [87, 88].

The Monte Carlo wave function method can be extended to treat the interaction of the primary system with a laser pulse explicitly. This problem has been investigated for the system NO/Pt(111) [94]. In that study, however, the Liouville–von Neumann equation has been solved directly by a Newton polynomial expansion of the time evolution operator, and the excitation was mediated by the substrate. The extension of the method to treat time-dependent fields needs to be handled with care: Since the Markov approximation is assumed to be valid, the timescale of the relaxation and of the external field should not be of the same order of magnitude [10]. It is not possible to test the validity of the Markov approximation within the Monte Carlo wave function framework since it is an inherent assumption. However, for the specific system NO/NiO(100) a justification can be given by comparison to the Surrogate Hamiltonian method (cf. Section 7.4).

The system Hamiltonian in Eq. (6.12) and hence the effective non-Hermitian Hamiltonian, Eq. (6.14) and Eq. (6.20) respectively, become time-dependent, if the interaction of the system with a laser pulse shall be included explicitly,

$$\hat{\mathbf{H}}(t) = \hat{\mathbf{H}}_S(t) - \frac{i}{2} \Gamma_{ge} |e\rangle \langle e|. \quad (6.22)$$

Since the propagation starts with all the population in the electronic ground state, and the only dissipation operator is  $\hat{\mathbf{C}}_k = \sqrt{\Gamma_{ge}} |g\rangle \langle e|$  as before, the problem of the lifetime depending on the amount of excited state population

and hence on the intensity of the laser again arises. This can be avoided by renormalizing the range of the random number  $\varepsilon$  or the loss of norm  $\delta p$  which is then again given by Eq. (6.21).

### 6.3.2 Results for NO/NiO(100)

For completeness, results for an instantaneous excitation of the wave packet are presented. This corresponds to irradiation of the surface with a nanosecond pulse [126]: In a perturbation treatment of the pulse, the excited state wave packet is given by [62]

$$|\Psi_e(t_p + c\tau_p)\rangle = i \int_{-c\tau_p}^{c\tau_p} d\tau \, e^{-i\hat{H}_e(c\tau_p - \tau)} \hat{\mu}_{tr} E(\tau) e^{-i\hat{H}_g(c\tau_p + \tau)} |\Psi_g(t_p - c\tau_p)\rangle, \quad (6.23)$$

with  $E(\tau)$  the electric field and  $\tau_p$  the width of the pulse.  $t_p$  denotes the time of maximum field strength, and  $c$  is a constant specifying the integration range. According to Eq. (6.23), the action of the pulse can be viewed as an energy filter. On the timescale of nuclear motion, a nanosecond pulse is almost infinitely long. Its action is hence a  $\delta$ -function energy filter, and instantaneous excitation corresponds to the assignment of a single energy to the wave packet created in the excited state.

The initial state is given by

$$\Psi_g^j(Z; t = 0) = 0, \quad \Psi_e^j(Z; t = 0) = \Phi_0(Z) \quad \forall j = 1, \dots, N, \quad (6.24)$$

where  $\Phi_0(Z)$  is the vibrational ground state of the electronic ground state. If a finite temperature,  $T > 0$ , shall be considered, a Boltzmann average over the vibrational eigenstates  $\{\Phi_n(Z)\}$  needs to be performed. The influence of temperature has been investigated for the system NO/Cr<sub>2</sub>O<sub>3</sub> [114] and is not of concern here.

The initial state Eq. (6.24) is propagated on the electronically excited state potential until the condition  $\varepsilon < \delta p$  is fulfilled. Since only one deexcitation channel is modeled, the wave packet as a whole is taken to the ground state. The equilibrium distance of the excited state potential is smaller than that of the ground state potential. The wave packet is therefore accelerated toward smaller distances and, after the jump has occurred, finds itself in the repulsive part of the ground state potential (cf. Antoniewicz scenario,

Section 5.1). Parts of the wave packet will thus gain enough kinetic energy to leave the ground state potential well and desorb (Fig. 6.6). How much momentum is gained and how much of the wave packet can reach the asymptotic region depends on the time spent in the excited state (residence time, Fig. 6.6) and on average on the lifetime  $1/\Gamma_{ge}$  (resonance time, Fig. 6.7). The wave packet is propagated on the electronic ground state until the trapped and the desorbing parts are well separated and the observables in the asymptotic region are converged. The grid change method described in Appendix A.6 is employed.

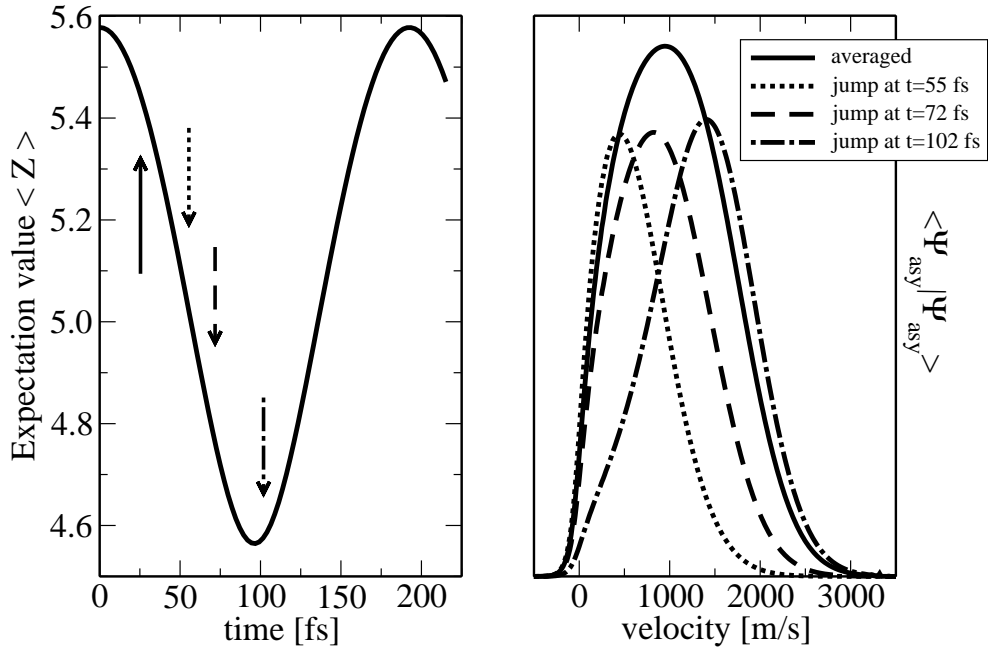


Figure 6.6: Different jump times lead to different velocity distributions, but the stochastic average results in a broad peak. The expectation value of coordinate of the excited state wave packet is plotted on the left, with the jump times and the average lifetime indicated by arrows. The velocity distributions for single sample trajectories (scaled for comparison) and the averaged velocity distribution are shown on the right.

This procedure is repeated for many realizations of  $\Psi^j(Z;t)$ . Fig. 6.8 shows the convergence of the method with an increasing number of such quantum trajectories. The excited state population decays exponentially with lifetime  $\tau = 1/\Gamma_{ge}$  as expected from the phenomenological model, Eq. (6.20). About  $N = 1000$  trajectories are necessary to converge the population in

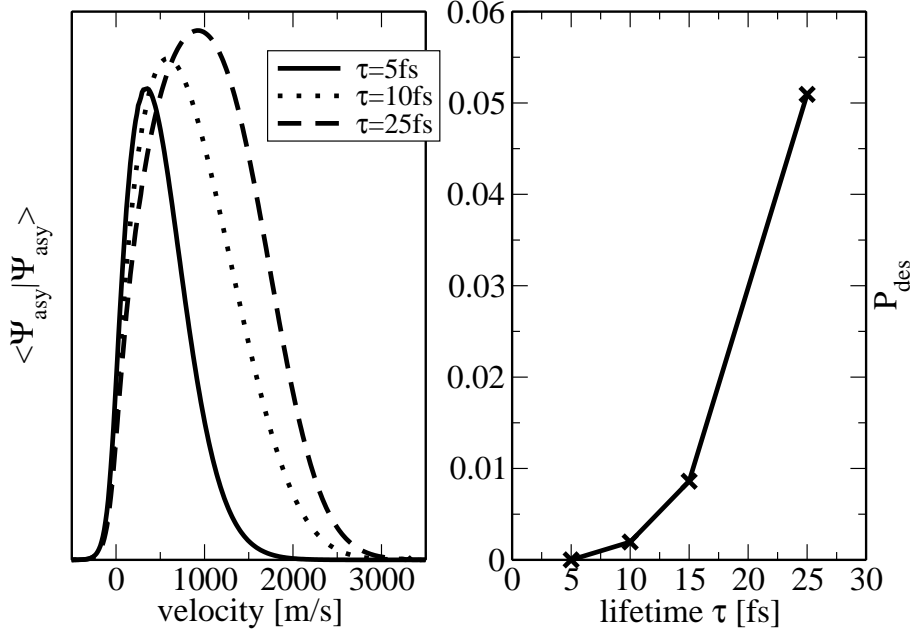


Figure 6.7: The influence of the lifetime  $\tau = 1/\Gamma_{ge}$  on the desorption probability (right) and the velocity distribution (left). Longer lifetimes bring about a larger gain in momentum and hence a larger desorption probability.

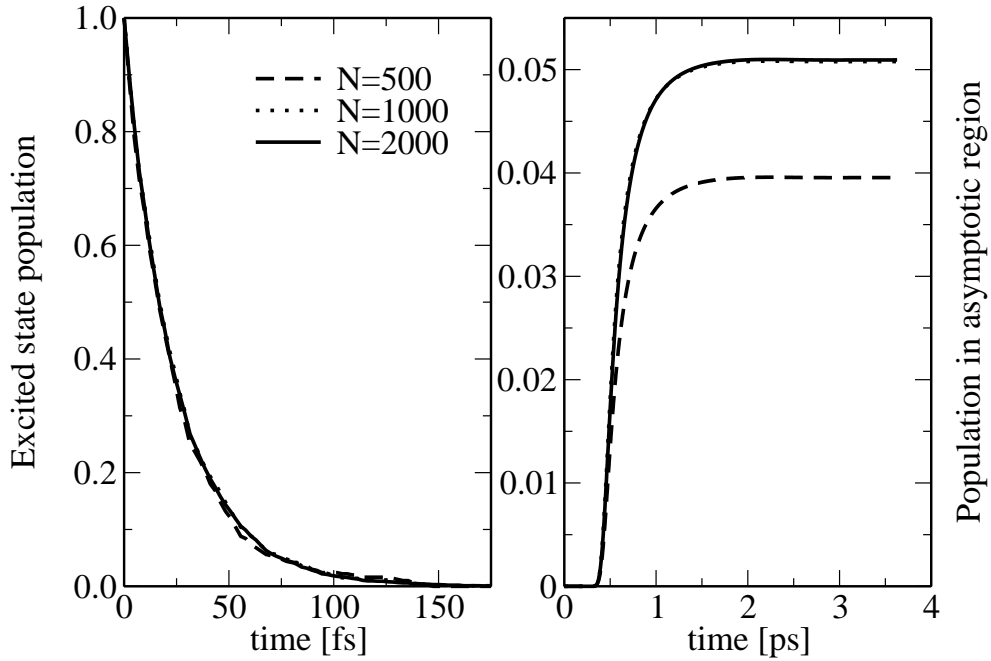


Figure 6.8: Convergence of the MCWF method for the excited state population (left) and the desorption probability (right),  $N$  is the number of quantum trajectories ( $\tau = 1/\Gamma_{ge} = 25$  fs).

the asymptotic region which can be interpreted as the desorption probability in the case of instantaneous excitation [127]. This is a much higher number than needed with Gadzuk's wave packet jumping method [87, 88] which in the case of the NO/NiO(100) system requires about  $N = 200$  trajectories to obtain converged observables [3, 105]. The reason for this inefficiency has been explained by Saalfrank [123] and Guo [125]: Since the population decays exponentially, the MCWF method favors jumps at short residence times. The trajectories which are important for desorption, however, are the ones with a long residence time in the excited state, i.e. the ones which the MCWF method is biased against. This also explains why the excited state population converges much faster with the number of trajectories than the desorption probability (Fig. 6.8). Gadzuk's method can be understood as an improved sampling scheme where all residence times are equally probable and associated with a statistical weight. A drawback of Gadzuk's method is that it cannot be applied if the Hamiltonian becomes explicitly time-dependent since it requires a well-defined excitation time from which to count the residence times.

If the excitation by the laser pulse is treated explicitly, the initial state is taken to be

$$\Psi_g^j(Z; t = 0) = \Phi_0(Z), \quad \Psi_e^j(Z; t = 0) = 0 \quad \forall j = 1, \dots, N, \quad (6.25)$$

i.e. all the population is in the electronic ground state, and temperature effects requiring higher vibrational states  $\Phi_n(Z)$  are neglected. The laser pulse excites part of the wave packet into the electronically excited state. Therefore the wave packet needs to be propagated on both electronic ground and excited state simultaneously. If the condition  $\varepsilon < \delta p$  is fulfilled, the population from the electronically excited state is transferred to the electronic ground state. The field of the pulse is considered non-zero for times  $t_{max} - 3\tau_p \leq t \leq t_{max} + 3\tau_p$ . If the jump occurs before  $t_{max} + 3\tau_p$  the wave packet may be excited again. For lifetimes of the electronic state smaller than pulse duration, several jumps will occur for one quantum trajectory, and quantum interference patterns may be expected. However, no such interference patterns are visible in the averaged velocity distributions of desorbed molecules, independent of pulse duration (cf. Fig. 6.9, bottom panel). Fig. 6.9, top shows the population of the excited state (left) and the des-



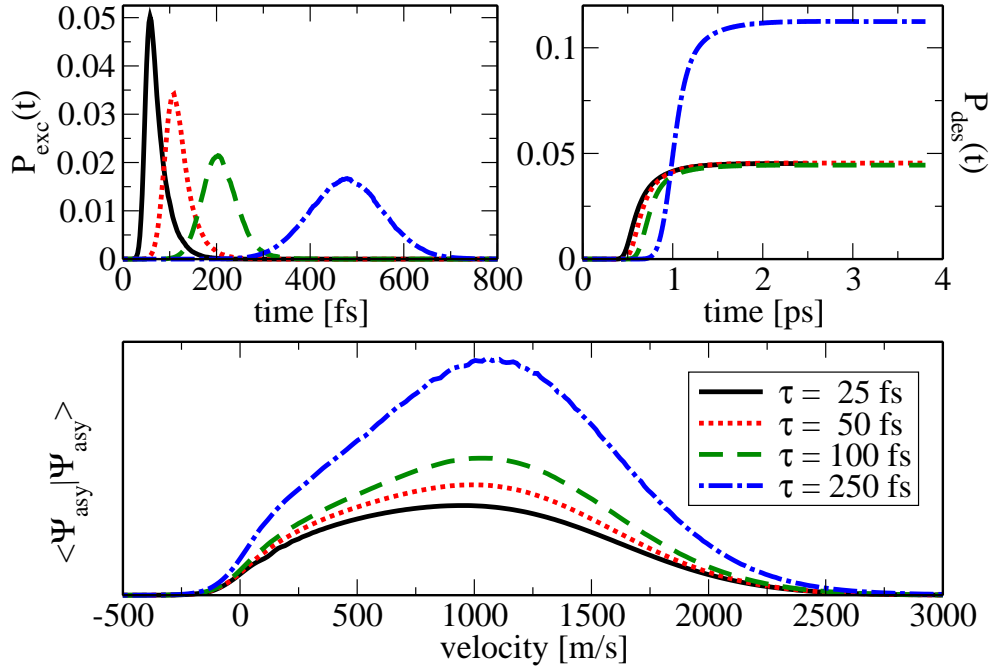


Figure 6.9: Dependence on the pulse FWHM of excited state population (top left), desorption probability (top right) and velocity distribution of desorbed molecules (bottom). The excited state lifetime is assumed to be  $1/\Gamma_{ge} = 25$  fs, i.e. the FWHM is varied between one and ten times the lifetime. No interference patterns are visible in the averaged velocity distributions (bottom), despite possible multiple quantum jumps.

orption probability (right) as a function of time. The desorption probability is obtained by weighting the population in the asymptotic region (cf. Appendix A.6) by the excitation probability. For pulse durations comparable to the excited state lifetime, the desorption probability does not depend on pulse duration (black, red and green curves in Fig. 6.9, top right). If the pulse duration is an order of magnitude larger than the excited state lifetime (blue curve), the desorption probability is increased. For such a long pulse, the wave packet is excited many times and hence the overall time spent in the excited state becomes longer. Thus, the gain in kinetic energy and hence the desorption probability are increased.

When the wave packet can be excited by the pulse several times, it will stay on the excited state for different residence times. When transferred to the electronic ground state it will gain different momenta. In coordinate space different distances  $Z$  are reached before jumping to the ground state,

as compared in Fig. 6.6. These different pathways should lead to an interference pattern also known as Stückelberg oscillations. Interference for one quantum trajectory within a stochastic average is slightly different from the interference discussed in the previous section, where one wave packet was propagated coherently and interference resulted from different partial wave packets. Fig. 6.10 (a) shows that interferences in fact occur for single quantum trajectories. However, no interferences show up in the averaged velocity distribution, i.e. in the observable. This can be understood by a closer inspection of jump times and hence time intervals spent in the excited state, see Fig. 6.10 (d). Three requirements must be met for an interference pattern to occur:

- (1) The interval between jumps must be sufficiently large. Otherwise, the wave packet will not gain enough momentum to desorb and it will stay trapped on the surface. All single trajectories plotted in Fig. 6.10 meet this requirement.
  - (2) The length of intervals between jumps must be comparable. This requirement is only met by the trajectories plotted in green and red. For the blue and black trajectories only one interval contributes to desorption.
  - (3) At least two intervals need to start at times after which the pulse is still "on", otherwise no population will be reexcited. In Fig. 6.10, this is only fulfilled for the red trajectory.
- (2) and (3) are necessary to have at least two intervals contribute to desorption. The fulfillment of all requirements is a comparatively rare event and the stochastic average does therefore not show Stückelberg oscillations.

One might expect that it is more likely for interferences to occur if the pulse duration is increased. However, for a fixed excited state lifetime of about 25 fs many more jumps occur, which leaves the probability of having two or more "in the right size, at the right time" more or less constant. Obviously, the dynamics are governed by an interplay of the timescales of pulse, nuclear motion on the excited state (guaranteeing the momentum gain) and electronic quenching. The picture might therefore change if together with pulse duration the excited state lifetime is increased. However, the choice of a lifetime of about 25 fs is motivated by the physical properties of the

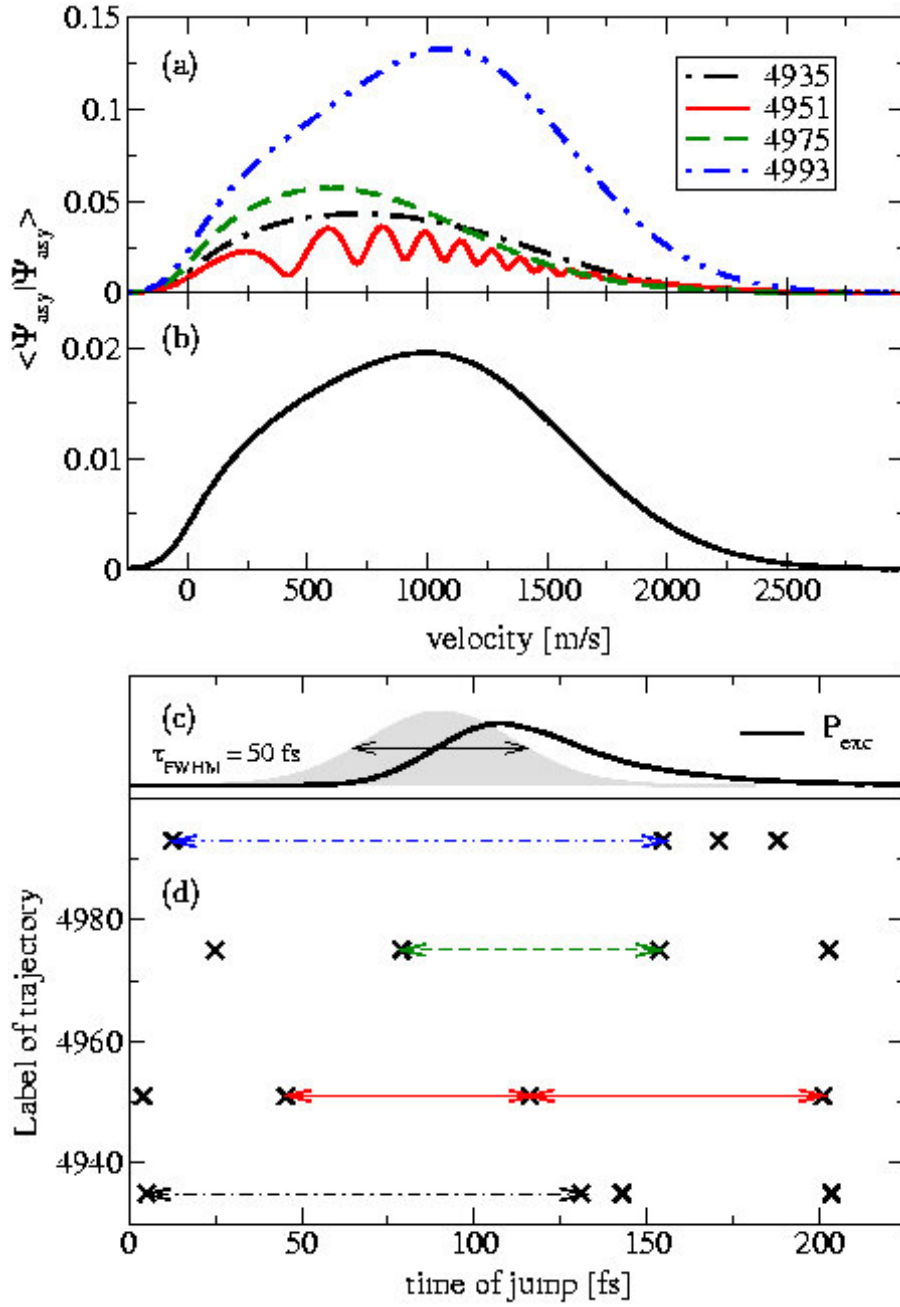


Figure 6.10: (a) Single quantum trajectories show interference patterns in the final velocity distribution, the trajectory index is listed in the legend. (b) After performing the stochastic average over all quantum trajectories, no interferences are visible since only a few single trajectories show interferences. (c) The excited state population is plotted vs. time, the pulse shape is indicated. (d) The jump times for trajectories plotted in (a) are given with colors corresponding to (a), the arrows show the time intervals between jumps relevant for desorption. Only specific combinations of jump times lead to interferences (see text), the probability of these combinations is too small to make a contribution in the stochastic average.

system [89], an increase of the lifetime was therefore not considered.

In summary, the desorption yield depends on pulse duration only if the FWHM of the pulse is significantly larger than the excited state lifetime. The mean velocity of the desorbing molecules is slightly increased with increasing pulse duration due to a longer time spent in the excited state. The qualitative shape of velocity distributions remains unchanged for different pulse durations, despite single trajectories exhibiting Stückelberg oscillations. A one-dimensional Monte Carlo wave function approach is therefore not capable of capturing the experimentally observed bimodality of final state velocity distributions independent on whether the excitation by the laser pulse is treated implicitly or explicitly. Bimodality of final state velocity distributions has been observed in a two-dimensional stochastic treatment of the NO/NiO(100) system [105, 3]. However, the authors of [105, 3] explained the bimodality in terms of the topology the excited state potential surface, and not in terms of different pathways. The next chapter will investigate the NO/NiO(100) system within a Surrogate Hamiltonian approach. A further discussion and a comparison of the methods will be given in Section 7.4.

# Chapter 7

## NO/NiO(100): A Surrogate Hamiltonian treatment

### 7.1 A microscopic model for bath and interaction

The NO/NiO(100)-system is partitioned into a primary system which is given by the NO-molecule adsorbed onto a finite  $\text{NiO}_5^{8-}$ -cluster and an environment which describes the influence of the infinite surface on the primary system (cf. Section 6.1). The NiO(100) surface is a complex entity characterized by its electronic structure, phonon spectrum, defects etc. For the ultrafast dynamics of laser induced desorption, O2p $\rightarrow$ Ni3d charge transfer states, i.e. electron-hole pairs play a crucial role. Hence, these are included in the

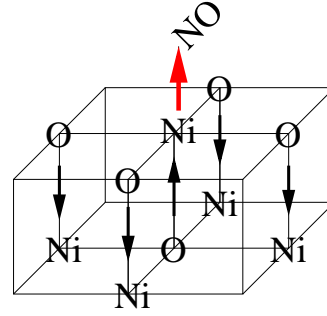


Figure 7.1: Sketch of the partitioning of system and bath

description while everything else such as phonons or other electronic excitations are neglected (see also the discussion in Section 6.1).

The electron-hole pairs are described as a TLS bath,

$$\hat{\mathbf{H}}_B = \varepsilon \sum_i \hat{\sigma}_i^+ \hat{\sigma}_i + \frac{\eta}{\log(N)} \sum_{ij(NN)} (\hat{\sigma}_i^+ \hat{\sigma}_j + \hat{\sigma}_j^+ \hat{\sigma}_i), \quad (7.1)$$

where  $(NN)$  stands for nearest neighbor, and  $\hat{\sigma}_i^+$ ,  $\hat{\sigma}_i$  are the creation and

annihilation operators for the  $i$ th TLS, respectively, as introduced in Chapter 3. Eq. (7.1) implies that one electron-hole pair located at site  $i$  is modeled by the  $i$ th TLS. The sites are Ni-O pairs in the lattice between which charge transfer can occur. The first term in Eq. (7.1) describes the excitation of localized TLS at the sites  $i$ . This is motivated by the Ni3d states being in general localized [128]. Delocalization is brought about by the O2p states and introduced into the model by the second term in Eq. (7.1). This term describes the transport of excitation from one electron-hole pair to its nearest neighbors. The bath is characterized by two parameters,  $\varepsilon$  and  $\eta$ . All electron-hole pairs are assumed to have identical excitation energy  $\varepsilon$ . In a molecular orbital (MO) picture this is the transition energy from the highest occupied molecular orbital (HOMO) to the lowest unoccupied molecular orbital (LUMO).  $\eta$  is the interaction strength between nearest neighbor TLS and leads to a finite width of excitation energy, i.e. an energy band of the bath: If the bath Hamiltonian, Eq. (7.1), is diagonalized, and  $N$  is the number of modes,  $N$  energies around  $\varepsilon$  corresponding to single excitations,  $N$  energies around  $2\varepsilon$  corresponding to double excitations, etc. are obtained. The spread of these eigenvalues around  $\varepsilon$  is determined by  $\eta$ . The scaling  $1/\log(N)$  of the second term in Eq. (7.1) needs to be introduced to make the procedure convergent, i.e. to have the spread of energies around  $\varepsilon$  independent of the number of bath modes  $N$ . The  $1/\log(N)$  factor results from the topology of the problem, i.e. from the mapping of two dimensions of the bath onto one (cf. Appendix F), the interaction itself does not scale with  $N$  since the bath modes are localized [19]. To summarize, the parameter  $\varepsilon$  can be viewed as the center of the bath energy band while  $\eta$  determines its width.

Eq. (7.1) represents an abstraction from the complicated electronic structure of actual O2p→Ni3d charge transfer states in the surface. Therefore, it should be possible to estimate reasonable values of  $\varepsilon$  and  $\eta$  from either electron spectroscopy or electronic structure theory. It is known from experiment [129, 130] as well as configuration interaction (CI) [131, 113] and *GW* calculations [132] that the band gap of NiO is about 4 eV with some surface states corresponding to d→d excitations of nickel at lower energies. The width of the energy band of single electronic excitations is about 10

eV [131]. However, laser energies between 3.2 and 6.4 eV [104, 110] do not probe the whole energy band. If  $\varepsilon$  and  $\eta$  are chosen in direct correspondence to the EELS (Electron Energy Loss Spectroscopy) data and CI calculations, all modes with energies higher than the laser energy are not needed, i.e. they are wasted. The parameters  $\varepsilon$  and  $\eta$  are therefore not only related to physical properties of the system, but also to convergence properties of the method, and a smart choice will put as many modes as possible into the physically relevant range, i.e. the energy range set by the laser energy. A thorough discussion of the role of  $\varepsilon$  and  $\eta$  will be given in Section 7.2.3.

The interaction of the electron-hole pairs with the  $\text{NO}^-$  like intermediate leads to quenching of electronic excitation of the primary system. The electron-hole pairs can be viewed as dipoles, and the laser excitation creates a non-zero transition dipole in the system (cf. Fig. 7.1). The interaction is therefore modeled as dipole-dipole interaction known from classical electrodynamics. This assumes that the electric field can be described classically and that the system dipole is in the far field of the bath dipoles. However, compared to the simplification of the  $\text{O}2\text{p} \rightarrow \text{Ni}3\text{d}$  charge transfer states to TLS, these additional approximations are expected to be negligible. The  $\hat{\mathbf{V}}_i$  in the interaction Hamiltonian,

$$\hat{\mathbf{H}}_{SB} = \begin{pmatrix} 0 & 1 \\ 1 & 0 \end{pmatrix} \otimes \sum_i \hat{\mathbf{V}}_i (\hat{\boldsymbol{\sigma}}_i^+ + \hat{\boldsymbol{\sigma}}_i), \quad (7.2)$$

are then given by the scalar product of the system's transition dipole,  $\hat{\boldsymbol{\mu}}_S$ , and the electric field of the bath dipoles,  $\vec{E}_i$ :

$$\hat{\mathbf{V}}_i = \hat{\boldsymbol{\mu}}_S \cdot \vec{E}_i = \frac{\hat{\boldsymbol{\mu}}_S \cdot \hat{\boldsymbol{\mu}}_i}{|\hat{\mathbf{r}}_i|^3} - 3 \frac{(\hat{\boldsymbol{\mu}}_S \cdot \hat{\mathbf{r}}_i)(\hat{\boldsymbol{\mu}}_i \cdot \hat{\mathbf{r}}_i)}{|\hat{\mathbf{r}}_i|^5}. \quad (7.3)$$

$|\hat{\mathbf{r}}_i|$  is the distance of the  $i$ th bath dipole from the system dipole, an illustration is given in Fig. 7.2. Note that the  $\hat{\mathbf{V}}_i$  are operators in the Hilbert space of the system. Taking into account the expectation value of the transition dipole instead of the operator  $\hat{\boldsymbol{\mu}}_S$  in Eq. (7.3) corresponds to a time-dependent self-consistent field (TD-SCF) approach [29, 96] and introduces the fast time dependence of the transition dipole into the Hamiltonian. Since evaluation of the operator expressions poses no difficulty when using the grid representation (cf. Appendix A.1), Eq. (7.3) was implemented as is, using

the operators and not expectation values. The bath dipoles are assumed to be located at the center of charge in between a nickel and an oxygen atom and the system dipole to be located in between the nickel atom and the NO molecule. Evaluating the scalar products then leads to

$$V_i(\hat{\mathbf{Z}}) = \pm \frac{qa_0\mu_{tr}(\hat{\mathbf{Z}})}{\left(\left(\frac{1}{2}(\hat{\mathbf{Z}} + a_0) + ma_0\right)^2 + n^2a_0^2\right)^{3/2}} \mp 3 \frac{qa_0\mu_{tr}(\hat{\mathbf{Z}})\hat{\mathbf{Z}}^2}{\left(\left(\frac{1}{2}(\hat{\mathbf{Z}} + a_0) + ma_0\right)^2 + n^2a_0^2\right)^{5/2}}, \quad (7.4)$$

where  $a_0$  is the distance between the Ni and O atoms, i.e. half the lattice constant, and  $n, m \in \mathbb{N}$ , with  $n$  labeling the sites within the surface and  $m$  labeling the layers (see Section 7.2.4 and Appendix F). If a one-dimensional primary system is considered, i.e. the tilt angle of NO versus the surface normal is neglected, only bath dipoles parallel to the surface normal contribute to the interaction. The only unknown parameter in Eq. (7.4) and therefore in the interaction Hamiltonian  $\hat{\mathbf{H}}_{SB}$  is the dipole charge  $q$  characterizing the completeness of charge transfer between a nickel and an oxygen atom. The role of  $q$  will be discussed in Section 7.3.1.

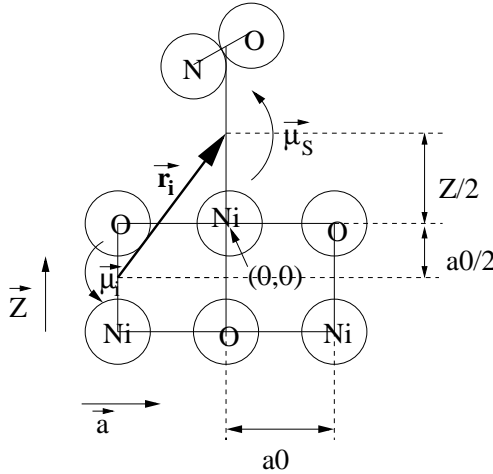


Figure 7.2: Sketch of the geometry of system and bath in a 1D model

The initial state is taken to be the vibrational ground state of the electronic ground state potential, analogously to the Monte Carlo wave function study, cf. Eq. (6.25). This corresponds to a factorizing initial state at zero temperature in density matrix formalism, i.e. no initial correlations between system and bath are considered. Due to the large band gap of about 4 eV in NiO, no electron-hole pairs are thermally excited at time  $t = 0$ , hence it is justified to neglect initial correlations between system and bath.

A direct optical excitation of the  $\text{NO}/\text{NiO}_5^{8-}$  cluster is assumed, a detailed



discussion of the excitation mechanism was given in Section 6.1. An indirect excitation mechanism can in principle also be treated within the framework of the Surrogate Hamiltonian. This would be modeled by a term  $\hat{\mathbf{H}}_{BF}(t)$  which had been introduced for completeness in Eq. (3.1) and Eq. (6.1), respectively, and which describes the excitation of TLS by the laser pulse,

$$\hat{\mathbf{H}}_{BF}(t) = E(t) \sum_i \mu_i (\hat{\sigma}_i^+ + \hat{\sigma}_i) . \quad (7.5)$$

Indirect excitation of the adsorbate has so far been treated semi-phenomenologically by the two-temperature model neglecting for example the non-thermal nature of excited electrons [94, 95]. Another approach took into account the nonlinear optical response of the substrate treating, however, the interaction between substrate and adsorbate in a TD-SCF framework [96, 97]. In contrast to these approaches a Surrogate Hamiltonian treatment allows for a microscopic description of the interaction between laser pulse and surface electrons. It is, however, not clear whether a comparatively small number of bath modes would be sufficient to model excitation *and* deexcitation of the system due to the bath, i.e. whether such an approach would be numerically feasible. The problem of obtaining convergence might become less severe with a parallelization of the computer program. This would allow for a comparison between direct and indirect excitation mechanisms in the case for NO/NiO(100) and for a comparison between a microscopic description and the two-temperature model for hot electrons in metals.

If a direct excitation mechanism is assumed, the laser pulse transfers population from the electronic ground to the electronically excited state around the Franck-Condon point. As described in Chapter 6 the wave packet starts to travel toward smaller distances  $Z$ . However, no discrete jumps occur, but population is continuously transferred to the electronic ground state due to the interaction with the bath. In other words, if the energy of a bath mode matches the potential difference  $\Delta V(Z)$ , it can accept this energy and induce an electronic transition in the system. In principle, while both electronic quenching and electronic excitation of the system are possible, the latter is much less probable. This becomes obvious when using the rotating wave approximation (RWA) and moving to the rotating frame (cf. Appendix D, in particular Eq. (D.9)). Then the bath creation operators couple only to

the electronic annihilator of the system, and the bath annihilators couple only to the electronic creation operator of the system. Electronic excitation of the system can therefore only occur after electronic quenching with the associated creation of bath excitations. The validity of the RWA has been thoroughly checked. The population which has been transferred to the electronic ground state will either be trapped in the potential well though vibrationally excited, or it has gained enough kinetic energy to leave the potential well of the ground state and it will thus desorb. Due to the neglect of vibrational relaxation, the ground state dynamics are analogous to the ground state dynamics described in Section 6.3.2.

Since the Surrogate Hamiltonian is an approximation to the "true" Hamiltonian for system and bath with infinitely many modes, the convergence of observables with respect to the number of bath modes needs to be checked. This is described in Section 7.2, in particular the role of the bath parameters for convergence is discussed. The system dynamics and hence observables depend furthermore on parameters with a direct equivalent in experiment such as fluence and duration of the laser pulse. Corresponding results will be presented in Section 7.3. Section 7.4 concludes this chapter with a comparison of the Surrogate Hamiltonian treatment of NO/NiO(100) to the Monte Carlo wave function approach of the previous chapter.

## 7.2 How to obtain convergence

### 7.2.1 Switching off the bath

The convergence of the Surrogate Hamiltonian with respect to the propagation time is limited due to recurrences in the bath: Since the bath Hamiltonian is finite, energy transferred from the system to the bath will eventually be reflected and transferred back to the system. At this point which shall be called  $t_S$ , the simulation should be stopped and the number of bath modes needs to be increased. In the bit representation (Appendix E),  $t_S$  can be determined by monitoring the population of the zeroth mode. The zeroth mode corresponds to all electron-hole pairs or TLS being deexcited. Therefore, if the transfer of energy from the primary system to the TLS shall be modeled, the population of the zeroth mode should always decrease.

Within the convergence time of the Surrogate Hamiltonian it is not possible to obtain converged expectation values in the asymptotic region ( $V_g(Z) \approx 0$ ) which can be compared to observables of laser induced desorption experiments. However, the Surrogate Hamiltonian is needed only to describe electronic quenching, i.e. to describe the population transfer from the excited state to the electronic ground state due to the interaction with the bath. It is not necessary to describe the nuclear motion on the electronic ground state leading to a separation of the wave packet into a trapped and a desorbing part: If the decay of the electronic excitation is fast, the quenching happens on a much shorter timescale (fs) than the nuclear motion in the ground state (ps), and the two phenomena can be separated.

After the interaction has been switched off at time  $t_S$  either due to complete deexcitation or due to recurrences, one option consists in propagating the  $2^N$  ground state wave packets until the observables in the asymptotic region are converged. However, a more efficient strategy can be used if the wave packet is still comparatively localized. One can construct the ground state density matrix  $\hat{\rho}_S$  of the system by tracing over the bath (cf. Section 3.1). Since no further dissipative processes are included in the description, the time evolution of this reduced density matrix is unitary. Therefore, if  $\hat{\rho}_S$  is diagonalized,

$$\rho_S(Z, Z'; t) = \hat{\mathbf{U}}^\dagger \hat{\mathbf{P}} \hat{\mathbf{U}} = \sum_k p_k |\psi_k(Z; t)\rangle \langle \psi_k(Z'; t)|, \quad (7.6)$$

no further mixing of the wave functions  $|\psi_k(Z)\rangle$  will occur during time propagation. The wave packet created by electronic quenching and nuclear dynamics is a mixed state, therefore more than one eigenvalue  $p_k$  will be non-zero. However, if indeed the wave packet is still localized the number of  $p_k$  which contribute significantly in the sum in Eq. (7.6) is small (usually between 15 and 20 in the examples presented below). It is then advantageous to propagate the  $|\psi_k(Z)\rangle$  instead of the spinor components (cf. Appendix E) and construct expectation values as

$$A(t) = \sum_k p_k \langle \psi_k(t) | \hat{\mathbf{A}} | \psi_k(t) \rangle. \quad (7.7)$$

Since the computer program implementing the Surrogate Hamiltonian is based on wave packet propagation, all that needs to be added is the di-

agonalization of the density matrix. The computational savings depend on the number of modes  $N$ , and they can reach several orders of magnitude for large  $N$ .

### 7.2.2 Increasing the number of modes and restricting simultaneously allowed excitations

The time interval for which propagation with the Surrogate Hamiltonian gives converged results depends on the number of bath modes  $N$  (cf. Chapter 3). This interval can be prolonged by increasing the number of bath modes. On the other hand, the convergence of observables with respect to  $N$  can be checked. Fig. 7.3 shows the population (left), coordinate (top right) and momentum (bottom right) expectation values on the electronically excited state for  $N = 35, 45, 55$ . Exponential decay of population can be observed after excitation by the laser pulse (left), while the wave packet is accelerated toward the surface (top right), i.e. the dynamics is similar to those presented in Chapter 6. The observables can be considered converged up to about 27 fs for  $N = 35$ , 40 fs for  $N = 45$ , and 60 fs for  $N = 55$ . The convergence time  $t_c$  is a bit smaller than the total length  $t_S$  of the curves in Fig. 7.3 since the interaction with the bath is switched off when recurrences reach the zeroth spinor component. By this time the energy reflected at the boundary of the finite system has already passed through the bath modes. Since the convergence time is comparatively short, pulses shorter than those in experiment ( $\tau_{\text{FWHM}} \approx 100$  fs [104, 110]) have been used in the simulations studying the convergence properties of the method. The longest pulses for which convergence could be obtained were between 25 fs and 50 fs long. The exponential decay of excited state population within the convergence interval can be fitted to obtain decay rates or lifetimes. Decay rates vs. the number of bath modes are plotted in Fig. 7.4, top panel, while the quality of exponential fit characterized by the correlation coefficient is shown in the bottom panel. Two different values of dipole strength  $q$  characterizing the strength of interaction between system and bath (cf. Section 7.3.1) have been used. The decay rates (lifetimes) saturate at about  $0.04 \text{ fs}^{-1}$  (25 fs) for  $q = 0.10$  and  $0.075 \text{ fs}^{-1}$  (13 fs) for  $q = 0.14$ . The correlation coefficient fluctuates between 0.9980 and 0.9995 showing a good agreement between data and exponential

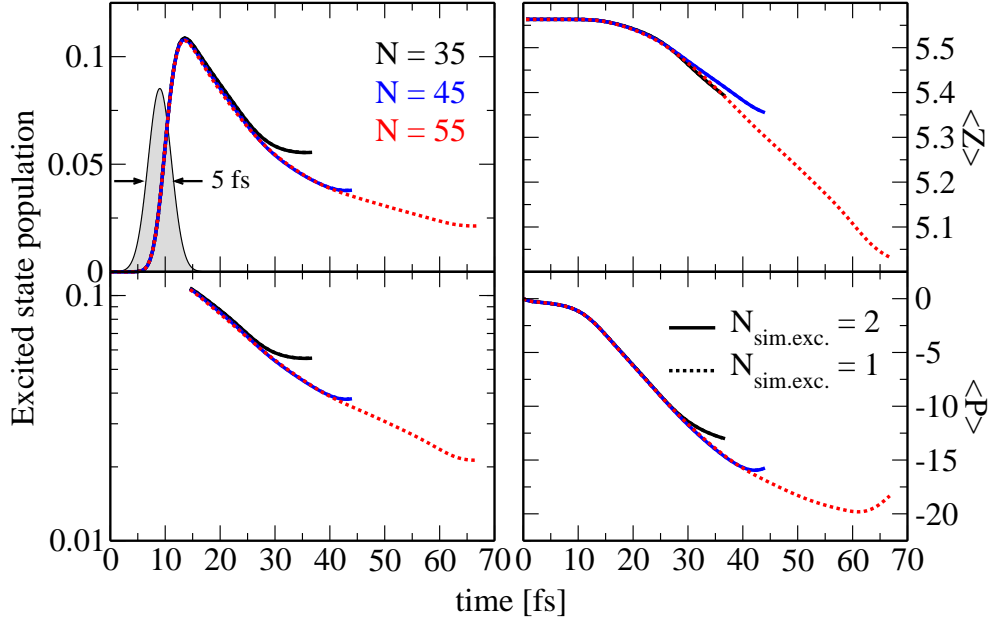


Figure 7.3: The excited state population vs. time is shown on the left, on a linear (top) and logarithmic scale (bottom). The expectation value of distance (top) and momentum (bottom) of the wave packet on the excited state vs. time are shown on the right. Increasing the number of modes  $N$  prolongs the convergence time. The number of simultaneously allowed excitations can be restricted to 1 since the solid and dotted curves (black and blue) are identical. The parameters are  $\varepsilon = 4.0$  eV,  $\eta = 2.0$  eV,  $q = 0.1$ ,  $\omega_L = 3.7$  eV.

fit.

### 7.2.3 Role of bath parameters

The TLS bath describes electron-hole pairs in the surface which cause the quenching of electronic excitation (cf. Section 7.1). It is characterized by the two parameters  $\varepsilon$  and  $\eta$  in Eq. (7.1), the TLS energy and the nearest neighbor interaction strength. These parameters are related to the center and width of the energy "band" of the bath. Fig. 7.5 shows the range of bath eigenenergies for different values of these parameters on the right. Only single excitations are considered, i.e. the number of simultaneously allowed excitations of the bath is restricted to one. The left of Fig. 7.5 displays the excited state potential and the difference potential,  $\Delta V(Z) = V_e(Z) - V_g(Z)$ . The Franck-Condon point indicated in the Figure determines the classical turning points

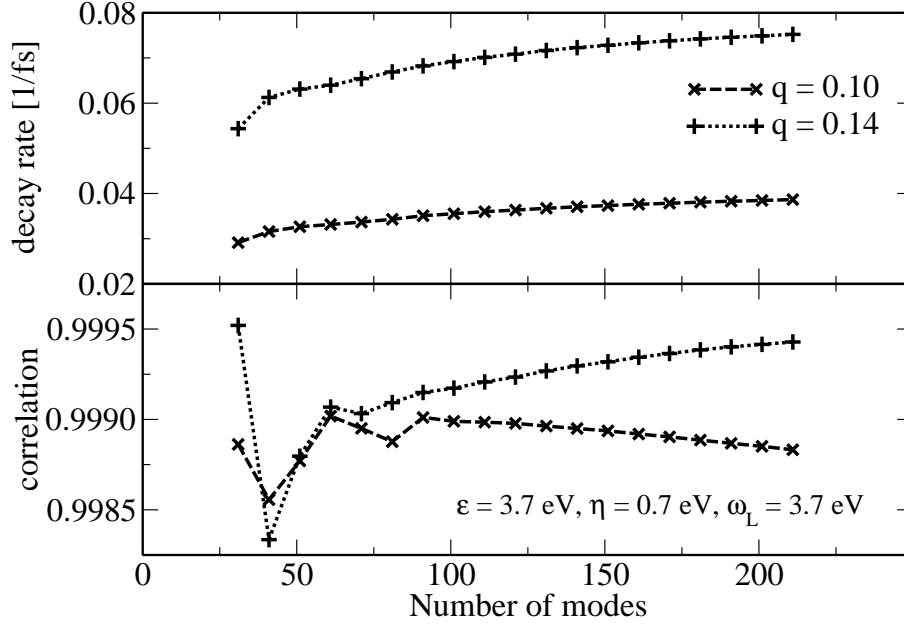


Figure 7.4: The excited state decay rate obtained from exponential fit (top) and the correlation coefficient of exponential fit (bottom) are plotted vs. the number of bath modes  $N$ . The decay rate reaches saturation when increasing  $N$ , while the correlation fluctuates in a range close to one.

for the wave packet motion on the excited state (blue arrow). The values of the difference potential  $\Delta V$  in between the classical turning points specify the range of bath energies relevant for quenching (fat red arrow), i.e. bath modes with energies within this range can accept energy from or give energy to the system causing a transition between electronic ground and excited state. The bath parameters are therefore chosen to obtain the best possible convergence of observables with respect to the number of modes, i.e. many electron-hole pair with energies much higher than the laser energy exist [130,131] but they are not needed.

Fig. 7.6 shows the influence of the TLS energy  $\varepsilon$  on the excited state dynamics. If  $\varepsilon$  is considerably larger than the laser energy, the range of bath eigenenergies does not match the values of the difference potential between the classical turning points, the TLS cannot accept energy from the system, and hence no decay of excited state population is observed (red curve in Fig. 7.6). For  $\varepsilon$  considerably smaller than the laser energy, there are no matching bath modes close to the Franck-Condon point. However,

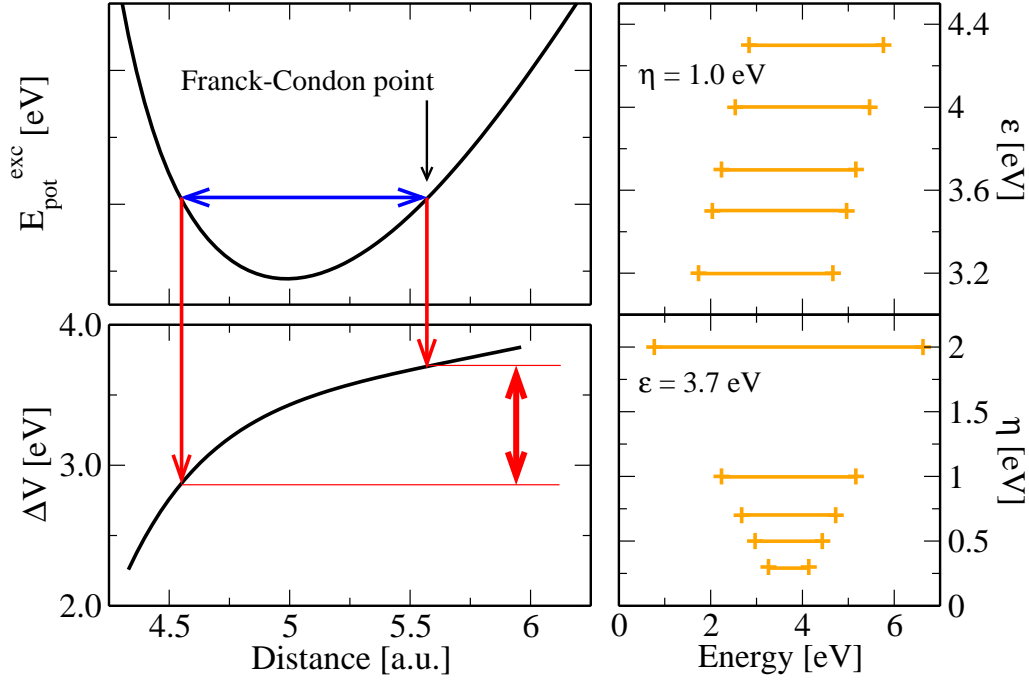


Figure 7.5: The range of bath eigenenergies needs to match the difference potential  $\Delta V$  for quenching to be efficient (left). It is determined by the bath parameters  $\epsilon$  and  $\eta$  (right). The difference potential is fixed by assuming resonant excitation at the Franck-Condon point with a laser energy of 3.7 eV.

as the wave packet travels toward smaller distances, the value of the difference potential is decreased (cf. Fig. 7.5), bath energies in the right range are found, and decay of excited state population may be observed with some delay (black curve in Fig. 7.6). For intermediate values of  $\epsilon$ , the excited state population decays exponentially. To illustrate this, the excited state population is plotted twice – on a linear scale (top panel) and on a logarithmic scale (bottom panel). Exponential decay corresponds to a constant relaxation rate and allows for a comparison of the Surrogate Hamiltonian method with the Monte Carlo wave function approach of Chapter 6. The specific value of  $\epsilon$  determines convergence as can be seen from comparison of the solid and dotted lines (101 and 91 bath modes, respectively) and from Table 7.1. An optimal choice places  $\epsilon$  close to the laser energy. This is reasonable also from a physical point of view. Since the laser pulse induces an electronic transition in the nickel oxide surface, its energy needs to be equal to or larger than the

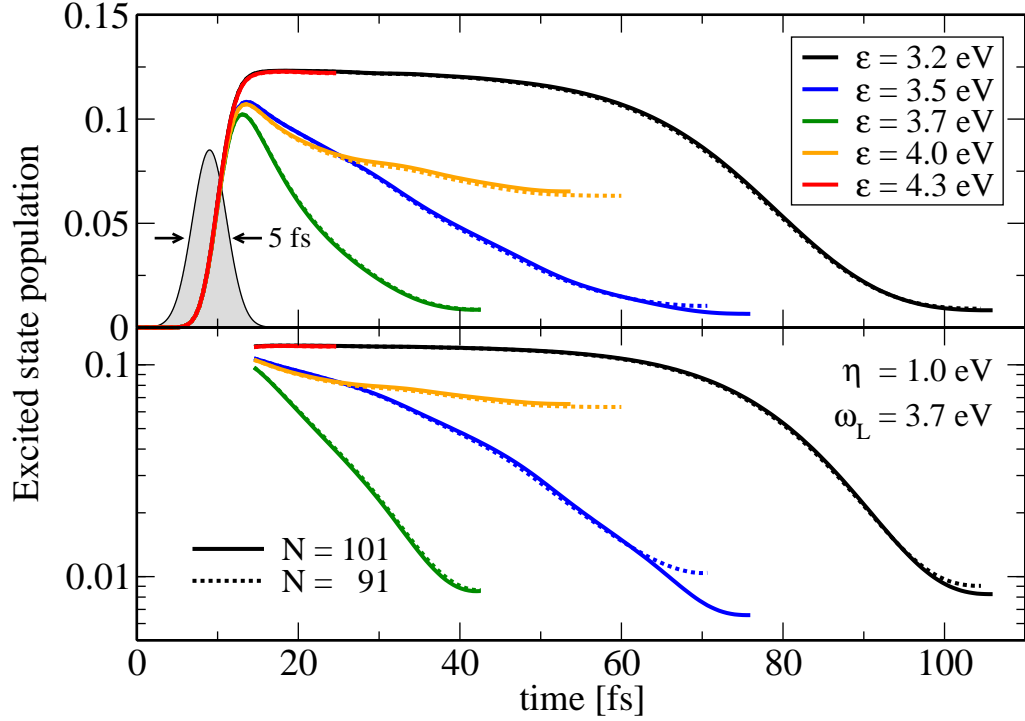


Figure 7.6: Dependence of excited state population vs. time on the TLS energy  $\varepsilon$ : If  $\varepsilon$  and therefore the center of the bath energy band is close to the system resonance fixed by the laser energy  $\omega_L$  (the blue, green and yellow curves) the decay of excited state population is exponential, and the choice of  $\varepsilon$  determines convergence. If the bath energies are larger than the system resonance (red curve), the system cannot give energy to the bath and no decay is observed. For bath energies smaller than the system resonance (black curve), the wave packet needs to travel to a region where the bath energies match the potential difference before decay can occur (see text for further explanation).  $N$  indicates the number of bath modes.

$\varepsilon$	decay rate [1/fs] ( $N = 101$ )	decay rate [1/fs] ( $N = 91$ )	correlation of fit ( $N = 101$ )	correlation of fit ( $N = 91$ )
3.5	0.050	0.046	0.988	0.991
3.7	0.096	0.095	0.997	0.998
4.0	0.011	0.010	0.977	0.967

Table 7.1: The quality of exponential fit for the decaying part of the excited state population with TLS energy  $\varepsilon$  varied is given by the correlation coefficient. The best fit is obtained for  $\varepsilon = \omega_L = 3.7$  eV. In this case, the quenching is also most efficient (largest decay rate).



band gap to which  $\varepsilon$  is related.

The dependence of excited state population on the nearest neighbor interaction strength  $\eta$  of the TLS is shown in Fig. 7.7. Since the dipole-dipole in-

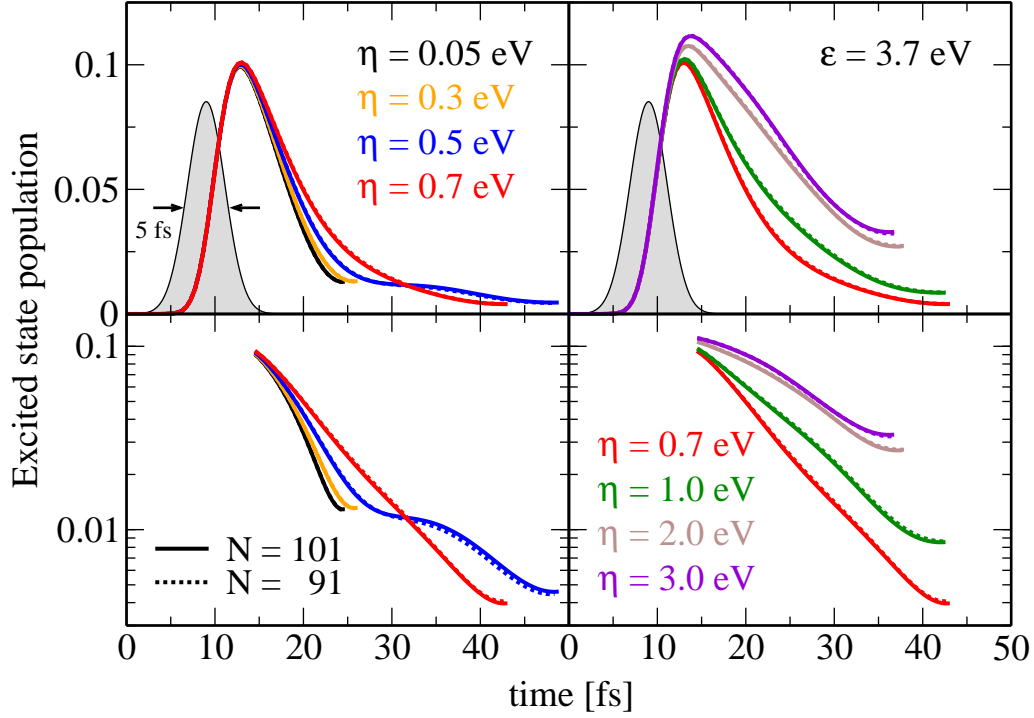


Figure 7.7: Dependence of excited state population vs. time on nearest neighbor interaction strength  $\eta$ : For small  $\eta$  (black and yellow curves) there is no transport of relaxed population out of the interaction region, the convergence time is very short and cannot be improved by increasing the number of modes  $N$ . Increasing  $\eta$  (blue curve) leads to transport, however on a timescale larger than the interaction with the system. For  $\eta \geq 0.7$  eV, the transport is efficient, and exponential decay of excited state population is observed (curves on the right). Large  $\eta$  causes less quenching of excitation during the interaction of the system with the pulse, and hence a larger maximum population of the excited state.

interaction exhibits a  $1/Z^3$  dependence, the system interacts only with electron-hole pairs which are very close to the NO molecule, and the nearest neighbor interaction between electron-hole pairs is needed to transport the excitation away from this interaction region. If  $\eta$  is very small (black and yellow curves in Fig. 7.7), the excitation cannot be given to TLS outside the interaction region, and the convergence time is determined by saturation of the few TLS close to the primary system. Increasing the number of modes thus cannot

prolong the convergence time: The dotted and solid curves differ only in the fifth digit, and decay rates from an exponential fit differ in the sixth digit for  $N = 101$  and  $N = 91$ . When  $\eta$  is increased, transport sets in leading to a longer convergence time, slower decay, and dependence on the number of modes (the decay rates differ now in the second or third digit for  $N = 101$  and  $N = 91$ ). Furthermore, the quenching of excitation during interaction of the system with the pulse is less efficient, hence the maximum population of the excited state is increased for larger  $\eta$  (cf. Fig. 7.7, right). The excited state population decays exponentially – independent of the value of  $\eta$  with the exception of  $\eta = 0.5$  eV. The decay rates obtained from an exponential fit of the excited state population vs. time (Fig. 7.7) are plotted vs. the number of modes in the upper panel of Fig. 7.8, while the lower panel shows the goodness of the exponential fit characterized by the correlation coefficient. The decay rate is decreased for increasing nearest neighbor interaction. This can be understood from both an energy and a coordinate representation point of view. In energy representation,  $\eta$  increases the spread of bath energies which will eventually become larger than the range required for quenching and determined by the difference potential  $V(Z)$  (cf. Fig. 7.5). Thus bath energies will be moved outside of this range and the corresponding bath modes are wasted. The quenching is then less efficient, and the decay becomes slower. In coordinate representation,  $\eta$  determines how quickly relaxed population is transported away from the primary system, but also from TLS close to the primary system. The interaction energy, i.e. the expectation value of the interaction Hamiltonian, Eq. (7.2), depends on the population of the primary system and of the bath modes close to it. If population is removed from these bath modes, the interaction energy is decreased and the decay becomes slower. In other words, the more electron-hole pairs are excited close to the NO molecule, the faster is the decay. The same argument explains the increase of the maximum excited state population, i.e. decrease of quenching during the interaction with the laser pulse. Since the timescale of this interaction is shorter than that of relaxation (the laser FWHM was chosen as 5 fs), the effect becomes visible only for large  $\eta$  (cf. Fig. 7.7, right). The correlation coefficients of the exponential fit lie within the interval  $[0.99, 1.0]$  with the exception of  $\eta = 0.5$  eV (Fig. 7.8, bottom). If the data for  $\eta = 0.5$  eV

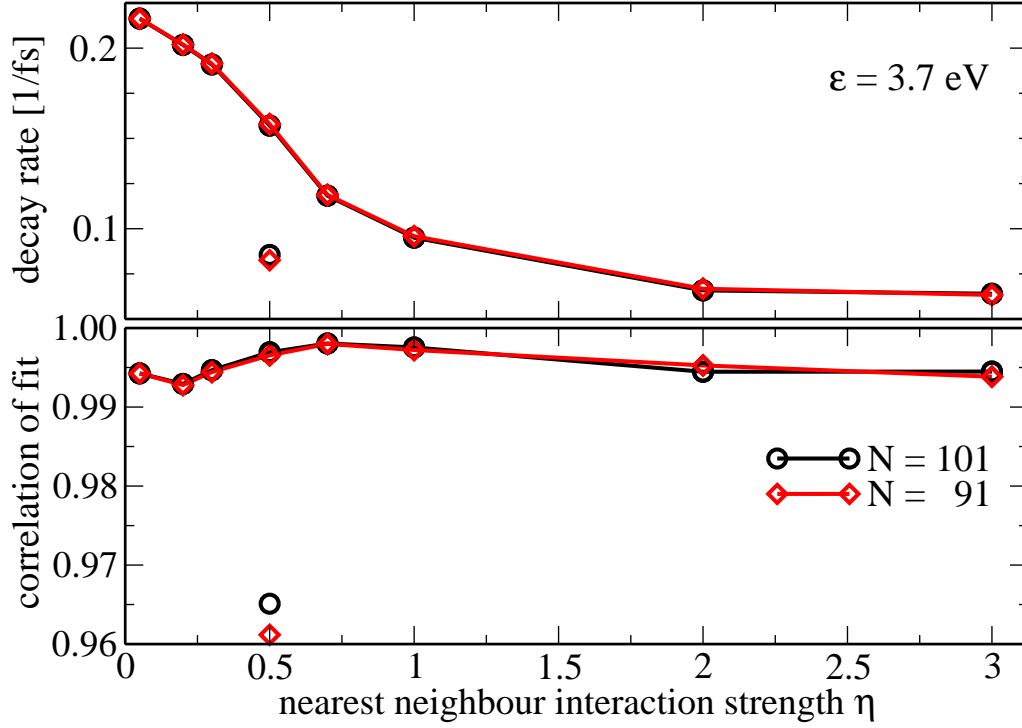


Figure 7.8: The decay rates of excited state population which were obtained from an exponential fit of the data shown in Fig. 7.7 are plotted vs. nearest neighbor interaction strength  $\eta$  (upper panel). It decreases for larger values of  $\eta$ . The goodness of exponential fit is more or less independent of  $\eta$  (lower panel). Two values for the decay rate and the correlation coefficient are plotted for  $\eta = 0.5$  eV, once the data of the whole range shown in Fig. 7.7 and once only values of excited state population up to 25 fs were used in fitting.

is fitted only up to 25 fs, its correlation coefficient also lies within  $[0.99, 1.0]$ . A similar behavior is found for  $\eta = 0.6$  eV, while the data for  $\eta = 0.4$  eV is similar to the one with  $\eta = 0.3$  eV. Thus, variation of  $\eta$  does not change the decay of excited state population qualitatively. This is different from the role of the TLS energy  $\varepsilon$  (cf. Fig. 7.6). However, since  $\varepsilon$  shifts the position of bath eigenenergies while  $\eta$  changes only their width (cf. Fig. 7.5), this is not surprising.

The considerations have so far been only numerical and suggest an optimal choice of about 0.7 eV to 1.0 eV for  $\eta$ . However, an upper limit to the nearest neighbor interaction strength is also set by the physics of the NO/NiO(100) system: The lowest states are surface states in the optical

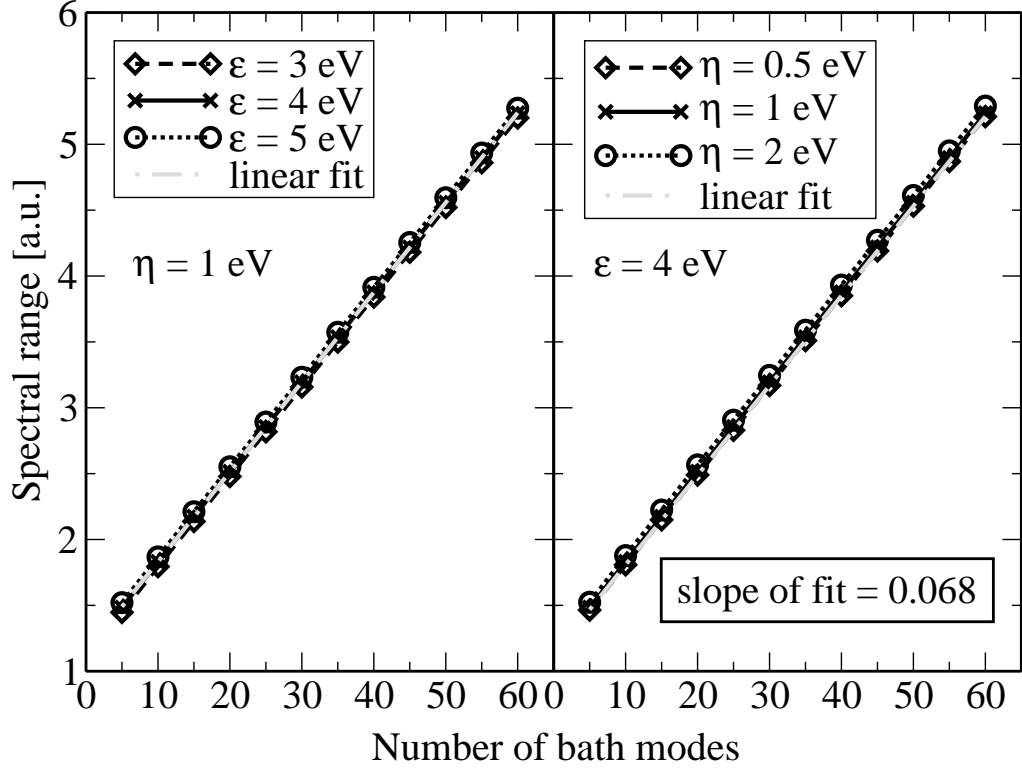


Figure 7.9: The spectral range depends on the bath parameters  $\epsilon$  and  $\eta$  and the number of bath modes  $N$ . Due to linear dependence it can be extrapolated for increasing  $N$ .

band gap at about 2.7 eV [129]. However, these are not charge transfer states, but Ni d→d excitations. The charge transfer states lie energetically above the band gap. Therefore no bath modes with energies much below 3.5 eV shall be considered. Of course, if the TLS energy  $\epsilon$  is shifted,  $\eta$  needs to be adjusted to result in a reasonable smallest bath eigenenergy. Accordingly, the optimal choice of bath parameters leading to best possible convergence of expectation values w.r.t. the number of bath modes is a combination of TLS energy  $\epsilon$  and nearest neighbor interaction strength  $\eta$ . In the following,  $\epsilon = 3.7 \text{ eV}$  and  $\eta = 0.7 \text{ eV}$  were used.

The bath parameters influence also the spectral range  $\Delta E$  of the total system and bath (cf. Fig. 7.9) which is calculated according to Appendix A.5. The spectral range, i.e. the difference between minimal and maximal energy of the problem in the chosen representation, is not an observable, but a quantity crucial for numerical stability of the propagation (Appendix A.2).

When using the RWA, the spectral range depends not only on the parameters of the model, but also on the number of bath modes (Appendix D). A linear dependence of the spectral range on the number of bath modes can be observed in Fig. 7.9. Therefore,  $\Delta E$  can be extrapolated and does not need to be calculated every time the number of modes is increased or the bath parameters are changed.

#### 7.2.4 Convergence of asymptotic observables

So far it has been shown that converged observables related to the excited state dynamics can be obtained, and it has been investigated how the convergence of these observables with respect to the number of bath modes is influenced by the bath parameters. While the excited state dynamics are crucial for the outcome of a laser desorption experiment, they are not directly accessible in a single pulse experiment. What is measured in such an experiment [107, 110] are the desorption yield and the state resolved velocity of desorbing molecules. In the language of the theoretical model, these are observables related to operators in the asymptotic region (cf. Appendix A.6). In particular, the desorption probability is obtained by weighting the norm in the asymptotic region of the ground state potential by the excitation probability.

Due to the Antoniewicz-like mechanism of desorption, the asymptotic observables are determined by partial wave packets which stay on the excited state for a comparatively long time. In this case, the partial wave packets end up high on the repulsive part of the ground state potential after the electronic quenching. They can then gain enough kinetic energy to leave the potential well and reach the asymptotic region. The convergence of the Surrogate Hamiltonian with respect to the number of modes is limited in time. It is therefore comparatively easy to obtain converged excited state dynamics, while it turned out to be more difficult to obtain converged asymptotic observables. A similar problem has been encountered within the MCWF approach (cf. Section 6.3.2). The technical reasons are, however, quite different for the two approaches: It is the finite size of the bath for the Surrogate Hamiltonian and the stochastic sampling for the MCWF method.

Two strategies can be employed to reach convergence of the asymptotic

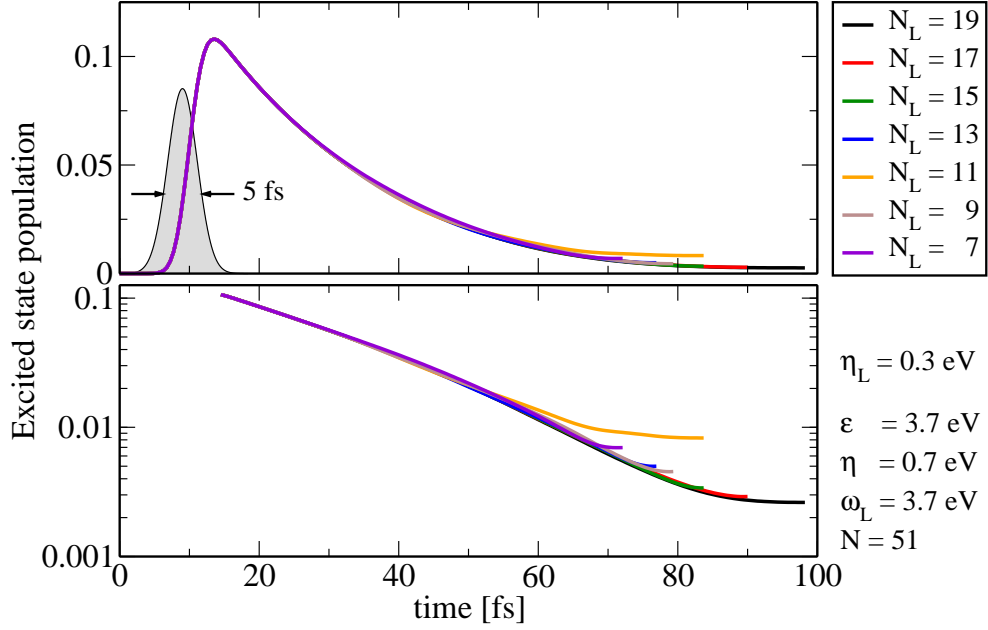


Figure 7.10: The population of the excited state vs. time. The coupling between electronic states is switched off when recurrences occur, therefore the graph lengths indicate the convergence time.

observables. Either the number of bath modes,  $N$ , or the number of layers in the surface,  $N_L$  (cf. Appendix F), can be increased. A combination of the two strategies, although possible in principle, is limited by the computer resources. An increase in the number of bath modes,  $N$ , enlarges the size of the bath horizontally, and more layers in the surface allow for vertical transport, i.e. transport into the surface. While both processes are equally likely for nickel oxide, they are not treated on the same footing in the model. This is discussed in more detail in Appendix F.

The goal to be reached is the prolongation of the convergence time of the Surrogate Hamiltonian. Considering several surface layers indeed leads to a longer convergence time (cf. Fig. 7.10). The treatment of more than one layer of dipoles introduces a new parameter into the model, the coupling between layers,  $\eta_L$ . Its influence on the excited state dynamics is shown in Fig. 7.11. A small value of the interlayer coupling (the blue as compared to the black curves in Fig. 7.11) does not change the lifetime of the excited state. Increasing the value of  $\eta_L$  leads to slower decay of the electronic excitation (red and green curves in Fig. 7.11). This can be understood by an argument

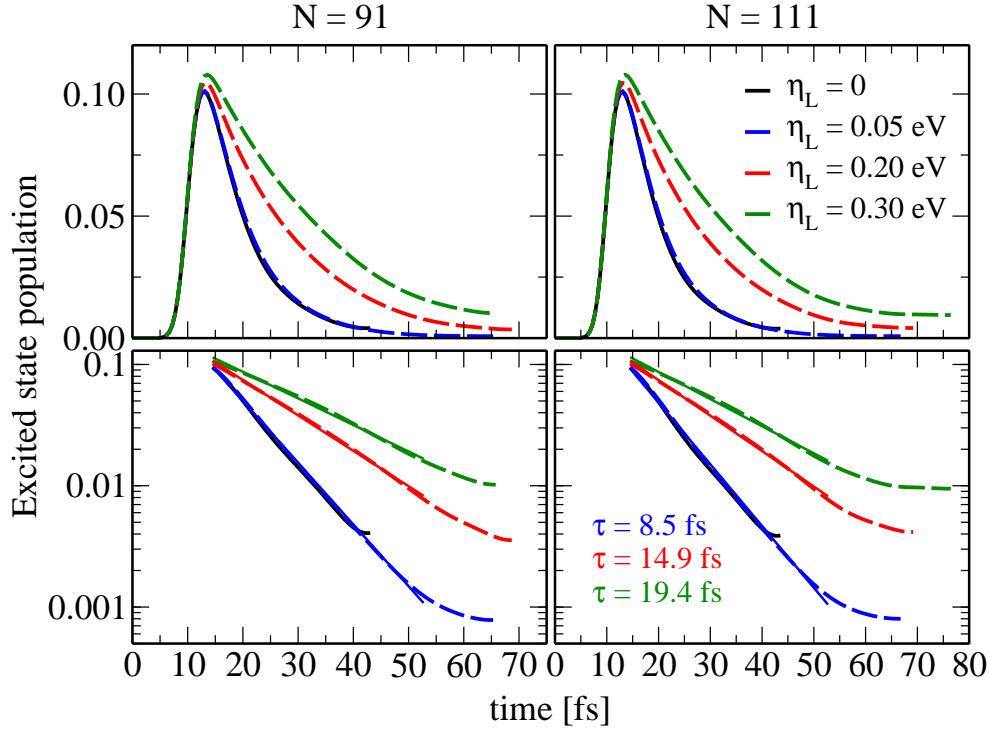


Figure 7.11: Increasing the interlayer coupling leads to a slower decay due to faster transport of relaxed population away from the interaction region (parameters as in Fig. 7.10, but  $N_L = 5$ ).

similar to the one explaining the dependence of the lifetime on the nearest neighbor interaction  $\eta$ . The strength of the system-bath interaction depends on the excited state population of the system and on the population of bath modes close to the system. An increase of  $\eta_L$  results in quicker transport of excitation from bath modes close to the system to bath modes further away. Thus the system-bath interaction becomes weaker and the lifetime longer.

As a consequence of the slower decay, increasing the interlayer coupling  $\eta_L$  also leads to a larger desorption probability (cf. Fig. 7.12). While the nearest neighbor interaction  $\eta$ , i.e. the intralayer coupling, has been directly related to the electronic structure of the system, such a connection has so far not been given for the interlayer coupling,  $\eta_L$ . However, since in the NiO surface the transport of excitation is equally likely horizontally as well as vertically, it is reasonable to assume that  $\eta_L$  should be of the same order of magnitude as  $\eta$ . On the other hand,  $\eta_L$  is related to the convergence properties of the model. This means that there exists an optimal value for which the largest

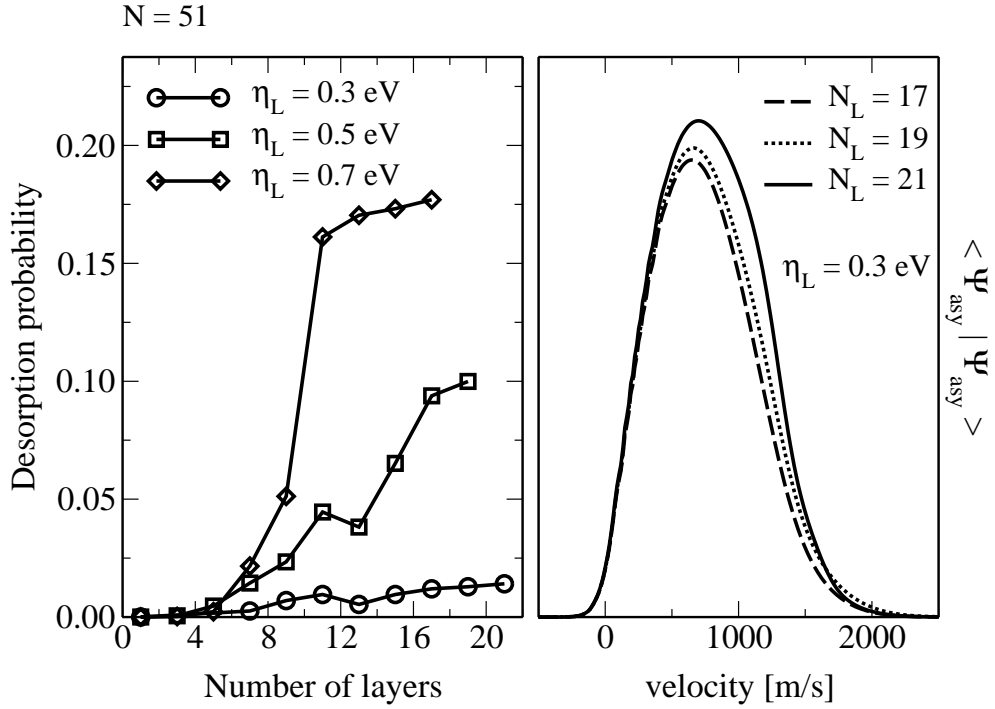


Figure 7.12: Increasing the number of layers leads to converged desorption probability (left) and velocity distributions (right). The interlayer coupling  $\eta_L$  influences the lifetime of the excited state and therefore also the desorption probability (parameters as in Figs. 7.10 and 7.11).

convergence time for a given number of modes and a given number of layers is obtained. If  $\eta_L$  is small, an increase in the number of layers, i.e. an increase of the vertical bath size, will not result in a larger convergence time. In this case, the excitation hits the horizontal boundary of the bath before reaching the vertical limit. For large values of  $\eta_L$  the opposite is true: The vertical is reached before the horizontal boundary. The best convergence is achieved, when both boundaries are arrived at at the same time. The optimal choice of  $\eta_L$  therefore depends on the number of bath modes and the number of layers.

For the parameters investigated, up to 21 layers with  $N \leq 51$  and up to 13 layers with  $N \leq 101$  bath modes in each layer were considered. The maximum convergence time was about 90 fs. This was enough to obtain converged desorption probabilities and velocities (cf. Fig. 7.12). Desorption probabilities between 1% and 20% were obtained. This is compatible with



estimates from experiment [92,87,127]. Furthermore, the velocities are found to be in the experimentally observed range between 0 and 2000 m/s [103,83].

The population of the excited state was decreased from its maximum value of about 0.11 to about 0.005 (at best 0.0034 shown in Fig. 7.10). This means that about 0.5% of the density were neglected when the bath was switched off. While this number is small in absolute value, it might be a considerable portion of the desorbing part. The desorption probability is obtained by weighting the norm in the asymptotic region by the excitation probability. One may assume that all or a substantial part of the neglected density desorbes since the coordinate expectation value approaches the value of the classical turning point. In case of a sudden electronic transition a lot of kinetic energy would be gained by the wave packet. Weighting the value of 0.5% with the excitation probability results in a possible increase of the desorption probability by 5%. While this is on the same order of magnitude as the desorption probability itself, it is still well within the uncertainty of the experimental estimation.

The second strategy, which was already discussed in Section 7.2.2, consists in increasing the number of bath modes,  $N$ , within one layer. A peculiarity is then observed: Above a certain number,  $N^*$ , of bath modes a further increase does not result in a prolongation of the convergence time. This phenomenon led to a closer examination of the bath. The exact value of  $N^*$  depends on the parameters, in particular on the dipole strength,  $q$ , which determines the system-bath interaction strength and hence the convergence.

Since every bath mode is connected with a NiO lattice position, an average distance of the excitation in the bath can be calculated. If this distance in the bath is plotted vs. time, an increase is observed until the finite boundary is reached. The reflection at the boundary leads to a subsequent decrease, i.e. the recurrences can also be detected in this expectation value. Therefore, an alternative criterion to switch off the bath can be defined using a decrease in the distance of the bath instead of an increase of the zeroth spinor component (cf. Section 7.2.1). For a small number of modes, the convergence times obtained from the two criteria are more or less equivalent, i.e. the finite boundary is usually reached at bit before population flows back into the system. For numbers larger than  $N^*$ , however, the finite boundary does not

seem to be reached when population backflow is observed. A possible interpretation of this phenomenon consists in a polarization of the bath dipoles which interacts with the system leading to the backflow of population. Both criteria rely on expectation values, i.e. averages. They can therefore both only give an estimate of the time at which recurrences occur. In addition to the bath distance, also its variance has been examined as switch-off criterion, but no differences could be observed.

A comparison of the two criteria is shown in Fig. 7.13. Due to the structure of the interaction operator in the RWA (cf. Appendix D, in particular Eq. (D.9)), the population backflow can be observed directly by an increase in the excited state population (cf. the upper left panel of Fig. 7.13). In spite of the backflow of population into the system, Fig. 7.13 shows that the switch-off criterion employing the distance of the bath is reasonable: The curves of excited state population overlap for an increasing number of bath modes for a time considerably longer than the convergence time given by the population backflow criterion (indicated by the black arrow in Fig. 7.13). The two switch-off criteria lead to different desorption probabilities (cf. the lower left panel of Fig. 7.13) owing to the different times the wave packet spent on the excited state. The different times spent on the excited state furthermore result in different velocity distributions (cf. the right panel of Fig. 7.13). In the case of the bath distance switch-off criterion (red curves in Fig. 7.13), the propagation on the excited state continued sufficiently long to pass the classical turning point. Therefore an interference can be observed in the velocity distribution.

The interference results from different pathways of partial wave packets which have reached the asymptotic region. Interferences in the velocity distribution were also observed for single trajectories in the MCWF approach (cf. Section 6.3.2). The causes of the different pathways are, however, different. In the MCWF approach, they result from the wave packet being excited by the pulse several times. In the case presented in Figs. 7.13 and 7.14, the pulse is too short for such multiple excitations ( $\tau_{\text{FWHM}} = 5$  fs). The interference is rather caused by partial wave packets which undergo electronic quenching at different times. Such a *coherent* phenomenon cannot be observed with the stochastic wave function method.

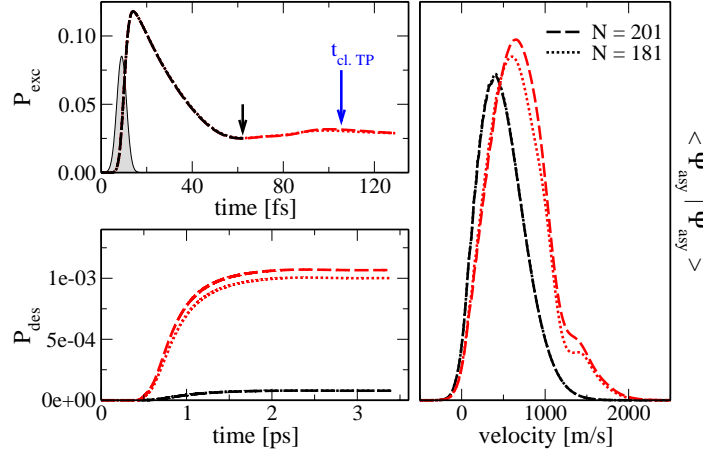


Figure 7.13: If the distance of the bath excitation (red) is used as convergence criterion instead of the population of the system (black), longer convergence times  $t_S$  can be obtained (indicated by the black arrow). The time the wave packet spent on the excited state is crucial for both the desorption probability (bottom left) and the shape of the velocity distributions (right, scaled for comparison). The second peak in the velocity distribution can be related to the passage of the classical turning point of the excited state potential (indicated in blue) which has only occurred for the red curves with  $N = 181$  and  $N = 201$ . The top left shows the population of the excited state with the pulse (not to scale) indicated (parameters as in the previous Figures, but  $N_L = 1$ ).

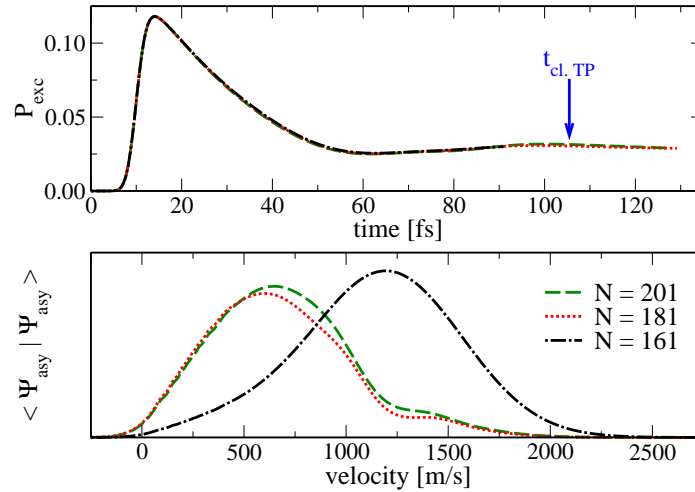


Figure 7.14: The red curves from Fig. 7.13 are plotted here for increasing number of bath modes  $N$ . The appearance of the high velocity peak is related to the passage of the classical turning point, but is independent of the increase in excited state population, i.e. it is not caused by the recurrences in the bath.

This point is clarified by Fig. 7.14 which shows the excited state population vs. time and velocity distributions for a different number of bath modes  $N$ . For all three cases in Fig. 7.14, the switch-off criterion employing the bath distance has been used. For  $N = 161$  bath modes (black curves in Fig. 7.14), the propagation with both electronic states had to be switched off before the classical turning point was reached. The corresponding velocity distribution therefore shows only a single peak. For  $N = 181$  and  $N = 201$  modes, the excited state propagation continued beyond the passage of the classical turning point. Consequently, the velocity distributions exhibit an interference pattern. In particular, it can be concluded from Fig. 7.14 that the interferences in the velocity distributions appear independent from the population backflow since the latter is observed for all three cases presented in Fig. 7.14. Furthermore, interferences can also be observed with the population backflow criterion – given that the propagation proceeded long enough on the electronically electronic state to pass the classical turning point. This was the case, for example, if an unphysically small TLS energy  $\varepsilon$  was chosen (cf. the black curves in Fig. 7.6). This leads to the conclusion that the interference pattern is not caused by recurrences in the bath, but it can unequivocally be related to the excited state dynamics.

To summarize this section, in the first attempt to theoretically study laser induced desorption with the Surrogate Hamiltonian method, converged excited state dynamics could be obtained. The convergence of asymptotic observables proved to be more difficult. The convergence behavior with respect to the parameters of the method was characterized. As a fully quantum mechanical, and therefore coherent method, the Surrogate Hamiltonian suggests that experimentally observed bimodality of velocity distributions can be caused by quantum interferences known as Stückelberg oscillations. While this is discussed in more detail in Section 7.4, the next section is dedicated to studying the influence of parameters of the model which can directly be controlled in the experiment.

### 7.3 Dependence on the experimentally adjustable parameters of the model

There is only parameter which enters the interaction Hamiltonian, Eq. (7.2), and the interaction constants, Eq. (7.3) – the dipole charge  $q$ . It characterizes the completeness of charge transfer between a nickel and an oxygen atom,  $0 \leq q \leq 1$ , and it determines the system-bath interaction strength. The dynamics can therefore be expected to depend crucially on  $q$ . While  $q$  is related to the electronic structure of the substrate, it has been included in this section because its value is determined by a peculiarity of the nickel oxide. The other two parameters related to the electronic structure of the substrate, the TLS energy  $\varepsilon$  and the nearest neighbor interaction  $\eta$ , correspond to features which can generally be observed for insulators – the band gap and the finite width of the energy band(s). The dynamics can furthermore be influenced by the parameters of the pulse – its length, its intensity or fluence, and its carrier frequency.

#### 7.3.1 Dipole strength

Increasing the dipole charge  $q$  leads to a stronger interaction between system and bath and therefore to a smaller lifetime on the excited state. This can be seen in Fig. 7.15. But the excited state dynamics is influenced in a twofold way: Besides the exponential decay which can be observed after the pulse has been applied, the maximum population of the excited state is decreased. The two phenomena are, of course, related. The latter, however, gives  $q$  the meaning of a parameter characterizing a metal to insulator transition, albeit in a very simplified way. For large  $q$ , no significant population of the excited state is observed at all. This corresponds to the case of metals where a direct optical excitation is immediately quenched due to the strong interaction with the substrate.

The exponentially decaying part of the excited state population vs. time can be fitted to obtain decay rates or lifetimes. The fit is indicated for three examples in the lower left panel of Fig. 7.15 (solid lines). The obtained decay rates vs.  $q$  are plotted in the right panel of Fig. 7.15. For  $q \geq 0.1$ , a linear dependence is observed. This corresponds to the coupling constants,

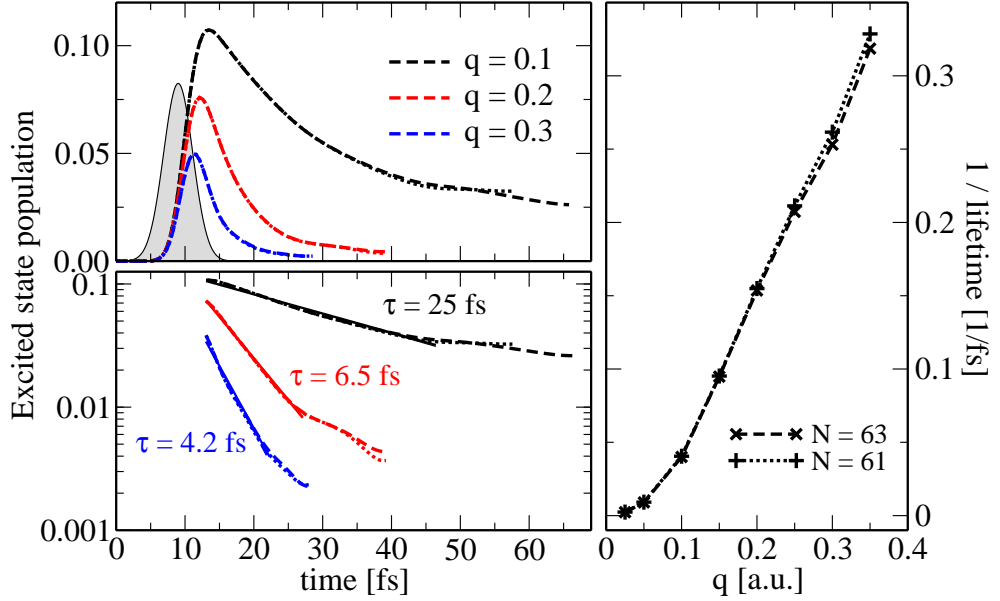


Figure 7.15: The lifetime decreases with increasing dipole strength  $q$  ( $N_L = 1$ ).

Eq. (7.3), being linear in  $q$ .

The lifetime of the electronic state was estimated as about 25 fs [105, 3]. With the Surrogate Hamiltonian, such a lifetime is obtained for a comparatively small value of  $q \approx 0.1$ . A value of this order of magnitude seems justified, however, by the following consideration: The O2p states are quite delocalized. One nickel atom therefore receives the electron from all its five or six neighboring oxygen atoms. But only the one or two charge transfer states with dipole moment parallel to the surface normal contribute to the dipole-dipole interaction. This gives a rough estimate of  $0.15 \lesssim q \lesssim 0.2$ . A similar number has been obtained in a population analysis of the O2p $\rightarrow$ Ni3d charge transfer states [133].

The lifetime on the electronically excited state and therefore  $q$  determine the desorption probability. While this is not confirmed by Fig. 7.16 (lower left panel) due to the convergence problem explained in the previous section, it can be observed in Fig. 7.17. The two Figures have been obtained with the population backflow vs. the bath distance criterion for switching off the bath. The desorption probability for  $q = 0.1$  (green line in Fig. 7.16) is too small because a comparatively large amount of population is neglected when

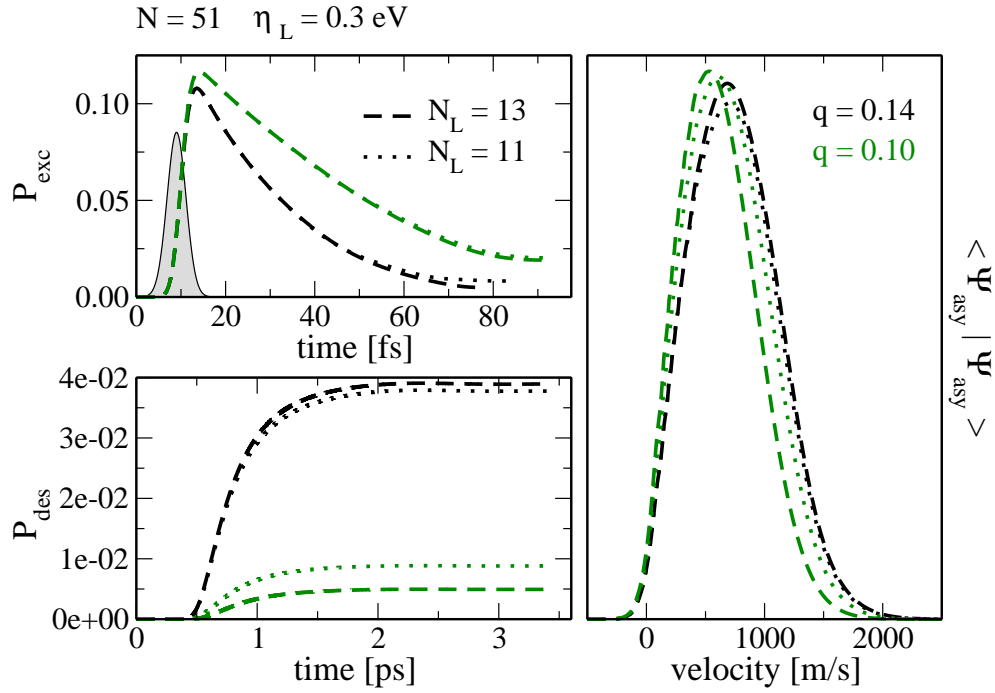


Figure 7.16: The dipole strength  $q$  determines the lifetime (top left) and it leads to a very slight shift in mean velocity (right). The desorption probability could be converged to give an order of magnitude estimation (bottom left).

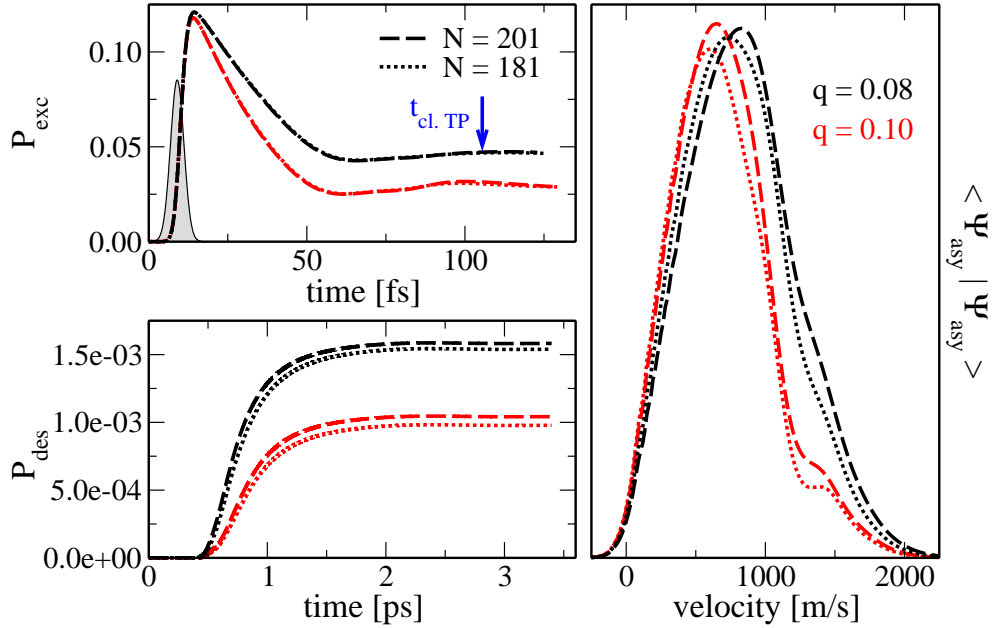


Figure 7.17: The same as Fig. 7.16 ( $q$  varied), but with bath distance switch-off criterion. The velocity distributions have been scaled for comparison.

switching off the bath. For  $q = 0.14$  (black line in Fig. 7.16), the observed desorption probability of about 4% is in the correct order of magnitude. In this case, the amount of neglected population was much smaller than for  $q = 0.1$ . While the bath distance criterion leads to a higher desorption probability for smaller  $q$  as expected, it leads to a trapping of population on the excited state which does not seem to be physical. One could argue that the excited state population does not have to decay in an overdamped way, i.e. purely exponentially. This would lead to additional, decaying oscillations in the excited state population due to multiple electronic transitions. It is, however, beyond the current feasibility of the method to obtain convergence times long enough to test this hypothesis.

The desorption velocities (right panel of Figs. 7.16 and 7.17) depend only slightly on  $q$ . This is, however, subject to the convergence behavior. The shape of the velocity distributions might be changed considerably by the density which has been neglected when switching off the bath. While it seems reasonable to assume, that all or most of the neglected population reaches the asymptotic region and desorbs, it is impossible to estimate with which velocities the desorption occurs. It should nevertheless once more be pointed out that in all cases the velocity distributions show intensity in the experimentally observed velocity range, and the desorption probability is of the expected order of magnitude for  $q = 0.14$ , i.e. for a value of  $q$  close to the estimate from electronic structure calculations.

### 7.3.2 Laser pulse

A characteristic result of femtosecond photodesorption experiments has been the observation of a nonlinear dependence of the desorption yield or probability on the laser fluence indicating a DIMET mechanism and a fluence dependent transition from DIET to DIMET regimes (cf. Chapter 5). Fig. 7.18 therefore shows the dependence of the excitation quenching and the excited state decay on the laser fluence. The Laser fluence is given by the pulse field integrated over time, i.e.  $\int_{-\infty}^{\infty} E(t) dt$ . It is therefore determined by the pulse intensity and duration. While the integral is sometimes called pulse energy, the term energy is avoided since it could be confused with the energy related to the carrier frequency,  $\hbar\omega_L$ .



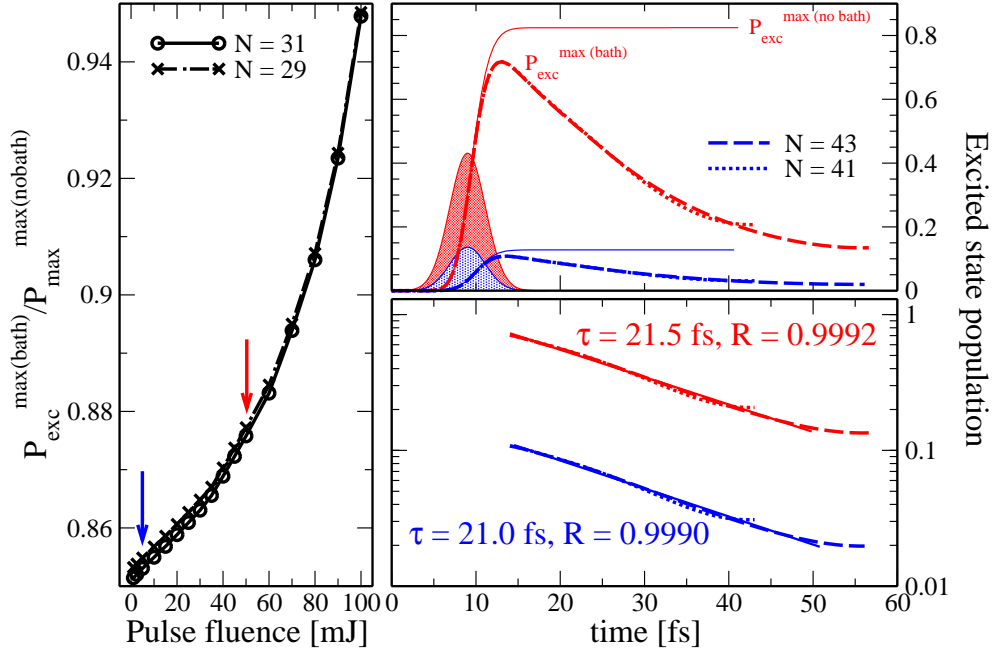


Figure 7.18: Dependence of excitation quenching on pulse fluence: energies leading to about 10% excited state population as employed in the other calculations are in the linear regime (indicated by an arrow). The bath parameters are  $\varepsilon = 4$  eV,  $\eta = 2$  eV with resonant system excitation at  $\omega_L = 3.7$  eV and a pulse duration of  $\tau_{\text{FWHM}} = 5$  fs. The excited state lifetime is not affected by increasing the pulse energy. The quality of the exponential fit is denoted by the correlation coefficient  $R$ .

The blue arrow in Fig. 7.18 indicates the pulse fluence which has been used in the remaining calculations. This value is still way above the fluence of experimentally employed pulses (about 200  $\mu\text{J}$  in [104]). The comparatively large value can be justified, however, to compensate for the simplification of just a single excited state which is accounted for in the theoretical model. This excited state is a representative of many, closely lying states which are on or close to resonance with the laser pulse in the experiment. The population transfer will therefore be higher than predicted by the model. This argument is supported by the independence of experimental results from the laser energy,  $\hbar\omega_L$  which indicates a manifold of excited states with a very similar topology of their potential energy surfaces [107]. A similar conclusion was furthermore reached by the CI calculations [89, 3].

The excited state decay rate does not depend on the laser intensity (cf.

$P_{\text{exc}}^{\text{max(bath)}}/P_{\text{exc}}^{\text{max(no bath)}}$	$\tau_{\text{FWHM}} = 5 \text{ fs}$	$\tau_{\text{FWHM}} = 10 \text{ fs}$	$\tau_{\text{FWHM}} = 25 \text{ fs}$
N = 59	0.8407	0.7053	0.4823
N = 61	0.8403	0.7045	0.4822
N = 63	0.8399	0.7038	0.4818

Table 7.2: The quenching of excitation is increased for longer pulses.

Fig. 7.18). This is reasonable since the decay is caused by the substrate. For weak to moderate pulses, the excitation quenching (left panel of Fig. 7.18) shows a linear dependence on the fluence. For strong pulses, Rabi cycling between the two electronic states becomes significant leading to a nonlinear dependence. These intensities are very high, and Rabi cycling is probably insignificant. It was furthermore shown in a simulation without bath, that Rabi cycling has no influence on the desorption. In that case the population transfer is solely caused by the coupling to the laser pulse. The time spent on the excited state, however, turned out to be insufficient for desorption - independent of pulse intensity and length. Since Rabi cycling is the only mechanism in the present model, which can lead to a nonlinear dependence of the desorption probability on the fluence, it is not surprising, that DIMET cannot be observed. DIMET can inevitably only be modeled by taking into account substrate-mediated excitation described by  $\hat{\mathbf{H}}_{BF}(t)$ .

The dependence of observables on the pulse duration is shown in Figs. 7.19 and 7.20. The lifetime of the excitation is also independent of pulse duration. This is expected and can be explained by the same argument as above: The decay is caused by the substrate, and its rate should not be altered by the pulse. The independence of the decay rate from the pulse parameters points to a consistent treatment of the excitation process in the model.

The excitation quenching, however, is influenced by the pulse FWHM – a longer pulse leads to an increased quenching (cf. Table 7.2 and Fig. 7.19). The system interacts simultaneously with the field and the bath. Therefore, in case of a larger FWHM and hence a longer interaction with the field, more population can be quenched.

The time in which the system simultaneously interacts with the field and the bath should furthermore influence the asymptotic observables. This is shown in Fig. 7.20. The results are, however, only preliminary due to the

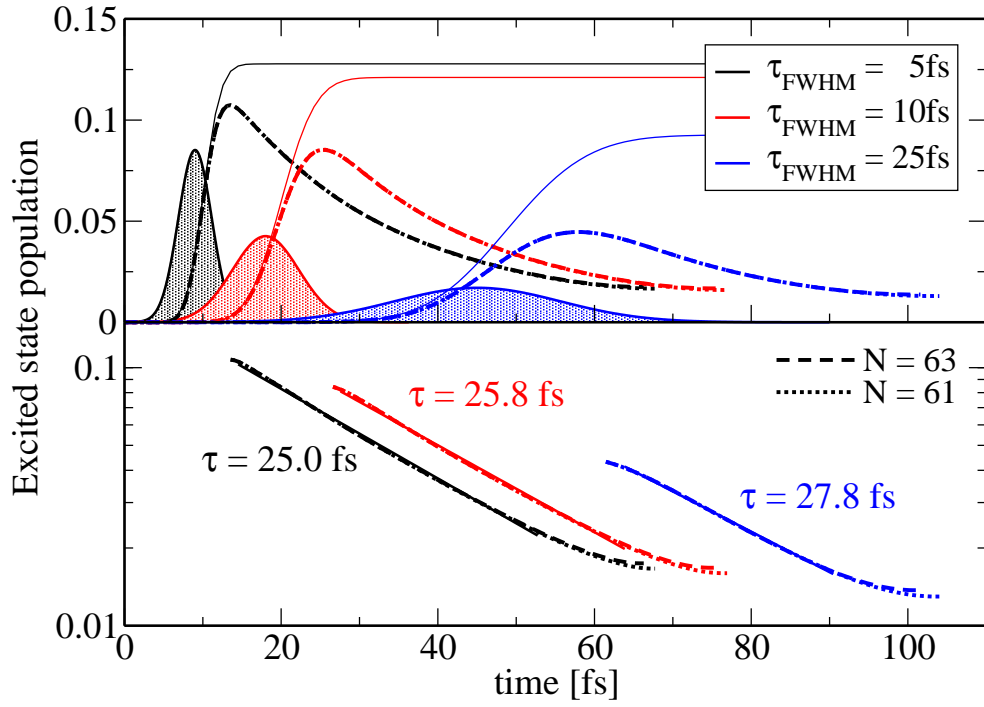


Figure 7.19: The lifetime of the excitation is independent of pulse duration. The bath parameters are  $\varepsilon = 4$  eV,  $\eta = 2$  eV and the excitation is resonant at  $\omega_L = 3.7$  eV.

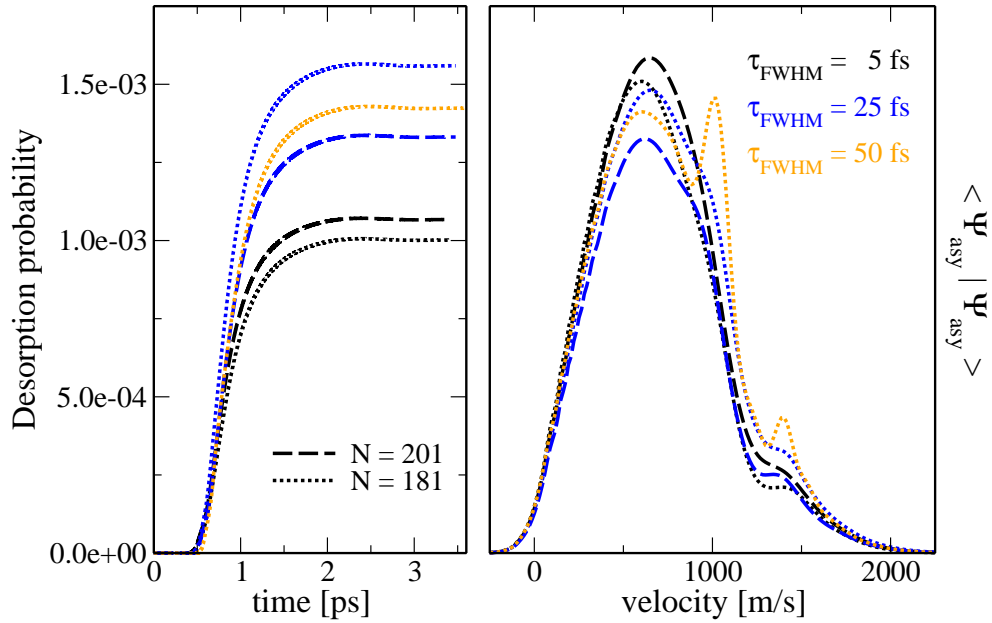


Figure 7.20: Desorption probability and velocity distributions for varied pulse duration. Interference phenomena can be observed when the timescales of the pulse and of the nuclear dynamics become comparable.

convergence problem discussed earlier. When the pulse duration becomes comparable with the vibrational period of the wave packet on the excited state potential, an interplay between pulse and nuclear dynamics can be observed. A longer pulse duration excites partial wave packets at times further away from each other. This leads to more different pathways which show up in the velocity distributions (Fig. 7.20, right). While this is consistent within the model, some caution is advisable when drawing conclusions with respect to the experiment. In the present treatment, electronic dephasing has been completely neglected. Electronic dephasing will certainly wash out some of the observed quantum coherences. This effect should become more pronounced as the pulse duration is increased.

In the present model the laser energy or carrier frequency,  $\omega_L$ , is always assumed to be on resonance with the electronic transition. It therefore determines the optimal choice of the bath parameters  $\varepsilon$  and  $\eta$ , i.e. parameters primarily related to the convergence properties of the method. A shift in  $\omega_L$  will require a readjustment of  $\varepsilon$  and  $\eta$ . New physical phenomena can, however, not be expected. A dependence on  $\omega_L$  was therefore not studied. This situation would change, if both direct and indirect excitation mechanisms were to be considered. Then,  $\omega_L$  on one hand and  $\varepsilon$  and  $\eta$  on the other were truly independent parameters, and an interplay between pulse and bath can be expected.

## 7.4 Comparison with other approaches and with experiment

In this chapter, the theoretical description of laser induced desorption with the Surrogate Hamiltonian method has been outlined and first results have been obtained. Alternative approaches were presented in Chapter 6. The Surrogate Hamiltonian treatment represents the first attempt to *microscopically* model the relaxation which subsequently leads to desorption. The only parameter entering the system-bath interaction was the dipole charge  $q$  which could be estimated by considering the geometry and electronic structure of the substrate. Desorption probabilities of the right order of magnitude and velocities in the experimentally observed range were obtained. This can be

seen as the key result of this chapter.

In contrast to the microscopic picture, which has been developed within the Surrogate Hamiltonian method, the model with diabatic coupling (cf. Section 6.2) and the stochastic wave packet approach (cf. Section 6.3) are semi-phenomenological: While in the first, the diabatic coupling had to be chosen empirically, the excited state lifetime needed to be adjusted in the second.

Comparing the Surrogate Hamiltonian to the MCWF approach justifies the use of a time-dependent Hamiltonian for the latter: It was shown in Fig. 7.3, that the number of simultaneously allowed excitations in the Surrogate Hamiltonian could be restricted to one. This means that there is only one timescale of the bath which needs to be addressed. This timescale which characterizes the decay of correlations in the bath can be estimated as the inverse of the excitation energy of the bath modes by a time-energy uncertainty argument. For excitation energies around 4 eV, a time of about 7 a.u. or 0.2 fs is obtained. When more than one simultaneous excitation needs to be considered, differences of the bath energies become important. These differences are considerably smaller than the bath energies themselves and hence lead to longer times involved. A time of about 0.2 fs is much shorter than the timescale of the pulses used in Chapter 6. By this argument, although qualitative, memory effects can be assumed to be insignificant.

From the point of view of the obtained velocity distributions, the two approaches of Chapter 6 mark two extreme cases with the Surrogate Hamiltonian in between: The diabatic coupling model leads to velocity distributions with a very complicated interference pattern. For the stochastic wave packet method, only a single, broad peak in the velocity distribution was obtained. Within the Surrogate Hamiltonian, the interference is shown to result from the excited state dynamics. In particular, it has been connected to the passage of the classical turning point of excited state motion. The interference therefore becomes dependent on the system-bath interaction strength: If the interaction is strong and the quenching is fast, the classical turning point cannot be reached. The quantum coherences from the diabatic coupling model are thus attenuated by the relaxation which is more rigorously modeled within the Surrogate Hamiltonian method. The differences between the

Surrogate Hamiltonian and the MCWF approach can be explained by the different treatment of the system-bath interaction. A constant, i.e. coordinate-independent decay rate was assumed in the MWCF treatment. Within the Surrogate Hamiltonian, the decay is caused by dipole-dipole interaction between system and bath which shows a pronounced coordinate dependence.

The results obtained with the Surrogate Hamiltonian method, in particular the shape of the velocity distributions of desorbing molecules, have to be seen as preliminary and subject to improved convergence. They suggest, however, that the experimentally observed bimodality can be explained by quantum interferences due to different pathways. A similar interpretation had been given in [117], albeit with a simplified treatment of the relaxation. An alternative reason was suggested within a two-dimensional stochastic wave packet treatment [105,3]. There the experimentally observed bimodality was connected to a bifurcation of the wave packet on the excited state caused by the topology of the excited state potential energy surface. These two hypotheses could be tested by an experiment as well as theoretical studies which change the vibrational frequencies of the potential while leaving the chemistry invariant. This could be accomplished, for example, by using different isotopes of the NO.

While the two approaches presented in Chapter 6 fail to simultaneously reproduce the two experimental observables, which can be captured within a one-dimensional treatment, the desorption yield and the desorption velocities, the Surrogate Hamiltonian method yielded observables in the right ranges. The exact shape of the velocity distributions could, however, not be reproduced. One reason for this is certainly the one-dimensionality of the problem: The results of a two-dimensional stochastic wave packet treatment showed a better compatibility with the experimental results, i.e. bimodal velocity distributions. A combination of two-dimensional *ab initio* potential energy surfaces with the microscopic treatment of the dissipation in the Surrogate Hamiltonian therefore paves the way toward a complete quantum mechanical description of the experiment. As explained in Section 5.2, the consistent description of excitation and relaxation mechanisms is furthermore required by current experimental developments introducing ultrashort pulses and pump-probe techniques into the experiments of laser induced desorption

from oxides [104]. The development of the Surrogate Hamiltonian method should therefore be continued.

Possible directions for future developments of the Surrogate Hamiltonian as applied to photodesorption include in particular the following:

- The bath description with respect to increasing the number of surface layers and the number of bath modes within one layer should be unified. This possibly helps to overcome the current convergence problem.
- An optimization and parallelization of the existing program would allow for the treatment of more than one nuclear degree of freedom. In a two-dimensional model, convergence of the observables with respect to the number of bath modes and surface layers can furthermore expected to be reached easier since the wave packet is subject to stronger gradients, i.e. the excited state dynamics are faster.
- Vibrational relaxation for the ground state dynamics should be included. This could be accomplished by employing a second bath modeling the surface phonons. While vibrational relaxation due to the difference in timescales can assumed to be insignificant for the excited state dynamics, the wave packet leaves the ground state potential well on the timescale of picoseconds. Vibrational relaxation can therefore start to play a role.
- The dynamical simulations of the Surrogate Hamiltonian should be supplemented by a detailed *ab initio* calculation of the dipole charge of nickel oxide. While an estimate based on CI calculations has been given in [133], a more accurate investigation would further reduce the uncertainty of this parameter in the Surrogate Hamiltonian approach.
- It should be investigated in more detail whether a substrate-mediated excitation is feasible within the Surrogate Hamiltonian. This would allow for a direct comparison of the currently applied semi-direct and a purely substrate-mediated excitation mechanism. It would furthermore permit a theoretical investigation of the DIET to DIMET transition.

In addition to these remarks, it should be noted that the description of a two-pulse experiment as currently performed [104] is comparatively straightforward within the Surrogate Hamiltonian. It requires, however, the characterization of a third electronic state describing the NO molecule, an unbound electron and the positively charged surface.

The mechanism regulating the intensity of peaks in the velocity distributions could not be determined: It remains a challenge for future theoretical as well as experimental work.



# Chapter 8

## Summary

The theoretical study of condensed phase quantum systems interacting with their environment has been the subject of this thesis. This class of problems constitutes a great challenge to theory – the non-separability of the timescales of all processes involved requires the development of new methodological tools. One example of new approaches addressing quantum dissipative dynamics is represented by the Surrogate Hamiltonian method. Its further development and application to phenomena under current intensive experimental investigation have been presented.

The single dissipative processes were classified and discussed in the first part of this thesis. In particular, a model of dephasing was introduced into the Surrogate Hamiltonian method. This is of importance in future work related to coherent control and quantum computing. In regard to these subjects, it is a great advantage of the Surrogate Hamiltonian over other available methods that it relies on a spin, i.e. a fully quantum mechanical description of the bath.

The next step consisted in the application of the Surrogate Hamiltonian method to a standard model of charge transfer in condensed phase: two nonadiabatically coupled harmonic oscillators immersed in a bath. While this model is still an oversimplification of, for example, a molecule in solution, it served as testing ground for the theoretical description of a prototypical ultrafast pump-probe experiment. The Surrogate Hamiltonian approach succeeded to reproduce all qualitative features of such an experiment and allowed to identify shortcomings of previous treatments. It was found, in

particular, that the dynamics generated by the interaction with the laser pulse and the nonadiabatic transfer cannot be separated.

Ultrafast experiments attempt to monitor reaction dynamics on a femtosecond timescale. This can be captured particularly well by the Surrogate Hamiltonian as a method based on a time-dependent picture. The combination of the numerical solution of the time-dependent Schrödinger equation with the phase space visualization given by the Wigner function allowed for a step by step following of the sequence of events in a charge transfer cycle in a very intuitive way. The utility of the Surrogate Hamiltonian was furthermore significantly enhanced by the incorporation of the Filter Diagonalization method. This allowed the obtainment of frequency domain results from the dynamics which can be converged within the Surrogate Hamiltonian approach only for comparatively short times. The application of the Surrogate Hamiltonian to this rather simple model of charge transfer revealed its potential when combined with an *ab initio* treatment of the electronic degrees of freedom.

Such a consistent treatment where *all* aspects of a given problem are described with the same level of rigor has been pursued in the second part of this thesis. The example studied has been laser induced desorption of small molecules from oxide surfaces. While potential energy surfaces from first principles were obtained in previous work, the description of the photodesorption dynamics, in particular of the excitation and relaxation processes, has so far in general been semi-phenomenological. In the standard method of wave packet jumping according to Gadzuk, for example, the desorption probability is used to adjust the lifetime of the electronic excitation.

In contrast to this, a microscopic model of the interaction between the excited adsorbate-substrate complex and substrate electron-hole pairs which causes the finite lifetime was developed. The picture is based on a simplified description of the electron-hole pairs as a bath of dipoles, and a dipole-dipole interaction between system and bath. All parameters were connected to results from electronic structure calculations. This direct derivation of the coupling constants from first principles is different from employing the spectral density and possibly classical molecular dynamics which is the standard procedure for harmonic baths.

The obtained desorption probabilities and desorption velocities were *simultaneously* found to be in the right range as compared to the experimental results. The Surrogate Hamiltonian approach therefore allowed for a complete description of the photodesorption dynamics on an *ab initio* basis for the first time. This opens up the way for the theoretical treatment of ultrafast two pulse studies as currently investigated experimentally.

Since the focus of this thesis has been the development of the Surrogate Hamiltonian method, the description has been restricted to one nuclear degree of freedom. In a next step, a second degree of freedom, the tilt angle of the molecule with respect to the surface normal, should be included into the description. The coupling between the angle and the distance is, as shown in previous work, one possible cause of the experimentally observed bimodality of the velocity distributions. It can therefore be expected, that a two-dimensional Surrogate Hamiltonian treatment will yield results comparable to experiment regarding the shape as well as the the range of observed velocities. Due to the completely mechanistic picture, it might moreover elucidate the origin of the two desorption channels and point to possible control mechanisms.

Theoretical physics relies on the separability and abstractability of the phenomenon of interest from the rest of the world. This might be one reason why dissipative processes, which connect the carefully separated "system", particularly if it is quantum, with its surroundings, has long been overlooked. Dissipation is, however, such a fundamental phenomenon that it eventually demanded entrance into the world of theoretical quantum physics. It succeeded thanks to experimenters who developed techniques monitoring quantum dynamics in real-time, and it is now up to theoreticians to find adequate tools to keep up with the experimental developments. The Surrogate Hamiltonian method has been shown in this thesis to be one possible candidate to help model phenomena from quantum control to surface science.



# Appendix A

## The representation and propagation of a wave function

The time-dependent Schrödinger equation,

$$i\frac{\partial}{\partial t}|\Psi(t)\rangle = \hat{\mathbf{H}}|\Psi(t)\rangle , \quad (\text{A.1})$$

shall be solved. To this end, a representation of the state  $|\Psi\rangle$  and of the operator  $\hat{\mathbf{H}}$  needs to be chosen and the action of  $\hat{\mathbf{H}}$  onto  $|\Psi\rangle$  needs to be defined. One possibility to solve Eq. (A.1) consists in finding a numerical approximation to the formal solution

$$|\Psi(t)\rangle = \mathbf{e}^{-i\hat{\mathbf{H}}t}|\Psi(0)\rangle . \quad (\text{A.2})$$

The two approximations which were employed in this thesis are the Chebyshev and the split-operator methods [134, 135, 136].

### A.1 The grid representation

Representing the state  $|\Psi(t)\rangle$  in the Schrödinger picture as a wave function  $\langle q|\Psi(t)\rangle = \Psi(q, t)$  on a grid in coordinate space is an extremely flexible choice. It allows for the treatment of a broad class of problems independent of the shape of the potential energy surfaces.

A wave function  $\Psi(q)$  can be approximated by a finite set of analytical

functions (see for example [135, 137])

$$\Psi(q) \approx \sum_{n=1}^{N_f} a_n g_n(q) . \quad (\text{A.3})$$

The expansion coefficients are determined by matching the approximation to the true wave function at  $N_g$  grid points  $q_j$ ,

$$\Psi(q_j) \equiv \sum_{n=1}^{N_g} a_n g_n(q_j) . \quad (\text{A.4})$$

If the  $g_n(q)$  are orthogonal functions and  $N_f = N_g$ , the expansion coefficients are given by

$$a_n = \sum_{j=1}^{N_f} \Psi^*(q_j) g_n(q_j) . \quad (\text{A.5})$$

A special case of the orthogonal representation is the Fourier method [135]. The functions  $g_n(q)$  are then chosen as plain waves,

$$g_n(q) = e^{2\pi i n q / L}, \quad n = -\left(\frac{N_f}{2} - 1\right), \dots, 0, \dots, \frac{N_f}{2}, \quad (\text{A.6})$$

with equally spaced sampling points  $q_j = (j - 1)\Delta q$  on a grid of length  $L$ . The approximation of the wave function becomes

$$\Psi(q) \approx \sum_{n=-(N_f/2-1)}^{N_f/2} a_n e^{2\pi i n q / L}, \quad (\text{A.7})$$

and the Fourier expansion coefficients,

$$a_n = \frac{1}{N_f} \sum_{j=1}^{N_f} \Psi(q_j) e^{-2\pi i n q_j / L}, \quad (\text{A.8})$$

represent the amplitude of the wave function in Fourier, or momentum, space. The grid distance in momentum space is given by  $\Delta p = 2\pi/L$ , the grid distance in coordinate space is related to the largest representable momentum by  $\Delta q = \pi/p_{max}$ .

The power of the Fourier method results from the fact that the operators entering the Hamiltonian can each be applied locally in coordinate or momentum space, and the transformation connecting these two representations

is the fast Fourier transform with its favorable scaling of  $N_f \log(N_f)$ . All operator functions depending on  $\hat{\mathbf{q}}$  like the potential energy operator correspond to diagonal matrices in coordinate space, and the wave function  $\Psi(q_j)$  can simply be multiplied by them. The kinetic energy operator as well as other operator functions depending on  $\hat{\mathbf{p}}$  can be applied by multiplication in momentum space,

$$T(p_j)\Psi(p_j) = \frac{p_j^2}{2m}\Psi(p_j) \quad (\text{A.9})$$

where  $m$  is mass and  $p_j$  are the momentum space grid points.

## A.2 The Chebychev propagator

The Chebychev method [138] employs the idea of a polynomial expansion of the time evolution operator,

$$\hat{\mathbf{U}}(t) = e^{-i\hat{\mathbf{H}}t} \approx \sum_{n=0}^N a_n P_n(-i\hat{\mathbf{H}}t) \quad (\text{A.10})$$

with complex Chebychev polynomials  $P_n(\hat{\mathbf{X}}) = \Phi_n(\hat{\mathbf{X}})$  as basis set. The complex Chebychev polynomials are defined in the range  $[-i, i]$ . Therefore the Hamiltonian has to be renormalized by its spectral range  $\Delta E = E_{max} - E_{min}$ , and for efficiency it should be shifted such that the spectral range is  $[-1, 1]$ :

$$\hat{\mathbf{H}}_{norm} = 2 \frac{\hat{\mathbf{H}} - \mathbb{I}(\frac{1}{2}\Delta E + V_{min})}{\Delta E} . \quad (\text{A.11})$$

Inserting Eq. (A.11) into Eq. (A.10) leads to

$$\Psi(t) = \hat{\mathbf{U}}(t)\Psi(0) \approx e^{-i(\frac{1}{2}\Delta E + V_{min})t} \sum_{n=0}^N a_n(\alpha) \Phi_n(-i\hat{\mathbf{H}}_{norm})\Psi(0) \quad (\text{A.12})$$

with the argument  $\alpha = \Delta Et/2$ . The expansion coefficients are related to the Bessel functions of the first kind  $J_n$ :

$$a_n(\alpha) = \int_{-i}^i dx \frac{e^{i\alpha x} \Phi_n(x)}{\sqrt{1-x^2}} = 2J_n(\alpha) , \quad (\text{A.13})$$

and the Chebychev polynomials are calculated using the recursion relation

$$\begin{aligned} \Phi_{n+1}(x) &= 2x\Phi_n(x) - \Phi_{n-1}(x) , \\ \Phi_0(x) &\equiv 1 , \quad \Phi_1(x) = x . \end{aligned} \quad (\text{A.14})$$

The error of the Chebychev method is uniformly distributed over the whole range of eigenvalues of  $\hat{\mathbf{H}}$  and can be reduced to machine precision due to a property of the Bessel functions  $J_n(\alpha)$ : When the order  $n$  becomes larger than the argument  $\alpha$ ,  $J_n$  decreases exponentially fast. The number of terms required in the expansion is therefore determined by the spectral range of the Hamiltonian and by the desired time step. It should be noted that the time step does not affect the accuracy of the method. The Chebychev method is therefore suited for large time steps, and a practical lower limit imposed by numerical efficiency is about 40 terms in the expansion [135]. The Chebychev propagator has been used throughout this thesis with the exception of the Monte Carlo wave function approach (cf. Section 6.3) for which it is not efficient.

### A.3 The split propagator

For a small time step, the exponential in the formal solution Eq. (A.2) can be approximated to third order by [139]

$$e^{-i\hat{\mathbf{H}}\Delta t} = e^{-\frac{i}{2}\hat{\mathbf{T}}\Delta t} e^{-i\hat{\mathbf{W}}\Delta t} e^{-\frac{i}{2}\hat{\mathbf{T}}\Delta t} + \mathcal{O}(\Delta t^3). \quad (\text{A.15})$$

$\hat{\mathbf{T}}$  is the kinetic energy operator which shall be applied in momentum space and  $\hat{\mathbf{W}}$  the operator applied in coordinate space,

$$\hat{\mathbf{W}} = \begin{pmatrix} V_g(\hat{\mathbf{Q}}) & \hat{\boldsymbol{\mu}}E(t) \\ \hat{\boldsymbol{\mu}}E^*(t) & V_e(\hat{\mathbf{Q}}) \end{pmatrix}$$

with  $V_g$ ,  $V_e$  the potential energy operators for the electronic ground and excited state,  $\hat{\boldsymbol{\mu}}$  the transition dipole operator, and  $E(t) = E_0 S(t) \exp(i\omega_L t)$  the electric field of the laser pulse with shape  $S(t)$ . Since  $\hat{\mathbf{W}}$  is not diagonal in the electronic degree of freedom, a unitary transformation [136]

$$U = \frac{1}{\sqrt{2}} \begin{pmatrix} 1 & -\frac{S(\Delta t)}{|S(\Delta t)|} e^{i\omega_L \Delta t} \\ \frac{S^*(\Delta t)}{|S(\Delta t)|} e^{i\omega_L \Delta t} & 1 \end{pmatrix} \quad (\text{A.16})$$

diagonalizing  $\hat{\mathbf{W}}$  is inserted into Eq. (A.15):

$$e^{-i\hat{\mathbf{H}}\Delta t} \approx e^{-\frac{i}{2}\hat{\mathbf{T}}\Delta t} \hat{\mathbf{U}}^{-1} \hat{\mathbf{U}} e^{-i\hat{\mathbf{W}}\Delta t} \hat{\mathbf{U}}^{-1} \hat{\mathbf{U}} e^{-\frac{i}{2}\hat{\mathbf{T}}\Delta t}.$$



Resolving the algebra leads to

$$\mathbf{e}^{-i\hat{\mathbf{H}}\Delta t} \approx \mathbf{e}^{-\frac{i}{2}\hat{\mathbf{T}}\Delta t} \frac{1}{2}\hat{\mathbf{W}}' \mathbf{e}^{-\frac{i}{2}\hat{\mathbf{T}}\Delta t}, \quad (\text{A.17})$$

where

$$\hat{\mathbf{W}}' = \begin{pmatrix} (\hat{\mathbf{U}}_g + \hat{\mathbf{U}}_e) \cos(A) + (\hat{\mathbf{U}}_g - \hat{\mathbf{U}}_e) & -i(\hat{\mathbf{U}}_g + \hat{\mathbf{U}}_e) \sin(A) \frac{S}{|S|} \mathbf{e}^{i\omega_L \Delta t} \\ -i(\hat{\mathbf{U}}_g + \hat{\mathbf{U}}_e) \sin(A) \frac{S^*}{|S|} \mathbf{e}^{-i\omega_L \Delta t} & (\hat{\mathbf{U}}_g + \hat{\mathbf{U}}_e) \cos(A) - (\hat{\mathbf{U}}_g - \hat{\mathbf{U}}_e) \end{pmatrix}$$

with  $\hat{\mathbf{U}}_{g/e} = \mathbf{e}^{-i\hat{\mathbf{V}}_{g/e}\Delta t}$  and  $A = \hat{\mu}E_0|S(\Delta t)|\Delta t$ .

If no interaction with a pulse is considered, it is more efficient to split the exponential such that only one application of  $\exp(\hat{\mathbf{T}})$  is involved since it requires a FFT into momentum space and an inverse FFT back into coordinate space.

The split propagator is very efficient, but it requires a small time step  $\Delta t$  and it might perturb the phase of the wave function. [140] It is therefore best suited for the Monte Carlo wave function method (cf. Chapter 6.3).

## A.4 Eigenfunctions through imaginary time propagation

The Fourier method can also be used to compute eigenvalues and eigenfunctions of a given Hamiltonian [134, 141]. To this end the imaginary time  $\tau = it$  is introduced into the formal solution of the time-dependent Schrödinger equation,

$$|\Psi(\tau)\rangle = \mathbf{e}^{-\hat{\mathbf{H}}\tau} |\Psi(0)\rangle. \quad (\text{A.18})$$

An arbitrary initial guess wave function can be expanded into eigenstates of the Hamiltonian,  $|\Psi(0)\rangle = \sum_n c_n |\varphi_n\rangle$ . For  $\tau \rightarrow \infty$ , only the ground state component of the initial guess will survive. The imaginary time propagation, Eq. (A.18), is obviously not unitary, the wave function therefore needs to be renormalized during propagation.

The choice of the initial guess determines the convergence of the method. The energy expectation value,  $\langle \Psi(\tau) | \hat{\mathbf{H}} | \Psi(\tau) \rangle$ , or the standard deviation of energy,  $\langle \Psi(\tau) | \hat{\mathbf{H}}^2 | \Psi(\tau) \rangle - \langle \Psi(\tau) | \hat{\mathbf{H}} | \Psi(\tau) \rangle^2$ , which is a measure of the purity of the eigenstate, is monitored to determine convergence. Higher eigenstates

than the ground state can be calculated by projecting out lower lying eigenstates, i.e. to obtain the  $n$ th eigenstate a new Hamiltonian,

$$\hat{\mathbf{H}}_n = \hat{\mathbf{H}} - \sum_{i=0}^{n-1} |\varphi_i\rangle\langle\varphi_i| \quad (\text{A.19})$$

can be defined and used in Eq. (A.18). Since all lower lying eigenstates  $|\varphi_i\rangle$  need to be stored to compute  $|\varphi_n\rangle$ , this is feasible only for a few eigenstates. Furthermore, long propagation times  $\tau$  are necessary to differentiate between nearly degenerate states due to a time-energy uncertainty relation.

However, imaginary time propagation with the Hamiltonian, Eq. (A.19), represents a special choice of the more general Filter Diagonalization approach (cf. Appendix C.2). The basic idea of Filter Diagonalization to extract eigenvalues and eigenstates of a given operator consists of a combined use of applying a filter and algebraic diagonalization [142]. The correlations present in the initial guess are eliminated through a short-time filter between distant eigenstates and by diagonalization between closely lying eigenstates [142, 143]. Imaginary time propagation can be viewed as a long term filter, with no diagonalization part. It is therefore less efficient than full filter diagonalization, but it requires only minor changes of existing programs.

## A.5 Spectral range

The spectral range of a Hamiltonian  $\hat{\mathbf{H}}$ ,

$$\Delta E = E_{max} - E_{min} , \quad (\text{A.20})$$

or more precisely the time-energy phase space volume  $\Delta E \Delta t$  with propagation time step  $\Delta t$  is a measure of the numerical effort required to solve the problem described by  $\hat{\mathbf{H}}$  [135]. If the Chebychev propagator (cf. Appendix A.2) is used for propagating the wave function, the spectral range of the Hamiltonian is explicitly needed to compute the number of terms in the expansion Eq. (A.12). In grid representation the maximum momentum  $p_{max}$  is determined by the grid spacing in coordinate  $\Delta q$  (cf. Appendix A.1). For one electronic state the spectral range is then simply given by

$$\Delta E = \frac{p_{max}^2}{2m} + V_{max} - V_{min} = \frac{\pi^2}{2m\Delta q} + V_{max} - V_{min} \quad (\text{A.21})$$

with mass  $m$  and  $V_{max}$  and  $V_{min}$  the maximum and minimum of potential energy. If the Hamiltonian contains more than one electronic state and off-diagonal matrix elements in the electronic basis, the spectral range needs to be calculated numerically. However, an explicit diagonalization of the Hamiltonian yielding *all* eigenvalues of  $\hat{\mathbf{H}}$  can be avoided, since only the smallest and largest eigenvalue are needed. An idea similar to the one of imaginary time propagation presented in the previous section can be employed [144]: if the Hamiltonian acts on an initial guess wave function many times, only components of the ground state or of the highest eigenstate survive in the wave function. The wave function needs to be renormalized after each iteration to avoid numerical overflow. If one of the desired eigenstates with eigenvalue  $\lambda_1$  has been obtained, a shifted Hamiltonian  $\hat{\mathbf{H}}' = \hat{\mathbf{H}} - \lambda_1$  can be defined. Repeating the iteration procedure with  $\hat{\mathbf{H}}'$  yields the second bound  $\lambda_2$  and the spectral range is given by

$$\Delta E = |\lambda_2 - \lambda_1|. \quad (\text{A.22})$$

This method to compute the spectral range has been applied for all system-bath calculations (cf. Chapters 3, 4 and 7) and for the calculations with diabatic coupling (cf. Section 6.2).

## A.6 Grid change

The simulations of laser induced desorption presented in Chapters 6 and 7 require comparatively long propagation times since upon deexcitation to the electronic ground state the wave packet splits into a part trapped in the potential well and a desorbing part. While the excitation-deexcitation cycle happens on the timescale of femtoseconds, the separation into trapped and desorbing part takes place in picoseconds. The desorbing partial wave packet has gained momentum in the deexcitation process which lets it travel toward larger distances, i.e. toward the finite boundary of the coordinate grid. If parts of the wave packet hit the (upper) boundary they are transferred to the lower boundary due to periodic boundary conditions. This leads to numerical artifacts. Observables of interest for desorption experiments are expectation values of operators in the asymptotic region of the ground state potential,

$V_g^A(Z) \approx 0$ . It is therefore not possible to employ absorbing boundary conditions [145] since then the information of interest is lost.

The simulations demand a coordinate grid extending from small to large distances, and possibly occurring high momenta require a small grid spacing (cf. Appendix A.1). To avoid grids with a huge number of grid points the grid change method by Heather and Metiu [146] has been employed. The wave function is then simultaneously propagated on two grids with a comparatively small number of grid points,

$$\Psi(Z, t) = \Psi_I(Z, t) + \Psi_A(Z, t) . \quad (\text{A.23})$$

Grid  $I$  represents the interaction region for which  $V_I(Z) \neq 0$  and grid  $A$  represents the asymptotic region. This separation of the wave function is possible due to the linearity of the Schrödinger equation. Parts of the wave function which reach the region in which the two grids overlap are transferred to the asymptotic grid

$$\begin{aligned} \Psi_A(Z, t) &= \Psi_A(Z, t - \Delta t) + f_{trans}(Z)\Psi_I(Z, t) , \\ \Psi_I(Z, t) &= (1 - f_{trans}(Z))\Psi_I(Z, t) \end{aligned} \quad (\text{A.24})$$

with transfer function

$$f_{trans}(Z) = 1 - \frac{1}{1 + \exp(a(Z - Z_0))} . \quad (\text{A.25})$$

The choice of the transfer function is rather arbitrary provided that it monotonously rises from zero to one. It determines, however, the error which is introduced by the grid change: a steep transfer function will result in numerical artifacts. A more detailed account has been given in [4, 3].

The grid change method has several advantages. It reduces the numerical effort of propagation since the wave function on the asymptotic grid can be propagated analytically by multiplication of a phase factor,  $\exp(-i\frac{P^2}{2m}\Delta t)$ , in momentum space. The number of grid points and the grid spacing do not have to be identical for the two grids. Since the momenta which occur in the asymptotic region are considerably smaller than those in the interaction region,  $p_{max}$  can be considerably smaller and  $\Delta Z$  larger. Furthermore, a representation of the wave function in coordinate space is not necessary since only expectation values which are calculated in momentum space shall be

obtained [4]. The number of grid points of the asymptotic grid is therefore only determined by the maximum representable momentum.

However, the grid change method also brings about some disadvantages. In its original version [146] it has been used only for analysis once the propagation was finished. Since for laser induced desorption simulations it is used for avoiding large grids and hence needs to be applied after every time step [3, 4] it leads to artificial interferences as long as parts of the wave packet stay in the region where both grids overlap. These artifacts emerge as oscillations in the total norm. They can be minimized by an appropriate choice of width and location of the transfer function (parameters  $a$  and  $Z_0$  in Eq. (A.25)). The grid change furthermore distorts the phase of the wave packet ruling out a phase space analysis (cf. Appendix C.1) of the wave function. Since only momentum space and no coordinate space observables are of interest in the asymptotic region, this is a minor annoyance.

Alternatives to the grid change method are represented by grid mapping [147] and flux analysis [127]. Grid mapping [147] avoids the distortion of the phase of the wave function. It introduces additional Fourier transforms to map between a grid with constant spacing and one with variable spacing. The variable grid spacing is determined by the largest possible total energy. However, grid mapping was revealed to be inefficient for laser induced desorption experiments due to large momenta in the interaction region [4]. It has therefore not been employed.

The grid change method was used for simulations presented in Chapters 6 and 7.



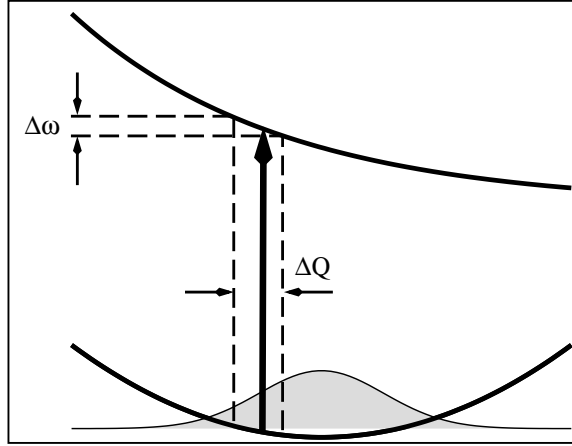
## Appendix B

# Perturbational treatment of weak fields: The window operator

The total energy which is absorbed of a pulse is related to the change in electronic ground state population [59],

$$\Delta E = -\hbar\omega_L\Delta N_g, \quad (\text{B.1})$$

where  $\omega_L$  is the frequency of the pulse.  $\Delta N_g$  can be determined by solving the time-dependent Schrödinger equation. For the description of a pump-probe



experiment this can be rather time-consuming since a separate simulation needs to be run for every time delay between pump and probe pulse. If the probe field is weak, however, perturbation theory can be employed. The total absorption is then represented by a window operator  $\hat{\mathbf{W}}$  [148, 62],

$$\Delta E \approx -\hbar\omega_L \text{tr}_S \{ \hat{\rho}_S(t_p) \cdot \hat{\mathbf{W}} \}, \quad (\text{B.2})$$

the explicit expression of which will be given below.  $\hat{\rho}$  denotes the system density operator, and  $t_p$  will turn out to be the time of maximum intensity

of the pulse. The physical concept of the window operator is to collapse the observation process which is completed in a time proportional to the pulse width  $\tau_p$  to a single instant in time  $t_p$ . The finite width in time which corresponds to a finite width in frequency  $\Delta\omega$  (the band width of the pulse) is then transformed into a finite width in coordinate  $\Delta Q$  via the resonance condition given by the electronic potentials (cf. Fig. B.1). This collapse of the measurement process assumes that the nuclear motion is frozen during the observation, i.e. that the excitation is impulsive, and that the window operator  $\hat{\mathbf{W}}$  is independent of the state of the system,  $\hat{\rho}_S(t_p)$  which is true when the intensity of the pulse goes to zero [62].

The expression for the window operator can be derived by perturbation theory. The initial state is taken to be the ground state wave packet at a time  $c\tau_p$  before the probing time  $t_p$  at which the field is still approximately zero, and  $c$  is a constant. The change in norm on the ground state can be measured on the excited state at a final time  $t_p + c\tau_p$  due to norm conservation,

$$\Delta N_g = -\Delta N_e = -\langle \psi_e(t_p + c\tau_p) | \psi_e(t_p + c\tau_p) \rangle. \quad (\text{B.3})$$

The excited state wave packet at the final time is given by

$$|\psi_e(t_p + c\tau_p)\rangle = i \int_{-c\tau_p}^{c\tau_p} d\tau e^{-i\hat{\mathbf{H}}_e(c\tau_p - \tau)} \hat{\boldsymbol{\mu}}_{tr} E^*(t) e^{-i\hat{\mathbf{H}}_g(\tau + c\tau_p)} |\psi_g(t_p - c\tau_p)\rangle, \quad (\text{B.4})$$

where  $E(t)$  is the field of the laser pulse,  $\hat{\boldsymbol{\mu}}_{tr}$  is the transition dipole operator, and  $\hat{\mathbf{H}}_g$  and  $\hat{\mathbf{H}}_e$  are the nuclear Hamiltonians on the electronic ground and excited state, respectively. Assuming that the wave packet does not move during the observation, i.e.  $[\hat{\mathbf{H}}_g, \hat{\mathbf{H}}_e]_- \approx 0$  for the integrand, Eq. (B.4) can be simplified to

$$|\psi_e(t_p + c\tau_p)\rangle = e^{-i\hat{\mathbf{H}}_e(c\tau_p)} \left\{ i \int_{t_p - c\tau_p}^{t_p + c\tau_p} d\tau e^{-i2\hat{\Delta}(\hat{\mathbf{Q}})\tau} \hat{\boldsymbol{\mu}}_{tr} E_0 S^*(\tau) \right\} e^{-i\hat{\mathbf{H}}_g(c\tau_p)} |\psi_g(t_p - c\tau_p)\rangle, \quad (\text{B.5})$$

where the difference potential  $\Delta(\hat{\mathbf{Q}}) = \frac{1}{2}(V_e(\hat{\mathbf{Q}}) - V_g(\hat{\mathbf{Q}}) - w_L)$  and the shape of the pulse  $E(t) = E_0 S(t) e^{i\omega_L t}$  have been introduced. Multiplying Eq. (B.5) by  $e^{+i\hat{\mathbf{H}}_e c\tau_p}$  from the left, the ground and excited state wave functions can be



synchronized to a single time  $t_p$ ,

$$|\psi_e(t_p)\rangle = \left\{ i \int_{t_p - c\tau_p}^{t_p + c\tau_p} d\tau e^{-i2\hat{\Delta}(\hat{\mathbf{Q}})\tau} \hat{\boldsymbol{\mu}}_{tr} E_0 S^*(\tau) \right\} |\psi_g(t_p)\rangle. \quad (\text{B.6})$$

The window operator is therefore constructed from the expression in the brackets in Eq. (B.6). If the pulse shape is Gaussian,  $S(t) = \exp(-\frac{(t-t_p)^2}{2\tau_p^2})$ , the integral can be solved leading to

$$\hat{\mathbf{W}}(\hat{\mathbf{Q}}, \hat{\mathbf{Q}}') = \pi(\tau_p E_0)^2 e^{-2\hat{\Delta}^2(\hat{\mathbf{Q}})\tau_p^2} \cdot \hat{\boldsymbol{\mu}}_{tr}^2(\hat{\mathbf{Q}}) \delta(\hat{\mathbf{Q}} - \hat{\mathbf{Q}}') \cdot |\alpha\rangle\langle\alpha|, \quad (\text{B.7})$$

where  $|\alpha\rangle$  labels the electronic state. The width of the window operator – or the precision of the coordinate measurement – is determined by the difference potential  $\hat{\Delta}(\hat{\mathbf{Q}})$ . For chirped pulses the window operator is modified [62], and a similar expression can be obtained for a *sinc*-shaped pulse [59].

With the use of the window operator, a single simulation suffices to calculate the pump-probe signal for all time delays between the pulses. The window operator has been applied in the calculation of transient absorption ( $|\alpha\rangle = |g\rangle$ ) and emission ( $|\alpha\rangle = |e\rangle$ ) signals in Chapters 3 and 4.



# Appendix C

## Tools for data analysis

### C.1 The Wigner function

The wave function describing the state of a quantum system is characterized by its absolute value and by its phase. While the density, i.e. the wave function squared and not the wave function itself is measured, both value and phase determine the measurement. Since in coordinate representation the phase of the wave function is related to momentum, a phase space picture is a useful tool to visualize a quantum state and gain some intuition for it. Historically phase space distributions have been introduced in the context of correspondence between quantum and classical mechanics. [24]

The Wigner function [24, 149] was the first quantum mechanical phase space distribution to be considered, it is given by

$$W(P, Q) = \frac{1}{2\pi} \int_{-\infty}^{\infty} dy \hat{\rho}(Q - y/2, Q + y/2) e^{iPy} \quad (\text{C.1})$$

for a density operator  $\hat{\rho}$ . A number of phase space distribution functions can be defined. The Wigner function is determined uniquely by the following requirements: it shall have real values, it shall give when integrated with respect to  $P$  or  $Q$  the correct probability densities and expectation values, it shall be Galilei invariant and invariant with respect to space and time reflections, and it shall obey the classical equation of motion if  $V \equiv 0$ . The Wigner function can be derived from a classical phase space function applying Weyl, i.e. symmetric ordering of operators [149].

Unlike a classical probability density, the Wigner function can have neg-

ative values. This is a result of Heisenberg's uncertainty principle between coordinate  $Q$  and momentum  $P$ . [24] The existence of these negative values indicates regions in phase space which are dominated by pure quantum phenomena, i.e. by correlations between the conjugated variables coordinate and momentum. If a coarse graining procedure is applied to the Wigner function, that is  $W(P, Q)$  is convoluted with a Gaussian  $h(Q, P)$  in phase space,

$$h(Q, P) = \frac{1}{\pi\hbar} \int dq dp W(q, p) e^{-\frac{(q-Q)^2}{2\Delta Q^2} - \frac{(p-P)^2}{2\Delta P^2}} \quad (\text{C.2})$$

with width  $\Delta Q = \Delta P = \sqrt{\hbar/2}$ , the Wigner function is smeared out over a phase space volume  $\Delta Q \Delta P = \hbar/2$  [150]. The resulting Husimi distribution function is non-negative for all  $P$  and  $Q$ . It does not, however, give correct expectation values when integrated over  $P$  or  $Q$ , respectively [149].

The equation of motion for  $W(Q, P)$  was shown to be the classical equation of motion plus quantum corrections which are of the order of  $\hbar^2$  and of the third derivative of the potential with respect to  $Q$  [24]. Therefore identical classical and quantum equations of motion are obtained for the harmonic oscillator indicating that the harmonic oscillator is not a generic quantum system.

In grid representation the density operator  $\hat{\rho}(Q, Q')$  corresponds to a matrix whose values  $\rho_{ij}$  are given at grid points  $Q_i, Q_j$ . The integral in Eq. (C.1) is then performed counter-diagonally. A schematic illustration is given in Fig. C.1. Grid points at can either be picked s.t. the red lines of the Wigner function matrix cross the diagonal in  $Q_i$  as in Fig. C.1 or s.t. they cross in  $Q_i + \frac{1}{2}\Delta Q$ . The counter-diagonal is written into a vector  $v$  at each point  $Q_i + \frac{1}{2}\Delta Q$ . Elements in the region where the two squares in Fig. C.1 do not overlap are filled with zeros. The density matrix must therefore die off sufficiently fast toward the grid boundaries, otherwise numerical artifacts are introduced. The vector  $v$  furthermore needs to be shuffled,  $v(1, \dots, \frac{N}{2}, \frac{N}{2} + 1, \dots, N) \longleftrightarrow v(\frac{N}{2} + 1, \dots, N, 1, \dots, \frac{N}{2})$ , to avoid artificial interferences in the Fourier transform. The scheme depicted in Fig. C.1 makes only use of half of the density matrix elements, i.e. phase space resolution is lost. This can be avoided leading, however, to a doubled dimension of the matrix corresponding to the Wigner function. The desired graphical resolution in displaying the Wigner function and the numerical effort to compute it should

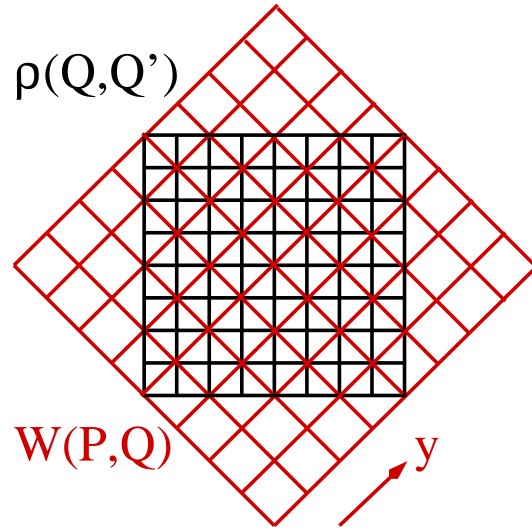


Figure C.1: The calculation of the Wigner function (red) for a density matrix  $\rho(Q, Q')$  (black). The arrow indicates the direction of integration.

therefore be considered when making a choice about the dimension of the Wigner function matrix.

As an example, Fig. C.2 shows the density matrix and Wigner function of the first excited state of the harmonic oscillator while a Schrödinger cat state is displayed in Fig. C.3. The color corresponds to the sign with red indicating positive and blue negative values. The height of the peaks shows the absolute value. The Wigner function of the harmonic oscillator ground state is simply a two-dimensional Gaussian. Excited states, however, exhibit negative values of the Wigner function. Fig. C.3 illustrates that a quantum mechanical superposition must be distinguished from an incoherent ensemble. Even if the two Gaussian wave packets do not overlap, interference is observed. The coherence of the state is represented by off-diagonal density matrix elements (cf. Fig. C.3, left) and negative values of the Wigner function (blue features in Fig. C.3, right).

The Wigner function can also be defined in time and energy domains [151, 152] to visualize, for example, the phase relation of a chirped pulse.

The Wigner function of the reduced density operator, Eq. (3.3), either on the ground or excited electronic surface, has been employed in Chapters 3 and 4.

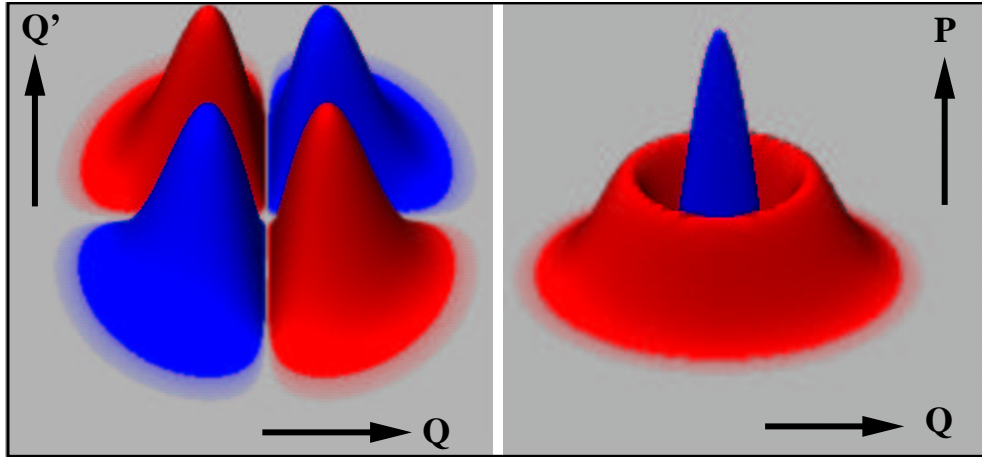


Figure C.2: Density matrix (left) and Wigner function (right) of the first excited state of the harmonic oscillator.

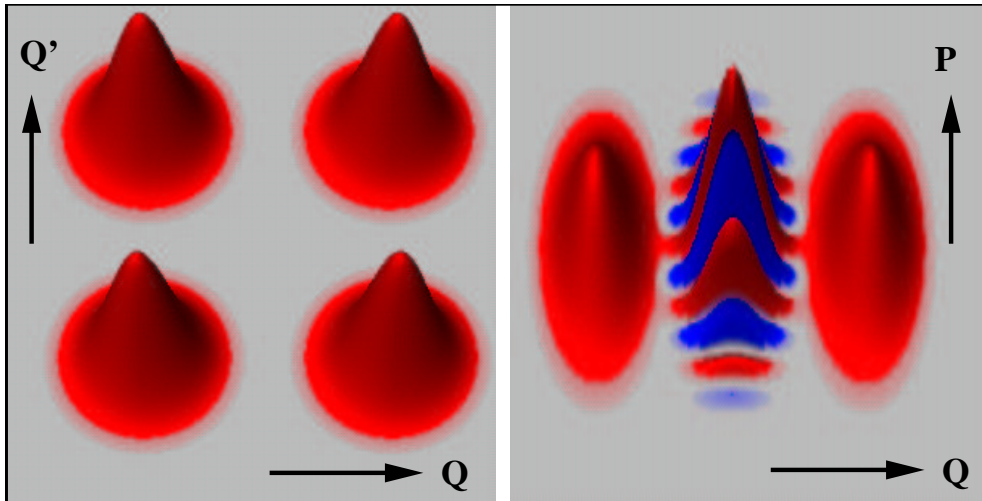


Figure C.3: Density matrix (left) and Wigner function (right) of a superposition of two Gaussian wave packets, a so called Schrödinger cat state.

## C.2 Filter Diagonalization

The convergence of the Surrogate Hamiltonian method is significantly faster for short propagation times. In order to obtain long time observables or frequency domain results which depend on them, the short-time observables have to be extrapolated. The Filter Diagonalization technique [142, 153, 154, 155] fits the short-time time-series to a model which then can be used for extrapolation.

The method is based on the assumption that the time signal can be represented by a sum of complex exponentials:

$$S(t) = \sum_{j=1}^K d_j \exp(-i\omega_j t) , \quad (\text{C.3})$$

where  $\Omega_j = \text{Re}(\omega_j)$  is the desired frequency,  $\tau_j = 1/\text{Im}(\omega_j)$  is the decay rate and  $d_j$  is the complex amplitude. The number of real fitting parameters is  $4K$ . The parameters specifying the accuracy of the Filter Diagonalization method are the smallest allowed eigenvalue of the overlap matrix  $s_{min}$  and a convergence criterion  $\epsilon$  for the obtained frequencies [154]. They were chosen as  $s_{min} = 10^{-8}$  and  $\epsilon = 10^{-6} \dots 10^{-3}$ .

The data window needs to be chosen such that the signal within the window corresponds to a sum of complex, i.e. decaying exponentials. The data shows decay only as long as the results are converged with respect to the number of bath modes in the Surrogate Hamiltonian method. The decay is perturbed by recurrences. The choice of the data window is therefore related to the convergence of the Surrogate Hamiltonian method. The recurrences were found to cause a splitting of the frequency with the highest weight. Filter Diagonalization can hence be used as an additional tool to test the convergence.

Filter Diagonalization was performed using a **Fortran** program written by V.A. Mandelshtam. It has been employed in Chapters 3 and 4.





# Appendix D

## The Rotating wave approximation for a system coupled to a bath

If the interaction of a system with a time-dependent field is modeled, the timescale of the field determines the time-step which can be used in the simulations. It is therefore advantageous to 'drop' the rapidly oscillating part of the field by rotating the frame of reference such that the rapidly oscillating part does not enter the equations explicitly anymore.

The Hamiltonian for a system interacting with a bath whose two electronic states are coupled by a pulse is

$$\begin{aligned} \hat{\mathbf{H}} = & \begin{pmatrix} \hat{\mathbf{H}}_g & E(t)\hat{\boldsymbol{\mu}} \\ E^*(t)\hat{\boldsymbol{\mu}} & \hat{\mathbf{H}}_e \end{pmatrix} \otimes \mathbb{1}_B + \mathbb{1}_S \otimes \sum_j \varepsilon_j \hat{\mathbf{a}}_j^\dagger \hat{\mathbf{a}}_j + \\ & \begin{pmatrix} g(\hat{\mathbf{Q}}) & f(\hat{\mathbf{Q}}) \\ f^*(\hat{\mathbf{Q}}) & g(\hat{\mathbf{Q}}) \end{pmatrix} \otimes \sum_j (V_j^* \hat{\mathbf{a}}_j^\dagger + V_j \hat{\mathbf{a}}_j) . \end{aligned} \quad (\text{D.1})$$

The pulse is given by

$$E(t) = E_0 S(t) \exp(i\omega_L t) , \quad (\text{D.2})$$

where the time-dependence has been separated into a shape function  $S(t)$  and a part oscillating with the carrier frequency  $\omega_L$ . The system-bath coupling in Eq. (D.1) is of the most general form.

As in the case of a bare primary system coupled to a bath [59] a rotation operator,

$$\hat{\mathbf{R}}(\theta) = \exp(i\theta\hat{\mathbf{S}}_z) \otimes \mathbb{1}_B, \quad (\text{D.3})$$

with  $\theta = \omega_L t$  and

$$\hat{\mathbf{S}}_z = \frac{1}{2} \begin{pmatrix} -1 & 0 \\ 0 & 1 \end{pmatrix}, \quad \hat{\mathbf{S}}_+ = \begin{pmatrix} 0 & 0 \\ 1 & 0 \end{pmatrix}, \quad \hat{\mathbf{S}}_- = \begin{pmatrix} 0 & 1 \\ 0 & 0 \end{pmatrix}$$

can be defined. The following commutation relations will be needed:

$$[\hat{\mathbf{S}}_{\pm}, \hat{\mathbf{R}}(\theta)]_{-} = (1 - \exp(\pm i\theta)) \hat{\mathbf{S}}_{\pm} \hat{\mathbf{R}}(\theta). \quad (\text{D.4})$$

Now the rotated wave function is given by  $|\tilde{\Psi}\rangle = \hat{\mathbf{R}}|\Psi\rangle$ , and the equation of motion is:

$$\begin{aligned} i \frac{\partial}{\partial t} |\tilde{\Psi}\rangle &= i \frac{\partial \hat{\mathbf{R}}}{\partial t} |\Psi\rangle + \hat{\mathbf{R}} i \frac{\partial |\Psi\rangle}{\partial t} \\ &= -\omega_L \hat{\mathbf{S}}_z \hat{\mathbf{R}} |\Psi\rangle + \hat{\mathbf{R}} \hat{\mathbf{H}} |\Psi\rangle \\ &= -\omega_L \hat{\mathbf{S}}_z \hat{\mathbf{R}} |\Psi\rangle + \hat{\mathbf{H}} \hat{\mathbf{R}} |\Psi\rangle - [\hat{\mathbf{H}}, \hat{\mathbf{R}}]_{-} |\Psi\rangle. \end{aligned} \quad (\text{D.5})$$

Since

$$\begin{aligned} [\hat{\mathbf{H}}, \hat{\mathbf{R}}]_{-} &= \left( E^*(t) \hat{\boldsymbol{\mu}} + f^*(\hat{\mathbf{Q}}) \right) [\hat{\mathbf{S}}_+, \hat{\mathbf{R}}]_{-} + \left( E(t) \hat{\boldsymbol{\mu}} + f(\hat{\mathbf{Q}}) \right) [\hat{\mathbf{S}}_-, \hat{\mathbf{R}}]_{-} \\ &= \left( E^*(t) \hat{\boldsymbol{\mu}} + f^*(\hat{\mathbf{Q}}) \right) (1 - \exp(i\omega_L t)) \hat{\mathbf{S}}_+ \hat{\mathbf{R}} \\ &\quad + \left( E(t) \hat{\boldsymbol{\mu}} + f(\hat{\mathbf{Q}}) \right) (1 - \exp(-i\omega_L t)) \hat{\mathbf{S}}_- \hat{\mathbf{R}} \end{aligned}$$

holds, the rotated equation of motion is obtained as

$$\begin{aligned} i \frac{\partial}{\partial t} |\tilde{\Psi}\rangle &= \left\{ \begin{pmatrix} \hat{\mathbf{H}}_g + \frac{1}{2}\omega_L & E_0 S(t) \hat{\boldsymbol{\mu}} \\ E_0 S^*(t) \hat{\boldsymbol{\mu}} & \hat{\mathbf{H}}_e - \frac{1}{2}\omega_L \end{pmatrix} \otimes \mathbb{1}_B + \mathbb{1}_S \otimes \sum_j \varepsilon_j \hat{\mathbf{a}}_j^+ \hat{\mathbf{a}}_j \right. \\ &\quad \left. + \begin{pmatrix} g(\hat{\mathbf{Q}}) & f(\hat{\mathbf{Q}}) e^{-i\omega_L t} \\ f(\hat{\mathbf{Q}})^* e^{i\omega_L t} & g(\hat{\mathbf{Q}}) \end{pmatrix} \otimes \sum_j (V_j^* \hat{\mathbf{a}}_j^+ + V_j \hat{\mathbf{a}}_j) \right\} \hat{\mathbf{R}} |\Psi\rangle, \end{aligned} \quad (\text{D.6})$$

where the braces contain  $\hat{\mathbf{H}}_{\text{RWA}}$ , the Hamiltonian in the rotating frame. It is clear from Eq. (D.6) that the fast time-dependence can only be eliminated by the transformation, Eq. (D.3), if the system-bath interaction is diagonal in the electronic degree of freedom of the system, i.e. it involves only nuclear relaxation or dephasing.

If the interaction with the bath describes electronic quenching or dephasing, an additional or counter rotation needs to be applied, this time in the bath Hilbert space. This is obvious from a physical point of view: Changing into the rotating frame for the system collapses the vertical energy difference of the potential energy surfaces which are coupled by the pulse at the Franck-Condon point. Before the rotation, the bath energies matched the difference of the potentials. Therefore, if the energy scale of the primary system is changed, the same must be done to the bath.

The counter rotation in the bath Hilbert space is given by the operator

$$\hat{\mathbf{U}}(\theta) = \mathbb{1}_S \otimes \exp \left( i\theta \sum_j \hat{\mathbf{S}}_{zj} \right) \quad (\text{D.7})$$

with  $\hat{\mathbf{S}}_{zj}$  the  $\hat{\mathbf{S}}_z$  operator of the  $j$ th bath mode (for details see Appendix E.2). Analogous commutation relations to Eq. (D.4) hold, and again the commutator

$$\begin{aligned} [\hat{\mathbf{H}}_{\text{RWA}}, \hat{\mathbf{U}}(\theta)]_- &= \begin{pmatrix} g(\hat{\mathbf{Q}}) & f(\hat{\mathbf{Q}}) e^{-i\omega_L t} \\ f^*(\hat{\mathbf{Q}}) e^{i\omega_L t} & g(\hat{\mathbf{Q}}) \end{pmatrix} \otimes \\ &\quad \left( [\hat{\mathbf{S}}_+, \hat{\mathbf{U}}(\theta)]_- + [\hat{\mathbf{S}}_-, \hat{\mathbf{U}}(\theta)]_- \right) \\ &= (1 - e^{i\omega_L t}) \begin{pmatrix} g(\hat{\mathbf{Q}}) & f(\hat{\mathbf{Q}}) e^{-i\omega_L t} \\ f^*(\hat{\mathbf{Q}}) e^{i\omega_L t} & g(\hat{\mathbf{Q}}) \end{pmatrix} \otimes \hat{\mathbf{S}}_+ \hat{\mathbf{U}} \\ &\quad + (1 - e^{-i\omega_L t}) \begin{pmatrix} g(\hat{\mathbf{Q}}) & f(\hat{\mathbf{Q}}) e^{-i\omega_L t} \\ f^*(\hat{\mathbf{Q}}) e^{i\omega_L t} & g(\hat{\mathbf{Q}}) \end{pmatrix} \otimes \hat{\mathbf{S}}_- \hat{\mathbf{U}} \quad (\text{D.8}) \end{aligned}$$

is needed. In Eq. (D.8), only one of the  $\exp(\pm i\omega_L t)$ -terms in the coupling matrix will cancel out, while in the other one the frequency is doubled. Using the rotating wave approximation amounts to neglecting these frequency

doubled terms [63]. The resulting Hamiltonian then is

$$\begin{aligned}
\hat{\mathbf{H}}_{\text{RWA}} = & \begin{pmatrix} \hat{\mathbf{H}}_g + \frac{1}{2}\omega_L & E_0 S(t) \hat{\boldsymbol{\mu}} \\ E_0 S^*(t) \hat{\boldsymbol{\mu}} & \hat{\mathbf{H}}_e - \frac{1}{2}\omega_L \end{pmatrix} \otimes \mathbb{1}_B \\
& + \mathbb{1}_S \otimes \sum_j \left( \varepsilon_j \hat{\mathbf{a}}_j^\dagger \hat{\mathbf{a}}_j - \omega_L \hat{\mathbf{S}}_z^j \right) \\
& + \begin{pmatrix} g(\hat{\mathbf{Q}}) e^{i\omega_L t} & f(\hat{\mathbf{Q}}) \\ 0 & g(\hat{\mathbf{Q}}) e^{i\omega_L t} \end{pmatrix} \otimes \sum_j V_j^* \hat{\mathbf{a}}_j^\dagger \\
& + \begin{pmatrix} g(\hat{\mathbf{Q}}) e^{-i\omega_L t} & 0 \\ f^*(\hat{\mathbf{Q}}) & g(\hat{\mathbf{Q}}) e^{-i\omega_L t} \end{pmatrix} \otimes \sum_j V_j \hat{\mathbf{a}}_j. \quad (\text{D.9})
\end{aligned}$$

Therefore, if the system-bath-coupling is either diagonal or off-diagonal in the system Hilbert space, it is possible to eliminate the fast time dependence of the laser pulse for the total Hamiltonian.

There are two points to note when Eq. (D.9) is used, i.e. when applying the rotating wave approximation in case of the bath coupling to the electronic degree of freedom of the system. Since  $\hat{\mathbf{S}}_+$  couples only to the annihilation operators  $\hat{\mathbf{a}}_j$ , no bath mode will be excited on the electronically excited state. The price to pay for eliminating the fast time dependence is a considerable increase of the spectral range due to  $\sum_i \hat{\mathbf{S}}_{iz}$ .  $\sum_i \hat{\mathbf{S}}_{iz}$  is given by the number of bits set in a spinor component minus  $N/2$  (see Appendix E.2), i.e. the 0th component is always shifted down by  $N/2$ .

# Appendix E

## The bit representation of the two level system bath

### E.1 The wave function

The state of the system combined with the bath is described by a  $2^N$ -dimensional spinor with  $N$  being the number of modes. The dimension  $2^N$  results from the number of possibilities to combine 2 states (spin-up/spin-down, bath mode excited/not excited, bit set/not set)  $N$  times, for an illustration see Fig. E.1.

For  $N = 1$  and  $N = 2$ , respectively, this wave function spinor becomes

$$\Psi^{N=1}(\hat{\mathbf{Q}}) = \begin{pmatrix} \psi_0(\hat{\mathbf{Q}}, \alpha) \\ \psi_1(\hat{\mathbf{Q}}, \alpha) \end{pmatrix}, \quad \Psi^{N=2}(\hat{\mathbf{Q}}) = \begin{pmatrix} \psi_0(\hat{\mathbf{Q}}, \alpha) \\ \psi_1(\hat{\mathbf{Q}}, \alpha) \\ \psi_2(\hat{\mathbf{Q}}, \alpha) \\ \psi_3(\hat{\mathbf{Q}}, \alpha) \end{pmatrix}, \quad (\text{E.1})$$

where  $\hat{\mathbf{Q}}$  represents the nuclear degrees of freedom of the wave function and  $\alpha$  the electronic degrees of freedom. The spinor is bit ordered, i.e. the  $k$ th bit set in the spinor index corresponds to the  $i$ th TLS mode excited if the counting of bits starts at  $k = 0$ , see Fig. E.1. This means that the zeroth component corresponds to no bath mode being excited, the first and second component to the excitation of the first and second bath mode, and the third component corresponds to the first and second bath mode being excited *simultaneously*, and so forth.

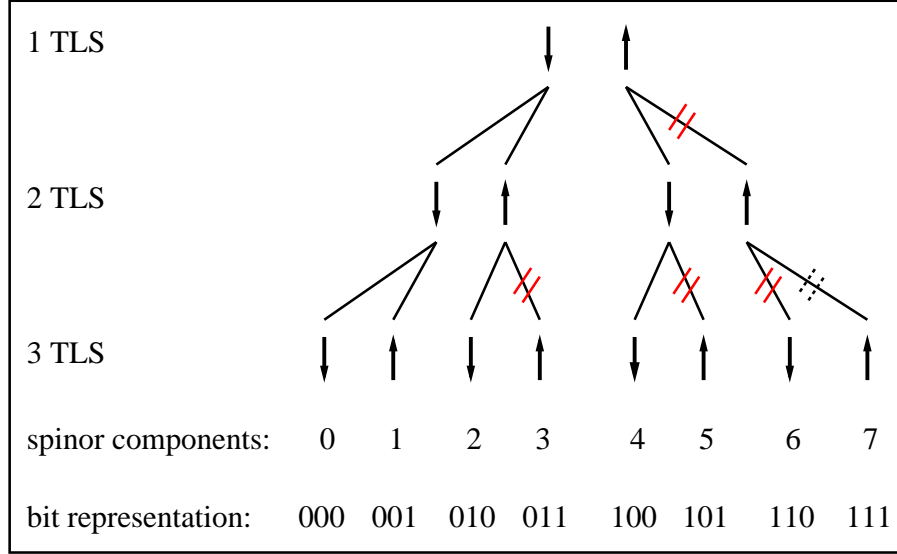


Figure E.1: There are four possibilities to combine two TLS and eight possibilities to combine three TLS, the combinations are indicated by lines connecting the arrows (TLS). The index of the spinor components has as many bits set in its binary representation as TLS are excited, bits are counted from right to left. If only two simultaneous excitations are allowed the component crossed out by the dashed line can be dropped, if only one simultaneous excitation is allowed, all crossed out components can be dropped.

The number of simultaneous excitations can be restricted. The occurrence of the  $k$ th excitation in  $N$  bits is a combination,

$$\binom{N}{k} = \frac{N!}{k!(N-k)!}.$$

The dimension of the spinor  $D$  is then given by the sum of binomial coefficients

$$D = \sum_{k=0}^{N_{exc}} \binom{N_{exc}}{k} \quad (\text{E.2})$$

with  $N_{exc}$  the number of simultaneously allowed excitations. Assume a bath with 4 modes and at most 2 simultaneous excitations. Then  $D$  is:

$$D = \binom{4}{0} + \binom{4}{1} + \binom{4}{2} = 1 + 4 + 6 = 11,$$

which means there is one spinor component corresponding to none of the bath modes excited, four components have one bit set and there are 6 possibilities

to excite 2 bits out of 4. Making use of the Binomial Theorem

$$(a + b)^N = \sum_{k=0}^N \binom{N}{k} a^{N-k} b^k$$

with  $a = b = 1$ , it again is found that  $D = 2^N$  if all  $N$  excitations are allowed simultaneously. The restriction of simultaneously allowed excitations leads to significant numerical savings, both in computation time and storage, and its validity can simply be checked by increasing  $N_{exc}$ .

## E.2 The operators

The bath operators entering the Hamiltonian are sums over the operators acting on a single mode. In bit representation the operator of mode  $k$  acts on bit  $k$  (assuming  $k = 0, \dots, N - 1$ ), i.e. on the spinor components which have the  $k$ th bit set in their indices. One should clearly distinguish between bath modes and spinor components. For example, the  $k = 0$  mode which may or may not be excited should not be confused with the zeroth spinor component corresponding to all modes deexcited.

As a simple example, consider the operator  $\hat{\mathbf{S}}_z = \frac{1}{2} \begin{pmatrix} -1 & 0 \\ 0 & +1 \end{pmatrix}$  and a bath consisting of  $N = 3$  modes. Then the total  $\hat{\mathbf{S}}_z^{(N=3)}$  is a diagonal  $8 \times 8$ -matrix. The  $\hat{\mathbf{S}}_z^{(k=2)}$  acts on the total 8-dimensional space with the first four diagonal elements  $-1$  since the  $k = 2$  bit is 0, i.e. the third mode is not excited, and the second four diagonal elements  $+1$  since the  $k = 2$  bit is 1, i.e. the third mode is excited (cf. Fig. E.1). The  $\hat{\mathbf{S}}_z^{(k=1)}$ -operator acting on the second mode acts on the two 4-dimensional subspaces with the first two diagonal elements  $-1$  and the second two  $+1$ . Finally the  $\hat{\mathbf{S}}_z^{(k=0)}$ -operator acts on the four 2-dimensional subspaces. Since the total  $\hat{\mathbf{S}}_z^{(N=3)}$ -operator is the sum over





with

$$\hat{\sigma}^+ = \begin{pmatrix} 0 & 0 \\ 1 & 0 \end{pmatrix}, \quad (\text{E.7})$$

and the  $k$ th annihilator is given by the conjugated expression built on  $\hat{\sigma}$ . With the help of Eq. (E.7) the bath operators needed in the interaction Hamiltonian, Eq. (3.19), can now be constructed.

The matrix representation of  $\sum_k d_k(\hat{\sigma}_k^+ + \hat{\sigma}_k)$  describing energy relaxation (cf. Sections 3.2 and 3.3) has already been given [2], it is noted here for completeness:

$$\sum_k d_k(\hat{\sigma}_k^+ + \hat{\sigma}_k) = \begin{pmatrix} 0 & d_0 & d_1 & 0 & d_2 & 0 & 0 & 0 \\ d_0 & 0 & 0 & d_1 & 0 & d_2 & 0 & 0 \\ d_1 & 0 & 0 & d_0 & 0 & 0 & d_2 & 0 \\ 0 & d_1 & d_0 & 0 & 0 & 0 & 0 & d_2 \\ d_2 & 0 & 0 & 0 & 0 & d_0 & d_1 & 0 \\ 0 & d_2 & 0 & 0 & d_0 & 0 & 0 & d_1 \\ 0 & 0 & d_2 & 0 & d_1 & 0 & 0 & d_0 \\ 0 & 0 & 0 & d_2 & 0 & d_1 & d_0 & 0 \end{pmatrix}. \quad (\text{E.8})$$

The upper triangle in Eq. (E.8) corresponds to annihilation, and the lower triangle to creation of bath modes. The action of the bath operators  $\sum_k d_k(\hat{\sigma}_k^+ + \hat{\sigma}_k)$  is given by an exclusive *or*, making use of the **Fortran90** function `ieor`. The exclusive *or* of two bits is true only if one of the bit is 1 while the other is 0. If  $i = \text{ieor}(2^k, j)$  then  $d_k \psi_j(Q)$  needs to be added to the  $i$ th component of the new spinor. To illustrate the exclusive *or*, for example for  $N = 3$  the fourth spinor component is obtained from

$$\tilde{\Psi}_4 = \underbrace{d_2 \Psi_0}_{\text{creation}} + \underbrace{d_0 \Psi_5 + d_1 \Psi_6}_{\text{annihilation}}$$

with

$$\begin{array}{lll} d_2 \rightarrow 2^2 : & 100 & d_0 \rightarrow 2^0 : \quad 001 & d_1 \rightarrow 2^1 : \quad 010 \\ \Psi_0 \rightarrow 0 : & \underline{000} & \Psi_5 \rightarrow 5 : \quad \underline{101} & \Psi_6 \rightarrow 6 : \quad \underline{110} \\ \tilde{\Psi}_4 \rightarrow 4 : & 100 & 100 & 100 \end{array}$$

(it should be remembered that bits are counted from right to left starting from 0). In the above example, all combinations of  $2^k$  and  $j$  leading to  $i = 4$

are listed. For all other combinations the exclusive *or* leads to false, i.e.

$$\begin{array}{ll} d_2 \rightarrow 2^2 : & 100 \\ \Psi_1 \rightarrow 1 : & \underline{001} \\ \tilde{\Psi}_4 \rightarrow 4 \neq 5 : & 101 \end{array} \qquad \begin{array}{ll} d_0 \rightarrow 2^0 : & 001 \\ \Psi_6 \rightarrow 6 : & \underline{110} \\ \tilde{\Psi}_4 \rightarrow 4 \neq 7 : & 111 . \end{array}$$

When using the RWA for a system with electronic relaxation, it is important to keep track of which components are created and which are destroyed (cf. Appendix D). This can easily be done by comparing the number of set bits in the index of the new and the old spinor component.

The dephasing operator  $\hat{\mathbf{O}} = \sum_{kl} c_{kl} (\hat{\boldsymbol{\sigma}}_k^+ \hat{\boldsymbol{\sigma}}_l + \hat{\boldsymbol{\sigma}}_l^+ \hat{\boldsymbol{\sigma}}_k)$  (cf. Sections 3.2 and 3.4) reads for  $N = 3$  modes

$$\sum_{k,l=0}^2 O_{kl} = \begin{pmatrix} 0 & 0 & 0 & 0 & 0 & 0 & 0 & 0 \\ 0 & 0 & c_{01} & 0 & c_{02} & 0 & 0 & 0 \\ 0 & c_{10} & 0 & 0 & c_{12} & 0 & 0 & 0 \\ 0 & 0 & 0 & 0 & 0 & c_{12} & c_{02} & 0 \\ 0 & c_{20} & c_{21} & 0 & 0 & 0 & 0 & 0 \\ 0 & 0 & 0 & c_{21} & 0 & 0 & c_{01} & 0 \\ 0 & 0 & 0 & c_{20} & 0 & c_{10} & 0 & 0 \\ 0 & 0 & 0 & 0 & 0 & 0 & 0 & 0 \end{pmatrix}. \quad (\text{E.9})$$

The application of Eq. (E.9),  $\Psi_i = \sum_{kl} O_{kl} \Psi_j$ , requires several bit tests: First, the number of excitations in the spinor indices  $i$  and  $j$  must be equal. This corresponds to the requirement that dephasing doesn't alter the energy of the bath, i.e. conserves the number of bath excitations. Second, the indices of  $O_{kl}$  in Eq. (E.9) numbering the bath modes bit-added,  $k+l$ , must be equal to the exclusive *or* of  $i$  and  $j$ . This is a generalization of the single application of the exclusive *or* described in the previous paragraph for the case when only one bath operator acts on the spinor, and not two consecutively.

Whenever the Surrogate Hamiltonian method was applied, it has been used in the bit representation (cf. Chapters 3, 4 and 7).

# Appendix F

## Mapping a 2D bath onto 1D

The electron-hole pairs which make up the bath are assumed to be localized on single Ni-O pairs. Then the bath is two-dimensional considering the uppermost layer of the NiO surface or three-dimensional in case several layers are considered. However, only the distance of each electron-hole pair from the NO molecule and the direction of its dipole moment are important. In a 1D treatment of the primary system only electron-hole pairs with dipole moments parallel or antiparallel to the surface normal contribute to the dipole-dipole interaction. Therefore the bath is effectively one-dimensional.

The fact that NiO has cubic lattice structure can be used to develop an algorithm to map a 2D or 3D bath onto one dimension (the distance) and a sign (the direction of the dipole). In 2D, each Ni-O pair is located at a point of a quadratic lattice. The lattice points correspond to numbers  $n$ ,  $0 \leq n \leq N_B \in \mathbb{N}$ , for which  $n = i^2 + j^2$  holds with  $i, j = 0, \dots \in \mathbb{N}$ . This means that all square numbers and sums of two square numbers need to be found to determine the lattice points. A theorem from number theory can be employed: Every integer can be factorized into prime numbers  $p = 2$ ,  $p = 4m + 1$  and  $p = 4m + 3$ . If and only if all prime factors  $p = 4m + 3$  of  $n$  occur an even number of times in the factorization,  $n$  is a sum of two square numbers. The distance of this lattice point to the origin (which is the site below the NO molecule) is then given by

$$\text{distance of TLS} = \sqrt{n}a_0 \quad (\text{F.1})$$

with  $a_0$  half the lattice constant. The sign of the dipole moment is given by

$$\begin{aligned}
i + j \text{ even} &\longrightarrow +, \\
i + j \text{ odd} &\longrightarrow -.
\end{aligned}
\tag{F.2}$$

If  $n$  can be factorized into different pairs  $(i, j)$ , the number of possible factorizations corresponds to the number of times this distance occurs,

$$\text{occurrence} = \text{Number of different } (i, j) \cdot 4, \tag{F.3}$$

where the factor 4 accounts for four-fold symmetry. Since points which are connected by a  $90^\circ$  rotation are identified, the surface slab is mapped onto a sphere. The usual assumption of periodic boundary conditions corresponds to a mapping onto a torus and does not make use of four-fold symmetry.

Prime factorization is a major topic of interest in computer science, particularly in cryptography and quantum computing, and a number of elaborate methods have been developed to cope with it. However, since the  $n$  are relatively small, no sophisticated tool like Shor's Algorithm [7] is needed to find their factorization, but all integers can simply be scanned and trial division applied.

This mapping of two dimensions onto one introduces a factor of  $1/\log(N)$  into the nearest neighbor interaction term of the bath (Section 7.1). It results from the ratio of points inside the lattice which have four nearest neighbors to points on the edges and diagonals of the lattice which in the one-dimensional model may have less than four nearest neighbors. If the matrix elements representing the second term in Eq. (7.1) are called  $c_{ij}$ , then points inside the lattice are counted twice in the above outlined algorithm when calculating the matrix, while points on the edges and diagonals are counted once. If the number of non-zero matrix elements is divided by the sum of all matrix elements, the factor  $1/\log(N)$  is obtained.

The outlined algorithm allows to map a 2D bath, namely the dipoles in the uppermost layer of Ni-O pairs, onto one dimension. If additional Ni-O layers shall be treated to account for transport into the surface, the simplest approach describes every layer as a separate bath (cf. Fig. F.1). This means that all correlations between layers are neglected.

For the NO/NiO(100) system this should not pose a serious restriction. From physical considerations, there is already one restriction on the corre-

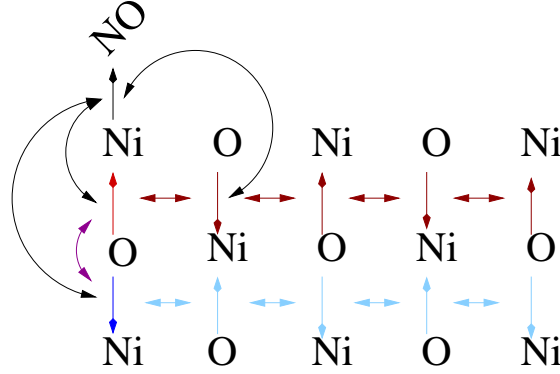


Figure F.1: Considering two layers of Ni-O pairs as two different baths: the system (black) interacts with each layer, the bath dipoles interact with each other within one layer (red and blue), the two layers are coupled by an interaction of dipoles on top of each other (purple). For the system-bath interaction (black) and the interaction between different layers (purple) only some representative arrows are drawn.

lations between layers: The light red and the dark blue dipole in Fig. F.1 get excited by an electron transfer from the same oxygen atom, therefore it is very unfavorable that they are excited simultaneously. Analogously, it is unlikely that a nickel atom gets an electron from both the oxygen above and below. Therefore this excitation can be excluded. So what really is neglected are the correlations between the dark blue and all dark red dipoles and the correlations between the light red and all light blue dipoles. Keeping in mind that so far only two to three simultaneous excitations within one layer needed to be allowed, this approximation should not be severe. It should be kept in mind, that the approximation relies on the electronic structure of NiO, in particular on the localized d-orbitals. Thus this algorithm is not general, and the validity of the approximation might break down for e.g. other oxides. However, then the whole ansatz of Eq. (7.1) might become questionable, for example more than nearest neighbor interaction should be included for a more delocalized electronic structure.

As an advantage of this approach there is no limit to  $N = 63$  modes (on a 64bit machine), this limit holds only within one layer. Furthermore it is not necessary to have the same number of dipoles in the surface, the number of dipoles can be selected such that the maximum distance from the system dipole is the same in each layer. This corresponds to a half sphere below

the NO instead of a cuboid and is motivated by the interaction between the system and the bath which only depends on distance. It was observed, however, that bath modes in deeper layers are almost exclusively populated due to the interaction between bath modes. It is therefore more favorable in terms of the convergence properties of expectation values with respect to the number of layers to assume the same number of dipoles in each layer.

# Appendix G

## Numerics

### G.1 The structure of the program

For the calculations presented in this thesis the development of a fairly complex program to solve the time-dependent Schrödinger equation was necessary. It is based on the wave packet programs developed earlier [3, 4] in **Fortran77**. Since the methodological development required frequent changes, the program was rewritten **Fortran90**. The adaption of object-oriented concepts allowed for more flexibility of the program, while the numerical efficiency of **Fortran** was retained.

The program consists of a number of modules, each devoted to a particular aspect. Within the modules, specific data structures were declared. For example, the module `psi.f90` contains all operations on the wave function while the module `grid.f90` takes care of everything related to the definition of the grid (*encapsulation*). The modules are hierarchically ordered with higher-level modules calling lower-level ones, such as `psi.f90` or `grid.f90`, without knowing what exactly happens in the lower levels of the hierarchy. The `output.f90` module, for example, simply calls the subroutine `expectationvalue` which is defined in `psi.f90`. Since expectation values can be calculated on one or more electronic states, in coordinate or momentum representation, the subroutines actually performing the calculations are *overloaded*. They can then be called by the common subroutine call `expectationvalue` in `output.f90`, and the module `psi.f90` decides according to the arguments of the subroutine call which specific subroutine should

be invoked.

As an advantage of such structured programming, changes in lower-level modules do not affect higher-level modules or the main program. For example, the definition of the bath, in particular the calculation of the interaction constants, differs considerably for a bath with an Ohmic spectral density (cf. Chapters 3 and 4) and a bath with microscopically derived interaction constants (cf. Chapter 7). These changes in `bath.f90`, however, did not affect higher-level modules such as the propagation module `prop.f90`. The programming and debugging effort can therefore be minimized by employing programming concepts borrowed from object-oriented programming.

## G.2 Parameters of the calculations

Unless stated otherwise, all parameters are in atomic units.

Table G.1: Parameters of the calculations for a relaxing harmonic oscillator presented in Figs. 3.2 to 3.6

mass	frequency	$\Delta t$	grid points	$Q_{min}$	$Q_{max}$	$\Delta Q$	$k_{max}$
1.0	1.0	0.05	64	-8.0	8.0	0.25	12.4

Spectral density  $J(\omega) = \eta\omega$  (Figs. 3.2 to 3.4)

sampling	$\omega_{max}$ ( $\eta = 0.01$ )	$\omega_{max}$ ( $\eta = 0.1$ )
equidistant	$6\omega$	$1.5\omega$

Spectral density  $J(\omega) = \eta\omega e^{-\omega/\omega_c}$  (Figs. 3.5 and 3.6)

sampling	$\omega_c$	$\omega_{max}$	$\omega_{min}$
equidistant	$1.5\omega$	$3\omega$	
exponential	$1.5\omega$	$3\omega$	$0.05\omega \dots 0.1\omega$



Table G.2: Parameters of the calculations for a relaxing anharmonic oscillator presented in Fig. 3.7

mass	frequency	$\Delta t$	grid points	$Q_{min}$	$Q_{max}$	$\Delta Q$	$k_{max}$
$2.0 \cdot 10^5$	$5.0 \cdot 10^{-4}$	100	64	-1.0	1.0	$3.18 \cdot 10^{-2}$	99.0

Spectral density  $J(\omega) = \eta\omega e^{-\omega/\omega_c}$  (Figs. 3.5 and 3.6)

sampling	$\eta$	$\omega_c$	$\omega_{max}$	$\omega_{min}$
exponential	2.0	$\omega$	$3\omega$	$0.4\omega \dots 0.5\omega$

Probe pulse

$E_0$	$\tau_{FWHM}$	$\omega_L$
$2.5 \cdot 10^{-5}$	$0.096T$ (20 fs)	0.005

Table G.3: Parameters of the calculations for nuclear dephasing of a displaced harmonic oscillator presented in Figs. 3.8 and 3.9 and Table 3.4

mass	frequency	$\Delta t$	grid points	$Q_{min}$	$Q_{max}$	$\Delta Q$	$k_{max}$
$2.0 \cdot 10^5$	$5.0 \cdot 10^{-4}$	100	64	-0.75	0.75	$2.38 \cdot 10^{-2}$	132

Spectral density  $J(\omega) = \eta\omega e^{-\omega/\omega_c}$

sampling	$\omega_c$	$\omega_{max}$	$\omega_{min}$
equidistant	$\omega$	$1.01\omega$	$0.9\omega \dots 0.99\omega$

Table G.4: Parameters of the calculations for electronic dephasing of a TLS presented in Figs. 3.10 to 3.13

TLS energy = 0.004, Spectral density  $J(\omega) = \eta\omega e^{-\omega/\omega_c}$  (Fig. 3.10 to 3.12)

sampling	$\omega_c$	$\omega_{max}$	$\omega_{min}$
equidistant	$\omega$	$1.05\omega$	$0.4\omega \dots 0.95\omega$

Probe pulse (Fig. 3.10)

$E_0$	$\tau_{FWHM}$	$\omega_L$
$1.2 \cdot 10^{-3}$	20 fs	0.004

Probe pulse (Figs. 3.11 and 3.12)

$E_0$	$\tau_{FWHM}$	$\omega_L$
$4.9 \cdot 10^{-5}$	5 fs	0.004

TLS energy = 0.006, Spectral density  $J(\omega) = \eta\omega e^{-\omega/\omega_c}$  (Fig. 3.13)

sampling	$\omega_c$	$\omega_{max}$	$\omega_{min}$
equidistant	$\omega$	$1.01\omega$	$0.4\omega \dots 0.99\omega$

Table G.5: Parameters of the calculations for the CW absorption spectrum presented in Figs. 4.2 and 4.3

mass	$\omega_g$	$\omega_e$	$Q_0$	$V_d$	$\Delta V$
$2.0 \cdot 10^5$	$10.0 \cdot 10^{-4}$	$0.7\omega_g$	0.2	$5\omega_g$	0.004
$\Delta t$	grid points	$Q_{min}$	$Q_{max}$	$\Delta Q$	$k_{max}$
100	64	-1.0	1.0	$3.18 \cdot 10^{-2}$	99.0

Spectral density  $J(\omega) = \eta\omega e^{-\omega/\omega_c}$

sampling	$\omega_c$	$\omega_{max}$	$\omega_{min}$
exponential	$2\omega_g$	$5\omega_g$	$0.4\omega_g \dots 0.5\omega_g$

Table G.6: Parameters of the calculations of the charge transfer dynamics presented in Figs. 4.5 and 4.12

mass	$\omega_g$	$\omega_e$	$Q_0$	$V_d$	$\sigma_d$	$\Delta V$
$2.0 \cdot 10^5$	$5.0 \cdot 10^{-4}$	$0.7\omega_g$	0.2	$\omega_g$	0.1	0.004
$\Delta t_1$	$\Delta t_2$	grid points	$Q_{min}$	$Q_{max}$	$\Delta Q$	$k_{max}$
5	100	64	-1.0	1.0	$3.18 \cdot 10^{-2}$	99.0

Spectral density  $J(\omega) = \eta\omega e^{-\omega/\omega_c}$

sampling	$\omega_c$	$\omega_{max}$	$\omega_{min}$
exponential	$\omega_g$	$1.5\omega_g$	$0.7\omega_g \dots 0.71\omega_g$

Pulses

$E_0$ (pump)	$E_0$ (probe)	$\tau_{FWHM}$	$\omega_L$
$2.5 \cdot 10^{-4}$	$2.5 \cdot 10^{-5}$	20 fs	0.004

Table G.7: Parameters of the calculations of the charge transfer dynamics presented in Figs. 4.4, 4.6 to 4.10 and 4.11

mass	$\omega_g$	$\omega_e$	$Q_0$	$\sigma_d$	$\Delta V$
$2.0 \cdot 10^5$	$5.0 \cdot 10^{-4}$	$0.7\omega_g$	0.2	0.1	0.004

$V_d = 5\omega_g$  (except for Fig. 4.11 where  $V_d = 0.2\omega_g$ )

Time steps and grid parameters as in Table G.6

Spectral density  $J(\omega) = \eta\omega e^{-\omega/\omega_c}$

sampling	$\omega_c$	$\omega_{max}$	$\omega_{min}$
exponential	$2\omega_g$	$5\omega_g$	$0.4\omega_g \dots 0.5\omega_g$

Pulse parameters as in Table G.6

Table G.8: Parameters of the calculations of diabatic coupling model for NO/NiO(100) presented in Figs. 6.1 to 6.5

mass	$\Delta t$	grid points	$Q_{min}$	$Q_{max}$	$\Delta Q$	$k_{max}$	$a$	$Z_0$
54686.649	100	512	3.0	15.0	0.0235	134	15	13.5

Parameters for fs pulses

fluence	radius	$E_0$	$\tau_{FWHM}$	energy
11 $\mu\text{J}$	2.5 mm	$8.93 \cdot 10^{-5}$	100 fs	4.7 eV

Parameters for CW pulses

fluence	radius	$E_0$	energy
5 mJ	2.5 mm	$1.9 \cdot 10^{-6}$	4.7 eV

Table G.9: Parameters of the MCWF calculations for NO/NiO(100) presented in Figs. 6.6 to 6.10

mass	$\Delta t_2$	grid points	$Q_{min}$	$Q_{max}$	$\Delta Q$	$k_{max}$	$a$	$Z_0$
54686.649	10	512	3.0	20.0	0.0333	94.4	4	17

Parameters for fs pulses

$\Delta t_1$	$E_0$	$\tau_{FWHM}$	energy
5	$1.9 \cdot 10^{-3}$	25 fs	3.7 eV
5	$1.2 \cdot 10^{-3}$	50 fs	3.7 eV
10	$8.2 \cdot 10^{-4}$	100 fs	3.7 eV
10	$6.6 \cdot 10^{-4}$	250 fs	3.7 eV

Table G.10: Parameters for the calculations for NO/NiO(100) with the Surrogate Hamiltonian method presented in Chapter 7

mass	$\Delta t_2$	grid points	$Q_{min}$	$Q_{max}$	$\Delta Q$	$k_{max}$	$a$	$Z_0$
54686.649	20	512	3.0	20.0	0.0333	94.4	6	17

Parameters for fs pulses

$\Delta t_1$	fluence	radius	$E_0$	$\tau_{FWHM}$	energy
1	5 mJ	2.5 mm	$8.5 \cdot 10^{-3}$	5 fs	3.7 eV
5	1 mJ	2.5 mm	$1.7 \cdot 10^{-3}$	25 fs	3.7 eV
10	0.5 mJ	2.5 mm	$8.5 \cdot 10^{-4}$	50 fs	3.7 eV

Tolerance (relative) for recursions:

$\epsilon = 10^{-5}$  (system population),  $\epsilon = 10^{-1}$  (bath distance)

Tolerance in density matrix construction:  $\epsilon = 2 \cdot 10^{-14}$

Bath parameters (unless specified otherwise in the Figure captions)

$\varepsilon = 3.7$  eV,  $\eta = 0.7$  eV,  $q = 0.1$



# References

- [1] C. Cohen-Tannoudji, B. Diu, and F. Laloe, *Quantum mechanics*, John Wiley & Sons, New York, 2nd, rev. and enlarged edition, 1977
- [2] R. Baer and R. Kosloff, J. Chem. Phys. **106**, 8862 (1997)
- [3] T. Klüner, *Theoretische Beschreibung der laserinduzierten Desorption kleiner Moleküle von idealen Metalloxidoberflächen*, Dissertation, Ruhr-Universität Bochum, 1997
- [4] S. Thiel, *Theoretische Untersuchungen zur laserinduzierten Desorption kleiner Moleküle von Oberflächen*, Dissertation, Freie Universität Berlin, 2000, <http://www.diss.fu-berlin.de/2001/36/index.html>
- [5] S. Haroche, Physics Today **51**, 36 (1998)
- [6] E. Joos, Decoherence Through Interaction with the Environment, In *Decoherence and the Appearance of a Classical World in Quantum Theory* [9]
- [7] A. Ekert and R. Jozsa, Rev. Mod. Phys. **68** (1996)
- [8] J. M. Raimond, M. Brune, and S. Haroche, Rev. Mod. Phys. **73**, 565 (2001)
- [9] D. Giulini, E. Joos, C. Kiefer, J. Kupsch, I.-O. Stamatescu, and H. Zeh, *Decoherence and the Appearance of a Classical World in Quantum Theory*, Springer, Berlin, 1996
- [10] K. Blum, *Density Matrix Theory and Applications*, Plenum Press, New York, 1981

- 
- [11] D. F. Walls and G. J. Milburn, *Quantum optics*, Springer, Berlin, 1995
  - [12] H. J. Carmichael, *An Open System Approach to Quantum Optics*, Lecture Notes in Physics, Springer, Berlin, 1993
  - [13] H. Guo, P. Saalfrank, and T. Seideman, *Prog. Surf. Sci.* **62**, 239 (1999)
  - [14] N. Delaney, J. Fader, and R. Parson, *J. Chem. Phys.* **111**, 651 (1999)
  - [15] A. Sanov, T. Sanford, S. Nandi, and W. C. Lineberger, *J. Chem. Phys.* **111**, 664 (1999)
  - [16] M. Bixon and J. Jortner, *Adv. Chem. Phys.* **106**, 35 (1999)
  - [17] H. A. Frank, J. A. Bautista, J. Josue, Z. Pendon, R. G. Hiller, F. P. Sharples, D. Gosztola, and M. R. Wasielewski, *J. Phys. Chem. B.* **104**, 4569 (2000)
  - [18] R. P. Feynman and F. L. Vernon Jr., *Ann. Phys.* **24**, 118 (1963)
  - [19] N. V. Prokof'ev and P. C. E. Stamp, *Rep. Prog. Phys.* **63**, 669 (2000)
  - [20] A. J. Leggett, S. Chakravarty, A. T. Dorsey, M. P. A. Fisher, A. Garg, and W. Zwerger, *Rev. Mod. Phys.* **59**, 1 (1987)
  - [21] U. Weiss, *Quantum dissipative systems*, World Scientific, Singapore, 1993
  - [22] W. T. Pollard, A. K. Felts, and R. A. Friesner, *Adv. Chem. Phys.* **93**, 77 (1996)
  - [23] V. May and O. Kühn, *Charge and Energy Transfer Dynamics in Molecular Systems*, Wiley-VCH, Berlin, 2000
  - [24] E. Wigner, *Phys. Rev.* **40**, 749 (1932)
  - [25] R. Alicki, preprint, <http://www.arXiv.org/abs/quant-ph/0205173>, 2002
  - [26] J. S. Bader and B. J. Berne, *J. Chem. Phys.* **100**, 8359 (1994)
  - [27] N. Makri, *J. Phys. Chem. A* **102**, 4414 (1998)



- 
- [28] N. Makri, J. Math. Phys. **36**, 2430 (1995)
- [29] N. Makri, Annu. Rev. Phys. Chem. **50**, 167 (1999)
- [30] K. M. Forsythe and N. Makri, Phys. Rev. B **60**, 972 (1999)
- [31] A. A. Golosov, S. I. Tsonchev, P. Pechukas, and R. A. Friesner, J. Chem. Phys. **111**, 9918 (1999)
- [32] Y. Zhao, V. Chernyak, and S. Mukamel, J. Phys. Chem. A **102**, 6614 (1998)
- [33] A. O. Caldeira, A. H. Castro Neto, and T. Oliveira de Carvalho, Phys. Rev. B **48**, 13974 (1993)
- [34] E. B. Davies, *Quantum Theory of Open Systems*, Academic Press, London, 1976
- [35] R. Kubo, M. Toda, and N. Hashitsume, *Nonequilibrium statistical mechanics*, Springer, Berlin, 2nd edition, 1991
- [36] S. Mukamel, *Principles of Nonlinear Optical Spectroscopy*, Oxford University Press, New York, 1995
- [37] S. Jang, J. Cao, and R. J. Silbey, J. Chem. Phys. **116**, 2705 (2002)
- [38] I. Kondov, U. Kleinekathöfer, and M. Schreiber, J. Chem. Phys. **114**, 1497 (2000)
- [39] P. Pechukas, Phys. Rev. Lett. **73**, 1060 (1994)
- [40] G. Lindblad, Commun. Math. Phys. **48**, 119 (1976)
- [41] V. Gorini, A. Kossakowski, and E. C. G. Sudarshan, J. Math. Phys. **17**, 821 (1976)
- [42] R. Kosloff, M. A. Ratner, and W. B. Davis, J. Chem. Phys. **106**, 7036 (1997)
- [43] N. Gisin and I. C. Percival, J. Phys. A: Math. Gen. **25**, 5677 (1992)

- 
- [44] C. W. Gardiner, A. S. Parkins, and P. Zoller, Phys. Rev. A **46**, 4363 (1992)
- [45] R. Dum, A. S. Parkins, P. Zoller, and C. W. Gardiner, Phys. Rev. A **46**, 4382 (1992)
- [46] M. B. Plenio and P. L. Knight, Rev. Mod. Phys. **70**, 101 (1998)
- [47] A. A. Golosov and D. R. Reichman, J. Chem. Phys. **115**, 9862 (2001)
- [48] T. Mančal and V. May, J. Chem. Phys. **114**, 1510 (2001)
- [49] C. Meier and D. J. Tannor, J. Chem. Phys. **111**, 3365 (1999)
- [50] A. Suárez, R. Silbey, and I. Oppenheim, J. Chem. Phys. **97**, 5101 (1992)
- [51] E. Geva, E. Rosenman, and D. Tannor, J. Chem. Phys. **113**, 1380 (2000)
- [52] J. Wilkie, J. Chem. Phys. **114**, 7736 (2001)
- [53] J. T. Stockburger and H. Grabert, Phys. Rev. Lett. (2002)
- [54] G.-L. Ingold, Dissipative quantum systems, in *Quantum fluctuations*, edited by S. Reynaud, E. Giacobino, and J. Zinn-Justin, volume 63 of *Les Houches Summer School Proceedings*, Elsevier Science Publishers B.V., 1997
- [55] G. Lindblad, J. Phys. A: Math. Gen. **29**, 4197 (1996)
- [56] W. T. Pollard and R. A. Friesner, J. Chem. Phys. **100**, 5054 (1994)
- [57] N. Makri, J. Phys. Chem. B **103**, 2823 (1999)
- [58] W. H. Louisell, *Quantum Statistical Properties of Radiation*, John Wiley & Sons, New York, 1990
- [59] G. Ashkenazi, U. Banin, A. Bartana, R. Kosloff, and S. Ruhman, Adv. Chem. Phys. **100**, 229 (1997)

- 
- [60] I. S. Averbukh, M. J. J. Vrakking, D. M. Villeneuve, and A. Stolow, Phys. Rev. Lett. **77**, 3518 (1996)
- [61] D. M. Lockwood, M. Ratner, and R. Kosloff, Chem. Phys. **268**, 55 (2001)
- [62] E. Gershgoren, J. Vala, S. Ruhman, and R. Kosloff, J. Phys. Chem. A **105**, 5081 (2001)
- [63] L. Mandel and E. Wolf, *Optical coherence and quantum optics*, Cambridge University Press, 1995
- [64] R. Kosloff, A. D. Hammerich, and D. Tannor, Phys. Rev. Lett. **69**, 2172 (1992)
- [65] G. Ashkenazi, R. Kosloff, and M. A. Ratner, J. Am. Chem. Soc. **121**, 3286 (1999)
- [66] P. Kambhampati, D. H. Son, T. W. Kee, and P. F. Barbara, J. Phys. Chem. A **104**, 10637 (2000)
- [67] D. H. Son, P. Kambhampati, T. W. Kee, and P. F. Barbara, J. Phys. Chem. A **106**, 4591 (2002)
- [68] R. A. Marcus, J. Chem. Phys. **24**, 966 (1956)
- [69] R. A. Marcus, J. Chem. Phys. **26**, 867 (1957)
- [70] O. Prezhdo, Phys. Rev. Lett. **85**, 4413 (2000)
- [71] P. Barbara, G. Walker, and T. Smith, Science **256**, 975 (1992)
- [72] U. Banin, A. Bartana, S. Ruhman, and R. Kosloff, J. Chem. Phys. **101**, 8461 (1994)
- [73] E. Geva, R. Kosloff, and J. Skinner, J. Chem. Phys. **102**, 8541 (1995)
- [74] D. H. Schirmer and V. May, Chem. Phys. Lett. **297**, 383 (1998)
- [75] T. Klüner, S. Thiel, and V. Staemmler, J. Phys. B: At. Mol. Opt. Phys **32**, 4931 (1999)

- 
- [76] T. Pacher, L. S. Cederbaum, and H. Köppel, *Adv. Chem. Phys.* **84**, 293 (1993)
- [77] A. Köhl and W. Domcke, *Chem. Phys.* **259**, 227 (2000)
- [78] M. Topaler and N. Makri, *J. Phys. Chem.* **100**, 4430 (1996)
- [79] G.-L. Ingold and H. Grabert, Sluggish decay of preparation effects in low temperature quantum systems, in *Quantum Probability and Applications V*, edited by L. Accardi and W. von Waldenfels, volume 1442 of *Lecture Notes in Mathematics*, pages 219–230, Springer, 1990
- [80] D. Yarkony, *J. Chem. Phys.* **114**, 2601 (2001)
- [81] H.-L. Dai and W. Ho, editors, *Laser spectroscopy and photochemistry on metal surfaces*, World Scientific, Singapore, 1995
- [82] X.-Y. Zhu, *Annu. Rev. Phys. Chem.* **45**, 113 (1994)
- [83] K. Al-Shamery, *Appl. Phys. A* **63**, 509 (1996)
- [84] D. Menzel and R. Gomer, *J. Chem. Phys.* **41**, 3311 (1964)
- [85] P. A. Redhead, *Can. J. Phys.* **41**, 886 (1964)
- [86] P. R. Antoniewicz, *Phys. Rev. B* **21**, 3811 (1980)
- [87] J. W. Gadzuk, L. J. Richter, S. A. Buntin, D. S. King, and R. R. Cavanagh, *Surf. Sci.* **235**, 317 (1990)
- [88] J. Gadzuk, *Surf. Sci.* **342**, 345 (1995)
- [89] T. Klüner, H.-J. Freund, J. Freitag, and V. Staemmler, *J. Chem. Phys.* **104**, 10030 (1996)
- [90] S. Thiel, M. Pykavy, T. Klüner, H.-J. Freund, R. Kosloff, and V. Staemmler, *Phys. Rev. Lett.* **87**, 077601 (2001)
- [91] S. Thiel, M. Pykavy, T. Klüner, H.-J. Freund, R. Kosloff, and V. Staemmler, *J. Chem. Phys.* **116**, 762 (2002)

- 
- [92] M. Menges, B. Baumeister, K. Al-Shamery, H.-J. Freund, C. Fischer, and P. Andresen, *J. Chem. Phys.* **101**, 3318 (1994)
- [93] J. W. Gadzuk, Hot electrons and photodesorption dynamics: Theory, In *Laser spectroscopy and photochemistry on metal surfaces* [81], pages 897–942
- [94] P. Saalfrank and R. Kosloff, *J. Chem. Phys.* **105**, 2441 (1996)
- [95] M. Nest and P. Saalfrank, *J. Chem. Phys.* **116**, 7189 (2002)
- [96] Z. Yi, D. A. Micha, and J. Sund, *J. Chem. Phys.* **110**, 10562 (1999)
- [97] D. A. Micha, A. Santana, and A. Salam, *J. Chem. Phys.* **116**, 5173 (2002)
- [98] K. Mishima and K. Yamashita, *J. Chem. Phys.* **110**, 7756 (1999)
- [99] T. Hertel, M. Wolf, and G. Ertl, *J. Chem. Phys.* **102**, 3414 (1995)
- [100] H. Kuhlenbeck, G. Odörfer, R. Jaeger, G. Illing, M. Menges, T. Mull, H.-J. Freund, M. Pöhlchen, V. Staemmler, S. Witzel, C. Scharfschwerdt, K. Wennemann, T. Liedtke, and M. Neumann, *Phys. Rev. B* **43**, 1969 (1991)
- [101] R. Wichtendahl, M. Rodriguez-Rodrigo, U. Härtel, H. Kuhlenbeck, and H.-J. Freund, *Surf. Sci.* **423**, 90 (1999)
- [102] R. Lindsay, P. Baumgärtel, R. Terborg, O. Schaff, A. M. Bradshaw, and D. P. Woodruff, *Surf. Sci.* **425**, L401 (1999)
- [103] T. Mull, B. Baumeister, M. Menges, H.-J. Freund, D. Weide, C. Fischer, and P. Andresen, *J. Chem. Phys.* **96**, 7108 (1992)
- [104] C. Rakete, Dissertation, Freie Universität Berlin, in preparation
- [105] T. Klüner, H.-J. Freund, V. Staemmler, and R. Kosloff, *Phys. Rev. Lett.* **80**, 5208 (1998)
- [106] T. Klüner, S. Thiel, H.-J. Freund, and V. Staemmler, *Chem. Phys. Lett.* **294**, 413 (1998)

- 
- [107] G. Eichhorn, M. Richter, K. Al-Shamery, and H. Zacharias, J. Chem. Phys. **111**, 386 (1999)
- [108] H. Zacharias, G. Eichhorn, R. Schliesing, and K. Al-Shamery, Appl. Phys. B **68**, 605 (1999)
- [109] D. G. Busch and W. Ho, Phys. Rev. Lett. **77**, 1338 (1996)
- [110] A. Braun, *Photodesorption von NO auf NiO(100) mit Femtosekunden-Laserpulsen aus dem Ultraviolett und Aufbau eines Flugzeitspektrometers für Elektronen optischer Energien*, Diplomarbeit, Freie Universität Berlin, 1999
- [111] S. Thiel, M. Pykavy, T. Klüner, H.-J. Freund, R. Kosloff, and V. Staemmler, J. Chem. Phys. **116**, 762 (2002)
- [112] M. Born and R. Oppenheimer, Ann. d. Phys. **84**, 457 (1927)
- [113] G. J. M. Jansen and W. C. Nieuwpoort, Phys. Rev. B **38** (1988)
- [114] S. Thiel, T. Klüner, M. Wilde, K. Al-Shamery, and H.-J. Freund, Chem. Phys. **228**, 185 (1998)
- [115] C. A. Mead and D. G. Truhlar, J. Chem. Phys. **77**, 6090 (1982)
- [116] T. Klüner, private communication
- [117] S. Thiel, T. Klüner, and H.-J. Freund, Chem. Phys. **236**, 263 (1998)
- [118] A. Ferretti, A. Lami, and G. Villani, J. Chem. Phys. **106**, 934 (1997)
- [119] K. Mølmer, Y. Castin, and J. Dalibard, J. Opt. Soc. Am. B **10**, 524 (1995)
- [120] R. Kosloff, M. A. Ratner, and W. B. Davies, J. Chem. Phys. **106**, 7036 (1997)
- [121] H. M. Wiseman and G. J. Milburn, Phys. Rev. A **47**, 1652 (1993)
- [122] T. A. Brun, Phys. Rev. Lett. **78**, 1833 (1997)
- [123] P. Saalfrank, Chem. Phys. **211**, 265 (1996)

- 
- [124] P. Saalfrank, G. Boendgen, K. Finger, and L. Pesce, *Chem. Phys.* **251**, 51 (2000)
- [125] H. Guo, *J. Chem. Phys.* **106**, 1967 (1996)
- [126] R. Schinke, *Photodissociation dynamics : spectroscopy and fragmentation of small polyatomic molecules*, Cambridge University Press, Cambridge, 1993
- [127] P. Saalfrank, *Chem. Phys.* **193**, 119 (1995)
- [128] A. Leitheußer, *Periodische Hartree-Fock-Rechnungen an Oxydoberflächen*, Dissertation, Ruhr-Universität Bochum, 2001, <http://www-brs.ub.ruhr-uni-bochum.de/netahtml/HSS/Diss/LeitheusserAndreas/>
- [129] H.-J. Freund, *Faraday Discuss.* **114**, 1 (1999)
- [130] H. Kuhlenbeck and H.-J. Freund, private communication
- [131] T. Klüner, private communication
- [132] F. Aryasetiawan and O. Gunnarsson, *Phys. Rev. Lett.* **74**, 3221 (1995)
- [133] T. Klüner, *Theoretische Beschreibung angeregter Zustände im System NO/NiO im Zusammenhang mit Laserdesorptionsuntersuchungen*, Diplomarbeit, Ruhr-Universität Bochum, 1994
- [134] R. Kosloff, *Annu. Rev. Phys. Chem.* **45**, 145 (1994)
- [135] R. Kosloff, *J. Phys. Chem.* **92**, 2087 (1988)
- [136] S. A. Rice and M. Zhao, *Optical control of molecular dynamics*, John Wiley & Sons, New York, 2000
- [137] R. Kosloff, Quantum Molecular Dynamics on Grids, in *Dynamics of Molecules and Chemical Reactions*, edited by R. Wyatt and J. Zhang, pages 185–230, Marcel Dekker, New York, 1996
- [138] H. Tal-Ezer and R. Kosloff, *J. Chem. Phys.* **81**, 3967 (1984)

- 
- [139] M. D. Feit, J. A. Fleck, and A. Steiger, J. Comput. Phys. **47**, 412 (1982)
- [140] C. Leforestier, R. H. Bisseling, C. Cerjan, M. D. Feit, R. Friesner, A. Guldborg, A. Hammerich, G. Jolicard, W. Karrlein, N. Meyer, H. D. Lipkin, O. Roncero, and R. Kosloff, J. Comp. Phys. **94**, 59 (1991)
- [141] R. Kosloff and H. Tal-Ezer, Chem. Phys. Lett. **127**, 223 (1986)
- [142] M. R. Wall and D. Neuhauser, J. Chem. Phys. **102**, 8011 (1995)
- [143] V. A. Mandelshtam and H. S. Taylor, J. Chem. Phys. **106**, 5085 (1997)
- [144] R. Baer, private communication
- [145] G. G. Balint-Kurti and A. Vibok, Complex absorbing potentials in time dependent quantum dynamics, in *Numerical Grid Methods and Their Application to Schrödinger's Equation*, edited by C. Cerjan, NATO ASI Series, Kluwer Academic Publisher, 1992
- [146] R. Heather and H. Metiu, J. Chem. Phys. **86**, 5009 (1987)
- [147] V. Kokoouline, O. Dulieu, R. Kosloff, and F. Masnou-Seeuws, J. Chem. Phys. **110**, 9865 (1999)
- [148] L. W. Ungar and J. A. Cina, Adv. Chem. Phys. **100**, 171 (1997)
- [149] M. Hillery, R. F. O'Connell, M. O. Scully, and E. P. Wigner, Phys. Rep. **106**, 121 (1984)
- [150] K. Takahashi, Prog. Theor. Phys. Suppl. **98**, 109 (1989)
- [151] A. Bartana, R. Kosloff, and D. J. Tannor, J. Chem. Phys. **99**, 196 (1993)
- [152] L. Cohen, *Time frequency analysis*, Prentice Hall signal processing series, Prentice Hall, Englewood Cliffs, NJ, 1995
- [153] J. W. Pang, T. Dieckmann, J. Feigon, and D. Neuhauser, J. Chem. Phys. **108**, 8360 (1998)



- 
- [154] V. A. Mandelshtam and H. S. Taylor, J. Chem. Phys. **107**, 6756 (1997)
- [155] V. A. Mandelshtam, J. Chem. Phys. **108**, 9999 (1998)



# Zusammenfassung

Ziel dieser Arbeit war die theoretische Behandlung des Relaxationsprozesses in der laserinduzierten Desorption kleiner Moleküle von Metalloxidoberflächen. Dies stellt ein Beispiel für ein dissipatives Quantensystem, d.h. ein Quantensystem, das Energie und Phase mit seiner Umgebung austauschen kann, dar. Die Einwirkung des Laserpulses erzeugt ein kurzlebiges Intermediat, das infolge der elektronischen Relaxation genügend kinetische Energie gewinnen kann, um von der Oberfläche zu desorbieren. Die kurze Lebensdauer des intermediären Zustandes läßt auf eine starke Wechselwirkung zwischen angeregtem Adsorbat-Substrat-Komplex und der restlichen Oberfläche schließen. Die Verwendung ultrakurzer Pulse im Experiment verhindert eine Zeitskalenseparation von Anregung und Relaxation und macht nicht-Markov-Effekte wahrscheinlich. Bisherige theoretische Ansätze sollten deshalb mit der Methode des Surrogate Hamiltonian verbunden werden, um An- und Abregungsprozesse mikroskopisch zu modellieren.

Kapitel 2 gibt einen kurzen Überblick über Dissipation in Quantensystemen und über Schwierigkeiten in ihrer theoretischen Behandlung. Insbesondere werden zwei Standardmethoden, die Quanten-Master-Gleichung und der Formalismus der dynamischen Halbgruppe, und einige neuere methodische Ansätze vorgestellt.

Die Methode des Surrogate Hamiltonian als ein nicht-Markovscher Ansatz zur Beschreibung dissipativer Quantensysteme wird in Kapitel 3 eingeführt. Der Surrogate Hamiltonian wird um die Berücksichtigung elektronischer Freiheitsgrade und um die Beschreibung von Dephasierung erweitert. Die Behandlung von Energie- als auch Phasenrelaxation wird an einfachen Beispielen demonstriert.

Eine erste Anwendung der Methode des Surrogate Hamiltonian auf ein Ladungstransferproblem ist in Kapitel 4 dargestellt. Dabei wird ein Pump-Probe-Experiment mit Femtosekundenlaserpulsen modelliert. Zwei nicht-adiabatisch gekoppelte elektronische Zustände mit harmonischen Potentialen, die Wechselwirkung mit dem elektrischen Feld des Lasers und Schwingungs- sowie Phasenrelaxation werden berücksichtigt. Es konnte gezeigt werden,

daß die Anwendung des Surrogate Hamiltonian eine vollständige Beschreibung des Ladungstransferereignisses liefert.

Theoretische Modelle zur Beschreibung der laserinduzierten Desorption werden in Kapitel 5 vorgestellt. Desweiteren sind bisherige experimentelle und theoretische Ergebnisse für die laserinduzierte Desorption von NO von der NiO(100)-Oberfläche zusammengefaßt. Die Anforderungen an eine theoretische Modellierung von Anregungs- und Relaxationsprozeß werden ausführlich diskutiert.

Kapitel 6 ist zwei semi-phänomenologischen Ansätzen zur Beschreibung des Relaxationsprozesses gewidmet. Zuvor werden mögliche Anregungsmechanismen diskutiert. Die Relaxation wird dann durch nichtadiabatische Kopplung des elektronisch angeregten an einen dritten Zustand sowie mittels der Monte-Carlo-Wellenfunktions-Methode modelliert.

Die Anwendung des Surrogate Hamiltonian auf die laserinduzierte Desorption ist in Kapitel 7 dargestellt. Dafür wird ein mikroskopisches Modell für die Wechselwirkung zwischen angeregtem Adsorbat-Substrat-Komplex und Elektron-Loch-Paaren in der Oberfläche entwickelt. Alle Parameter des Modells können aus Rechnungen zur elektronischen Struktur von NiO abgeschätzt werden. Die Konvergenzeigenschaften der Methode sowie die Abhängigkeit der Observablen von experimentell justierbaren Parametern werden ausführlich diskutiert. Insbesondere werden Desorptionswahrscheinlichkeiten und Desorptionsgeschwindigkeiten in derselben Größenordnung wie im Experiment erhalten. Damit gelingt erstmalig eine vollständig mikroskopische Beschreibung der laserinduzierten Desorption von NO/NiO(100).

Die Arbeit wird in Kapitel 8 zusammengefaßt. Die mathematischen und numerischen Grundlagen sowie die Parameter der Simulationen sind im Anhang im Detail aufgeführt.

# Acknowledgements

## – Dank – תודות

I wish to express my gratitude toward Prof. Hans-Joachim Freund and Thorsten Klüner who gave me the opportunity to pursue a PhD at the Fritz-Haber-Institut and who introduced me to the field of surface science. Many thanks to Volkhard May who accepted to be the official advisor of my thesis. I am most grateful to Prof. Ronnie Kosloff who has been a very patient, cheerful and encouraging teacher. **רוני, תודה רבה!**

Many people at the Hebrew University Jerusalem made my stays there very pleasant. I would like to particularly mention Nick Wright, José Palao, Dani Steinitz and Shelly Tzlil. Furthermore, I would like to thank Roi Baer, Jiří Vala, Prof. David Tannor, Efrat Rosenman and Anna Pomyalov for very helpful discussions. Financial support from the German-Israeli Foundation is gratefully acknowledged.

At home in Berlin, the staff of the Fritz-Haber-Institut made up for the lack of sunshine. Stephan Thiel and Anne-Claire Dupuis have been amiable office mates. Mike Wesemann and Heinz Junkes were there when help with system administration was needed. Karin Klug and Heiko Hamann offered besides cookies support and encouragement many times. I am grateful to Randall Meyer and Thorsten Klüner for proof-reading the manuscript.

I wish to thank my friends and family for their interest and words of support. I am grateful to Yvonne Rothmund for accompanying me a long way. Karen Böhme has been an invaluable source of strength during the writing of this thesis.

Danke!



Hiermit erkläre ich, daß ich diese Dissertation selbständig und ohne unerlaubte Hilfe angefertigt habe.

Berlin, den 26. Juni 2002

Christiane Koch